Development of Silk Based Matrices for Cartilage and Osteochondral Tissue Engineering

A Thesis

Submitted in Partial Fulfillment of the

Requirements for the Degree of

DOCTOR OF PHILOSOPHY

by

YOGENDRA PRATAP SINGH

Department of Biosciences and Bioengineering

Indian Institute of Technology Guwahati

Guwahati – 781039, Assam, India

December 2021

Dedicated to my

Family and Friends

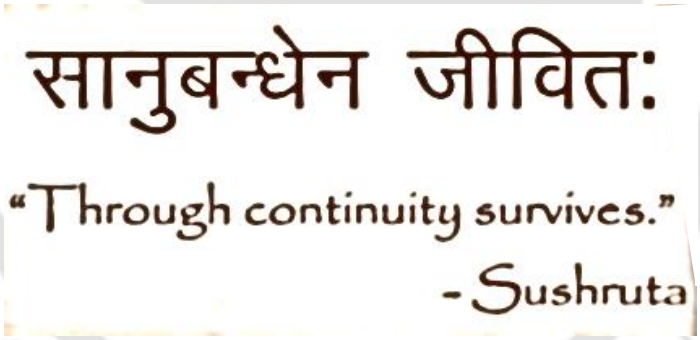

INDIAN INSTITUTE OF TECHNOLOGY GUWAHATI

DEPARTMENT OF BIOSCIENCES AND BIOENGINEERING

STATEMENT

I do hereby declare that the research findings of this thesis are the result of research work carried out by me in the Department of Biosciences and Bioengineering, Indian Institute of Technology Guwahati, Guwahati, India, under the supervision of Prof. Biman B. Mandal.

As per the general norms of reporting research findings, due acknowledgments have been made, wherever the research findings of other researchers have been cited in this thesis.

Date: 16.12.2021 **Yogendra Pratap Singh**

INDIAN INSTITUTE OF TECHNOLOGY GUWAHATI

DEPARTMENT OF BIOSCIENCES AND BIOENGINEERING

CERTIFICATE

It is certified that the work described in this thesis entitled "**Development of silk based matrices for cartilage and osteochondral tissue engineering**" by **Mr. Yogendra Pratap Singh** for the award of degree of **Doctor of Philosophy (Ph.D.)** is an authentic record of the results obtained from the research work carried out under my supervision in the Department of Biosciences and Bioengineering, Indian Institute of Technology Guwahati, India, and this work has not been submitted elsewhere for the award of any other degree.

CERTIFIED

Yogendra Pratap Singh
(Candidate)
Roll No: 146106044

Biman B. Mandal, Ph.D.
(Thesis Supervisor)

Date: 16.12.2021

ACKNOWLEDGEMENT

This PhD journey has been a truly life-changing experience for me and it would not have been possible without the support and guidance that I received from many people.

First and foremost, I would like to express my sincere gratitude to my thesis advisor Prof. Biman B. Mandal, BSBE, IIT Guwahati for his continuous support, encouragement, and thoughtful insights. I thank him for his guidance, constant feedback, and valuable suggestions in successful completion of this thesis. His dynamism, vision, and enthusiasm has always inspired and encouraged me not only in academic research but also in daily life. It has been a sheer honor and a privilege to have learned from him.

Many thanks to the esteemed members of my Doctoral Committee, Dr. Manish Kumar (Chairperson), Dr. Shankar Prasad Kanaujia, Department of Biosciences and Bioengineering (BSBE), and Dr. Akshai Kumar Alape Seetharam, Department of Chemistry, IIT Guwahati for their valuable and constructive suggestions throughout this journey.

I would also like to thank the present Head of the Department of BSBE, Prof. Latha Rangan, and former HODs Prof. Kannan Pakshirajan, and Prof. V. Venkata Dasu for providing the necessary administrative support, along with allowing me to use the departmental central instruments facilities.

I am also grateful to all faculty members and staff of Dept. BSBE, the Institute R&D section, Student Affairs, and Academic section for all their help throughout my Ph.D. tenure. I would also like to thank the Central Instruments Facility (CIF), IIT Guwahati for providing access to high-end equipments to execute my experiments.

I gratefully acknowledge the funding received from the funding agencies that provided me the financial support to conduct my research. I am grateful to the funding support from several research grants received by Prof. Mandal from Department of Biotechnology (DBT), Department of Science and Technology (DST), Science and Engineering Research Board (SERB), and Defence Research and Development Organization (DRDO), Government of India. I am sincerely grateful to Ministry of Education (MoE) and IIT Guwahati for providing me with fellowship during my Ph.D. tenure. I also thank the Indo French Centre for Promotion of Advanced Research

(CEFIPRA) for awarding me with “Raman-Charpak Fellowship 2017-18” to carry out research in France, and the Newton-Bhabha Fund (Department of Biotechnology, Government of India and British Council, UK) for awarding me with “Newton Bhabha Ph.D. Placement Programme 2017-18” to carry out research work in the UK during my Ph. D. tenure.

I would like to extend my sincere gratitude to Dr. Chris Holland, Natural Materials Group, University of Sheffield, UK for hosting me during Newton-Bhabha fellowship and Pete, Andreas, Edgar, Anastasia, Jamie, and Nicola for help, suggestions, and creating a good working environment at Dr. Holland’s lab. My sincere thanks to Prof. Daniele Noel, INSERM, France for hosting me during Raman-Charpak fellowship, Prof. Jorgensen for all administrative support and guidance, and Claire, Karine, Marie Maumus, Marie Morille, Maxime for help, suggestions, and creating a good working environment at Prof. Noel’s lab.

Special thanks to Dr. Nandana Bhardwaj, Sr Scientist, STANVAC for collaborative works and giving her invaluable expert advice whenever needed. Her friendly guidance, unconditional support and technical suggestions were instrumental in the successful completion of my thesis work.

The help provided by Prof. Samit Kumar Nandi, WBUAFS, Kolkata in animal experimentations is deeply acknowledged. I thank Prof. Niranjan Karak, Tezpur University for collaborative work. I also thank my co-authors Joseph, Ashutosh and Bibhas for their active support in all the scientific collaborations. Many thanks to all the media outlets and news reporters who highlighted and conveyed our research to the wider community.

My heartfelt thanks to all my current lab members - Bibhas, Shreya, Prerak, Joseph, Janani, Ashutosh, Bibrita, Chitra, Souradeep, Sayanti, Ananya, Priyanka for their help, feedback and cooperation. I would also like to thank former lab members Dr. Manishekhar, Dr. Praveen, Dr. Dimple, Dr. Ankit, Dr. Rocktotpal, Dr. Deepika, Dr. Bhaskar, Dr. Biswajeet, Dr. Rajiv, Dr. Chandramouli, Salma Di, Omkar, Sohenii, Suvro, Namit, Mimi, and Tarishi for sharing their knowledge and stimulating discussion with me. Thank you all for constantly providing the friendly environment in the lab and making this journey a memorable one.

Thanks to my fellow marathon-runners Joseph, Amarendra, Ashutosh, Zubin, and Prerak who accompanied me and kept me motivated. Running indeed refueled me and kept me healthy, happy, and stress-free.

A very special thank you to Dr. Gaurangi Maitra, my all-time well-wisher, teacher, friend, fellow-biologist, fellow-nature club member, and fellow-traveler for being on this journey with me. I remember dreaming of this day together. Thank you for all the motivation, guidance and bearing with me. A big thank you to Nived amma for always being there for advice and guidance for a balanced life.

Last but not the least; I would like to thank my family, especially my Dad for the tremendous understanding and encouragement throughout this journey. Special thanks to Chajis, Debo, Mohit, Ravi, Rohini, Shweta for their love and support and my super sweet Grandmother for blessing me and sharing with me so many interesting anecdotes about life and beyond.

Thank you, Universe, for showering your blessing upon me to complete my thesis work successfully.

Yogendra Pratap Singh

CONTENTS

ABBREVIATIONS

µL	Microliter
µm	Micrometer
2D	2-dimentional
3D	3-dimentional
ACAN	Aggrecan
ACI	Autologous chondrocyte implantation
ADAMTSs	A Disintegrins and metalloproteinases with thrombospondin motifs
ADMSCs	Adipose derived mesenchymal stem cells
AM	Additive manufacturing
β-TCP	β-tricalcium phosphate
BMMSCs	Bone marrow derived mesenchymal stem cells
BMPs	Morphogenic proteins
CAD	Computer aided design
CAGR	Compound annual growth rate
CaP	Calcium phosphate
CD68	Cluster of differentiation 68
COX	Cyclooxygenase
CS	Chondroitin sulfate
CT	Computed tomography
CXB	Celecoxib
DAB	3,3'-diaminobenzidine

Abbreviations

DAPI	4′,6-diamidino-2-phenylindole
Dex	Dexamethasone
DLP	Digital light processing
DLS	Dynamic light scattering
DMEM	Dulbecco's modified eagle medium
DMMB	1,9-dimethylmethylene blue
DNA	Deoxyribonucleic acid
EBB	Extrusion-based bioprinting
EBP	Extrusion-based printing
ECM	Extracellular matrix
EDC	1-ethyl-3(3-dimethyl aminopropyl) carbodiimide
EDTA	Ethylenediaminetetraacetic acid
FBS	Fetal bovine serum
FESEM	Field emission scanning electron microscope
FDA	Food and drug administration
FDM	Fused deposition modelling
FGF	Fibroblast growth factor
FTIR	Fourier transform infrared spectroscopy
G′	Storage modulus
G″	Loss modulus
GAPDH	Glyceraldehyde-3-phosphate-dehydrogenase
GDF-5	Growth and differentiation factor-5
GelMA	Gelatin methacryloyl
GFs	Growth factors

GPa	Gigapascal
h	hour
H&E	Hematoxylin and eosin
HA	Hyaluronic acid
HAp	Hydroxyapatite
HCl	Hydrochloric acid
HIF-1α	Hypoxia inducible factor-1α
HRP	Horseradish peroxidase
IBD	Image-based design
IHC	Immunohistochemistry
IL	Interleukin
IPN	Interpenetrating network
iPSCs	Induced pluripotent stem cells
ITS+	Insulin-transferrin-sodium selenite
kDa	Kilo dalton
kPa	Kilopascal
kV	Kilo volt
LiBr	Lithium bromide
LPS	Lipopolysaccharide
LVER	Linear viscoelastic region
M	Molar
MAPK	Mitogen activated protein kinase
MF	Microfracture
mg	Milligram
mL	Milliliter

mM	Millimolar
mm	Millimeter
MMPs	Matrix metalloproteinases
MPa	Megapascal
MRI	Magnetic resonance imaging
MSCs	Mesenchymal stem cells
MW	Molecular weight
MWCO	Molecular weight cut-off
N	Newton
NBF	Neutral buffered saline
NF-κB	Nuclear factor kappa B
ng	Nanogram
NHS	N-hydroxysuccinimide
nM	Nanomole
nm	Nanometer
NO	Nitric oxide
NSAIDs	Nonsteroidal anti-inflammatory drugs
OA	Osteoarthritis
OATS	Osteochondral autograft transfer system
OC	Osteochondral
OCA	Osteochondral allograft transplantation
PAGE	Polyacrylamide gel electrophoresis
PBS	Phosphate buffered solution
PCL	Poly(ε-caprolactone)
PDLLA	Poly(D,L-lactide)

PDMS	Polydimethylsiloxane
PEGDA	Poly(ethylene glycol) diacrylate
PEGDMA	Poly(ethylene glycol) dimethacrylate
pg	Picogram
PGA	Polyglycolic acid
PGE2	Prostaglandin E2
Phe	Phenylalanine
pHEMA	Poly(2-hydroxyethyl methacrylate)
PLGA	Poly(lactic-co-glycolic)
PLLA	Poly(L-lactic acid)
PNIPPAm	Poly(N-isopropyl acrylamide)
PPF	Polypropylene fumarate
PRP	Platelet rich plasma
PTH	Parathyroid hormone
PVA	Polyvinyl alcohol
PVP	Poly(vinyl pyrrolidone)
RGD	Arginine-glycine-aspartic acid
RHN	Rhein
RNA	Ribonucleic acid
ROS	Reactive oxygen species
RSF	Regenerated silk fibroin
RT	Room temperature
RT-PCR	Real time polymerase chain reaction
SD	Standard deviation
SDS	Sodium dodecyl sulfate

SEM	Scanning electron microscopy
SF	Silk fibroin
SFF	Solid free form
SS	Silk sericin
sGAGs	Sulfated glycosaminoglycans
tan δ	Loss modulus/storage modulus
TCP	Tissue culture plate
TGF-β	Transforming growth factor-β
THAA	Total hydrolysable amino acids
TIMPs	Tissue inhibitors of MMPs
TNF-α	Tumor necrosis factors-α
Trp	Tryptophan
Tyr	Tyrosine
UTM	Universal testing machine
v/v	Volume/volume
w/v	Weight/volume
γ	Shear strain
η	Complex viscosity
µg	Microgram
µS/cm	Microsiemens per centimeter
ω	Angular frequency

LIST OF TABLES

CHAPTER 4

CHAPTER 5

CHAPTER 6

CHAPTER 7

LIST OF FIGURES

CHAPTER 3

CHAPTER 4

CHAPTER 5

CHAPTER 6

CHAPTER 7

SUMMARY

Chapter 1

Introduction and Literature Review

Introduction and Literature Review

1.1 Introduction

1.1.1 The structure

The osteochondral unit is present in the articulating joints and consists majorly of articular cartilage and a subchondral bone. The articular cartilage is hyaline cartilage, 2-4 mm thick, avascular, alymphatic, and aneural tissue with a dense extracellular matrix (ECM) and sparsely distributed chondrocytes which constitute around 2% of the total cartilage volume [1]. The osteochondral tissue possesses a discrete zonal structure where each zone has a unique ECM composition, collagen fiber orientation, and chondrocyte number, and morphology [2]. These zones arranged from the articulating cartilage surface to the inner bone are termed: the superficial zone (SZ), middle zone (MZ), deep zone (DZ), a tidemark, calcified zone (CZ), and finally the subchondral bone section separated by the cement line [3], as shown in **Figure 1.1**. The unique zonal arrangement specifically modulates the functioning of the osteochondral tissue. The topmost SZ (10-20%) has collagen fibrils aligned parallel to the articular surface and consists of squamous chondrocytes. The thin and densely packed collagen fibrils of this layer provide strength and resistance to shear through articulation and control fluid permeability. The MZ (40-60%) has the highest proteoglycan content with obliquely arranged collagen fibers and rounded chondrocytes. The DZ (30%) has collagen fibrils that are organized perpendicular to the articular surface and have vertical columns of chondrocytes. These collagen fibrils strengthen the bonding between cartilage and bone. The next layer is CZ which is separated from the DZ by a discrete band of mineralized cartilage called the “tidemark”. The CZ is the point of transition from the soft cartilage to the stiff subchondral bone and functionally cements the non-calcified cartilage to bone. Chondrocytes present here are bigger and more widely dispersed with an increased tendency towards hypertrophy. The vertical collagen fibrils that extend from the DZ to the calcified cartilage *via* the tidemark play a crucial role in transitioning mechanical forces and providing mechanical stability to the tissue [1]. Directly underneath the CZ lies a subchondral bone plate consisting of a bony lamella (cortical endplate, 1–3 mm thick), which is separated by a “cement line” from the calcified cartilage. Along with the trabeculae and subarticular spongiosa, they form the subchondral bone unit [4].

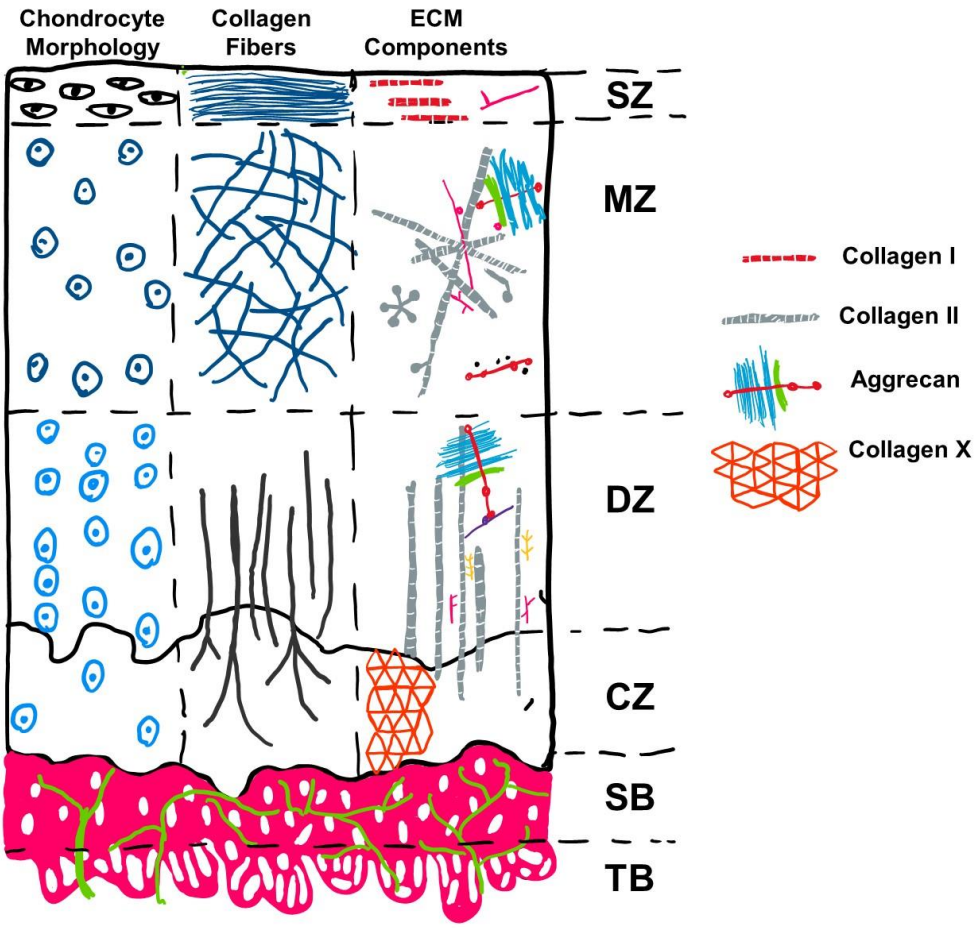

Figure 1.1. *Schematic representation of osteochondral tissue structure. SZ, superficial zone; MZ, middle zone; DZ, deep zone; CZ, calcified zone; SB, subchondral bone plate; and TB, subchondral trabecular bone.*

The osteochondral tissue has unique biomechanical properties owing to its unique structure [3], where the articular cartilage is made up of ECM (95%–99% total volume, 80% water, and 20% solid contents), majorly composed of collagen and proteoglycans. Among the collagens, type II collagen is predominant in articular cartilage, where it accounts for approximately 90% of the total collagen [5]. Collagen fibers are arranged in a hierarchical manner formed due to the assembly of procollagen monomers resulting in fibrils [6] with an anisotropic depth-dependent arcade-like organization. The fibers are organized parallelly and densely packed at the superficial zone while perpendicular at the deep regions with considerably more isotropically organized small fibers in the middle zones. Additionally, the fiber diameter also increases with depth with ~ 20–50 nm in the superficial zone and ~ 110 nm in the deep zones [7]. Other collagens are found in lower quantities, such as type I (mainly found in fibrocartilaginous tissue) present in the superficial zone,

while type IX, and type XI help in the crosslinking between fibrils, and communication with other biological molecules [5]. Collagen X is another crucial component present in the deep and calcified zones and involved in the mineralization procedure in the osteochondral tissue [8]. This variation in the structure, organization and collagen type in the osteochondral unit is responsible for the innate mechanical strength of the tissue giving it load-bearing capabilities. Proteoglycans (mucoproteins) are other major ECM components of the articular cartilage, composed of a core protein and covalently attached glycosaminoglycans (GAGs). GAGs are highly negatively charged linear polysaccharides with building blocks (disaccharides) involving an amino sugar (either N-Acetylglucosamine or N-Acetylgalactosamine) and a uronic acid (glucuronic acid and iduronic acid) [9]. The amount of proteoglycans and GAGs varies with depth in articular cartilage with the maximum presence in the middle zone [10]. Aggrecan is a key proteoglycan attached to GAGs, keratan sulphate, and chondroitin sulphate. These bind to hyaluronic acid (HA) backbone to form negatively charged aggrecan-hyaluronan aggregates which cause an osmotic pressure, the Donnan effect, created as water is entrapped inside causing swelling [11]. This causes high tensile stress on the neighboring collagen network due to the turgidity and the structural detention provided by the collagen fibers which limits dislocation of the GAGs and proteoglycans providing cartilage with the high mechanical load-bearing capability to transfer and distribute loads efficiently.

The transition from cartilage to subchondral bone is another critical component consisting of the subchondral bone plate which is a dense bony lamella that fuses into a network of trabecular bone named the subarticular spongiosa [12]. The collagen fibers in the radial zone outspread to the tidemark zone into calcified cartilage. The thickness of the subchondral plate differs according to the biomechanical force it experiences and also on the joint geometry, loading conditions, and reasons such as age, weight, and exercise [13]. The subchondral plate undergoes remodeling due to altered biomechanics as a result of joint damage or injury to adjoining cartilage. As opposed to cartilage, the subchondral bone contains blood vessels, thus providing nutrients to itself and the overlaying cartilage [12]. The concentric lamellar layers around osteons and flat layers are indicative of new bone development. The subchondral bone also functions to anchorage the collagen fibrils and helps in the maintenance of the joint. The cortical region of the subchondral layer shows high stiffness, low porosity (5-30%), and vascularity, while the trabecular region exhibits randomly oriented trabeculae with higher porosity (30-90%) [14]. Most of the porous regions in the subchondral bone are occupied by vessels and nerve fibers that provide bone cells

with nutrients and disposes the generated waste. Cellular constituent of subchondral bone includes osteoblasts, osteocytes, and osteoclasts that modulate the tissue remodeling. The hematopoietic (HSCs) and mesenchymal stem cells (MSCs), along with adipose depot in the trabecular pores occupied with bone marrow support the process of regeneration.

The specifically arranged ECM components of the cartilage and subchondral bone tissues determine their strength with a depth-dependent variation in compressive modulus from the top cartilage to the deep zone with values of 0.079, 2.1, and 320 MPa of superficial, middle, and deep zones, respectively [15]. The organic and inorganic components of the bone impart its anisotropic properties with a compressive modulus of subchondral bone being 5.7 GPa, which is higher than that of cartilage, while the tensile modulus is ~2 GPa [16, 17]. Trabecular bone shows better performance under compression than tension, and its compressive elastic modulus and compressive strength are in the range of 1–900 MPa and 1–10 MPa, respectively [14, 18]. Thus, the varied compositions and mechanical characteristics of bone and cartilage direct the complexity of these tissues and their interface, representing a major challenge for the fabrication of tissue-engineered scaffolds for OC joint repair.

1.1.2 The function

The articular cartilage and subchondral bone tissues are linked by an interface allowing them to work together to help the entire osteochondral unit perform its functions and to maintain healthy joint homeostasis. Damage to any one of these subunits modifies the fine mechanical and biochemical balance prevailing within the tissue, leading to more complex conditions if left unattended. The osteochondral tissue performs mainly structural and biomechanical roles majorly as load-bearing with tribological functions such as lubrication, and reduced friction and wear-and-tear of the tissue [1]. The articular cartilage is a specialized connective tissue with viscoelastic properties which can withstand high cyclic loads with prime function to provide a smooth, lubricated surface for low friction articulation and transfer of load to the subchondral bone [1, 19]. The compressive properties are a result of a combination of viscoelasticity and permeability. The matrix of articular cartilage can be considered to be a biphasic medium with a fluid phase (water with inorganic ions), and a solid phase composed of the ECM [11, 20]. The articular cartilage exhibit both creep (due to constant loading) and stress relaxation behaviour which are two important characteristics of a viscoelastic material. As cartilage undergoes compression, it

undergoes a constant deformation and responds with high initial stress which decreases until an equilibrium is reached. This time-dependent stress response is stress-relaxation [11]. Due to its viscoelastic nature, the stiffness of cartilage depends directly on the compressive force applied to it, forming a stiffer matrix when a force applied is rapid.

Compression in the joint causes cartilage to deform and produce a bulk flow of water from the ECM into the synovial space [21]. This ability of the ECM to limit water permeability imparts its resistance to compression [22], which is ideal in healthy cartilage where the water flow can dissipate most of the energy imparted onto the tissue during compression. However in the case of damaged cartilage, there is less restriction in movement of water movement, and more of the compression force is imparted to ECM, which leads to degeneration [13]. Thus, the resistance to water flow is regulated by viscosity, osmolarity, and interstitial pressure of the ECM. Collagen type II and proteoglycans (notable aggrecan) are two major ECM molecules that play a crucial role in the load-bearing property. The interaction between these highly negatively charged cartilage molecules provides the compressive and tensile strength of the tissue [23]. Furthermore, the complex gradient organization of cartilage in terms of collagen fibrils and ECM in the middle zone plays a significant role in its shear-resistant properties while the stretching of the randomly dispersed collagen fibrils offers cartilage with its shear stress response [24].

The compressive force experienced by cartilage is passed to the stiffer underlying bone via the interface. During physiological loading, most of the tissue deformation happens in the superficial layer of cartilage, with very little compression occurring in the radial zone near the cartilage/bone interface. This interface provides anchorage of cartilage to the underlying bone and conducts force transfer from cartilage to subchondral bone. The subchondral bone serves to provide mechanical strength, nutrition, and nociception (the detection of pain stimulus). It is vital to the functioning and homeostasis of the joint as it enhances the load-bearing capacity by attenuating the majority of the load. The subchondral bone attenuates about 30% of the overall load of the joint while only 1–3% is attenuated through cartilage [4]. The tensile and shear properties also play a crucial role in the proper functioning of the tissue. Thus, all components of the osteochondral tissue must remain healthy for the proper functioning of the unit. Any damage to it, warrants its repair on time, as if left untreated it advances into complex conditions such as osteoarthritis.

1.1.3 The clinical condition – "Osteoarthritis"

The clinical condition associated with the damage of cartilage and osteochondral tissue is called as osteoarthritis (OA). OA is the most common form of arthritis and a chronic degenerative joint disease. This musculoskeletal disorder affects millions of people globally making it one of the prominent causes of disability worldwide, particularly in the aging population. OA has a considerable impact and economic burden on the individual patient and society. Its prevalence reached a soaring 303 million people globally in 2017 [25], and is predicted to touch 350 million by 2025. Factors such as the fast-growing older population, along with an increasingly sedentary lifestyle, are expected to establish OA as the most common form of the musculoskeletal disease by 2040. In December 2016, the Osteoarthritis Research Society International (OARSI) submitted a White Paper entitled "Osteoarthritis: A Serious Disease" to the U.S. Food and Drug Administration, advocating OA as a severe condition with no known cure, and no interventions to halt its progression or manage its symptoms with an acceptable benefit-risk profile [26].

The etiology of OA is complex and multifactorial; thus, its prevention and treatment remain challenging. OA can affect any joint, but the most common are the knee, hands, hip, and spine. The joint is a multi-tissue organ composed of articular cartilage, subchondral bone, and the synovial membrane, and its effective functioning relies on the sustenance of joint homeostasis, which is a dynamic balance among the anabolic and catabolic processes [27]. Increasing evidence illustrates a complex interplay between the components of the joint, making our understanding of OA pathogenesis ever more challenging [28]. The clinical symptoms of OA include thinning of cartilage causing the bone ends to rub together creating stiffness, inflammation, pain, and impaired movement. Old age, lack of physical activity, high impact sports, genetic predisposition, occupational injury, obesity, trauma, bone density, and gender are some factors involved in its development [29]. Amending these factors may well decrease the risk of OA and avert subsequent pain and disability.

The signs and symptoms of OA include pain, swelling, stiffness, bone spurs, tenderness, loss of flexibility, grating sensation, crepitus, loss of function, and joint deformity. The diagnosis is performed using imaging tests and other laboratory tests. Imaging tests such as X-rays and MRI are most commonly used. The use of X-ray images doesn't directly image cartilage, but cartilage loss is revealed by visible bone spurs and a narrowed space between the end of long bones.

However, MRI gives a detailed analysis of both the bone and soft tissues, including cartilage. The laboratory test includes analyzing the blood or joint fluid for OA markers. An appropriate and early-stage diagnosis helps better management of OA. Based on the severity, there are different stages of knee OA. Stage 1 is "Minor" where patients develop bone spurs and minor wear-and-tear of the cartilage and can be treated using supplements such as glucosamine and chondroitin sulfate. Stage 2 is "Mild" where diagnosis indicates more bone spur growth in the knee joints, with increased wear-and-tear of the cartilage initiating pain in the joint. The cartilage and soft tissues may look healthy but the breakdown of the cartilage matrix has been initiated and treatment includes different nonpharmacologic therapies to help relieve the pain and discomfort. Stage 3 is "Moderate" where clear erosion of the cartilage surface with a narrowing gap between the end of long bones. The broken collagen and proteoglycan fragments increase in the synovial fluid as the disease progresses, with prominent and rougher bone spurs along with joint, pain, stiffness, and inflammation. Treatments include NSAIDs, intra-articular injection of hyaluronic acid, and other pain-relief therapies. Stage 4 is "Severe" where the space between the end of bones in the joint is considerably reduced, causing the cartilage of the end of long bones to rub against each other causing them to wear off, leaving the joint stiff and painful. The cartilage breakdown products further lead to chronic inflammation, with decreased synovial fluid that causes friction, greater pain, and discomfort in joint movement. This is accompanied by increased production of synovial MMPs, and cytokines which cause further damage and inflammation of the joint tissues. Treatments include performing osteotomy or bone realignment surgery which protects the joint by shifting the weight of the body away from the site of bone damage. In most severe cases, total knee replacement, or arthroplasty is the only available option where the damaged or arthritic joint is surgically replaced with a plastic, metal, or ceramic prosthesis. However, this is an expensive and technically demanding surgery with disadvantages such as wearing out of the prosthesis over time, wound healing issues, difficulties with some movements, and numbness of the site.

Being a load-bearing tissue, the osteochondral unit is subjected to a lot of stress and therefore is more prone to damage. The caused injuries, if left untreated may eventually lead to the development of OA with progression over time, where the osteochondral tissues undergo significant alterations in terms of structure and function. This OA is marked by loss of articular cartilage, remodeling of subchondral bone, and thickening of the articular joint capsule (**Figure 1.2**) [30]. Current data from medical sources indicate that OA is also caused by mechanically

induced conditions with a complex etiology contributed by both genetic and acquired (due to environmental factors) [31]. Despite the initial dilemma over the progression of OA, whether first lesions are changes in the articular cartilage or the underlying bone; growing evidence clearly demands inclusion of OA among degenerative diseased conditions prevalent in the whole joint in general and OC tissue in particular. The involvement of both bone and cartilage in OA degeneration, renders their unrelated investigations inconclusive [32].

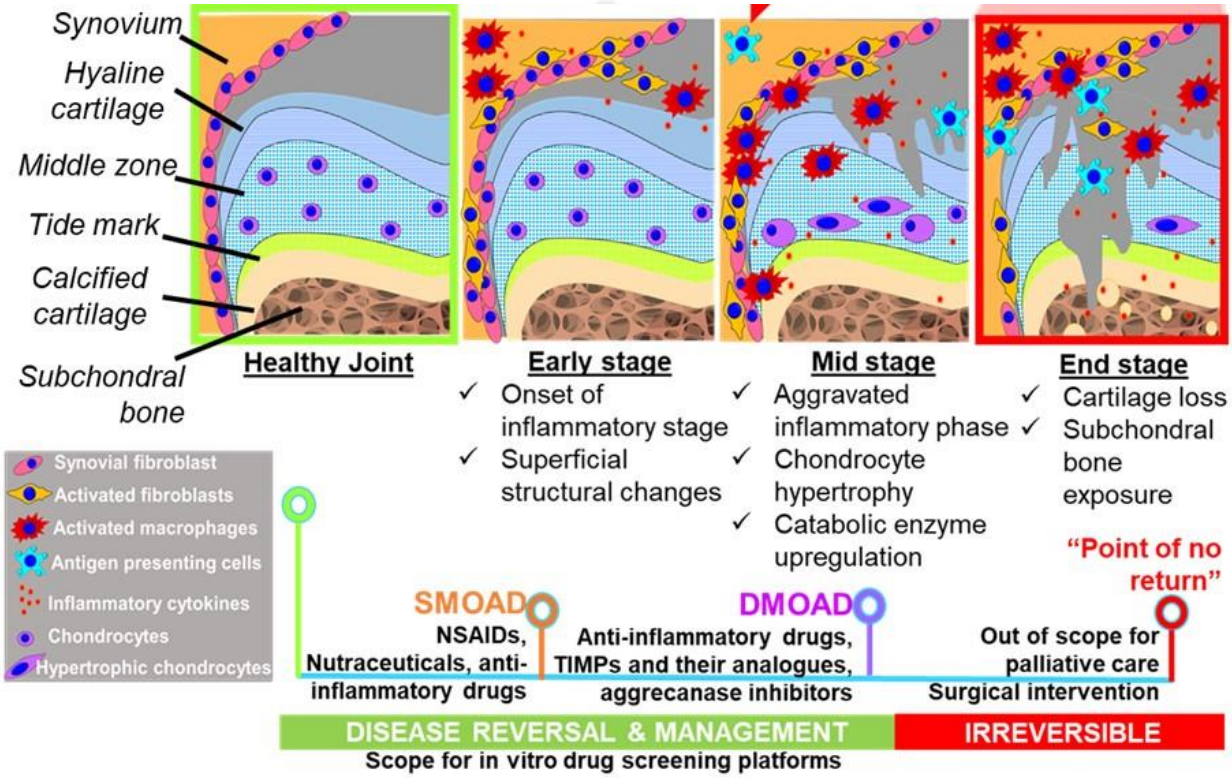

Figure 1.2. *Overview of different stages of osteoarthritis with their characteristic traits and plausible intervention stages using structure modifying and disease-modifying OA drugs.*

1.1.4 Current treatment strategies

In the clinic, the current approaches to treat osteochondral lesions can be classified into palliative, reparative, and restorative techniques [33]. Palliative procedures include articular debridement and lavage for the relief of the patient's symptoms. The early stages of OA are usually dominated by symptoms such as pain and stiffness, with treatment strategies such as physical therapy, analgesics, and NSAIDs aimed to reduce the pain and stiffness and to resist the structural deterioration of the damaged tissue [34]. Methods such as the intra-articular injection of long-acting glucocorticoids is an effective treatment in managing the inflammation. Hyaluronic acid has shown improved

results in the management of knee pain when used as intra-articular injections for the treatment of OA [35].

Reparative procedures including arthroscopic abrasion arthroplasty, abrasion chondroplasty, and microfracture are bone marrow stimulating techniques and the next level of treatment. The microfracture (MF) marrow stimulation has shown to be a beneficial treatment especially in the case of smaller cartilage defect areas. MF is a minimally invasive technique where the injured cartilage is removed and the underlying bone surface is drilled to allow blood and bone marrow along with MSCs to come through to the osteochondral interface and contribute to the formation and repair of the osteochondral tissue [4]. However, in most cases, the regenerated cartilage is mainly fibrocartilage which has lower durability as compared to the hyaline cartilage. Fibrocartilage majorly consists of collagen type I with a disorganized matrix that does not possess the required viscoelastic and biomechanical characteristics of normal hyaline cartilage and can fatigue due to high shear forces experienced in the joint, aggravating to articular surface irregularity and further arthritic damage [36].

Other treatment strategies for the treatment of osteochondral defects include osteochondral autograft procedures such as the osteochondral autograft transfer system (OATS), which involves the transplantation of osteochondral plugs taken from low weight-bearing joint areas to fill the defect site. The technique is advantageous in terms of repairing the defect with mature hyaline cartilage with the possibility to treat the entire osteochondral unit [37]. However, it is most feasible only for focal chondral defects diagnosed during the early stages of OA. Also, depending on the requirement, osteochondral allograft (OCA) transplantation for the knee has been performed in the treatment of large chondral or osteochondral defects. OCA transplantation includes the transfer of a natural, matching piece of mature, viable hyaline cartilage tissue to the recipient's defect site [38]. However, the risk of disease transmission from the allograft is a major challenge with OCA and this is not recommended for OA. Taking advantage of being a one-step autologous strategy and decreasing the risk associated with donor site morbidity, the cartilage paste grafting technique is another procedure [39]. It involves taking the patient's marrow-based stem cells, pieces of bone, and cartilage from non-weight bearing intercondylar notch of the knee, and grinding it into a paste, and implanting back into the defect. The favorable environment resulting from the interaction of bone marrow stem cells with the combination of osteochondral matrix and live chondrocytes

stimulates the repair of cartilage. However, limitations include the chances of delamination, the graft remains fragile for several months after the procedure, chances of more pain, stiffness, loss of motion, and generation of fibrous tissue.

Finally, restorative methods that make use of bioengineering techniques to develop hyaline cartilage tissue such as autologous chondrocyte implant (ACI) have become important surgical alternatives in the treatment of chondral lesions of the knee. ACI as a technique has evolved for the betterment and could be understood in 4 generations [40]. The first-generation ACI involved inoculation of expanded chondrocytes under a membrane flap but was associated with periosteal graft hypertrophy, delamination, and technical difficulties in fixating the flap in addition to immune reaction, large surgical exposition, and time-consuming. In the second-generation ACI, a porcine collagen membrane (ACI-C) was used to cover the treated lesion thereby decreasing the operating time and reducing the graft complications. The third-generation ACI used a matrix (commonly referred to as MACI, matrix-assisted chondrocyte implantation) seeded with autologous chondrocytes for cartilage repair. The matrix has chondro-inductive or chondro-conductive properties and a specific mechanical profile that allows for better distribution and growth of the chondrocytes. The fourth-generation ACI used a matrix (MASI, matrix-induced autologous stem-cell implantation) seeded with stem cells to treat the cartilage lesion. Most of these ACI procedures have shown good clinical outcomes as compared to other previously described techniques, however, these improvements are not always statistically significant. Overall, it could be said that the partial success of current treatments has been handicapped by the need for complicated surgical procedures, donor site morbidity, lack of donors, risk of infections, poor integration with the surrounding tissue, and formation of mechanically and chemically inferior fibrocartilage instead of hyaline cartilage. Therefore, viable alternatives to develop strategies that repair and restore the incapacitated osteochondral tissue function, are vital to clinicians and their patients.

The pharmacological management of OA includes controlling the inflammation through the use of non-steroidal anti-inflammatory drugs (NSAIDs), which are inhibitors of cyclooxygenase-2, and intra-articular corticosteroid injections [41]. However, these treatments do not restore the damaged tissues and joints to normal functional health. As the molecular mechanisms associated with the initiation and progression of OA are not well understood, it is quite challenging to develop

appropriate therapeutic interventions for the restoration of degraded OC tissue and to decelerate OA progression. Several therapeutic approaches include drugs to target inflammation modulators like nitric oxide (NO) or reactive oxygen species (ROS); inhibitors of pro-inflammatory cytokines such as IL-1 or TNF; and matrix metalloproteinases (MMPs) that degrade the cartilage morphology [30]. Several reports from genetic mouse models promote growth factors such as Wnt3a, transforming growth factor-β (TGF-β) and Indian hedgehog, and signaling molecules, such as β-catenin, Smad3, and hypoxia inducing factor-2α (HIF-2α), are associated with the development of OA [42-44]. Often RunX2, vital to regulating genes coding for matrix breakdown articular chondrocytes is found to be upregulated [45]. Parallel to these changes in cartilage, increased cellular activity in the subchondral bone stimulates subchondral bone sclerosis accompanied by cortical plate enlargement, considerable trabecular restructuring, and osteophyte regeneration at the outer edges of the joint [46]. A detailed understanding of these molecular mechanisms will enhance the growth of newer approaches for OA prophylaxis. Additionally, emerging techniques such as tissue engineering are being explored as an alternative treatment.

1.1.5 Tissue engineering

Tissue engineering, as defined by Langer & Vacanti, 1993 is 'an interdisciplinary field that applies the principles of engineering and life sciences toward the development of biological substitutes that restore, maintain, or improve tissue function or a whole organ' [47]. The strategy utilizes scaffold matrices to provide structural support to the cells and to deliver growth factors and/or cells that eventually form tissue substitutes for implantation. The process of tissue engineering typically involves three major components: cells, signals, and scaffolds, which represent the "triad of tissue engineering". Much research is currently focused on developing improving and finding the best-suited option of the triad for a specific application.

Cells: The selection of the most suitable cell source is very important in the development of a functional tissue-engineered model. Factors such as the availability of tissue-specific cellular phenotypes, able to mimic the native tissue, and the cellular density in the model should be carefully considered to ensure a physiologically relevant tissue model [48]. The use of cells from human sources to develop *in vitro* models would help in bridging the gap between animal models and clinical trials. Currently, adult primary cells isolated from patients are commonly used, however, they possess limited life span, low proliferation rate, and turnover, and their isolation

procedure is complex [49]. The use of stem cells could help overcome these limitations. The characteristics of stem cells such as the ability to self-renew and the capability to differentiate into other specialized cells have encouraged their application. However, concerns such as the capability to manage cell differentiation toward the desired cell lineages, and the possibility of resultant immature cell phenotype remain unresolved. Nonetheless, human stem cells are predominantly used in the development of new *in vitro* systems for regeneration and drug screening applications. Additionally, the induced pluripotent stem cells (iPSCs) obtained from differentiated somatic cells by overexpression of specific transcription factors have recently emerged as cells of choice due to their ability to use cells from the patient avoiding graft rejection and do not involve ethical concerns [50]. The iPSCs have characteristics similar to pluripotent embryonic stem cells and, possess the ability to differentiate into various phenotypes. Furthermore, iPSCs obtained from patients affected by a specific pathological condition, allow for the development of *in vitro* model of different stages of the disease to study the intricate mechanisms of its onset and progression.

Signals: The signaling or bioactive molecules, such as peptides, growth factors, cytokines, therapeutic molecules, etc. play a crucial role in regulating the microenvironment *in vivo*. These can be incorporated into the scaffolds or provided directly. They provide the fundamental molecular cues that direct cell behavior influencing cellular morphology, division, proliferation, apoptosis, and secretion of ECM components which is essential to successfully engineer tissues. The inclusion of chemical (growth factors/bioactive molecules/therapeutic agents), and mechanical signals are essential to avoid local concentrations limitation and to overcome the diffusion limits to obtain a functional engineered tissue [51]. Moreover, depending on the type of tissue, the cells respond to cues, such as dynamic stimulation, electric stimulation, osmotic and hydrostatic pressure, stress/strain, and fluid flow [52]. Specifically designed bioreactors have been used to provide mechanical stimuli to tissue-engineered constructs, especially in cartilage and osteochondral tissue engineering, where the native conditions include load-bearing properties.

Scaffolds: The scaffold must be designed to mimic the native architecture of the tissue, where the matrix allows cell adherence, spreading, proliferation, differentiation, maturation, and production of ECM. The selection of the most suitable biomaterial for scaffold fabrication is very crucial as it greatly influences biological functions. Thus, biomaterials should be carefully chosen based on the tissue/organ to be modeled, as an artificial ECM that interacts with cells at the molecular level,

inducing cell functions and driving the complex cellular interactions, that result in the fabrication of an efficient and functional *in vitro* engineered tissue model. The selection of biomaterial selection is also dependent on the mechanical properties of the tissue, as it is important to match the native properties of the healthy or diseased tissue to model it. Owing to their high mechanical and load-bearing properties, ceramics and their composites are typically used in the engineering of hard tissues, while polymers are mainly used in the engineering of soft tissues [53]. Additionally, material surface properties are crucial in guiding cell fate including integrin-binding RGD peptide modifications for enhanced cell attachment. The scaffold should also possess a high porosity, interconnected pores, and pore dimension suitable for cell migration and growth for a specific application. The porous structure allows homogenous distribution of cells by helping them migrate to the inner parts of the 3D construct along with allowing nutrient exchange, oxygen diffusion, and waste removal [54]. For designing tissue-engineered constructs, both top-down and bottom-up approaches have been used. The top-down method involves culturing of cells on scaffolds designed to mimic the native tissue-like conditions in terms of strength and structure. Whereas, the bottom-up approach involves mimicking and replicating the functional unit of tissue and creating modular scaffolds fabricated using microencapsulation and microfabrication techniques along with the cellular components [55].

The biomaterial used to fabricate the scaffold may be of natural/synthetic source and include a variety of formats such as hydrogels, films, mesh, nanoparticles, mats, etc. The scaffold serves as a transient ECM until cells mature and produce their matrix, eventually replacing the scaffold. Accordingly, scaffold architecture is indispensable for the actualization of osteochondral tissue engineering, regulating cell migration, proliferation, and ECM generation. Ideally, the scaffold for regeneration of tissues such as cartilage and bone depend on porosity, greatly enhanced biocompatibility, mechanical stability, competent to induce cell proliferation and differentiation, degradable in response to the neo-tissue formation, and compatible for integration with endogenous tissue. These mentioned scaffold characteristics are responsible for the level of resistance to mechanical loading and the regenerative capacity of tissues. Therefore, research is focused on engineering scaffold/matrix systems for osteochondral tissue with similar structural and mechanical profiles as that of native cartilage–bone interface, which would allow effective osteochondral tissue regeneration. Diverse forms of matrices such as porous scaffolds, fibers, and

hydrogels have been designed to restore cartilage, intermediate calcified cartilage, and bone tissues concurrently [56-59].

The goal of cartilage and osteochondral tissue engineering is to find and innovate novel solutions to replace the diseased joint tissues with a functional counterpart. The implanted engineered construct is envisaged to degrade over time while facilitating neo-tissue formation. One of the most critical aspects of tissue-engineered osteochondral units is maintaining the complex hierarchy and the mechanical resilience of the tissue. An ideal biomaterial fulfilling these pre-requisites should support tunable biodegradation, suitable mechanical strength, and biocompatibility, among others, to allow implant remodeling (**Figure 1.3**).

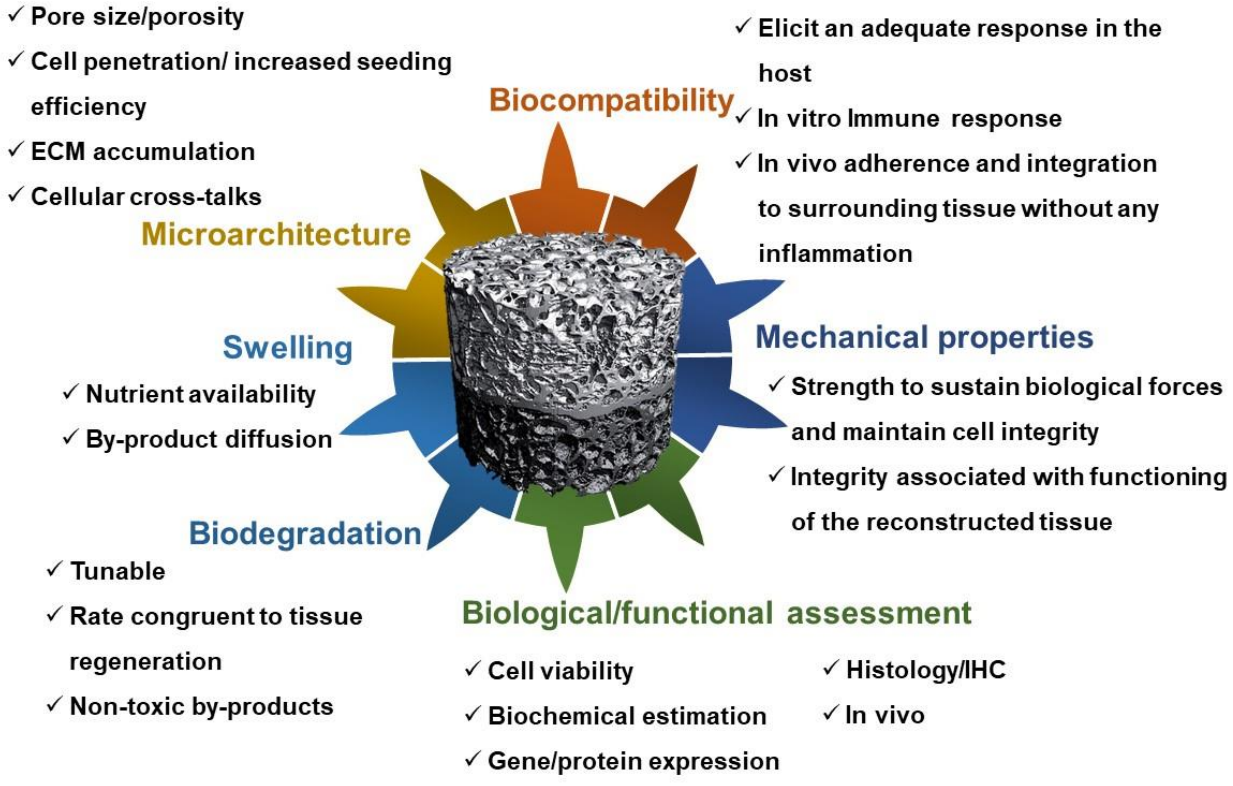

Figure 1.3. *Schematic diagram of various vital parameters in terms of assessment of scaffolds for cartilage and osteochondral tissue engineering applications.*

1.1.6 Conventional to advanced scaffold manufacturing techniques

Several scaffold techniques have evolved over the years in terms of polymers processing and fabrication of different types and formats of scaffolds. Both, manual or conventional, as well as new advanced technologies, are widely used for scaffold fabrication as shown in **Figure 1.4**. The

manual methods include techniques such as solvent casting and particulate leaching, melt molding, gas foaming, freeze-drying, etc. and advanced techniques include electrospinning, stereolithography, selective laser sintering, fused deposition modeling, and 3D bioprinting for fabricating composite scaffolds using both natural as well as synthetic polymers [60]. Scaffold fabrication using polymers has evolved in complexity and feasibility with developments in the field of tissue engineering; with a shift from using a combination of traditional and modern fabrication methods to eventually more advanced techniques due to their advantages. **Figure 1.4** describes some of the basic challenges of the conventional fabrication technique and the advantages of the advanced methods. Briefly, the conventional/manual techniques for scaffold fabrication may not be sufficient for creating complex scaffolds with precisely controlled microarchitecture and properties; specifically, they have limitations such as longer processing time, low scale production, poor reproducibility, higher cost, and seeding multiple cells in a spatially uncontrolled manner [61]. With the advancement in 3D fabrication techniques, most of these limitations are overcome. Towards this end, 3D bioprinting has gained vast attention recently due to its ability to fabricate patient-specific, and anatomically relevant shapes/constructs in a rapid, automatic, high-throughput, high scalable manner, with better reproducibility as desired by pharma companies involving drug screening studies. Therefore, it is essential to perform an initial assessment of scaffold fabrication techniques considering the potential advantages and disadvantages of each technique, and the required final product properties as per the needs of specific tissues to be regenerated.

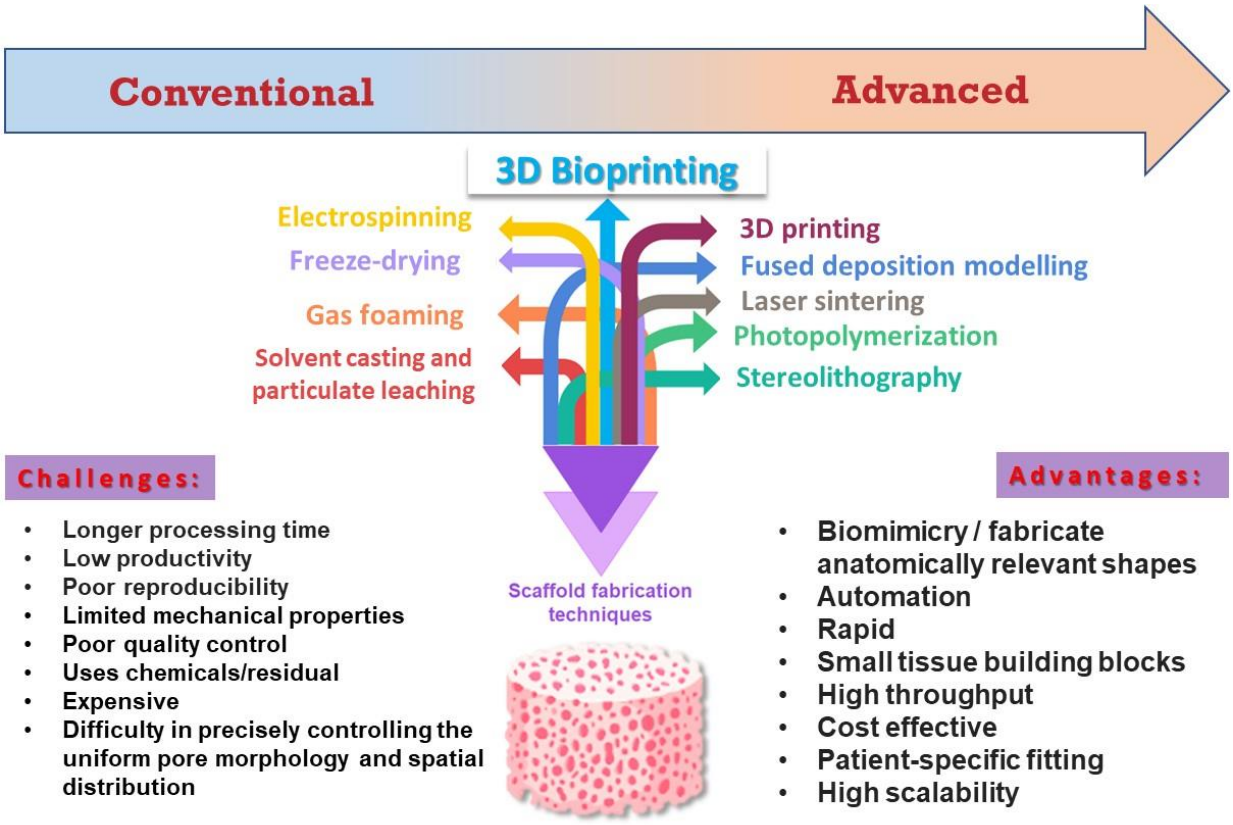

Figure 1.4. *The conventional technologies, their limitations, the advanced technologies, and their advantages for scaffold fabrication.*

1.2 Literature review

The clinical need for better treatment options for patients with cartilage and osteochondral damage has inspired tissue engineers towards *in vitro* development of acellular or cell-based substitutes; or implants with improved functional properties such as the ability for load-bearing and better integration with the host tissues. The advances in tissue engineering approaches involve factors such as improving the mechanical properties, and mimicking the native tissue hierarchical gradient environment, to allow the development of tissue constructs that can meet the implantation demands. To achieve tissue functionality, several biomaterials, scaffold matrices, cells, and bioactive molecules have been explored for successful cartilage and osteochondral repair and regeneration. **Table 1.1** lists the advantages and limitations of some commonly used polymers used for osteochondral tissue engineering.

Table 1.1. Properties of some commonly used polymers for osteochondral tissue engineering.

Polymer	Advantages	Limitations	Ref.
Collagen	ECM component, cytocompatibility, high structural integrity, highly bioresorbable	Potential of immunogenicity through presentation of telopeptides, lack of inherent rigidity, low mechanical strength, expensive	[62, 63]
Gelatin	Low cost, low immunogenicity in comparison to collagen, highly biocompatible, ease of processing and functionalization	Low mechanical strength, thermosensitivity and poor stability of aqueous gelatin preparations	[64-66]
Chitosan	Chondroprotective; structurally similar to glycosaminoglycans (GAGs), antibacterial properties, temperature-controlled phase transition	Limited solubility at physiological pH, polycationic and hemostatic properties, inferior mechanical properties	[67, 68]
Hyaluronic acid	ECM component, good hydration capacity, good cellular encapsulation, promotes angiogenesis	Poor mechanical strength, faster degradation	[65, 69]
Heparin	Ease of chemical modifications, anticoagulation, anti-inflammatory	Poor cellular infiltration	[70, 71]
Alginate	High functionality, chelating ability, pH-sensitive	Limited *in vivo* degradation, poor cell adhesion, mechanically weak	[72, 73]
Silk fibroin	Biocompatibility, bioresorbability, low immunogenicity, mechanical resilience, ease of processing and functionalization	Source variability, dissolution of silk fibers and low yield of non-mulberry silk fibroin	[74-76]
Chondroitin sulphate	ECM component, anti-inflammatory, role in cell recognition and signaling	Rapid degradation in contact with bodily fluids, poor thermal resistance, poor mechanical properties	[77-79]
PLGA	Hydrophilic and biodegradable, low immunogenicity, FDA approval in various biomedical applications	Limited bioactivity, generates acidic degradation by-products	[80, 81]
PEG/PEO	High biocompatibility, versatility in functionalization and processing, resistant to protein adsorption (anti-fouling), FDA approval in various biomedical applications	Bio-inert, non-biodegradable	[82, 83]
PVA	Ease of aqueous processing, good mechanical properties	Poor cell adhesion	[84]
PPF	High strength, injectability	Limited bioactivity	[85, 86]
PNIPAm	Thermosensitive, ease in grafting bioactive additives	Poor cell affinity	[87, 88]

1.2.1 Hydrogels

Towards gaining an improved functionality of implants, agarose has shown promising results. Agarose is a clear, thermoreversible polysaccharide hydrogel that can be modified to melt and gel at a variety of temperatures [89], used widely for maintaining lasting chondrocyte cultures, and has been a part of clinical trials in Europe as a composite with alginate for cartilage repair [90]. Benya *et al.* showed that dedifferentiated chondrocytes recovered their original differentiated chondrogenic phenotype when encapsulated and cultured in 0.5% agarose gels indicated by the increased proteoglycan and collagen levels [91]. Buschmann *et al.* showed the capability of agarose gel to form and assemble a mechanically functional cartilage-like ECM using a high density of chondrocytes from calf articular cartilage [92]. Mauck *et al.* reported a custom-made bioreactor to dynamically culture chondrocyte-seeded agarose disks in unconfined compression which resulted in a sixfold rise in the equilibrium aggregate modulus along with a greater increase in sGAG and collagen content [93]. Rennerfeldt *et al.* reported an enhancement in the mechanical performance of interpenetrating networks (IPNs) of PEG-DA and agarose with good viability of encapsulated chondrocytes and GAG content [94]. Cigan *et al.* used agarose scaffold to encapsulate human chondrocyte where the engineered construct mimicked the native human cartilage with compressive Young's and dynamic moduli of about 250 and 950 kPa, respectively along with the formation of 5.7% (w/w) of GAG and 1.5% (w/w) collagen [95]. Factors such as the lack of attachment sites, hydrophilicity, and electrical neutrality are reported to contribute to the efficacy of agarose. Although, known as a "gold standard" material for *in vitro* cartilage tissue engineering as it allows to maintain the chondrocyte morphology, and formation of higher GAG, and supports greater chondrogenesis compared to other natural hydrogels [96], agarose can be immunogenic, nondegradable, and its structure, composition, and mechanical properties cannot be customized, restricting its wide usage.

1.2.2 Fiber-reinforced scaffolds

The native matrix microenvironment of most soft tissues is usually a fiber network and microstructure with multiple constituents. For example, articular cartilage ECM is composed of collagen fibers embedded in a proteoglycan matrix. The collagen fibers in the ECM provide the compressive stiffness and strength in tension, while the hydrogel-like proteoglycans develop a mechanism to overcome and distribute the compressive load by establishing a fluid pressure [97].

In the direction of scaffold-based cartilage tissue engineering, a diverse range of biomaterials have been explored, however, most of them are unable to meet the required features of resilience and mechanical strength. The strength of articular cartilage is depth-dependent and varies from 1.5 MPa up to even 30 MPa in the deep regions with high fiber presence. To achieve the required mechanical strength, the use of fiber-reinforced strategies has achieved impressive outcomes in several developed scaffold approaches. Agrawal *et al.* reported the development of a cartilage-like structure using a fiber-reinforced hydrogel composite consisting of elastic polyurethanes fibers in an epoxy-amine hydrogel. The results showed that the parallel arrangement of fibers to the stress axis, increased the elastic modulus by 2-fold with higher fracture strain [98]. This work showed that fiber reinforcement could provide the required enhanced strength of the native cartilage tissue, however, the use of polyurethane had drawbacks such as the inability to be degraded and absorbed rapidly in the body, which may cause adverse reactions. Moving towards the use of natural polymers, Mirahmadi *et al.* reinforced electrospun silk fibers and degummed silk fibers to the thermosensitive chitosan/glycerophosphate hydrogels for cartilage regeneration. The fiber-reinforcement resulted in the increased formation of proteoglycan and collagen type II and improved the mechanical properties of the hydrogel, however, the native-like compressive modulus could not be reached. Yodmuang *et al.* reported fiber-reinforced hydrogel scaffolds, where silk fiber–hydrogel composites made from silk microfibers and silk hydrogels were investigated for cartilage tissue engineering. The results demonstrated good chondrocyte viability of the reinforced gels supporting deposition and localization of GAG and collagen, around the fibers with improved mechanical characteristics [99]. Visser *et al.* reinforced gelatin methacrylamide (GelMA) hydrogels with organized, high-porosity PCL microfibres based on the melt-electrospinning writing technology. This significantly increased the stiffness of the reinforced scaffold by 54-fold, reaching that of native articular cartilage. In addition, the cultured chondrocytes retained their round morphology and survived *in vitro* under a physiological compression load, indicating their potential for articular cartilage repair [100]. Thus, the use of fiber-reinforced scaffolds has been shown to improve the mechanical properties required for load-bearing tissues such as cartilage along with the improved formation of neo-cartilage matrix.

1.2.3 Multilayer scaffolds

Being a load-bearing tissue, cartilage is very much prone to damage and if left untreated results in damage of the subchondral bone ultimately progressing to osteochondral defect and OA. Given the proximities and intimate involvement of the articular cartilage and subchondral bone, it is essential to understand the regeneration of the entire osteochondral tissue (consisting of cartilage, subchondral bone, and the interface between them), and study the crosstalk among them. Additionally, the interface between both tissues plays a very crucial role in the health and disease of the osteochondral tissue. Therefore, the treatment of osteochondral defect requires a hierarchical continuous graded scaffold to support the simultaneous reconstruction of both cartilage and bone phases with a connecting interface. An osteochondral ECM is characterized by gradual changes in composition, mechanics, and structure. In its composition, there is a gradient of proteoglycans, collagen type II, water content, and mineral concentration. Water and collagen type II content increase, whereas mineral content decreases from osseous to chondral surface. In bone, collagen fibers are highly insoluble due to numerous intra- and intermolecular cross-links, in contrast to the relatively soluble fibers in cartilage [101]. Regarding the mechanics, the compressive modulus of ECM also diminishes from osseous to chondral face [102]. The compressive modulus of trabecular bone is 4.4 to 229 MPa, whereas the modulus of articular cartilage varies between 1.36 MPa to 39.2 MPa [101, 103, 104]. From a structural viewpoint, porosity and pore size decrease from bony to cartilaginous ECM [102]. These smooth deviations between vascular/mineralized bone and non-vascular/non-mineralized cartilage are crucial to preserving cartilage-to-bone stability. Various approaches for the fabrication of osteochondral constructs include: (i) a single homogenous scaffold for both cartilage and bone; (ii) different scaffolds for the bone and the cartilage components combined using sealant; (iii) a single but heterogeneous composite scaffold. These scaffolds may be seeded with primary cells for both cartilage and bone or using mesenchymal stem cells endowed with both chondrogenic and osteogenic differentiation capacity [56].

Several studies report the use of multi-layered cartilage and osteochondral constructs made up of a single homogenous material. Towards this end, Waldman *et al.* reported developing tissue-engineered cartilage *in vitro,* consisting of a layer of cartilaginous tissue attached to a biodegradable calcium polyphosphate (CPP) substrate for the better anchorage of the cartilage upon its implantation. The CPP substrate supported chondrocyte culture and deposited a

continuous layer of native-like cartilaginous tissue with increased proteoglycans and type II collagen, that unified with the substrate [105]. Further, Kandel *et al.* from the same group used the developed CPP-based constructs for implantation into full-thickness osteochondral defects in the trochlear groove of the sheep knee. As opposed to the ceramic-only control implants which showed fibrous tissue on the articulating surface post-implantation, the composite constructs maintained ECM contents over the 9 months, while enhancing the mechanical characteristics [106]. However, a single homogenous scaffold is unable to mimic the distinctly different structural and functional properties of the cartilage and bone phases of the osteochondral tissue.

Thus, research progressed into using two separate layers, each with specifically distinct characteristics to the native cartilage and bone. Towards this end, Gao *et al.* fabricated a bilayered scaffold composed of a hyaluronan derivative (HYAFF®-11) sponge for engineering cartilage tissue and a calcium phosphate ceramic sponge for bone regeneration. MSC-loaded HYAFF-11 sponge and ceramic sponge were joined together with fibrin sealant (Tisseel) to form a composite osteochondral graft. After 6 weeks of *in vivo* culture in subcutaneous pockets of syngeneic rats, immature fibrocartilage in the upper layer and bone development in the lower layer was observed [107]. Later, Filardo *et al.* investigated the integrity of 2-layer and 3-layer collagen-hydroxyapatite (C-HAp) osteochondral scaffolds in a human cadaveric knee. The results showed that the use of fibrin glue stabilized the multi-layer scaffolds regardless of lesion location. However, depending on the defect size, the scaffold involved and the experienced stress on the implant, this arrangement of assembly of multilayers dependent on an external glue is always prone to delamination and dislodgement.

Thus, single but heterogenous composite scaffolds with a continuous and stable interface became the preferred strategy for osteochondral repair and regeneration. Towards this, Galperin *et al.* reported a sphere-templating method to develop an integrated bi-layered scaffold using pHEMA hydrogel, where the cartilage layer had a larger pore size and was coated with hyaluronan, while the bone layer had smaller pores and coated with hydroxyapatite particles. The scaffold supported the growth and ECM deposition by the cultured chondrocytes and primary human MSCs indicating its potential for osteochondral tissue engineering [108]. Oliveira *et al.* reported fabricating hydroxyapatite (HAp)/chitosan (CS) 2-layer scaffolds utilizing sintering/freeze-drying techniques for osteochondral tissue-engineering applications. The compressive modulus for the HAp and CS

dry scaffold individually was found to be 153 ± 12 and 2.9 ± 0.4 MPa, respectively which is suitable for bone and cartilage tissue engineering. Results showed no cytotoxic effect of the scaffolds and that the HAp and CS layers, supported the growth and differentiation of goat marrow stromal cells into osteoblasts and chondrocytes, respectively [109]. Li *et al.* developed a biphasic scaffold where the 2 phases possessed different pore morphologies to match the cartilage and bone phases of osteochondral tissue, using a flexible and robust silk scaffold for the cartilage phase and a mechanically strong and bioactive SHG-silk scaffold for the bone phase. The results showed that the mechanical properties of the two phases mimicked the load-bearing property of native osteochondral tissue with similar compressive properties. Further, the biphasic scaffold directed *in vitro* preferential chondrogenic or osteogenic differentiation of human MSCs [110]. The multi-layered scaffolds showed promising results in terms of osteochondral repair and regeneration, however, most of the approaches involved the use of manual or conventional fabrication techniques, limiting its facile and wide applicability, thus, warranting advanced, automated, biomimetic, and rapid fabrication techniques.

1.2.4 3D bioprinted constructs

3D bioprinting is an additive manufacturing (AM) technique that involves 3D biofabrication of tissues *via* a layer-by-layer deposition of bioink composed of biomaterials, cells, and growth factors [111]. It allows for custom design of complex patient-specific geometries recapitulating the native tissue for implantation, or development of *in vitro* models for therapeutic screening of drugs. 3D bioprinting has gained wide attraction recently due to easy, rapid, and high-throughput fabrication of complex tissues, in addition to providing a potential answer to organ shortages and the replacement of animal models. Bioprinting can recapitulate native tissue conditions and develop biomimetic 3D constructs with uniform or graded cell distribution, allowing dynamic cell-cell, and cell-ECM interactions. It starts with a model of the structure to be printed, which is generally a computed tomography (CT), a magnetic resonance imaging (MRI) scan, a computer-generated design (CAD) file or even downloaded from several online tools. This model is further sliced and stored as a g-code file, which is sent to the bioprinter for printing using the bioink. Over the years, numerous bioprinting technologies have been developed and classified as per the working mechanism behind them. Among these, the pressure-assisted (extrusion-based) being low-cost is the most commonly available and used technique especially for cartilage tissue

engineering (**Table 1.2**). Other strategies include thermal-assisted, acoustic-assisted, laser-assisted, piezo-assisted, and microfluidic driven bioprinting [111, 112]. These techniques require different physical and rheological properties for effective ink, and can be used alone or in combination to achieve the desired tissue fabrication. Bioinks play a crucial role in successfully bioprinting 3D constructs, thus their development and optimization is an area of intense research globally. Certain criteria that the bioinks need to fulfill include biocompatibility, printability, and mechanical stability, along with a cell-friendly microenvironment to support cell metabolism and tissue formation *via* new ECM deposition [113, 114].

Sherwood *et al.* reported constructing integrated bi-layered scaffolds using a 3D printing process and salt leaching technique, to produce a 90% porous cartilage phase composed of PLGA/PLA and 55% porous bone phase composed of and PLGA/TCP, with a transition region between the two phases. The chondrocytes favored the cartilage layer of the construct with new ECM formation and the tensile strength of the bone layer reached that of the native cancellous human bone [115]. Cui *et al.* reported a thermal inkjet-based bioprinting approach using PEGDMA, encapsulating human articular chondrocytes in a layer-by-layer manner into a cartilage defect within an osteochondral plug for cartilage repair. The printed construct showed a compressive modulus of 395.73 ± 80.40 kPa and supported chondrocyte viability along with the formation of neo-cartilage ECM and expression of cartilage gene markers [116]. Xu *et al.* described a hybrid inkjet printing/electrospinning system for engineering cartilage tissue. A 5-layer tissue construct was fabricated using alternating electrospun PCL fibers and printing fibrin–collagen hydrogel encapsulating rabbit elastic chondrocytes. The results showed that the hybrid construct supported chondrocyte viability, demonstrated enhanced mechanical properties, and formed cartilaginous tissues both *in vitro* and *in vivo* as demonstrated by the deposition of collagen type II and GAGs [117]. Kundu *et al.* reported an additive manufacturing approach to fabricate 3D printed scaffolds using layer-by-layer deposition of PCL and chondrocyte embedded alginate hydrogel. The PCL–alginate gels with growth factors showed higher ECM formation both *in vitro* and *in vivo* [118]. Pati *et al.* established a decellularized extracellular matrix (dECM) based bioink for bioprinting of tissues such as cartilage. The capability of dECM to support differentiation of human inferior turbinate-tissue derived MSCs into the chondrogenic lineage was established by the formation of cartilage matrix as indicated by the synthesized collagen type II and gene expression of cartilage markers [119].

Initially, 3D printing was used in combination with traditional scaffold fabrication techniques, such as freeze-drying and particulate leaching, to obtain bi-layered constructs. Most such cases report the use of a polymeric scaffold for the cartilage tissue, and a ceramic scaffold for the subchondral bone phase [120]. Towards this, Schek *et al.* explored image-based design (IBD) and solid free-form (SFF) approach using PLA/HAp to fabricate biphasic composite scaffolds which were seeded with differentiated chondrocytes in the polymeric phase and modified fibroblasts in the ceramic phase. The *in vivo* analysis indicated the formation of cartilage, bone, and a mineralized interface tissue [121]. Zhang *et al.* explored the stereolithography process to 3D print biphasic composites using PEG hydrogel and β-TCP ceramic. The implanted constructs in rabbit trochlea within a critical size defect model in a year-long study showed the formation of hyaline-like cartilage along with repaired subchondral bone [122]. Using fused deposition modelling (FDM), Cao *et al.* fabricated a honey-comb-like PCL scaffold to create anisotropic structures by coculturing osteogenic cells and chondrogenic cells [123]. Yang *et al.* reported a 3D plotting system for fabricating a biphasic graft using PLGA and alginate along with additives such as cartilage-derived ECM (cECM) or Hap; with human cartilage-derived progenitor cells in the cartilage or subchondral bone layer for engineering osteochondral defects. The biphasic graft showed good integration between cartilage and subchondral bone layers with ECM formation and no visible toxicity [124].

Table 1.2. Extrusion-based 3D bioprinting approaches for cartilage and osteochondral tissue engineering.

Type (Pure/Hybrid)	Components	Cells Sources	Construct Type	Ref.
Single hydrogel Blend	Alginate, Calcium chloride	Human MSCs, Human articular chondrocytes	OC	[125]
Hybrid	PCL, Alginate	Human nasal septum chondrocytes +MG63	OC	[126]
Hybrid	PCL, (Alginate/Alginate + growth factor)	Human nasal septum chondrocytes	Cartilage	[127]
Hybrid	PCL, dECM	Human turbinate MSCs	Cartilage	[128]
Hybrid	GelMA, Gellan Gum, PLA microcarriers functionalized with Collagen I	Rat BMMSCs	OC	[129]
Single hydrogel blend	HA-NIPAAM, HAMA	Bovine chondrocytes	Cartilage	[130]
Single hydrogel blend (1 coaxial print head)	Alginate + (CS/AEMA/ GelMA/HAMA), Calcium chloride	BMMSCs	Neo-Cartilage	[131]
Single hydrogel blend (handheld coaxial)	GelMA, HAMA	Allogenic ADMSCs	Cartilage	[132, 133]
Single hydrogel blend	Nanofibrillated cellulose, Calcium chloride	Human BMMSCs	Cartilage	[134]
Multiple hydrogel blends	GelMA, Gellan, HAMA	Chondrocytes/Equine metacarpophalangeal cells/Equine BMMSCs	Cartilage	[135]
Hybrid	PCL, Alginate/Collagen I	Rabbit tracheal chondrocytes	Tracheal Cartilage	[136]
Single hydrogel blend	Bacterial Nanocellulose, Mannitol	Human nasal chondrocytes	Cartilage	[137]
Single hydrogel blend	Alginate, Pluronic F127	Human BMMSCs	Cartilage	[138]
Single hydrogel blend	Silk fibroin, gelatin	Procine auricular chondrocytes	Cartilage	[139]

Hybrid	PCL, BMSC hydrogel, GDF5 hydrogel (hydrogel = Gelatin, Fibrinogen, HA, glycerol)	Rabbit BMMSCs	Cartilage	[140]
Single hydrogel blend	Nanofibrillated cellulose, Alginate	Human nasal chondrocytes/ Human BMMSCs/ co-culture of both	Neocartilage	[141]
Hybrid	PEG/Alginate/Thrombin bath, Fibrin for cells	Human MSCs	Cartilage	[142]
Single hydrogel blend	Nanocellulose, Alginate	Human iPSCs	Cartilage	[143]
Hybrid	Supporting Scaffold: PCL, Photopolymer Bioink: dECM of articular cartilage	Human ADMSCs	Nasal Cartilage	[144]
Single hydrogel blend	Norborene, Hyaluronic acid	Bovine MSCs	Cartilage	[145]
Single hydrogel blend	Gelatin, Alginate, Fibrinogen	Human BMMSCs	Cartilage	[146]
Two hydrogel blends	Bone: PVP, Silk fibroin, Nano apatite Cartilage: PVP, Silk fibroin	Porcine ADMSCs	OC	[147]
Single hydrogel blend	Silk, Platelet rich plasma	Rabbit chondrocytes	Cartilage	[148]
Hybrid	PCL, GelMA	Sheep articular chondrocytes	Cartilage	[149]
Single hydrogel blend	HAMA+4arm PEG	Cell-free	Cartilage	[150]

Abbreviations: - PCL: Polycaprolactone; OC: Osteochondral; dECM: decellularized extracellular matrix; GelMA: Gelatin methacryloyl; PLA: Polylactic Acid; NIPAAM: N-Isopropylacrylamide; HAMA: Hyaluronic acid methacrylate; CS/AEMA: chondroitin sulfate amino ethyl methacrylate; GDF5: Growth differentiation factor 5; PEG: Polyethylene glycol; PVP: Polyvinylpyrrolidone.

1.2.5 Osteoarthritis models

The therapeutics for any particular pathological condition required a good understanding of its underlying cellular and molecular mechanisms. Towards this, various 2D monolayer cultures and animal models are some of the highly used methods. In the case of OA, both *in vivo* and *in vitro* models have been used in the past and each has its advantages and limitations. The *in vivo* models may reflect the native-like pathological conditions to an extent, however, the ease of manipulating an *in vitro* system, as well as a shift towards the 3R philosophy of refining, reducing, and replacing the use of animals in research, make *in vitro* disease models advantageous. Methods such as enzymatic treatment, injury-based, extreme mechanical loads to cartilage to initiate/induce damage have been used. For example, De Vries-van Melle *et al.* developed an *in vitro* osteochondral model to study cartilage repair mechanisms by producing defects of different depths using a dermal biopsy punch and scalpel [151]. Towards studying the effect of surface damage on the mechanical properties of articular cartilage, Grenier *et al.* developed an *in vitro* cartilage degradation model targeting early-stage OA using collagenase-treated cartilage explants. The enzymatic degradation indicated reduced proteoglycans content and increased cartilage deformation and degeneration [152]. However, utmost care and caution need to be taken while establishing the relevance of *in vitro* models to clinical disease. Various research groups including De chant *et al.* have investigated the varying dosages of glucosamine and chondroitin sulphate on normal and interleukin-1α conditioned equine cartilage explants, and reported that the combination of glucosamine and chondroitin sulphate is more effective in preventing or treating OA in horses [153]. However, this understanding did not hold effective under *in vivo* trials. Sawitzke *et al.* showed beneficial but not significant trends when evaluating the efficacy and safety of glucosamine and chondroitin sulphate, alone or in combination, as well as celecoxib and placebo on painful knee OA over 2 years [154].

The main pathways involved in the development of pathological conditions and repair of the cartilage matrix are mostly mediated through cytokines and chemokines. Models of OA which use cytokines for induction of OA-like conditions are very common, generally well understood, typically cost-effective, and easily customizable. The extensive cell expansion ability allows the possibility of many replicates, permitting multiple hypotheses to be tested from single sources of tissue [155]. The predominant proinflammatory cytokines interleukin-1β (IL-1β) and tumor necrosis factor-α (TNF-α) are synthesized during the OA process and are used for induction of

OA-like conditions [156]. Maccoux *et al.* investigated the cytokine expression levels in different articular tissues from the healthy and OA joints of dogs. The results showed increased levels of IL-1β, IL-6, and IL-10 in OA synovial membrane, increased levels of IL-1β and IL-6 in ruptured (OA) ligament, and reduced levels of IL-8 in OA synovial membrane [157]. Liacini *et al.* showed that TNF-α can induce catabolism (induction of MMP-13) and inhibit anabolic pathways mediated by MAP kinases, AP-1, and NF-κB transcription factors in joint tissues and articular chondrocytes [158]. Cytokine-induced proteolytic enzyme release is regulated by inflammatory mediators such as nitric oxide, PGE2, and ROS. The ECM proteins cleaved by the activated proteases further induce both proinflammatory cytokines and matrix proteases leading to greater damage [159].

Due to their capability to recapitulate the tissue microenvironment, 3D *in vitro* models offer a more realistic approach with higher utility in exploring disease development and drug screening. Cortial *et al.* developed an *in vitro* cartilage model, using bovine articular chondrocytes cultured in a collagen scaffold with or without IL-1β, to induce cartilage degradation. IL-1β treatment upregulated the catabolic MMP1 and MMP3 and downregulated the ECM proteins collagen type II and aggrecan [160]. This 3D system allowed study of the responses of chondrocytes due to inflammatory cytokines; however, it did not test the feasibility of the system to study the effect of anti-inflammatory drugs, and did not include the effect of inflammatory immune cells. Sun *et al.* developed an early-stage *in vitro* 3D OA system using silk scaffold seeded with primary chondrocytes, along with treatment with cytokines (IL-1β and TNF-α) or the use of macrophage conditioned media (MCM). The addition of the cytokines or MCM increased the expression of MMP-1 and MMP-3, in agreement with native inflamed cartilage conditions [161]. However, the study did not test the feasibility of the platform to evaluate the efficacy of anti-inflammatory drugs. Aydin *et al.* developed a 3D *in vitro* model of OA using doxycycline and doxycycline-chondroitin sulfate (D-CS) loaded PCL microspheres (MS). A significant reduction in MMP-13 and GAG levels were observed upon drug treatment in both microspheres compared to untreated OA-chondrocytes. The promising results of injection of MS to rabbit knee in hyaluronic acid (HA) also indicated the effectiveness for OA therapeutics [162]. Cross-linked hyaluronic acid (cHA) hydrogel and dexamethasone (Dex) have been used in the clinic to treat knee OA owing to their chondroprotective and anti-inflammatory effects, respectively. Zhang *et al.* compared the treatment effects of the cHA gel combined with/without Dex in a surgery-induced OA model in

rats. The results indicated increased proteoglycan and type II collagen levels and less cartilage damage in the cHA-Dex gel group with reduced inflammatory cell infiltration [163].

There are increasing reports involving 3D bioprinting of cartilage, bone, and the osteochondral tissue with an immense research on the development of new bioinks, the integration of diverse 3D printing methods, the development of more complex devices able to mimic native tissues, and moving towards an integration of advanced techniques such as 3D bioprinting. However, currently, the literature reports no 3D bioprinted model for screening anti-inflammatory OA drugs. Thus, there are expectations of new humanized models based on 3D printing with the ability to replicate the inflamed osteochondral unit of the joint and to screen drugs towards OA therapeutics.

1.2.6 Clinical status and commercial products

Many scaffolds/constructs have been designed, developed, and explored in bone, cartilage, and osteochondral tissue engineering. Of those, only a few have been progressed to clinical trials [164]. In the case of articular cartilage, the focal and degenerative lesions significantly decrease the quality of the patient's life. Despite the progress in several therapies, including surgical treatment, a definitive treatment strategy towards cartilage repair is not yet known [165]. The regeneration and formation of fibrocartilage instead of the desired hyaline cartilage of the neo-tissue is a significant challenge for clinicians. There is a constant requirement of new and improved strategies with the best cost-effective treatment for cartilage regeneration, with high-quality randomized clinical trials. Biomimetic ceramics and composites have recently garnered success in bone regeneration therapies in patients [166, 167]. A recent comprehensive review by Oryan *et al.* reports the status of the various commercially available bone graft substitutes and their clinical applications [168], and states that autografts remain as the gold standard for bone regeneration by functioning better to the tissue engineering scaffolds. Therefore, much understanding and advancements are required to fabricate clinically relevant constructs that mimic the natural bone. Similarly, in the case of osteochondral tissue, several multilayer scaffolds and composite constructs have been explored with a focus on the specific anatomical details of each tissue layer. These constructs are investigated comprehensively in osteoarthritic patients for repair and regeneration of osteochondral defects, with some of them achieving limited success and commercially available in the market [164]. The preclinical and clinical trials help us to understand where we stand, create the correct strategies towards better and efficient tissue repair with

improved cost-benefit ratios. Towards clinical translation of grafts, most of the pre-clinical studies are either ongoing or are waiting to undergo clinical trials, with the results from several current trials of bone, cartilage and osteochondral grafts showing promising results for future clinical applications.

In the global market for tissue engineering, the field of Orthopedics, Musculoskeletal & Spine applications constitute the largest share in terms of application, which is estimated at 60.5% or US$13.5 billion in 2018 and is projected to reach US$34.7 billion by 2024 at a CAGR of 17.1%. Over the past decade, research and advancement in the field of tissue engineering and regenerative medicine have resulted in several clinically approved products. The role of biomaterials in tissue regeneration to fabricate scaffolds is crucial to support the growth of cells that will regenerate the defective site by creating new tissue while the scaffold itself biodegrades out of the system. In osteochondral regeneration, several formats of materials have been employed as templates to supports ECM and new matrix formation, however, the most commonly used technique consists in designing bilayered scaffolds able to regenerate both cartilage and subchondral bone, seeded with autologous chondrocytes for the application of implantation. Inspired from Bicho *et al.* [169], **Table 1.3** lists some of the current commercial products in the market.

Table 1.3. List of some commercial products used for the repair and regeneration of bone, cartilage, and OC defects.

Product	Manufacturer	Composition	Applications
Chondromimetic™	TiGenix NV	Collagen, GAG, and CaP	OC
Trufit™	Smith & Nephew	Calcium sulfate, PLGA/ PGA	OC
MaioRegen®	Med&Care	Collagen type I and magnesium enriched-HAp	OC
OsseoFit® plug		Type I collagen, and 80% β-TCP + 20% PLA	OC
BST-Cargel®	Piramal Life Sciences	Chitosan gel, glycerophosphate, and autologous blood	OC

Bioseed®-C	Biotissue Technologies GmbH	PLA/PGA	OC
Agili-C™	CartiHeal	Calcium carbonate and aragonite with hyaluronic acid	OC
Collagraft®	Nuecoll Inc	Collagen with granules of HAp and β-TCP	OC
Chondrotissue®	Biotissue	PGA/hyaluronan	Cartilage
HYAFF® 11	Anika Therapeutics	Hyaluronan	Cartilage and OC
Chondrocushion	Advanced Bio Surfaces, Inc	Polyurethane	Cartilage
BST-Cargel®	Piramal Life Sciences	Chitosan with glycerol phosphate and autologous blood	Cartilage
SaluCartilage™	SaluMedica	Polyvinyl alcohol hydrogel	Cartilage
Gel-One®	Zimmer	Hyaluronic acid	Knee OA

Abbreviations: OC- osteochondral, OA- osteoarthritis, GAG- glycosaminoglycans, CaP- calcium phosphates, PLGA- poly(lactic-co-glycolic) acid, HAp- hydroxyapatite, PLA- polylactic acid, PGA- polyglycolic acid.

As reviewed above from the current literature, several natural and artificial biomaterials have been studied and of these the natural polymers have proven to be the preferred sources. Of the natural polymers, silk fibroin has gained immense attention for use as a biomaterial in tissue engineering applications due to its characteristics.

1.2.7 Silk fibroin

Silk is a natural fibrous biopolymer that has gained worldwide attention and has been in use for centuries in diverse applications including textiles, optics, electronics, food industry, environmental engineering, and biomedicine [170]. Owing to its high biocompatibility, it has been widely used as suturing material in clinical settings for over a century [171]. In recent times, silk

has been extensively explored for biomedical applications and is FDA approved for use as biomedical sutures (Wax coated, Ethicon Inc. and others), surgical mesh (SERI-surgical scaffolds for soft tissue regeneration by Sofregen Medical, Inc., Medford, MA, USA), and hydrogel (Silk Voice for augmenting vocal fold tissue by Sofregen Medical, Inc., Medford, MA, USA) [171]. Silk is produced by arthropods namely spiders, scorpions, mites, and lepidopteran insects such as silkworms. Among the silkworms, silk from the domesticated *Bombyx mori* (mulberry) of the Bombycidae family is found globally and is well studied, however, the Indian wild varieties (non-mulberry) such as *Antheraea assamensis* (commonly known as Muga), *Antheraea mylitta* (commonly known as Tasar), and *Philosamia ricini* (commonly known as Eri) of Saturniid family are relatively untapped. Silk from silkworm is composed of the core silk fibroin (SF) protein that forms the structural fibers and silk sericin (SS) which is a gum coating the fibers. Post-processing, the biocompatible silk fibroin is collected and used for various applications while the water-soluble sericin is discarded. The different silk has distinct physicochemical characteristics mostly due to their varied amino acid composition [172]. In the case of spiders, the orb-weaving spiders (*Nephila clavipes* and *Araneus diadematus*) are well studied, especially the female orb-weaving spiders that yield up to seven different silk types from different glands and spinnerets situated at the posterior abdomen side. Among these, the major ampullate silk (dragline silk), which has superior tensile strength and toughness and is made by the major ampullate glands has been investigated in most detail [173]. The silkworm silk is synthesized in the posterior part of the silk gland, concentrated and stored in the middle part, and then transported to the anterior segment before being spun into fibers when it comes in contact with the air, drawn into cocoons. Both SF and SS proteins are involved in cocoon formation. Towards its application, the 2 silk proteins have been reported to be used individually but not together due to biocompatibility issues [174]. SF is a widely explored biomaterial due to its favourable biocompatibility, tunable degradation rates, adjustable molecular structure, remarkable mechanical properties, and the ability to be fabricated into several formats of matrices [175, 176].

Structurally, SF from *B. mori* is composed of light (L) and heavy (H) chain polypeptide linked by a disulphide bond. The H-chain is made of hydrophobic region with ordered amino acid sequence repeats, eventually organizing the SF into β-sheet (crystalline structures) via inter- or intramolecular forces such as the hydrogen bonds, hydrophobic interactions, and van der Waals forces [177]. In general, the presence of larger hydrophobic crystallite domains interspersed with

smaller hydrophilic amorphous domains allows the assembly of SF and imparts silk its strength and resilience. The chemical structure of these silk varieties differs from each other and is highly influenced by their amino acid composition [172]. Additionally, SF can exist in 4 different morphologies (silk I, silk II, silk III, and random coil), under different stages and conditions. Silk I consist of alternating α-helix and β-sheets (mainly is SF solution), silk II consists of dominant β-sheet content (present in hydrogels), while silk III is dominantly α-helix structure, while the random coil form exists in the SF solution [178]. The properties of SF can be tuned by regulating its crystalline and amorphous domains which makes this protein attractive to explore. The chemical structure of these silks differs from each other and is highly influenced by the varying amino acid contents. The amino-acid composition of *B. mori* SF includes multiple repeats of $(Gly\text{-}Ala\text{-}Gly\text{-}Ser\text{-}Gly\text{-}Ala)_n$ conferring crystallinity to the structure [179]. Concurrently, the amino acid structure of non-mulberry silk consists of poly-alanine $(Ala)_n$ repeats and is responsible for the higher crystallinity in non-mulberry silks as compared to mulberry. Crystallinity is a vital parameter for the *in vivo* biodegradability of SF matrices, which can be tuned using various treatments. The wild silk has been reported to show improved physicochemical, thermal, and mechanical stability [180, 181]. Another advantage that the wild non-mulberry variety possesses over the mulberry silk is the presence of cell binding tripeptide Arg-Gly-Asp (RGD), which are integrin-binding receptors for cell adhesion mediating better cell-material interaction [182]. The ease of processing and ability of SF solution to be fabricated into various formats such as sponges, mats, hydrogels, films, and nanoparticles is another desired characteristic. The suitable properties make it a favourable contender for tissue engineering applications including complex osteochondral tissues.

Preparation of 2D hydrogel films or coatings and 3D porous scaffolds and sponges using silk fibroin hydrogels has been adapted for strengthening the hydrogels and ensuring their presence in the targeted volume of repair and regeneration. Moreover, they ensure the sustained delivery of biological factors while acting as a harbour for the housing and proliferation of cells. Silk fibroin hydrogel scaffolds have been repurposed for osteochondral repair either in a reinforced state or in a blended state (**Table 1.4**).

Table 1.4. Silk hydrogel-based delivery vehicles for osteochondral repair.

Delivery Format	Delivered Cargo (Biomolecule/Cell)	Application	Ref.
Nanospheres	Kartogenin/E7 Peptide/Rhodamine B	*In situ* osteochondral regeneration	[183]
Nanoparticles and nanofibers	Hydroxyapatite	Bone regeneration	[184]
Hydrogel	miR-675 containing exosomes	Prevention of vascular dysfunction in mouse hind limb	[185]
Hydrogel	Chondrocytes	Cartilage repair in rabbit model	[186]
Hydrogel	Bioactive glass nanoparticles	*In situ* bone formation in calvarial defect model	[187]
Hydrogel	Mature chondrocyte embedded Silk elastin-like recombinamers	Cartilage regeneration	[188]
Hydrogel	Betamethasone	Anti-inflammatory action for prevention of rheumatoid arthritis	[189]
Hydrogel	RGD sequences (Gelatin) and porcine chondrocytes	Cartilage tissue regeneration	[190]
Hydrogel	RGD sequences (non-mulberry silk fibroin) and annulus fibrosus cells	Intervertebral disc degeneration therapy	[191]
Hydrogel	Horseradish Peroxidase as a model drug loaded into Sericin methacrylate	Cartilage regeneration applications	[192]
Hydrogel scaffolds	Chitosan nanoparticles	Articular cartilage defect repair	[193]
Hydrogel/Microfiber scaffolds	Chondrocytes	Cartilage tissue repair	[99]

Multilayered hydrogel scaffolds	Growth factor microspheres containing rhBMP-2 or rhTGF-β3, nanohydroxyapatite	Osteochondral defect repair	[194]
Hydrogel constructs	Tricalcium phosphate	Osteochondral tissue regeneration	[195]
Hydrogel constructs	Zinc, Strontium and Tricalcium phosphate	Osteochondral tissue regeneration with antibacterial properties	[196]
Electrospun hydrogel constructs	Bioactive glass	Osteochondral interface regeneration	[197]
Nanotextured Hydrogel membrane	Hydroxyapatite	Osteochondral defect repair	[198]
Hydrogel constructs	Bioactive glass	Patient specific bone defect repair	[199]
Composite hydrogel scaffolds	Kartogenin, stem cells, and BMP-2-derived peptides	Osteochondral defect repair	[200]
Composite hydrogel	Chondroitin sulphate	Articular cartilage repair	[201]
Composite hydrogels	Chitosan and Magnesium hydroxide	Antimicrobial active osteochondral repair substitute	[202]
Hydrogel constructs	Platelet-rich plasma	Cartilage regeneration	[203]
Hybrid hydrogel scaffolds	L-ascorbic acid and Platelet rich plasma	Chondrogenic differentiation of Wharton's jelly derived mesenchymal stromal cells	[204]
Hydrogel scaffolds	Platelet rich plasma	Bone tissue engineering	[205]

SF has been developed into a bioink or biomaterial ink in addition to several other polymers for the fabrication of cartilage tissue. **Table 1.5** summarizes the various silk-based bioinks and biomaterial inks, the bioprinting parameters, and the various cell types used in the formulation of the bioink for cartilage and OC tissue fabrication.

Table 1.5. Detailed characteristics of silk-based bioinks and bioprinting parameters for cartilage and osteochondral tissue engineering.

Bioink/ Biomaterial ink composition	Crosslinking parameters	Construct type / Applications	Cell sources	Printing process	Ref.
SF + PRP + PEG	Chemical mediated: PEG	Cartilage, Model cylinder scaffolds	Rabbit chondrocyte	EBB	[148]
BMSF + GMA + LAP	Photopolymerization LAP (photoinitiator)	Trachea	Rabbit chondrocyte	DLP	[206]
BMSF + PRSF + Gelatin	Physical entanglement and self-gelling	Cartilage, Model grid scaffold, Ear	Porcine auricular chondrocyte	EBB	[139]
Silk Fibroin + Collagen/Chitosan (without cells)	Chemical mediated: Ethanol	Cartilage	Wistar rats BM MSCs	EBP	[207]
BMSF + cartilage acellular matrix (Without cells)	Chemical mediated: Methanol Or EDC and NHS	Cartilage	Rabbit BMMSCs	EBP	[208]
BMSF + Gelatin + BMSC-specific affinity peptide E7 (without cells)	Chemical mediated: Ethanol and Genipin	Cartilage	SD rats BMMSCs	Indirect AM	[209]
BMSF + PVA (without cells)	Physical crosslinking: Freeze-thaw cycle	Cartilage	SD rats auricular chondrocyte	Indirect AM	[210]
BMSF (without cells)	Chemical mediated: Ethanol	Cartilage	Porcine articular chondrocyte	Indirect AM	[211]
Cartilage Ink: BMSF + AASF + PVP; Bone Ink: BMSF + AASF + PVP + strontium doped nano HAp	Enzyme mediated: HRP and H_2O_2	Osteochondral	Porcine ADMSCs	EBB	[147]
BMSF + AASF + Gelatin (without cells)	Physical entanglement and self-gelling behavior Chemical mediated:	Fibrocartilage Grid infill scaffolds;	Primary porcine meniscal	EBP	[212]

	EDC and NHS	Tri-layered meniscus	fibrochondrocytes		
BMSF	Enzyme mediated: HRP and H_2O_2 Chemical mediated: Ethanol	Fibrocartilage Cylinder scaffolds; Meniscus	Human ADMSCs	EBP	[213]
BMSF + Elastin (without cells)	Enzyme mediated: HRP and H_2O_2 Chemical mediated: Ethanol	Fibrocartilage Model scaffolds (cube); AF	Human ADMSCs	EBP	[214]
BMSF + Gelatin+ Glycerol + BCNF (without cells)	Chemical mediated: Ethanol and Genipin	Cartilage Model square blocks; Meniscus	L929 cells	EBP	[215]

Abbreviations: SF: Silk fibroin; SD: Sprague Dawley; PRP: Platelet-rich plasma; PEG: Polyethylene glycol; BMSF: Bombyx mori silk fibroin; PRSF: Philosamia ricini silk fibroin; AASF: Antheraea assama silk fibroin; GMA: Glycidyl Methacrylate; LAP: Lithium phenyl (2,4,6-trimethylbenzoyl) phosphinate; EBP: Extrusion-based Printing; EBB: Extrusion-based Bioprinting; DLP: Digital Light Processing; EDC: 1-ethyl-3-(3-dimethylaminopropyl) carbodiimide hydrochloride; NHS: N-hydroxysuccinimide; PVA: Polyvinyl Alcohol; PVP: Polyvinylpyrrolidone; HRP: Horse Radish Peroxidase; H_2O_2: hydrogen peroxide; AF: Annulus Fibrosus; AM: additive manufacturing; BCNF: bacterial cellulose nanofibers; BM-MSCs: Bone marrow derived mesenchymal stem cells; AD-MSCs: Adipose derived mesenchymal stem cells; SI: Subcutaneous implantation.

MOTIVATION AND OBJECTIVES OF THE PRESENT INVESTIGATION

MOTIVATION AND OBJECTIVES OF THE PRESENT INVESTIGATION

Osteoarthritis (OA), characterized by deterioration of osteochondral tissue (consisting of articular cartilage, subchondral bone, and an interface) in the articular joints, is a common chronic health disorder with more than 100 million people suffering from OA globally. The articular cartilage, central to OA etiology, functions as a biomechanical, load-bearing, and friction reducing tissue. Structurally, the cartilage is a dense, avascular, aneural, and alymphatic connective tissue, with low self-regeneration capacity. Hence, on injury, it affects the entire osteochondral tissue, degenerates into OA, and limits the effective functioning of the entire joint. The current repair strategies often prove insufficient in sustaining long-term restoration of normal or at least, functional physiology. The development of alternative treatment strategies with promising therapeutic outcomes, thus become imperative. The research work carried out current thesis is aimed to explore the emerging techniques of tissue engineering, develop suitable matrices, and reinforce scaffold-based regeneration of cartilage and osteochondral tissue. Fabrication of scaffolds using natural and synthetic polymers, to support cell proliferation, differentiation and provide biological cues and have been investigated. The advantage of using natural polymers lies in their inherent bioactivity that supports graft regeneration and acceptance. The natural polymers like collagen, fibrin, elastin, gelatin, and agarose, though widely used in tissue engineering are also expensive, have low mechanical properties, and require complex isolation/extraction methods.

Silk fibroin, a natural polymer has garnered good traction in tissue engineering, endorsed by a wealth of positive attributes. Fibroin displays biocompatibility, tunable biodegradability to amino acids, robust mechanical properties, ease of processing, affordable, and ability to undergo aqueous processing into different formats such as gels, films, powder, and sponges. Silk fibroin has therefore been extensively explored for biomedical applications and is FDA approved for use in some formats. Silk fibroin from silkworms such as *Bombyx mori* (mulberry silk) silkworms is the most commonly explored silk type. Recently, SF from non-mulberry wild species such as *Antheraea assamensis*, *Antheraea mylitta*, and *Philosamia ricini* silkworms have become the focus of attention, backed by their notable mechanical properties and presence of intrinsic cell-binding arginine–glycine–aspartic acid (RGD) tripeptide. Consequently, their SF has been considered suitable for development of matrices as part of the objectives of this thesis. The abovementioned

characteristics of silk render it suitable for the development of matrices in the current thesis, discussed as follows:

Agarose hydrogel is considered a gold standard matrix for cartilage tissue engineering by its ability to maintain the morphology of chondrocytes and encourage good ECM secretion. Our ability to explore the mechanisms underlying cartilage formation using agarose is cut back by its composition, immunogenic reactions, non-degradability in sync with structure, and mechanical properties not conducive to customization. Thus, in *Objective 1*, the aim was to blend agarose with silk fibroin to form a hydrogel that retained the positive attributes of the agarose standard and nullified its negatives. In addition, a load bearing robustness was required of the hydrogel implant to withstand the stress characteristic of an articular joint. Thus, in *Objective 2*, the aim was to fabricate fiber-reinforced scaffolds with enhanced mechanical strength for the repair and regeneration of cartilage. Further, the structural proximities of articular cartilage and subchondral bone implicate their combined role in OA, and call for regeneration of entire osteochondral unit, inclusive of articular cartilage and underlying bone. Therefore, in *Objective 3*, the aim was to fabricate a biphasic silk scaffold with a spongy fiber-free phase attributed to cartilage and a fiber-reinforced phase for bone revival. The continuous biphasic scaffold was also directed to overcome the common problems with the 2 phases fabrication methods where each phase is developed separately and then glued together.

The matrices developed so far used conventional and manual fabrication methods such as freeze-drying. These methods are handicapped by long duration, low reproducibility, unpredictable pore morphology and spatial distribution, and higher cost burden. Therefore, 3D bioprinting, an advanced manufacturing technology was used to fabricate anatomically generated relevant shapes, that allowed patient-specific fitting on the site of implantation, in a high-throughput, automated, and cost-effective manner, using a suitable and crucial bioink. Inspired by recent reports of silk self-assembly in blends of mulberry and non-mulberry, in *Objective 4*, the aim was to understand the possible mechanism for this gelation and further investigate its usage as bioink for 3D bioprinting application. Therefore, in *Objective 5*, the aim was to use the suitable silk blends from our learning from objective 4 for developing the bioink for cartilage 3D bioprinting. Importantly,

the aim also was to develop a crosslinker-free approach to make the bioink, thus avoiding the possible toxicity and cost burden associated with using crosslinkers.

Finally, the development of therapeutics for OA requires an understanding of the molecular mechanisms of OA initiation and progression. Towards this, several disease models such as animal models have been explored but they lack the biomimetic human pathophysiological conditions, require a longer timeline, and have associated ethical concerns. To overcome the limitations of 2D monolayers and animal models, and with no existing inflamed 3D bioprinted model so far, we aimed to develop an inflamed 3D bioprinted physiologically relevant *in vitro* model in *Objective 6*, to cater to the demand for a robust, high-throughput platform for screening novel anti-inflammatory drugs used in OA therapeutics.

Thus, with the enormous potential of scaffold-based matrices in tissue engineering of cartilage and osteochondral tissue, the current thesis aims to use silk fibroin polymer as a biomaterial to develop various 3D matrices with progress in biomimicry, biofunctionality, and mechanical properties and transitioning from conventional methods of scaffold fabrication to the advanced techniques. The said hypothetical strategies were designed and investigated through the following objectives:

Objectives:

1. Potential of agarose/silk fibroin blended hydrogel for *in vitro* cartilage tissue engineering
2. Silk fiber reinforcement modulates *in vitro* chondrogenesis in 3D composite scaffolds
3. Hierarchically structured seamless silk scaffolds for osteochondral interface tissue engineering
4. Wild silks enable controlled gelation and increase silk hydrogel composite performance
5. 3D bioprinting of cross-linker free silk-gelatin bioink for cartilage tissue engineering
6. Mimicking early-stage osteoarthritis *in vitro* by 3D bioprinting inflamed osteochondral unit for high-throughput anti-inflammatory drug screening applications

Chapter 2

Potential of Agarose/Silk Fibroin Blended Hydrogel for *In Vitro* Cartilage Tissue Engineering

The present work aimed at bringing together the innate advantages of agarose and mulberry/non-mulberry SF to fabricate a blended hydrogel for application in cartilage reconstruction. The physicochemical properties such as swelling behavior, degradation, structural conformation, and rheological properties of the blend hydrogel were studied. The fabricated hydrogels were evaluated with porcine auricular chondrocytes for cellular, biochemical, histological properties, and gene expression studies for cartilage-specific markers.

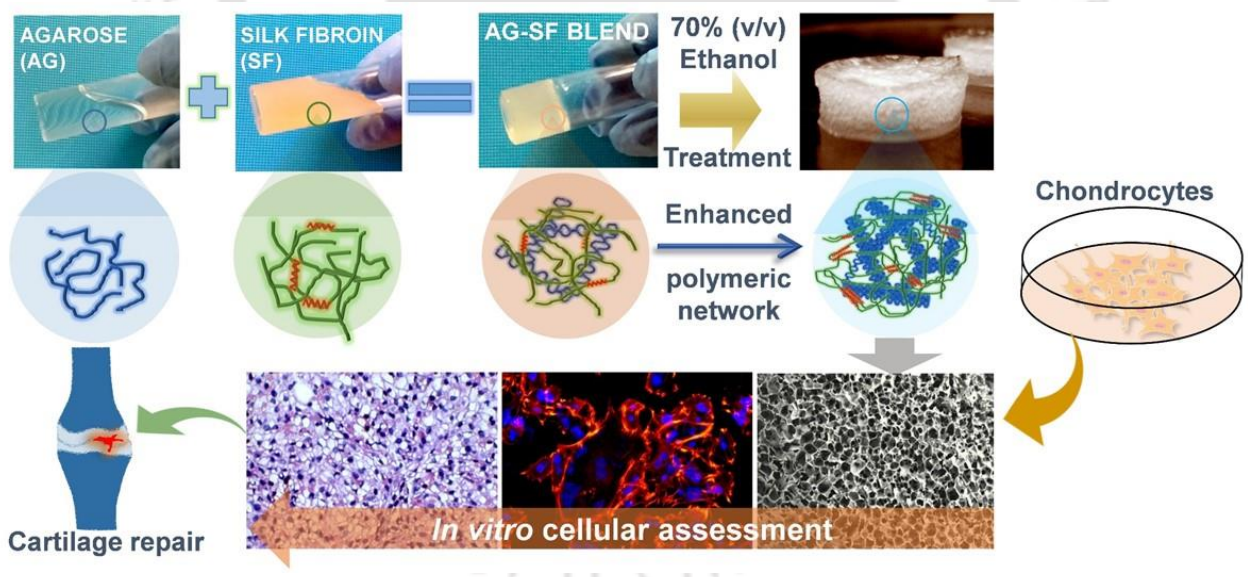

The work embodied in this chapter is published as follows:

Yogendra Pratap Singh, Nandana Bhardwaj, and Biman B. Mandal. "Potential of agarose/silk fibroin blended hydrogel for *in vitro* cartilage tissue engineering." ***ACS Applied Materials & Interfaces*** 8(33), 2016: 21236-21249.

ABSTRACT

Osteoarthritis pandemic has accelerated exploration of various biomaterials for cartilage reconstruction with special emphasis on silk fibroin from mulberry (*Bombyx mori*) and non-mulberry (*Antheraea assamensis*) silk worms. Retention of positive attributes of the agarose standard and nullification of its negatives are central to the current agarose - silk fibroin hydrogel design. In this study, hydrogels of mulberry and non-mulberry silk fibroin blended with agarose were fabricated and evaluated *in vitro* for 2 weeks for cartilaginous tissue formation. The fabricated hydrogels were physico-chemically characterized and analyzed for cell viability, proliferation and ECM deposition. The amalgamation of silk fibroin with agarose impacted the pore size as illustrated by FESEM studies, swelling behaviour and *in vitro* degradation of the hydrogels. FTIR results indicated the blend formation and confirmed the presence of both components in the fabricated hydrogels. Rheological studies demonstrated enhanced elasticity of blended hydrogels with $G'>G''$. Biochemical analysis revealed significantly higher levels of sulphated glycosaminoglycans (sGAGs) and collagen ($p \leq 0.01$) in blended hydrogels. More specifically, non-mulberry silk fibroin blend showed higher sGAG and collagen content (~1.5-fold) than mulberry blend ($p \leq 0.05$). Histological and immunohistochemical analyses further validated the enhanced deposition of sGAG and collagen indicating maintenance of chondrogenic phenotype within constructs after 2 weeks of culture. Real-time PCR analysis further confirmed up-regulation of cartilage specific aggrecan and Sox-9 (~1.5-fold) and collagen type II (~2-fold) marker genes ($p \leq 0.01$) in blended hydrogels. The hydrogels demonstrated immunocompatibility, which was evidenced by minimal *in vitro* secretion of tumour necrosis factor-α (TNF-α) by murine macrophages. Taken together, the results suggested promising attributes of blended hydrogels and particularly the non-mulberry silk fibroin-agarose blends as alternative biomaterial for cartilage tissue engineering.

2.1 Introduction

Osteoarthritis (OA) characterized by deterioration of cartilage in articular joints is a common chronic health disorder that has attained pandemic status. Globally, 100 million people suffer from OA, making it the eighth leading cause of disability [216], with the rate in women (18%) double than that of men (9.6%) in the age group of ≥ 60 years [217]. The articular cartilage is central to this pandemic playing important biomechanical roles as a load-bearing tissue and reducing joint friction. Unfortunately, this avascular, aneural and alymphatic dense connective tissue is structurally predisposed to low self-regeneration capacity. The latter stems from sparse population of differentiated and non-dividing chondrocytes, slow matrix turnover, and low availability of progenitor cells which is aggravated by vasculature paucity [218]. Contemporary cartilage repair strategies include arthroscopic repair, soft tissue grafts, osteochondral transplantation of autogenic and allogeneic tissues, autologous chondrocyte implantation (ACI) and others procedures [219, 220]. However, these treatment options are often insufficient in maintaining the long term restoration of normal physiological function and thus necessitating imperative development of alternative treatment strategies with promising therapeutic ramifications [220]. The development of chondral construct to replace diseased and/or damaged native cartilage is dependent on scaffolds, available functional cell sources and growth factors which facilitates cell proliferation and generation of ECM [221, 222].

In tissue engineering approach, hydrogels have played crucial roles as platforms to chaperon nascent tissue formation. The optimal functioning of any hydrogel is dictated by physical parameters of degradation, swelling, mechanical strength and biological performance parameters of cell attachment, proliferation and secretion [223]. Though the hydrogel based methodologies have taken on vital roles endorsed by their biochemical resemblance with the highly hydrated glycosaminoglycans (GAGs) components of connective tissues [224], the story is far from being comprehensively complete. The agarose polysaccharide is transparent, neutrally charged and thermoreversible [225]. It has been used extensively in cartilage tissue engineering and human clinical trials as a scaffolding material for autologous chondrocyte implantation strategy [226]. Several features such as effect of mechanical loading and cell-seeding density have been studied extensively using agarose hydrogels for cartilaginous tissue formation [227, 228]. It is considered a gold standard biomaterial for *in vitro* tissue engineering of cartilage as it provides superior base for chondrogenesis and higher GAG deposition to yield constructs with functional properties

approaching those of native articular cartilage [99, 229]. Chondrocytes cultured in agarose hydrogel maintain the gene expression of aggrecan and collagen II [91]. Agarose hydrogel helps the formation of a mechanically functional cartilage-like matrix upon long term culturing of chondrocyte [92]. However, agarose can be immunogenic, non-degradable with structure, composition and mechanical properties not conducive to customization, thus curtails our ability to explore the mechanisms underlying cartilage formation in agarose [230]. Along with the aforestated reasons, agarose shows significantly low cell adhesiveness, cell proliferation [231] and low graft integration with the host tissue, thereby limiting its study in animal models [232]. Therefore, blending with other polymers such as chitosan and gelatin, in order to overcome the valid drawbacks has escalated in recent years [233, 234].

Conversely, silk fibroin (SF) is a natural fibrous protein showing immense potential in the field of tissue engineering. Besides being biodegradable and biocompatible, it also exhibits ease of processing, fabrication into various formats (fiber, film, porous scaffold, hydrogel, electrospun mats etc.) and tunable mechanical characteristics [235, 236]. The reported low inflammatory response of SF [237] is supportive of its use in biomedical applications. SF has been extensively utilized in *in vitro* studies as a scaffolding material for bone [238], ligament [239], adipose tissues [240], and cartilage [241]. Subsequently, it has been examined *in vivo* in bone [242], blood vessels [243], adipose [244], cartilage [211], and osteochondral tissue [59]. Recently, FDA approval was granted to Serica Technologies, Inc. for the use of silk scaffolds (*SeriScaffold*™) in soft tissue repair. Owing to its natural ECM like aqueous environment, silk hydrogels have shown promising results in tissue engineering applications [99, 230]. Mulberry SF from *Bombyx mori* has been studied extensively in comparison to non-mulberry SF (*Antheraea assamensis*) for its use in cartilage repair. It is reported that silk fibroin matrices from the two species of silkworms are divergent in their morphology, degradation and bioactivity [236, 245, 246]. A recent study provided an insight into the molecular architecture of *A. assamensis* fibroin, reporting arginine-glycine-aspartic acid (RGD) tripeptide towards N and C-termini of the Gc motif [247]. RGD is an integrin binding site that aids in cell attachment, proliferation and differentiation [182, 248]. Another unique feature of *A. assamensis* SF is that it has uninterrupted polyalanine stretches unlike other saturniid family SF where serine residues break up polyalanine stretches. This hallmark delivers superior tensile strength and mechanical properties of *A. assamensis* SF over *B. mori* SF [247, 249]. SF-based scaffolds of *A. assamensis* have displayed suitable cytocompatibility with

desirable cell adhesion, spreading, and migration, which enhances its applicability in tissue engineering and regenerative medicine [245, 250, 251].

Consequently, the present work is aimed at bringing together the innate advantages of agarose and mulberry/non-mulberry SF in order to fabricate a blended hydrogel for prospective application in cartilage reconstruction using auricular chondrocytes as a cell source. Previous reports supported that auricular source demonstrate higher chondrocyte yield with comparable morphology and gene expressions to the articular source, which indicates the potential of porcine auricular chondrocytes for cartilage repair [252]. The physicochemical properties such as swelling behaviour, degradation, structural conformation, and rheological properties of the blend hydrogel were studied. The fabricated hydrogels were evaluated with porcine auricular chondrocytes for cellular, biochemical, histological properties and gene expression studies for cartilage specific markers. Simultaneously, pure agarose ("gold standard") hydrogels were taken as control for comparison.

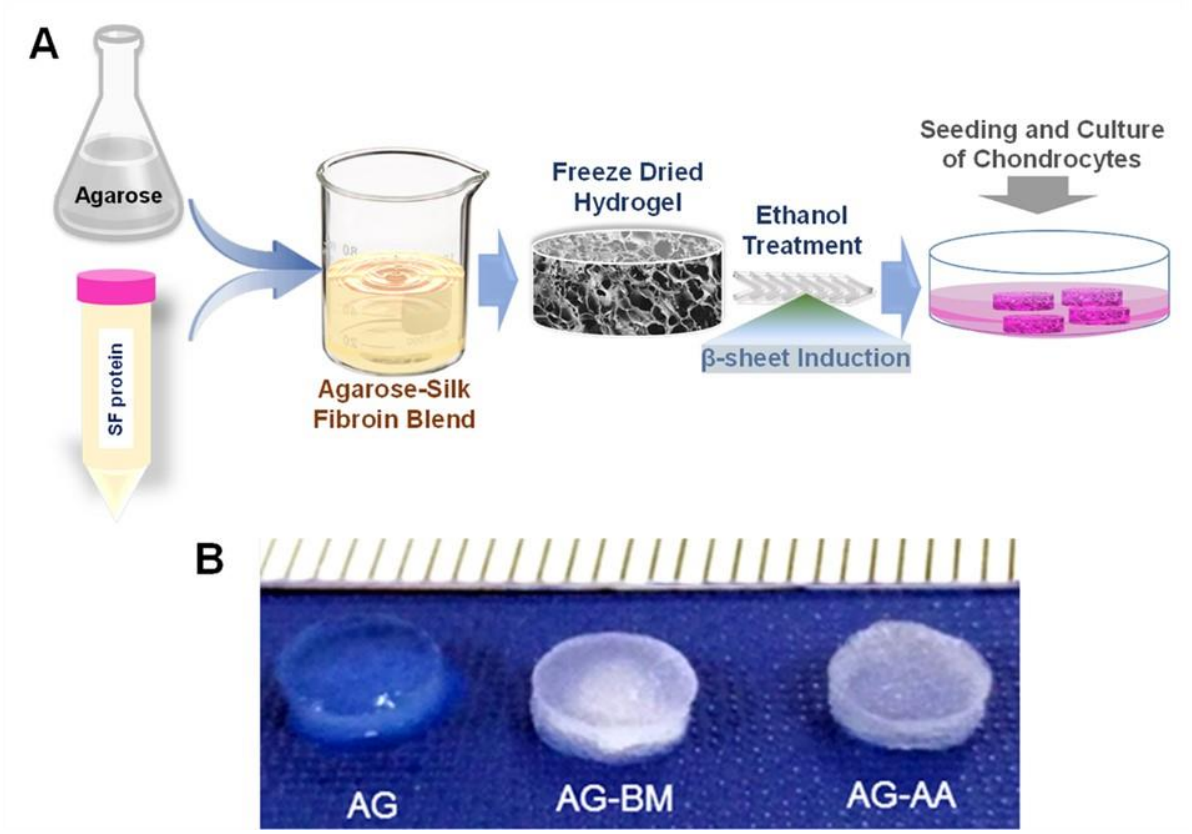

Figure 2.1. *(A) Schematic representation of fabrication of hydrogels and (B) macroscopic appearance of the hydrogels.*

2.2 Materials and methods

2.2.1 Materials

Silk cocoons (*Bombyx mori*) and matured 5th instar larvae of non-mulberry silkworm (*Antheraea assamensis*) were collected from Mangaldoi Silk Farm, Assam, India. Chemicals for cell culture such as Dulbecco's modified Eagle's medium (DMEM), fetal bovine serum (FBS), trypsin–EDTA and amphotericin B were acquired from Gibco BRL Rockville, USA. Protease XIV from *Strepyomyces griseus*, sodium azide, collagenase (type I-A), 1, 9-Dimethylmethylene blue, Alcian blue, Hoechst 33342, Dexamethasone and low-melt agarose (Type VII) were obtained from Sigma-Aldrich, USA. PicoGreen dye (Invitrogen), SYBR Green (Invitrogen), TNF-α kit (Invitrogen), Anti-collagen II monoclonal antibody (Abcam), Vectastain universal elite kit (Vector Laboratories), TMB substrate (Vector Laboratories), live/dead assay kit (Molecular Probes) and other chemicals used were of analytical grade.

2.2.2 Extraction of silk fibroin

Silk fibroin was extracted from cocoons of mulberry *B. mori* silkworm and silk glands of *A. assamensis* silkworm as per earlier established protocols [236, 251, 253, 254]. Briefly, cocoons of *B. mori* were cut into pieces, degummed in boiling 0.02 M Na_2CO_3 solution, washed in distilled water and air dried. The degummed fibres were dissolved in 9.3 M LiBr and dialyzed against milli-Q water using 12 kDa molecular weight cut-off dialysis membrane for 48 h. In parallel, silk fibroin protein of *A. assamensis* was extracted from silk gland of fifth-instar matured larva of silkworm. Silk protein from cocoons of non-mulberry silkworms fail to dissolve in conventional LiBr or any other chaotropic solvent, thus it was isolated from the silk glands of the silkworms. Protein was squeezed out from the isolated glands and dissolved in 1% SDS followed by its extensive dialysis. The concentration of obtained silk fibroin solution was determined by gravimetric method and adjusted to a final concentration of 2% (w/v) in water for further studies.

2.2.3 Preparation of hydrogel

The agarose/silk fibroin blended hydrogels (AG-SF) were prepared by addition of SF solution to dissolved agarose solution. 2% (w/v) solution of each component was used for hydrogel fabrication. The components were mixed gently and allowed to gel; thereafter a 6 mm round disposable (Acuderm Inc) biopsy punch was used to get hydrogels of 6 mm diameter and 2 mm thickness. These punched hydrogels were then frozen at -20 °C for 12 h followed by lyophilization in a freeze drier for 24 h. The lyophilized hydrogels were further treated with 70% (v/v) ethanol

for 4-6 h in order to induce β-sheet in SF protein. The macroscopic appearance of the hydrogels is shown in **Figure 2.1B**.

2.2.4 Morphological analysis of hydrogels

The surface morphology, pore size and interconnectivity of pores were examined using field emission scanning electron microscope (FESEM) (Zeiss, Sigma, USA). The hydrogels were freeze dried and sputter coated with gold followed by scanning analysis. The pore size was determined by taking 20 random pores followed by analysis using Image J software (NIH, USA).

2.2.5 Swelling behaviour

Swelling property of the hydrogels was studied using conventional gravimetric method. Briefly, the dry weight of hydrogels was recorded and then immersed in phosphate buffered saline (PBS, pH 7.4) at 37 °C till they attained equilibrium. The swelled weight of hydrogels was taken at various time intervals. The experiment was conducted in sets of three (n = 3) under identical conditions and percent swelling was calculated using the equation:

$$\text{Swelling (\%)} = [(Ws - Wd)/Wd] \text{ X } 100$$

where, Ws is the swelled weight and Wd is the dry weight of the hydrogel (mg).

2.2.6 *In vitro* enzymatic degradation

The *in vitro* enzymatic degradation of hydrogel was assessed using protease XIV from *S. griseus* with an activity of ≥3.5 units/mg. The hydrogels were immersed in 1mL PBS (pH 7.4) having 2U of protease XIV enzyme and incubated at 37 °C. Enzyme solution was replaced every 3 days for a period of 28 days. 0.05% sodium azide was added to solution in order to prevent microbial growth. Samples without the protease enzyme (i.e., only PBS) were taken as control. The experiment was conducted in sets of three (n = 3) under identical conditions. Weight loss was calculated using the equation:

$$S = [(W_0 - W_1)/W_1] \text{ X } 100$$

where, S is percentage solubility, W_0 is initial weight of hydrogel (mg) and W_1 is the final weight of the hydrogel (mg).

2.2.7 Fourier transform infrared spectroscopy (FTIR)

FTIR study was carried out using an FTIR spectrophotometer (Perkin Elmer BX) and spectra was recorded in the range of 400-4000 cm^{-1} by accumulation of 32 scans with a resolution of 4 cm^{-1}.

Background readings were subtracted from sample readings. All spectra were recorded at room temperature and analyzed using Microcal origin version 8.0.

2.2.8 Rheological characterization

Rheological experiments of hydrogels were carried out using Physica MCR 101 (Anton Paar). Amplitude sweep and frequency sweep were executed using stainless steel (25 mm diameter) parallel plate. For each measurement, the preformed hydrogel (20 mm diameter) was placed on the lower plate of the rheometer and the gap between the plates was maintained at 1.4 mm. Frequency sweep was carried out in the range of 0.01-100 Hz at a constant strain of 5% to get storage modulus (G′), loss modulus (G″) and complex viscosity (η). The amplitude sweep was done between 0.01-100% strain (γ) to obtain the yielding point of the gel. All experiments were performed at 25 °C.

2.2.9 Isolation of porcine auricular chondrocytes

Auricular chondrocytes were harvested from the ear of freshly slaughtered pig obtained from a local abattoir. Porcine ear was cleaned and dissected free of skin using sterile scalpels. The obtained cartilage was cut in small fragments and rinsed with sterile PBS (pH 7.4). The obtained fragments were treated with antibiotic solution (Invitrogen) before digestion with 0.2% protease (type XIV, ≥3.5 U/mg). Further digestion with 0.05% collagenase (type I-A, ≥125 collagen digestion units/mg) in high glucose DMEM supplemented with 10% fetal bovine serum (FBS) media was carried out overnight at 37 °C with 95% relative humidity and 5% CO_2. The auricular chondrocytes were centrifuged (2000 rpm for 5 min) and the resultant cell pellet was washed 2-3 times with high glucose DMEM media (**Figure 2.2**). The viability of cells was determined by trypan blue dye (Sigma-Aldrich, USA) followed by culture in high glucose DMEM media. For *in vitro* experiments, passage three (P3) chondrocytes were used.

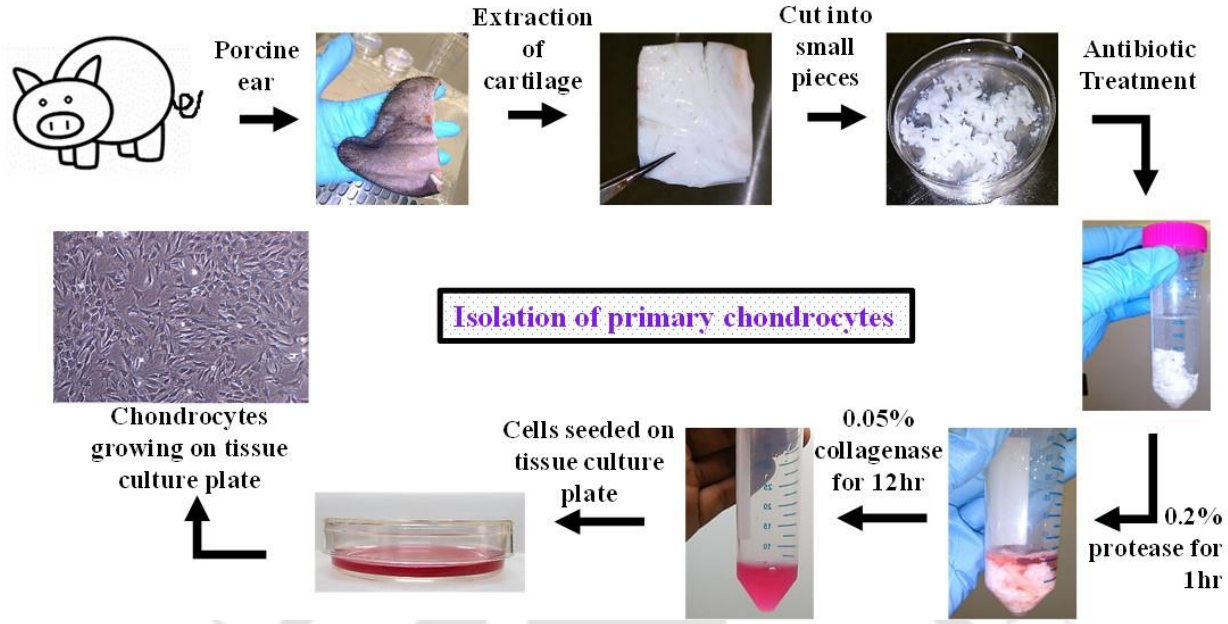

Figure 2.2. *Schematics of isolation of primary chondrocytes from porcine ear.*

2.2.10 Cell seeding and culture

The fabricated pure agarose and blended hydrogels (6 mm in diameter and 2 mm thick) were preconditioned in complete medium for 2 h before cell seeding. The preconditioned hydrogels in 24 well plates were seeded with 0.5 million cells per 6 mm hydrogel construct and incubated at 37 °C, 5% CO_2 for 3 h for initial cell attachment to the hydrogel. Further, 2 mL of fresh high glucose DMEM was added to all the wells. After 3 h, hydrogels were shifted to fresh wells containing chondrogenic media. The chondrogenic media was constituted with high glucose DMEM, 10% FBS, 1% antibiotic-antimycotic solution, 100 nM dexamethasone, 50 mg/mL ascorbic acid, 1 X ITS +3 (contains 1.0 mg/mL insulin from bovine pancreas, 0.55 mg/mL human transferrin, 0.5 µg/mL sodium selenite, 470 µg/mL linoleic acid, 470 µg/mL oleic acid and 50 µg/mL bovine serum albumin) and 40 µg/mL L-proline. The cultures were further maintained in complete chondrogenic media and changed every 3 days for a period of 14 days.

2.2.11 Cell viability assay

Chondrocytes viability was assessed using live dead assay kit. Briefly, the cell seeded hydrogels were washed with PBS (pH 7.4) and incubated in 4 mM calcein-AM (stains live cells) and 2 mM ethidium homodimer (stains dead cells) in PBS for 15-20 min at 37 °C. Constructs were pre washed with PBS (2-3 times) prior to visualization using a fluorescent microscope (EVOS FL, Life

Technologies). Viable cells are identified by the green fluorescence produced as a result of intracellular esterase activity which converts calcein-AM to calcein. Concurrently, dead cells are recognized by the entry of ethidium homodimer into cells through damaged membrane and it's binding to DNA resulting in red fluorescence. Further, to visualize cellular arrangement, nuclei were stained with Hoechst 33342 for 30 min under dark condition followed by imaging under fluorescent microscope (EVOS FL, Life Technologies).

2.2.12 Biochemical analysis

The hydrogels for estimation of DNA and sGAG were digested by papain solution (125 mg/mL papain, 5 mM L-cysteine, 100 mM Na_2HPO_4, and 5 mM EDTA, pH 6.2) at 60 °C for 16 h. DNA content was measured according to manufacturer's protocol using PicoGreen DNA assay kit (Invitrogen). Briefly, the digested samples were centrifuged and 25 µL of supernatant was taken in 96 well-plate having 75 µL of 1X TE buffer. To each well, 100 mL of Quant-iT PicoGreen reagent (1:200 dilution) was added and fluorescence was measured using microplate reader (Tecan infinite M200 PRO) with an excitation and emission wavelength of 480 and 528 nm, respectively. Lambda phage DNA (0-10 µg/mL) was used to generate a standard curve for DNA measurement. For estimation of total sulfated GAG (sGAG), 1,9-dimethylmethylene blue (DMMB) assay was used [255] where, 200 µL of DMMB reagent was added to 50 µL of papain digested sample and absorbance was recorded at 525 nm. Additionally, sGAG secreted in the media from spent culture medium was assessed using similar protocols. Chondroitin sulfate (Sigma-Aldrich, USA) in the range of 0-100 µg/mL was used to prepare standard for GAG estimation. Collagen content was measured using a modified Hride Tullberg-Reinert method [256]. Briefly, the samples were digested using pepsin cocktail (1 mg/mL pepsin, pH 3.0) at 4 °C for 48 h and dried at 37 °C for 24 h in a 96 well plate followed by addition of 100 µL of Sirius red dye solution (prepared in picric acid–saturated solution to a final concentration of 1 mg/mL) for 1 h with mild shaking. Sample containing wells were then washed three times with 0.01 normality HCl followed by resolution of dye sample complex using 0.1 normality NaOH. The absorbance was recorded at 550 nm. Total collagen content was estimated using a standard curve prepared with rat tail collagen type I (Sigma-Aldrich, USA). Hydrogel without cells were used as control. GAG and collagen contents were normalized against DNA content and hydrogel weight in order to avoid variations from cell numbers and hydrogel sizes.

2.2.13 Histology and immunohistochemistry (IHC)

For histological examination the chondrocyte seeded hydrogels were fixed in 10% neutral buffered formalin (NBF) for 24 h. These fixed samples were dehydrated, cleared and embedded in paraffin wax. The paraffinized hydrogels were sectioned (3 µm thick) using microtome (Leica) and stained using hematoxylin and eosin (H&E) for cell morphology and 1% Alcian blue (Sigma-Aldrich, USA) (prepared in 3% acetic acid solution, pH 2.5) for sulphated proteoglycan. Immunohistochemistry (IHC) was done for localization of type II collagen, which is a bulk component of the cartilage ECM. Herein, the paraffinized slide was deparaffinised, cleared and rehydrated. Following this, it was stained as per manufacturer's protocol using Vectastain Elite Universal ABC kit (Vector laboratories). Briefly, samples were incubated with normal horse serum (blocking serum) for 20 min and further treated with monoclonal antibody (Abcam) against Col II (1: 300) for 30 min, followed by incubation with biotinylated universal antibody. The samples were then reacted with ABC reagent provided with the kit, and finally developed using TMB substrate kit for peroxidase (Vector laboratories) to get a soluble blue reaction product. Stained sections were visualized by photo-microscopy using bright-field illumination (EVOS FL, Life Technologies).

2.2.14 Real time PCR analysis

Total RNA was extracted from cell seeded hydrogels using TRIzol (Sigma-Aldrich, USA) and RNeasy mini-spin columns (Qiagen) following manufacturer's instruction [67, 257]. Briefly, hydrogels with cultured cells were taken in 2 mL tubes and 1 mL TRI reagent was added to it followed by its chopping with micro scissors on ice and centrifugation at 12,000 g for 10 min/4 °C. The obtained supernatant was taken in a fresh tube and incubated for 10 min in 200 µL of chloroform followed by centrifugation at 12,000 g/4 °C for 15 min. The upper aqueous layer was carefully transferred to a RNeasy mini-spin column. RNA was washed and eluted according to manufacturer's protocol. The obtained RNA was then quantified using Nanodrop (Eppendorf) and further cDNA was prepared using high-capacity cDNA reverse transcription kit (Applied Biosystems) according to manufacturer's protocol in PCR thermal cycler (Takara). Real time PCR was performed using SYBR Green dye (Invitrogen) in a 7500 real time PCR system (Applied Biosystems). SYBR Green mix, forward primer, reverse primer and cDNA was added to make a reaction volume of 20 µL and run under the set conditions of holding stage (2 min at 50 °C, 10 min at 95 °C) and cycling stage (40 cycles of 95 °C for 15 s, and 60 °C for 45 s). Cartilage specific

genes namely aggrecan, Sox-9 and collagen type II were quantified. The obtained results were analyzed through comparative Ct method ($2^{-\Delta\Delta Ct}$) and normalized to an endogenous housekeeping gene glyceraldehyde-3-phosphate-dehydrogenase (GAPDH). All samples were analyzed in triplicates (n = 3). **Table 2.1** lists the primers used.

Table 2.1. Sequence of primers for real time PCR.

Gene	Sequence	Accession No.
Aggrecan	F 5′-CCCAACCAGCCTGACAACTT-3′ R 5′-CCTTCTCGTGCCAGATCATCA-3′	NM_001164652.1
Sox-9	F 5′-TTCCGCGACGTGGACAT-3′ R 5′-GGCGGCAGGTACTGGTCAAACTC-3′	NM_213843.1
Collagen II	F 5′-CAGGTGAAGGTGGGAAACCA-3′ R 5′-ACCCACGAGGCCAGGA-3′	AF201724.1
GAPDH	F 5′-TCGGAGTGAACGGATTTGG-3′ R 5′-CCAGAGTTAAAAGCAGCCCT-3′	NM_001206359.1

2.2.15 Macrophage stimulation and determination of TNF-α release

The murine macrophage cell line RAW 264.7 was grown in DMEM containing 10% FBS, 1% antibiotic-antimycotic solution at 37 °C and 5% CO_2. Cells were plated at 1×10^5 cells per well in 12-well plate and incubated overnight. The next day, hydrogels were added to the cell containing wells. After 12 h and 24 h of incubation the medium was collected and assayed for tumor necrosis factor alpha (TNF-α) release. Medium without hydrogel was used as negative control, while lipopolysaccharide (500 ng/mL) (LPS from *Escherichia coli*, Sigma-Aldrich, USA) was taken as positive control. The level of TNF-α was measured by ELISA as per manufacturer's protocol (Invitrogen). Briefly, the diluted samples (2-fold with standard diluent buffer) were taken in 8-well strip and 50 µL of biotinylated secondary antibody was added to it followed by incubation for 90 min at room temperature (RT). Post incubation, the wells were washed 4 times followed by addition of 100 µL of strepavidin-HRP working solution and its incubation for 30 min at RT. After washing, 100 µL of stabilized chromogen solution was added to each well and incubated in dark for 30 min. Final steps included addition of 100 µL stop solution and measuring its absorbance at 450 nm. The amount of TNF-α secreted was calculated using standard curve values plotted in the range of 0-1000 pg/mL TNF-α.

2.2.16 Digital image analysis

Color de-convolution technique was used for semi-automated digital analysis of Alcian blue stained images [250]. Briefly, image thresholding was done followed by color de-convolution technique for creating a complementary image. Herein, the range of pixel intensities was from 0 to 255, where the darkest and lightest shade color in the image were represented by 0 and 255 respectively. Further, the histogram profile, which represents the number of pixels of a specific intensity value vs. their respective intensity of every image was acquired using Image J plugin with assignment of automated score (high positive, positive and negative) to each image depending upon the intensity.

2.2.17 Statistical analysis

All experimental data are reported as mean ± standard deviation (n = 3). Statistical analysis was performed by one way analysis of variance (ANOVA) using Sigma Plot 11.0 and Holm-Sidak test was carried out to assess variance across groups. The differences between groups of $*p \leq 0.05$ were considered statistically significant and $**p \leq 0.01$ as highly significant.

2.3 Results

2.3.1 Morphological analysis of hydrogels

Blended hydrogels were fabricated using 2% (w/v) each of agarose and SF solution in a 1:1 ratio. The preparation scheme is presented in **2.A**. Fabricated hydrogels had a translucent appearance in the hydrated state without any noticeable phase separation, as shown in **Figure 2.1B**. Microstructure of the hydrogels as examined by FESEM images revealed interconnected heterogeneously porous structures in all hydrogels (**Figure 2.3A**). Herein, freeze drying technique was utilized to create porous structure of hydrogels and the range of pore size is presented in **Figure 2.3B**. The pore size of the agarose (AG) hydrogels was 138 ± 26 μm, whereas that of agarose-*B. mori* silk fibroin (AG-BM) and agarose-*A. assamensis* silk fibroin (AG-AA) blended hydrogels were 158 ± 26 μm and 170 ± 23 μm, respectively. Pore size of blended hydrogels were

bigger as compared to pure agarose hydrogels. The AG-AA hydrogel exhibited significantly larger pore size as compared to AG ($p \leq 0.05$).

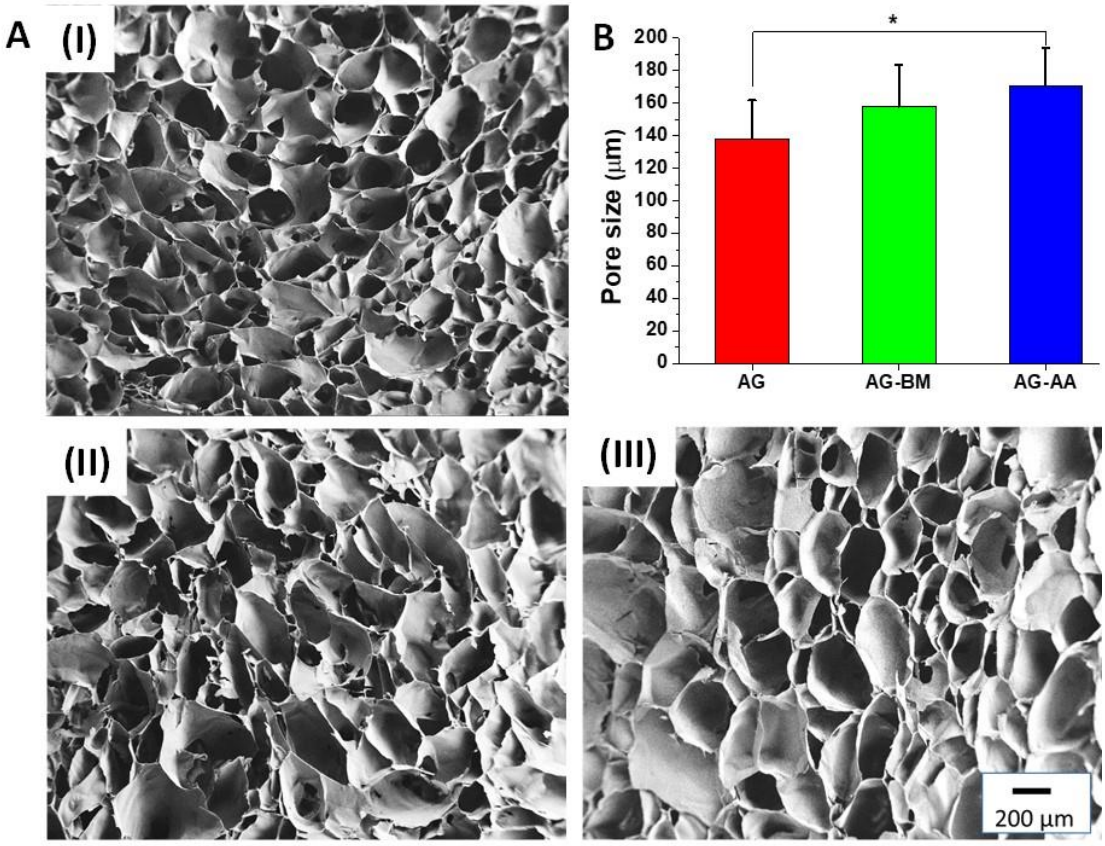

Figure 2.3. *(A) FESEM images of the hydrogels; (I) pure agarose (AG), (II) agarose - B. mori (AG-BM) and (III) agarose - A. assamensis (AG-AA) hydrogels. (B) Average pore size of the hydrogels, (*$p \leq 0.05$). Scale bar represents 200 µm.*

2.3.2 Swelling behaviour

Absorption and retention of large quantities of water is cardinal to 3D polymeric networks such as hydrogels. Thus, assessment of its swelling ability is an important characterizing feature. The degree of swelling in various hydrogels after immersing in PBS and weighing at predefined time points is shown in **Figure 2.4A**. All samples exhibited swelling behaviour and reached equilibrium within 3 h. Rapid maximal swelling was observed within first 30 min with a swelling ratio of 30. Higher swelling (~1.2 times) was observed in AG hydrogel as compared to the blends ($p \leq 0.05$). Among the blends, AG-BM hydrogel showed higher swelling compared to AG-AA.

2.3.3 Enzymatic degradation

The *in vitro* enzymatic degradation assessed by monitoring the weight loss of the hydrogel post 28 days of incubation with protease XIV solution is shown in **Figure 2.4B**. PBS (pH 7.4) was used as a control. The control hydrogels showed no significant degradation over the 28 days. The enzyme treated AG-BM blended hydrogel showed a maximum of 45% reduction in mass followed by AG-AA blend, showing approx. 35% reduction in mass after 28 days ($p \leq 0.01$). However, pure agarose hydrogels did not show any significant degradation in PBS (pH 7.4) or in protease solution. The results indicated that degradation rate of AG-BM was higher (~1.2-fold) than AG-AA ($p \leq 0.05$).

2.3.4 Fourier transform infrared spectroscopy (FTIR) analysis

The structural conformation of the fabricated hydrogels using FTIR spectra is shown in **Figure 2.4C**. Pure agarose showed its characteristic peaks at 1071 cm^{-1} (C–O, axial deformation), 930 cm^{-1} (3, 6-anhydro-galactose), and 891 cm^{-1} (C-H, angular deformation of β anomeric carbon). FTIR spectra of only silk fibroin (both *B. mori* and *A. assamensis*) showed absorption peaks at 1630 cm^{-1} (amide I) and 1520 cm^{-1} (amide II) which corresponds with the β-sheet conformation. Another peak at 1235 cm^{-1} indicates the amide III region. In blended hydrogels, characteristic peaks of both agarose and silk fibroin were recorded, which confirmed the blend formation. However, there was slight shift in amide I and amide II peaks in case of blends.

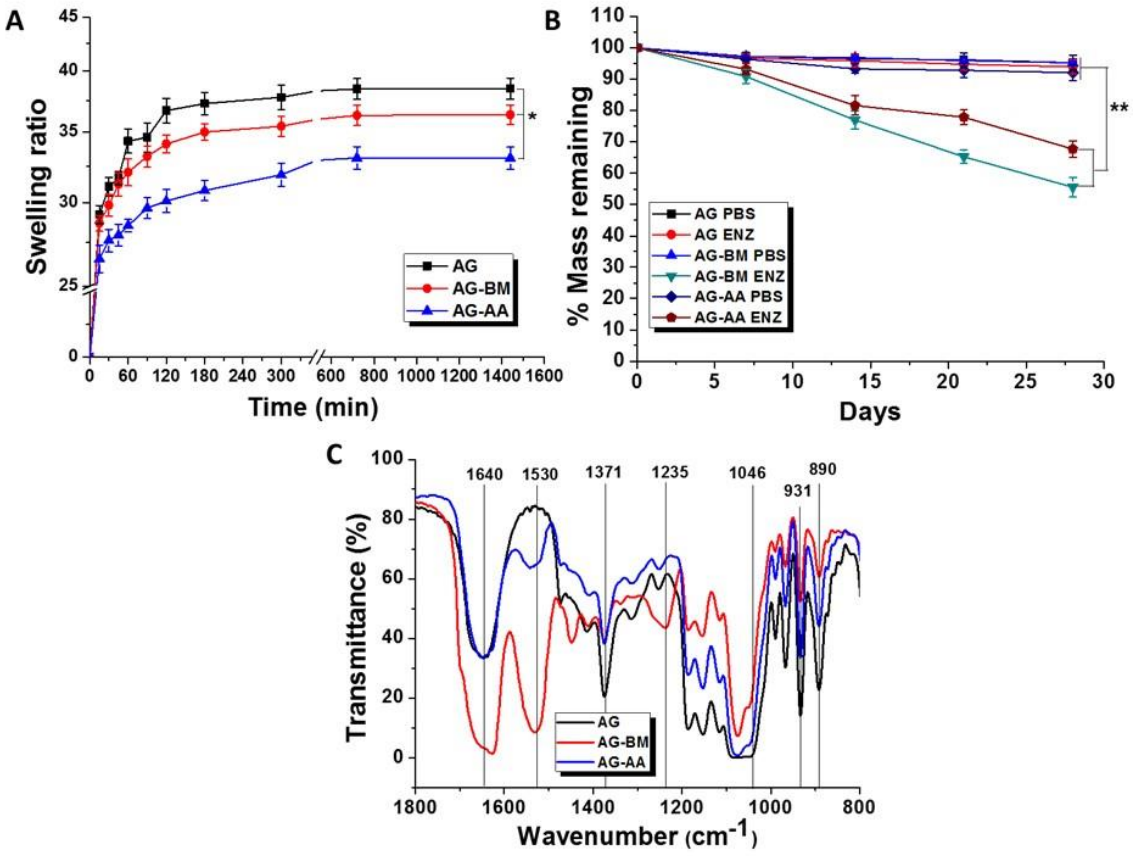

Figure 2.4. *(A) Swelling ratio (B) degradation behaviour and (C) FTIR spectra of the pure agarose and blended hydrogels. Data are plotted as mean ± standard deviation, n = 3. (*p ≤ 0.05, **p ≤ 0.01).*

2.3.5 Rheological characterization

Amplitude sweep was performed to analyze the physical nature of the gel. **Figure 2.5A** shows storage modulus (G′) and loss modulus (G″) representing elastic and viscous behaviour of the hydrogels, respectively. Linear Viscoelastic Region (LVER) was determined using shear strain (0.01 –100%). As the strain increased at fixed ω, the storage modulus decreased and the loss modulus peaks at the onset before dipping finally. At a particular strain the G′ and G″ intersect each other. The intersection was at a strain amplitude of about 2.5% for pure agarose, 10% for AG-BM and 9% for AG-AA. The frequency sweep revealed G′ to be higher than G″ in all hydrogels and were dependent on frequency (**Figure 2.5B**). Along with high G′ values, the blend hydrogels showed higher difference between G′ and G″. **Table 2.2** displays G′ and G″, and loss angle (tan δ = G″/G′) data at a fixed frequency of 0.1 Hz for the hydrogels.

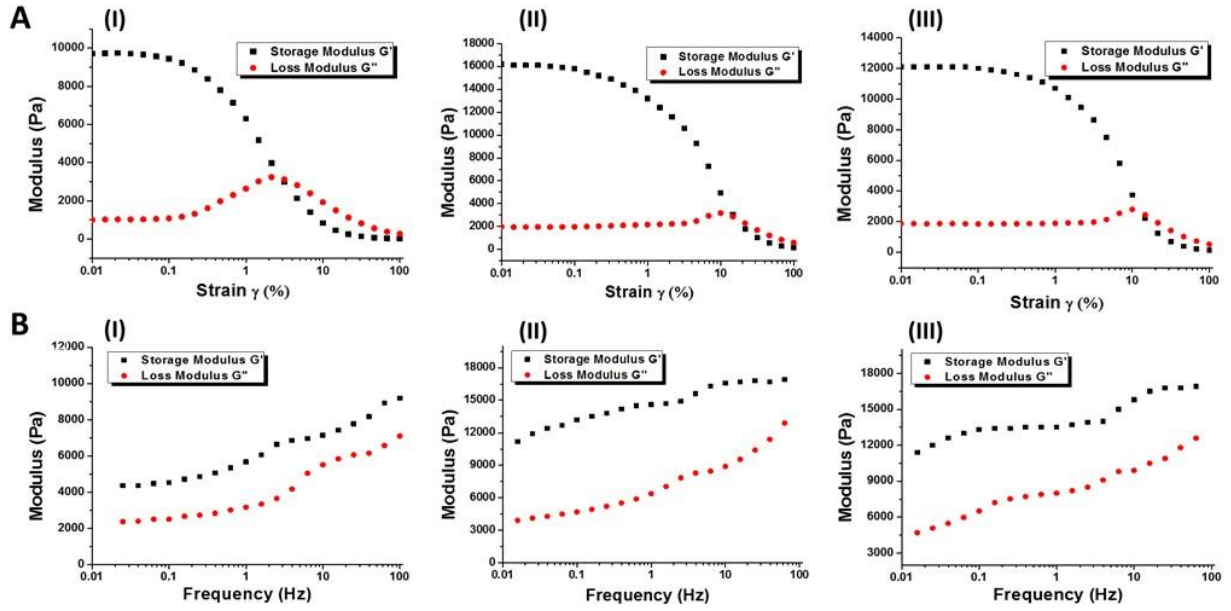

Figure 2.5. *Amplitude sweep (A) and frequency sweep (B) of the hydrogels. (I) Pure agarose, (II) AG-BM and (III) AG-AA displaying storage modulus (G') and loss modulus (G'').*

Table 2.2. Storage modulus (G′), loss modulus (G″) and loss angle (tan δ) of the hydrogels.

	AG	**AG-BM**	**AG-AA**
G′ (KPa)	4.52	13.20	13.30
G" (KPa)	2.51	4.69	6.51
tan δ	0.55	0.35	0.48
δ (°)	~29 °	~19 °	~25 °

2.3.6 Cell viability

Live-dead assay demonstrated the cellularity and localization of porcine chondrocytes in hydrogels. The fluorescent images obtained showed live (green) chondrocytes when cultured on hydrogels over a period of 14 days (**Figure 2.6A**). All hydrogels showed uniform distribution and displayed a spherical morphology of cells throughout the culture conditions. No cell death was observed within hydrogels. The uniform cellular distribution was further confirmed by Hoechst 33342 staining, which stains the nucleus (**Figure 2.6B**).

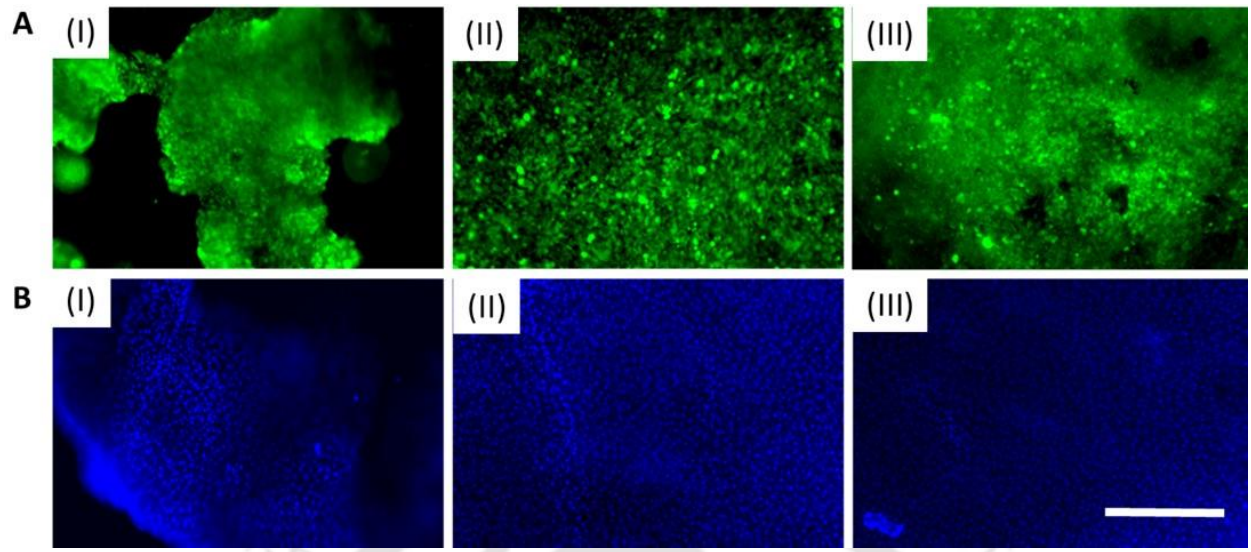

Figure 2.6. *(A) Live/dead staining and (B) Hoechst staining of chondrocytes on hydrogels after 14 days of culture. (I) AG, (II) AG-BM and (III) AG-AA. Scale bars = 400 µm.*

2.3.7 Biochemical analysis

Biochemical analysis of the hydrogels post 14 days of chondrocyte culture was performed to quantify DNA, secreted sGAG and collagen content. DNA content increased significantly in all the hydrogels on day 14 as compared to day 1 ($p \leq 0.01$) (**Figure 2.7A**). More specifically, the DNA content increased ~1.5-fold,~1.8-fold and ~2-fold in AG, AG-BM and AG-AA, respectively on day 14 ($p \leq 0.01$). The blended hydrogels showed higher total DNA content (~200 ng) than the pure agarose hydrogel (~150 ng) ($p \leq 0.01$). Similar trend was observed when total DNA was normalized with hydrogel mass, showing~2-fold increase on 14^{th} day as compared to day 1 ($p \leq 0.05$).

The total sGAG content (both in hydrogel and media) indicated increase in all hydrogels, reaching approx. 110 µg at day 14 compared to 15 µg at day 1 (~7-fold increase) ($p \leq 0.01$). On day 14, sGAG content of the blended hydrogels was higher compared to the AG hydrogel ($p \leq 0.05$). Among the blends, AG-AA hydrogel showed higher (~1.5-fold) secretion of sGAG as compared to AG-BM ($p \leq 0.05$). sGAG in medium constituted 25-30% of the total secreted sGAG (**Figure 2.7B**). To minimize the discrepancies due to cell seeding, total sGAG was normalized per unit DNA which showed an increment (~4-fold) on day 14 as compared to day 1. On day 14, sGAG content per DNA in AG-AA was significantly higher (~1.2-fold) in comparison to AG ($p \leq 0.01$). Individual hydrogel mass effect on the growth and maturation of chondrocytes was assessed by

normalizing total sGAG content with hydrogel mass. sGAG content normalized to hydrogel mass showed similar trend, where blended hydrogels showed significantly higher content on day 14 as compared to pure agarose hydrogels ($p \leq 0.05$). Overall, the AG-AA blend hydrogel showed significantly higher sGAG content than AG-BM hydrogel.

Total collagen content in all hydrogels increased from 60 μg on day 1 to 250 μg (~4-fold) on day 14 ($p \leq 0.01$). Collagen content in blended hydrogels was higher (~1.5-fold) as compared to pure agarose hydrogel (**Figure 2.7C**) ($p \leq 0.01$). Among the blends, AG-AA hydrogel exhibited higher total collagen content than AG-BM ($p \leq 0.05$). Normalized collagen content per DNA showed ~2-fold increase on day 14 as compared to day 1 ($p \leq 0.001$). On day 14, AG-AA hydrogel exhibited significantly higher collagen per DNA as compared to AG ($p \leq 0.05$). Similarly, on normalization with hydrogel mass, AG-AA hydrogel exhibited higher collagen content (~1.2-fold) as compared to AG-BM ($p \leq 0.05$).

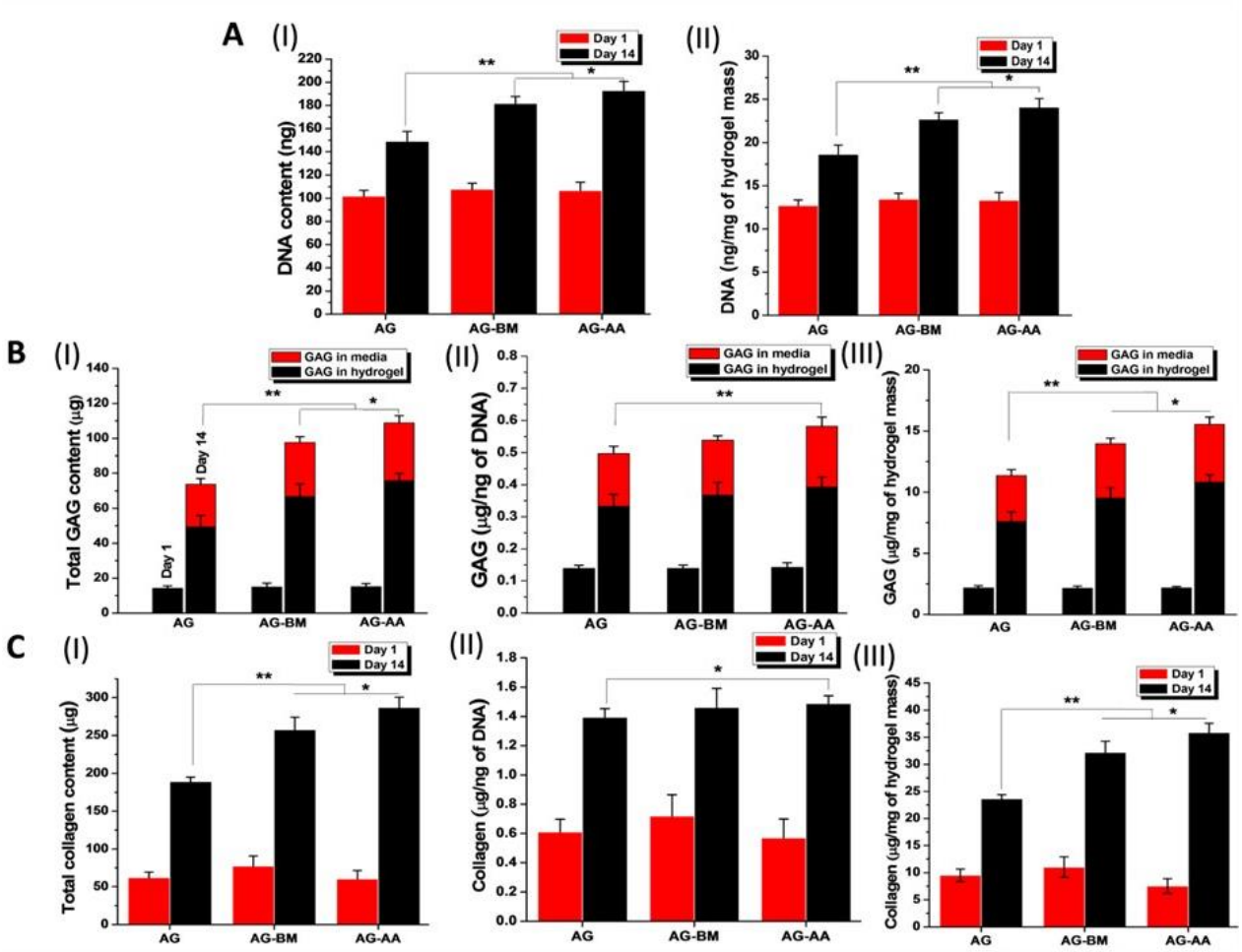

Figure 2.7. *Biochemical assay showing (A) DNA content, (B) GAG and (C) Collagen content in the hydrogels cultured with chondrocytes for 14 days. Data are depicted as mean ± standard deviation, n = 3. (*p ≤ 0.05, **p ≤ 0.01).*

2.3.8 Histology and immunohistochemistry (IHC)

The histological assessment was done by H&E staining and Alcian blue staining post 14 days culture period. H&E-stained images showed growth of cells in all constructs with the nuclei-stained blue by hematoxylin (**Figure 2.8A**). The cartilage-specific sGAG was stained positive by Alcian blue staining (**Figure 2.8B**), giving an intense blue colour, which is a hallmark of sGAG deposition, suggesting the presence of sGAGs in the ECM. AG-AA blended hydrogel showed more sGAG deposition as compared to other hydrogels. With collagen type II being the focal ECM protein of cartilage, analysis of IHC displayed positive staining for Col II in all hydrogels after 14 days of culture (**Figure 2.8C**). In contrast, non-seeded hydrogels exhibited minimal or no staining for Col II staining. The AG-AA blended hydrogel exhibited most intense staining and growth of cells than other hydrogels.

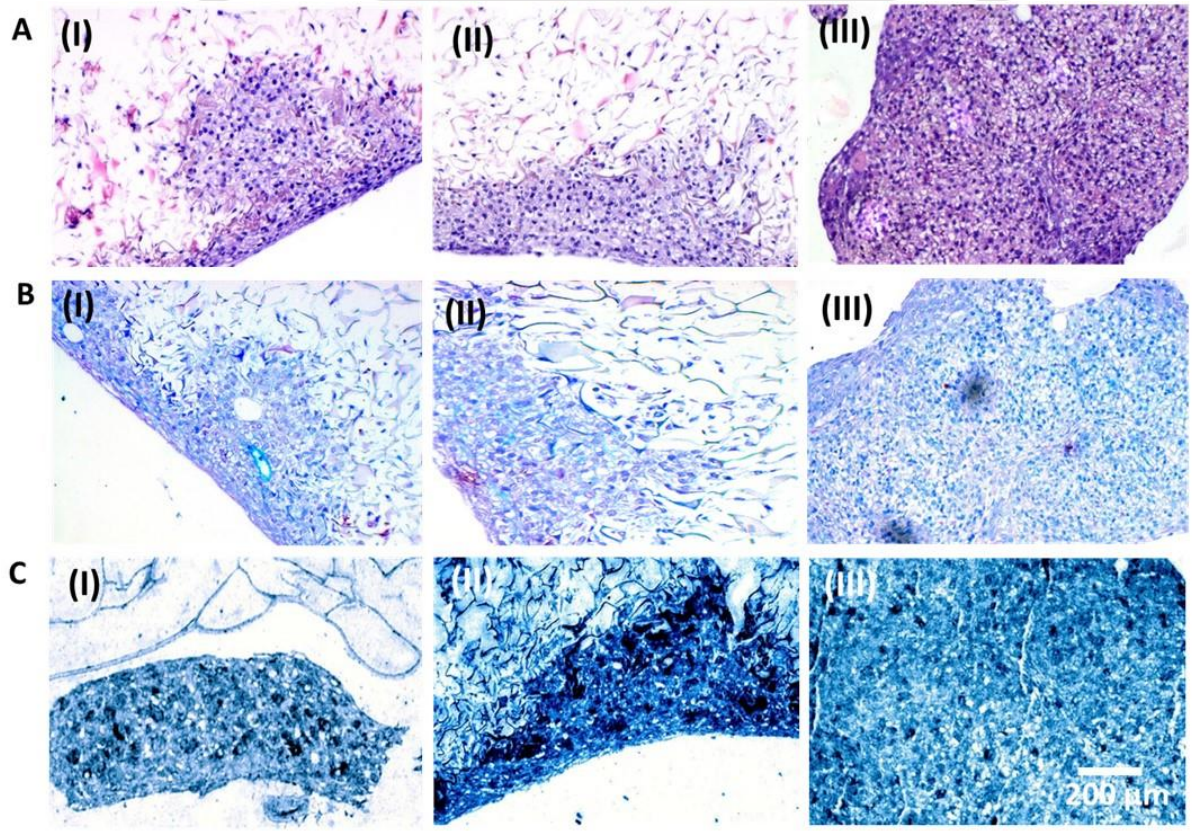

Figure 2.8. *(A) Images of H&E staining, (B) Alcian blue staining and (C) IHC staining showing growth of chondrocytes on hydrogel and ECM formation in chondrogenic medium after 14 days of culture. (I) AG, (II) AG-BM and (III) AG-AA. Scale bar represents 200 µm.*

Additionally, the color de-convolution plugin of Image J software was used for data analysis of Alcian blue stained images with higher magnification. The analysis showed the histogram profile of pixel against the intensity of Alcian blue stained images and their respective score (**Figure 2.9**). The AG hydrogel showed a "positive" score, whereas the AG-BM and AG-AA hydrogels indicated a "high positive" score.

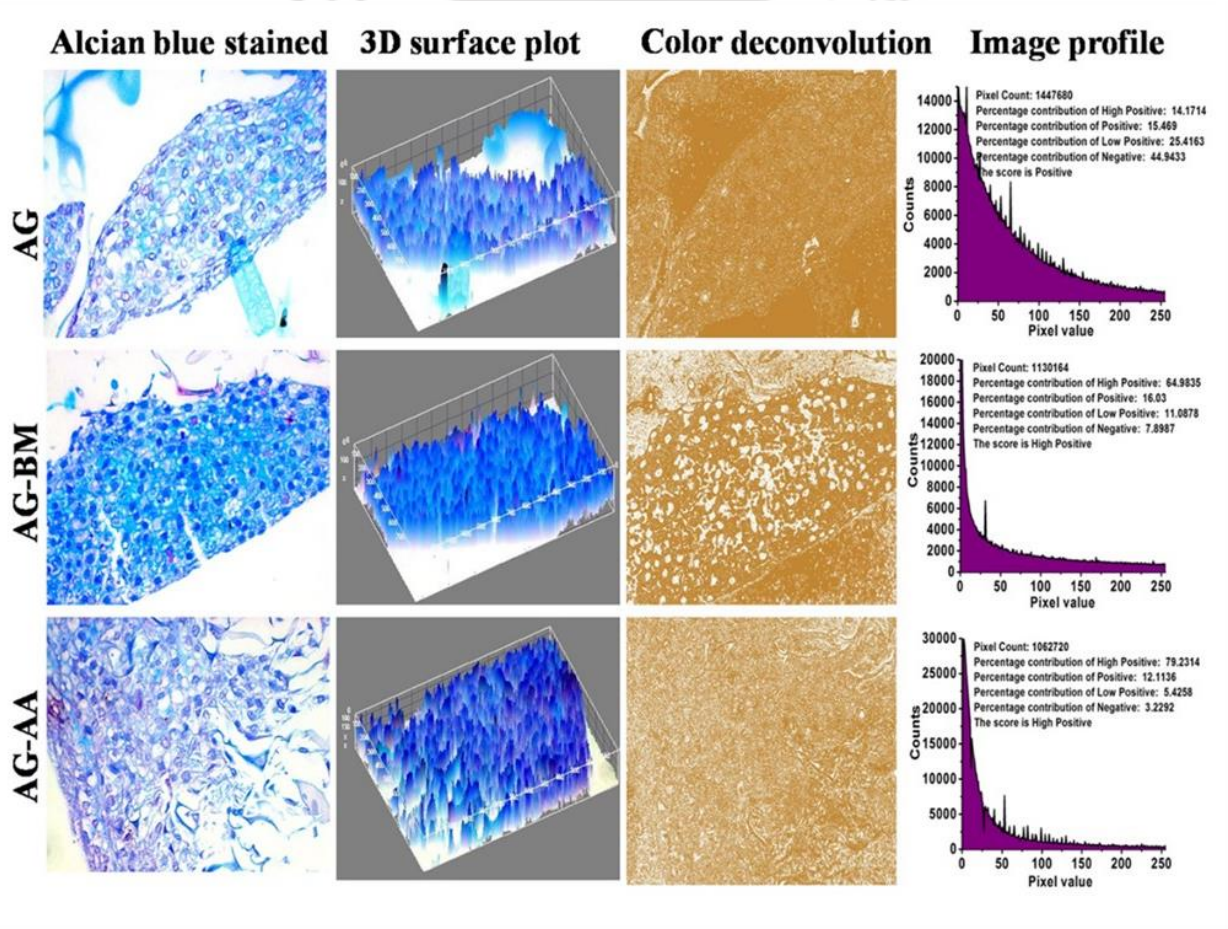

Figure 2.9*. Micrographs showing Alcian blue stained images, their 3D surface plot indicating the deposition of sGAGs in the hydrogels, their color de-convoluted images and pixel analysis data with scores post 14 days of in vitro culture. Data was analyzed using Image J (NIH, USA.) software.*

2.3.9 Real time PCR analysis of chondrogenic marker genes

Chondrogenic markers genes namely *ACAN*, *Col-II*, and early chondrogenic transcription factor *Sox-9* were analyzed post 14 days of culture period by real-time PCR (**Figure 2.10**). Results showed an upregulation of the genes for all hydrogels on day 14 as compared to day 1. The blended hydrogels showed significantly higher expression levels of *ACAN* and *Sox-9* (~1.5-fold) and *Col-II* (~2-fold) as compared to pure agarose ($p \leq 0.05$ and $p \leq 0.01$). Among blended hydrogels, AG-AA showed significantly higher expression for *ACAN* gene (~1.2-fold) ($p \leq 0.05$). For *Sox-9* and *Col-II* gene, the blended hydrogels did not exhibit any significant difference.

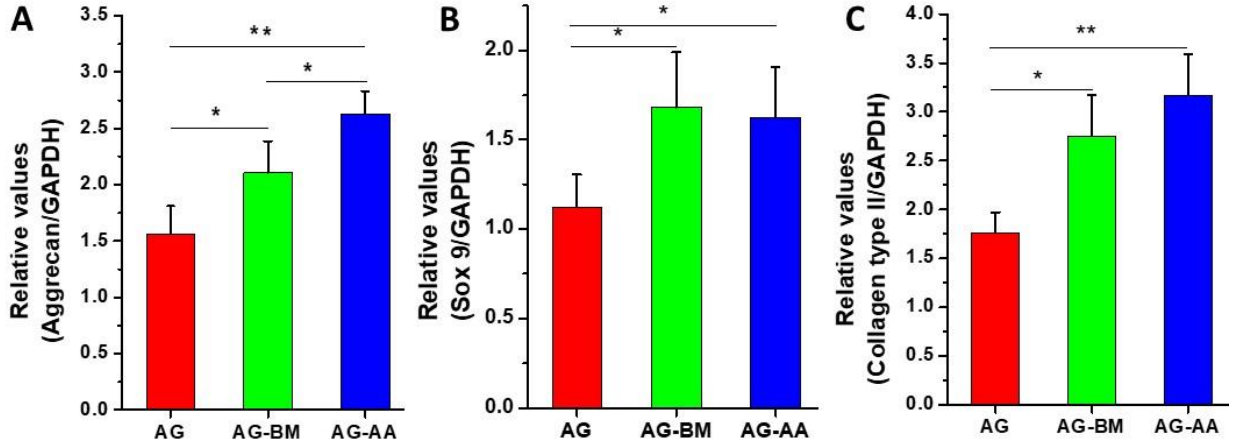

Figure 2.10. *Real time PCR results showing transcript level of cartilage related genes after 14 days of chondrocytes culture (A) ACAN, (B) Sox-9 and (C) collagen type II. The genes were normalized to GAPDH and expressed as relative values to day 1. Data are shown as mean ± standard deviation, n = 3. (*p ≤ 0.05 and **p ≤ 0.01).*

2.3.10 Macrophage stimulation and concomitant TNF-α release

Macrophages are primary source of pro-inflammatory mediators like IL-1 and TNF-α and regulate the immune responses and inflammation. The propensity of the fabricated hydrogels to stimulate the production of TNF-α was examined using RAW 264.7 (murine macrophage cells). After 12 h and 24 h of incubation, the blended hydrogels showed significantly lower (~1.5-fold) secretion of TNF-α as compared to positive control lipopolysaccharide (LPS) ($p \leq 0.01$) (**Figure 2.11**). The secretion of TNF-α for blended hydrogels were comparable with the negative control, tissue culture plate (TCP) ($p \geq 0.05$).

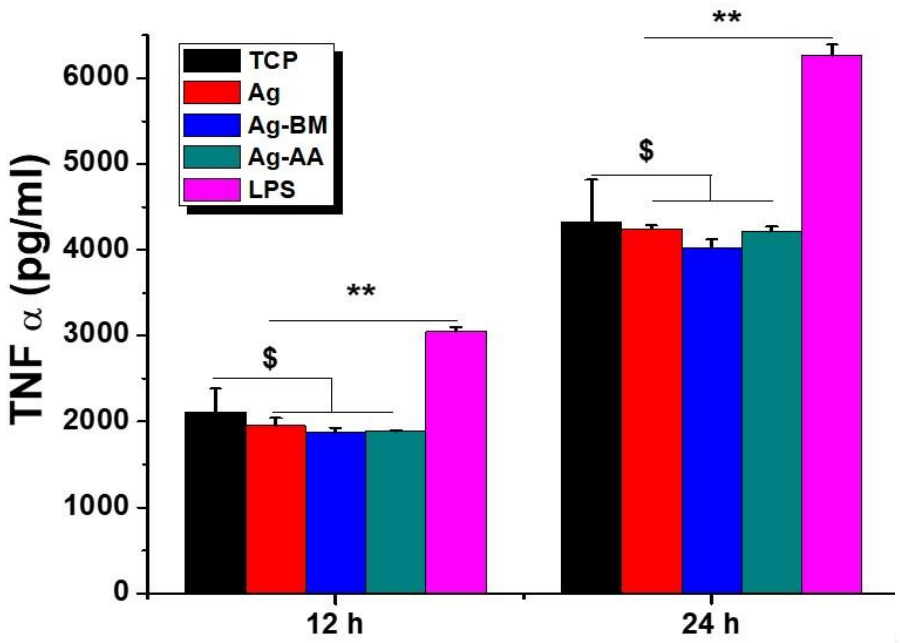

Figure 2.11. *ELISA based determination of TNF-α release induced by hydrogels from mouse macrophage cell line RAW 264.7. TCP and LPS were used as negative and positive control, respectively. The data are represented as mean ± SD (n = 2). (**$p \leq 0.01$ and $^{\$}p \geq 0.05$).*

2.4 Discussion

The intrinsic low regeneration capacity of cartilage significantly impedes orthopaedics cartilage malfunction management. The cartilage tissue containing only chondrocytes was initially considered to be an easy goal; however, recurrent hurdles are the norm instead of being one-time exceptions. Generating tissue engineered cartilage requires successful cellular response of chondrocytes within a suitable biomaterial construct with functional properties that mimic native conditions to unlock the full biological potential of the chondrocytes. Consequently, natural biomaterials are gaining ground as their biochemical activities are in sync with a variety of cellular processes. Agarose, a "gold standard" for cartilage tissue engineering [229] is handicapped by non-biodegradability and immunogenicity upon implantation making viable augmentation of its functionality as constant domain of research. Analogous to agarose, silk fibroin hydrogels maintain a hydrophilic, neutral ambience essential for sustaining chondrocyte phenotype [230]. Silk offers the advantages of biodegradability, minimal immunogenicity and ease of aqueous-based solvent matrix fabrication [237, 238]. Silk fibroin from mulberry silkworm (*B. mori*) is well explored for its application in regenerative medicine but fibroin of Indian non-mulberry silkworm (*A.*

assamensis) is far less explored. The latter is known to possess RGD tripeptide that promotes cell attachment and proliferation. Although silk fibroin and agarose have been studied separately for *in vitro* chondrogenesis [91, 230], the influence of agarose/silk fibroin blended hydrogels on chondrocyte morphology and function has not been studied yet. In the present study, we evaluated the formation of cartilaginous tissue by culturing porcine chondrocytes on agarose/SF blend hydrogels. Herein, we have developed a novel blended hydrogel system using two natural polymers, silk fibroin and agarose, which in theory would overcome the shortcomings of agarose hydrogels. The addition of silk fibroin to agarose showed improved functionality and encouraged appraisal of its potential for cartilage tissue engineering. The developed blended hydrogels were tested in parallel with pure agarose for physico-chemical characteristics such as pore size, swelling, degradation, structural composition, rheological studies and the viability and proliferation of chondrocytes. It was further optimized and studied for cellular viability, attachment, ECM constituent secretion and chondrogenesis specific gene expression analysis.

The blended hydrogel developed in this study is a porous matrix with internal interconnected pores, formed as a result of freeze drying. The increased interconnectivity between pores could enhance migration of cells toward internal pores. The SEM studies revealed larger pore size in the blended hydrogels compared to the only agarose hydrogel. Among the blended hydrogels, the AG-BM exhibited smaller pore size (158 ± 26 μm) compared to AG-AA (170 ± 23 μm). The pure agarose hydrogel had the smallest pore size (138 ± 26 μm). Earlier reports suggest that pore size in the range of 100-500 μm greatly supports chondrogenesis and promotes better ECM production and gene expression [68, 258]. The microporosity of hydrogel are central to oxygen and nutrient delivery, allowing better cell attachment and proliferation. The volume of ECM secretion shows concomitant rise with larger pore size between 150 to 300 μm than that of < 150 μm [258]. The results of our study also concurred that AG-AA blended hydrogels by virtue of their larger pores exhibited higher ECM production as compared to AG-BM and AG hydrogels.

The swelling ability of the hydrogel is testimony to its ability to retain medium, which is necessary for cell growth [259]. The prepared hydrogels retained their shape after being immersed in aqueous solution, which is vital during cell culture or implantation process. The swelling study results showed that the blended hydrogels swelled less than pure agarose hydrogels. This was in contrast to the earlier reports, where scaffolds with larger pore size showed higher water absorption ability

[259]. Thus, it is safe to assume that swelling behaviour of a matrix is intrinsic to polymer property and not dependent on pore size alone. The reason for high swelling ability of AG hydrogels is probably enhanced by presence of hydroxyl groups on the agarose monosaccharide units, making it highly hydrophilic [260]. In contrast, the recurring hydrophobic regions of alanine and glycine residues in SF form β-sheet structure resulting in its high strength and rigidity [261]. The higher percentage of non-polyalanine repeats with lower percentage of polar residues possibly contributes to the higher hydrophobicity of non-mulberry SF [247]. Therefore, among the blends, AG-AA hydrogel with larger pore size showed less swelling as compared to AG-BM. Biodegradability is an important feature of biomaterial for use in tissue engineering. Rate of degradation defined by crystalline structure quantity in fibroin and specific sequence of crystalline-amorphous region; should in function ideally mirror the rate of tissue healing [259]. If the biomaterial degrades faster, it may lead to its collapse and may not serve the purpose. For cartilage tissue engineering, a slow degrading hydrogel is an essential criterion as it would give the implanted construct ample time for repair process. The fact that protease XIV could cleave silk non-discriminately at multiple locations along the length of the protein [262] along with earlier evidences [250, 263] supported its choice in our study. The AG-BM hydrogels showed highest weight reduction (45%) in 28 days followed by AG-AA (35%). The abundant repeats of (–Ala–)n, very compact crystal structure, high α-helix content and β-sheet structure in SF of *A. assamensis* possibly makes it more hydrophobic with increased tensile strength in comparison to *B. mori* silk [247], which consequently imparts more resistance to enzymatic attack [264]. Pure agarose hydrogel did not show any degradation as it lacked the peptide bonds, the sites where protease cleaves [265]. FTIR spectroscopy provided information on the structural composition of blend and therefore helped in better understanding of the blended hydrogels. The shifting of SF amide peaks (I and II) after blending with agarose is indicative of intermolecular interaction between the hydrogel constituents. Our results were in agreement with previous studies showing FTIR spectroscopy of various polymer blends [266, 267].

Furthermore, the mechanical characteristics of hydrogels were evaluated by oscillatory rheological studies. Rheological studies showed that G′>G″ for all hydrogels indicating predominantly elastic nature of the fabricated hydrogels. The intersection of G′ and G″ corresponds to the moment where the applied mechanical force overtakes the molecular forces and the material starts to yield or flow and there is a transition from a solid-like (elastic) behaviour where G'>G" to a fluid-like (viscous)

behaviour where G">G'. The results indicated that blended hydrogels are relatively stronger and therefore yield at a higher amplitude strain as compared to pure agarose. Among the blends, both the hydrogels showed a similar yielding behaviour at an amplitude strain of around 10%. The rigidity of a gel system network is defined by its elastic modulus (G′). Reports indicate that an increase between 1% to 4% (w/v) in the concentration of agarose gels translates into a sixfold increase of G′ [268]. Thus, our results were in agreement with the above values with the 2% pure agarose showing G' of 1×10^4 Pa and the blends showing G' of 1.2×10^4 to 1.6×10^4 Pa. The higher difference between value of the G' and G" in blended hydrogels compared to pure agarose indicated that they are more stable. Goff *et al.* [269] showed that the critical strain of the nano whisker filled hydrogels decreases in comparison to pure agarose hydrogel (4%), indicative of a more fragile system. However, our results indicate the formation of a more stable and stiffer hydrogel system on blending which are suitable for load bearing tissues such as cartilage. After conducting the strain sweeps, a strain of 5% was chosen for subsequent frequency sweep test because it was clearly in the LVE region of all hydrogels. The frequency sweep showed modulus as a function of frequency (Hz) for the hydrogels. It was observed that in all the hydrogels G′ is higher than the G″, which indicated a predominantly elastic behaviour of the gel system. In addition, as frequency increased, the G′ and G″ values also increased and were nearly parallel to each other showing a frequency dependent viscoelastic moduli, a characteristic of a solid-like viscoelastic behaviour [269]. However, the values of the viscoelastic moduli, G′ and G″ were about~2.5 times higher in case of blend hydrogels as compared to pure agarose, indicating a more stable system. At 0.1 Hz, modulus of blended hydrogels was higher compared to pure agarose hydrogel, indicating a positive strengthening of the hydrogels on blending. Furthermore, the loss angle for all the hydrogels were in between 19° to 29°. This indicated that hydrogels are of solid dominating nature along with a liquid component ($\delta = 0°$ for purely solid and $\delta = 90°$ for purely liquid). The results were in agreement to a study by Priya *et al.* [270] which showed phase angle values between 4° and 6° for chitin-agarose composite hydrogels

The cartilage reconstruction is generally described using macroscopic morphological outcome parameters such as cellularity, biochemical analysis, histological and IHC staining. We have utilized porcine auricular chondrocytes to assess the potential of blended hydrogel for cartilage regeneration. Cellular studies included assessment of chondrocytes for their attachment and viability. Chondrocytes retained their spherical morphology after 14 days of culture in all the

hydrogels, which was quite evident from the live/dead staining and Hoechst staining results. The results of this study showed that AG-AA blended hydrogels provided suitable microenvironment for chondrocytes suggesting that larger pore size favours chondrogenesis by allowing cells to migrate through the matrix and facilitate their proliferation. Matsiko *et al.* in a report showed that larger mean pore sizes stimulated significantly higher cell proliferation, chondrogenic gene expression and cartilage-like matrix deposition [271]. In another recent study, Han *et al.* showed that silk fibroin scaffolds with pore sizes in the range of 90-250 μm provided the best environment for adhesion and proliferation of chondrocytes [272]. The cellular proliferation was assessed by studying the DNA content of the hydrogels. The results showed higher DNA content for the blended hydrogels as compared to pure agarose. The AG-AA blend showed the highest DNA content indicating higher cell proliferation. This enhanced proliferation index of the AG-AA blend can be credited to synergistic effect of both AG and AA, where AG provides a suitable microenvironment for the chondrocytes to maintain their morphology and also the presence of intrinsic RGD motif of AA blend facilitated enhanced cellular attachment thus improving their proliferation and functionality [91, 182, 251]. A similar study by Sakai *et al.* showed that agarose-gelatin conjugate gel displayed enhanced attachment and proliferation of cells compared to control agarose [273].

The ECM comprising mainly of collagen fibers and proteoglycan, is an important component of the cartilage matrix that provides suitable microenvironment to chondrocytes. For cartilage repair, the construct should be capable of supporting the secretion and deposition of cartilage specific matrix. Thus, blended hydrogels were further assessed for cartilaginous tissue formation by biochemical analysis. Herein, the contents of sulphated GAG and collagen produced by the porcine chondrocytes after their *in vitro* culture on the hydrogels for 14 days were analyzed. Results indicated that the blended hydrogels showed significantly higher sGAG and collagen content than AG hydrogel. Among the blends, AG-AA produced significantly higher ECM components than AG-BM. This was in agreement with earlier reports showing that larger pores facilitated chondrogenesis and accumulation of ECM [258]. In earlier study, Bhardwaj *et al.* also demonstrated higher GAG and collagen content in the SF-chitosan blended scaffolds cultured with bovine chondrocytes [68]. In yet another recent report, Bhardwaj *et al.* showed significantly higher production of sGAGs and type II collagen in *A. assamensis* silk fibroin scaffolds compared to *B. mori* scaffolds [250]. Furthermore, histological and IHC analysis of the sectioned hydrogel

demonstrated that blended hydrogels had significantly higher ECM deposition (GAG and collagen content) with more extensive immunostaining for collagen II. Additionally, the data analysis of Alcian blue stained images by color de-convolution plugin of Image J software also revealed a "high positive" score of the blends as compared to the "positive" score of pure agarose. These results were in accordance with the cell viability, cell proliferation and biochemical studies indicating that the blended hydrogels supported the chondrogenesis of chondrocytes through increased cellular proliferation and cartilaginous matrix production.

The higher level of matrix production, as seen *via* histology and staining or total biochemical analyses in the blends were consistent with the upregulation of most common markers of cartilage specific genes namely aggrecan, collagen type II and sox-9. Aggrecan, a major proteoglycan component of the ECM consists of core protein and GAGs binds to it. Thus, its expression also reflects the overall GAG content. Collagen II is the chief collagen expressed in cartilage tissues and sox-9 is a transcription factor that binds directly to the promoters of collagen II and aggrecan serving as a master regulator of chondrogenesis [274]. Thus, the higher gene expression of the cartilage specific markers for the chondrocytes cultured for 14 days on the blended hydrogels showed their ability to support and stimulate cell growth and matrix synthesis. Zhang *et al.* in a recent study showed that upon *in vivo* implantation, a scaffold with a pore size of 150–250 μm promoted the expression and production of type II collagen and aggrecan leading to increased cartilage formation with suitable mechanical characteristics [275].

Macrophages are the first cells to identify invading pathogens. Following contact with foreign elements, macrophages release cytokines such as IL-1 and TNF-α. The results of our study indicated that the level of TNF-α production was comparable to TCP and significantly lower to positive control LPS. Thus, it can be safely assumed that the fabricated blended hydrogels show minimal inflammatory activity. Agarose, a polysaccharide may trigger an immune response [276], on the other hand SF has previously reported to elicit minimal or no immune response [174]. The fabricated hydrogels in this study intends to minimize chances of an immune response by curtailing the use of agarose and blending it with non-immunogenic SF.

2.5 Significant findings

1. Blended hydrogel with agarose and silk fibroin from mulberry (*B. mori*) and non-mulberry (*A. assamensis*) silkworms were fabricated.
2. The physico-chemical characterization of the hydrogels revealed a porous structure with water retention and degradation capability. The degradation capability of blended hydrogel circumvents the drawbacks of the otherwise non-degradable pure agarose. The blending of SF to agarose forms a more stable, stiffer, and biocompatible hydrogel system.
3. The cellular studies demonstrated good viability and proliferation of chondrocytes on the blended hydrogels.
4. The biochemical analysis indicated enhanced GAG and collagen production as compared to pure agarose hydrogels. The non-mulberry SF blends with larger pores showed higher ECM production as compared to mulberry blends, which was also confirmed *via* histological and IHC studies.
5. Upregulation of the common cartilage specific marker genes in the blended hydrogels further affirmed their innate suitability for cartilage repair applications.
6. Altogether, the results suggest that the blended hydrogels showed enhanced cellular proliferation and ECM production as compared to pure agarose hydrogels.
7. Non-mulberry blends in particular displayed superior qualities that clearly designate them as potential alternatives for cartilage repair.

Chapter 3

Silk Fiber Reinforcement Modulates *In Vitro* Chondrogenesis in 3D Composite Scaffolds

In this study, silk fiber-reinforced composite scaffolds based out of mulberry and non-mulberry silk were fabricated to evaluate their role as a matrix for cartilage tissue engineering using primary porcine chondrocytes as a cell source. The fabricated composites were physico-chemically characterized for surface morphology, porosity, swelling, degradation and mechanical properties. Further, the suitability of the composite was evaluated through the cellular properties such as viability, proliferation, biochemical evaluation along with ECM formation using histology, immunohistochemistry and gene expression analysis. Additionally, the immuno-compatibility of the scaffolds was evaluated by *in vitro* TNF-α released using murine macrophages.

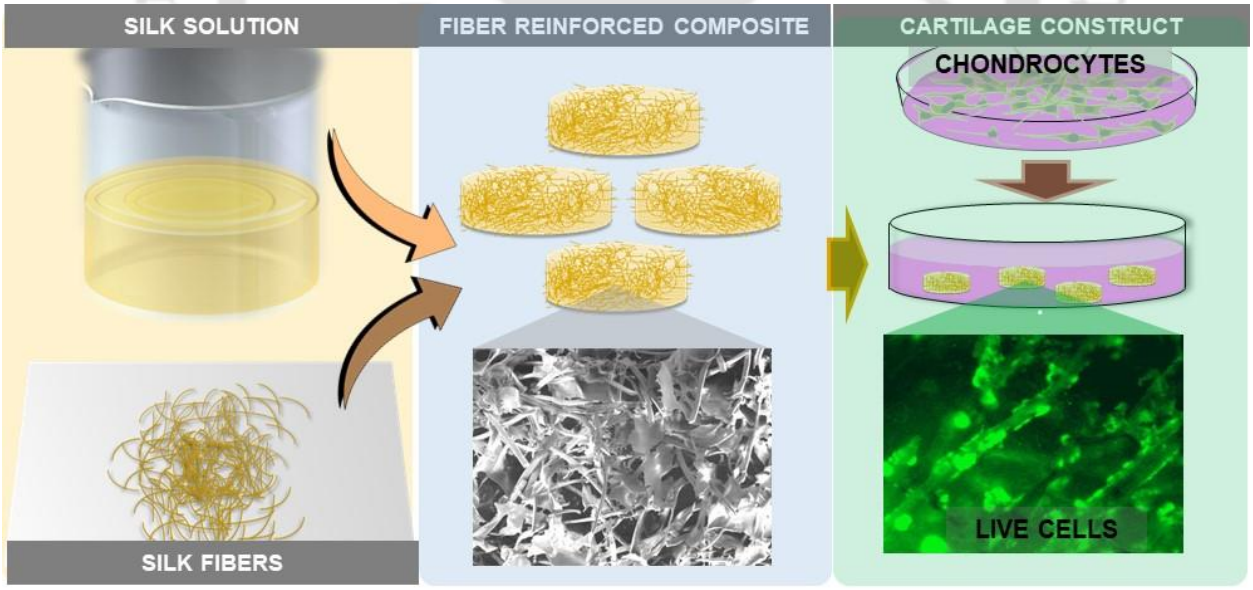

The work embodied in this chapter is published as follows:

Yogendra Pratap Singh, Mimi Adhikary, Nandana Bhardwaj, Bibhas Kumar Bhunia, and Biman B. Mandal. "Silk fiber reinforcement modulates *in vitro* chondrogenesis in 3D composite scaffolds." ***Biomedical Materials*** 12(4), 2017: 045012.

ABSTRACT

The limited self-regenerative capacity of adult cartilage has steered the upsurge in tissue engineered replacements to combat the problem of osteoarthritis. In the present study, the potential of fiber-reinforced silk composites from mulberry (*Bombyx mori*) and non-mulberry (*Antheraea assamensis*) silk has been investigated for cartilage tissue engineering. The fabricated composites were physico-chemically characterized and analyzed for cellular viability, proliferation, extracellular matrix (ECM) formation and immunocompatibility. Both mulberry and non-mulberry silk composites showed effective swelling (25-30%) and degradation (10-30%) behaviour, owing to their interconnected porous nature. The non-mulberry fiber-reinforced composite scaffolds showed slower degradation (~90% mass remaining) than mulberry silk over a period of 28 days. The reinforcement of silk fibers within silk solution resulted in an increased compressive modulus and stiffness (nearly 8-fold). The biochemical analysis revealed significant increase in DNA content, sulphated glycosaminoglycan (sGAG) (~1.5 fold) and collagen (~1.4 fold) in reinforced composites as compared to pure solution scaffolds ($p \leq 0.01$). Histological and immunohistochemical (IHC) staining corroborated enhanced deposition of sGAG and localization of collagen type II in fiber-reinforced composites. This was further substantiated by gene expression studies, which indicated an up-regulation (~1.5 fold) of cartilage-specific gene markers namely collagen type II, Sox-9 and aggrecan. The minimal secretion of TNF-α by murine macrophages further demonstrated *in vitro* immunocompatibility of the scaffolds. Taken together, the results signified the potential of silk fiber-reinforced composite (particularly non-mulberry, *A. assamensis*) scaffolds as viable alternative biomaterial for cartilage tissue engineering.

3.1 Introduction

Articular cartilage is a specialized connective tissue found in synovial joints where the surfaces of limb bones articulate. It has a limited capacity for intrinsic healing and repair mainly due to low matrix turnover, inadequate supply of progenitor cells and insufficient vasculature [218]. Therefore, maintaining the sustained health of the articular cartilage is mandatory for lifelong functional endurance. However, the cartilage is prone to damages by traumatic injuries to the joint, abnormal joint loading, and degenerative joint diseases like OA. OA is the most prevalent disorder of articulating joints in humans, which affects almost half of the world's population aged 65 years or older and presents a major healthcare burden [277]. Current therapies to repair damaged cartilage include subchondral drilling, abrasion arthroplasty, prosthetic joint replacement and autologous chondrocytes or tissue transplants [278]. Unfortunately, these methods do not sufficiently restore the normal cartilage functional physiology, durability and full load-bearing properties. In addition, formation of dense fibrocartilage is often encountered instead of the functional hydrated hyaline cartilage when these strategies are employed [56, 279]. Therefore, the lack of a benchmark procedure for cartilage repair and the mediocre efficacy of the current surgical procedures demands a viable alternative.

Cartilage tissue engineering has transpired as an encouraging approach for joint repair. The properties of mechanical strength and structural resilience are incumbent for scaffold fabrication in cartilage tissue engineering [280]. A variety of techniques such as freeze-drying, salt leaching and gas foaming have been used to fabricate porous 3-D matrices from natural and synthetic polymers [281-284]. Scaffolds from natural polymers possesses potential advantages of biodegradability, biocompatibility, bioactivity, intrinsic cellular interactions and versatility of chemistry [285]. Furthermore, in order to augment appropriate mechanical properties, a number of chemical and physical alterations have been offered, which includes reinforcement of fibers or other particulates and/or cross-linking using physical and chemical methods [99, 286-288]. Polymers from synthetic sources often augment higher mechanical properties to biomaterials being utilized in tissue engineering applications. However, many of these polymers are limited by non-degradability under physiological conditions and lack of biological cues inherent in cell-binding motifs of natural materials [285].

Silk is a natural protein polymer produced by silkworms and spiders. It is basically composed of two major protein components namely hydrophobic fibroin and a glue like, hydrophilic, sericin [235]. Silk fibroin (SF) from *B. mori* silkworm has been utilized extensively as a scaffold material for a variety of tissue engineering applications including cartilage [67, 230, 238, 289]. The interest in SF based matrices has escalated as a natural consequence of their superior biocompatibility, biodegradation and mechanical strength. In addition, minimal inflammatory reaction *in situ* and the ease of processing into various material formats like mats, fibers, porous scaffolds, films, particles and hydrogels has extended further advantage [290]. SF from *A. assamensis* silkworm has also been investigated as a promising biomaterial for cartilage tissue engineering in recent years [291, 292]. In a recent study, Gupta *et al.* reported presence of arginine-glycine-aspartic acid (RGD) tripeptide towards N and C-termini of the Gc motif of *A. assamensis* silk fibroin [247]. RGD is a known integrin binding site that facilitates better cellular attachment and proliferation [182]. Additionally, *A. assamensis* SF has uninterrupted polyalanine stretches, unlike other saturniid family SF where serine residues break up polyalanine stretches, which confer it superior tensile strength and mechanical properties [247, 249]. *A. assamensis* SF scaffolds have displayed suitable cytocompatibility with desirable cell adhesion, spreading, and migration, which enhances its applicability in tissue engineering and regenerative medicine [291, 292]. Recent investigation of Bhardwaj *et al.* focused on fabrication of 3D porous silk fibroin scaffolds using non-mulberry (*A. assamensis)* SF and assessment of their ability to support cartilage tissue formation. The scaffolds displayed improved attachment of chondrocyte followed by enhanced proliferation with enhanced production of cartilaginous ECM; sGAGs and collagen type II. Additionally, the subcutaneous implantation of the scaffolds in a rat model manifested *in vivo* biocompatibility and good integration properties with host after 8 weeks of implantation [292].

In recent years, fiber-reinforced composite scaffolds have achieved a good measure of success for their application in biomedical applications [238, 293]. The approach of blending fibers with the matrix material might improve the mechanical properties to a remarkable degree. In a recent study, Li *et al.* demonstrated significant enhancement in tensile strength and burst performance of the silk scaffolds by reinforcement with silk microfibers [294]. In another study, Yodmuang *et al.* demonstrated the versatility of silk fiber-hydrogel composites as functional cartilage constructs in cartilage tissue repair [99]. Furthermore, Subramanian *et al.* reported that the increased stiffness of cross-linked chitosan scaffolds seemed to augment articular canine chondrocyte growth and

proliferation with additional mechanical stimulus [286]. Among the spectrum of biomimetic materials, the fiber-reinforced composites are being used for fabricating mechanically robust scaffolds where a polymer matrix is embedded with high-strength biocompatible fibers, including fibers of silk [99, 238, 295].

In the present study, silk fiber-reinforced composite scaffolds based out of mulberry and non-mulberry silk were fabricated to evaluate their role as a matrix for cartilage tissue engineering using primary porcine chondrocytes as a cell source. A schematic representation of the fabrication of the fiber-reinforced composite scaffolds is shown in **Figure 3.1**. The fabricated composites were physico-chemically characterized for surface morphology, porosity, swelling, degradation behaviour and mechanical properties. Further, the suitability of the composite was evaluated through the cellular properties such as viability, proliferation, biochemical evaluation along with ECM formation using histology, immunohistochemistry and gene expression analysis. Additionally, the immuno-compatibility of the scaffolds was evaluated by *in vitro* TNF-α released using murine macrophages. Our study concurrently includes a comparative assessment of mulberry (*B. mori*) and non-mulberry (*A. assamensis*) silk in all parameters investigated for studying their implication in cartilage tissue engineering. Herein, pure SF solution scaffolds were used as controls throughout the study.

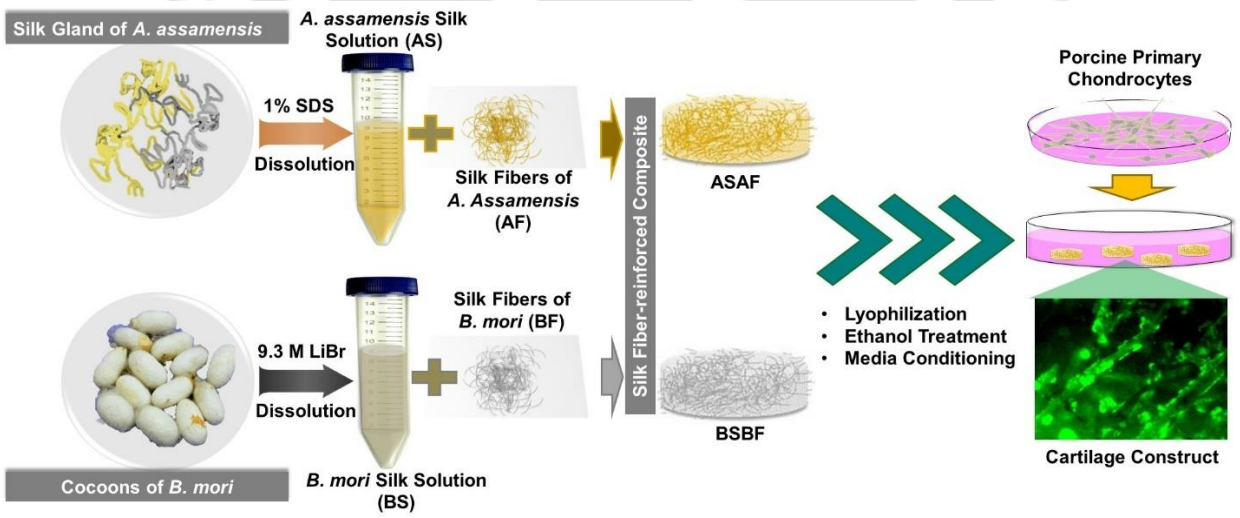

Figure 3.1. *Schematic representation of the fabrication and chondrocyte culture of silk fiber-reinforced composite scaffolds.*

3.2 Materials and methods

3.2.1 Materials

Silk cocoons of mulberry silkworm (*B. mori*) and matured 5th instar larvae of non-mulberry silkworm (*A. assamensis*) were obtained from Mangaldoi Silk Farm, Assam, India. Cell culture grade chemicals such as Dulbecco's modified Eagle's medium (DMEM), fetal bovine serum (FBS), trypsin–EDTA were obtained from Gibco BRL, Rockville, USA. 1,9-Dimethylmethylene blue (DMMB), protease XIV from *Streptomyces greiseus*, sodium azide, collagenase (type I-A), alcian blue, Hoechst 33342, calcein-AM were obtained from Sigma-Aldrich, USA. Rhodamine phalloidin, alamar blue, 100X antibiotic-antimycotic solution, PicoGreen dye, SYBR Green dye, tumor necrosis factor alpha (TNF-α) ELISA kit were obtained from Invitrogen, USA. Anti-collagen type II monoclonal antibody (Abcam, USA), Vectastain universal elite kit (Vector Laboratories), 3,3'-diaminobenzidine (DAB) substrate (Vector Laboratories), and other chemicals used were of analytical grade.

3.2.2 Isolation of silk fibroin and fibers

Silk fibroin was isolated from the cocoons of *B. mori* and matured larvae of *A. assamensis* silkworms as previously reported [236, 291]. Briefly, the cocoons of *B. mori* were cut into pieces and degummed in a boiling 0.02 M Na_2CO_3 solution for 30 min. The degummed fibers were rinsed in milli-Q water and air dried. Dried fibers were dissolved in 9.3 M LiBr (Sigma-Aldrich, USA) followed by extensive dialysis against milli-Q water using dialysis membrane of 12 kDa molecular weight cut off. Concurrently, 5th instar matured larvae of *A. assamensis*, were dissected just before spinning and silk glands were isolated. Silk fibroin was extruded from the glands using fine forceps. The isolated silk protein was subsequently dissolved in 1% SDS followed by dialysis against milli-Q water. The resultant concentration of regenerated silk solution was determined by gravimetric method. Herein, finely chopped fibers from both *B. mori* and *A. assamensis* cocoons were used for reinforcement. Briefly, pieces of cocoons were degummed using 0.02 M Na_2CO_3 for 30 min to remove sericin. The obtained silk fibers were dried and finely chopped with scissors for further use. The length of chopped fibers showed a heterogeneous distribution and ranged between 0.5 and 2.5 mm, as observed under bright field microscope [296].

3.2.3 Fabrication of scaffolds

The composite scaffolds were fabricated using finely chopped silk fibers and regenerated silk fibroin solution (2%, w/v). The finely chopped silk fibers were packed into a cylindrical mould (10 mm X 10 mm) and silk fibroin solution was added to it in the ratio of 2:1 (w/w, 40 mg of silk fibers to 20 mg of regenerated silk), respectively [296]. The moulds were frozen at -20 °C for 12 h followed by freeze drying for 24 h. The freeze-dried scaffolds were treated with 70% (v/v) ethanol to induce β-sheets. The fabricated composite scaffolds were designated as BSBF and ASAF; where BSBF represents *B. mori* solution with *B. mori* fibers, and ASAF represents *A. assamensis* solution with *A. assamensis* fibers. Pure *B. mori* solution (BS) and *A. assamensis* solution (AS) based scaffolds without any fiber were used for comparison.

3.2.4 Field emission scanning electron microscopy (FESEM)

The surface morphology and pore size of the freeze-dried composites were examined using FESEM (Zeiss, Germany). The freeze-dried composites were sputter coated with gold and analysed using FESEM. The pore size of the composites was determined by analyzing 20 random pores using ImageJ 1.48v software (NIH, USA).

3.2.5 Porosity measurement

Porosity of fabricated scaffolds was measured using hexane through a liquid displacement method [297]. Hexane is a non-solvent liquid for silk that permeates easily through the interconnected scaffold pores without causing much swelling or shrinkage. The scaffolds were immersed in a graduated cylinder holding a known volume (V_1) of hexane. Further, the total volume of hexane and hexane-impregnated scaffold was noted (V_2). Lastly, the residual volume of hexane in the cylinder after removal of hexane-impregnated scaffold was noted (V_3) and the porosity of the scaffolds was determined using the formula:

$$\% \text{ Porosity} = [(V_1-V_3)/(V_2-V_3)] \times 100$$

3.2.6 Swelling behaviour of scaffolds

Swelling potential of the scaffolds was determined using conventional gravimetric procedure [298]. The dry weight of the lyophilized composite scaffolds was noted followed by its immersion in phosphate buffered saline (PBS, pH 7.4). At predetermined time points, composites were carefully taken out and the amount of water absorbed was determined by weighing the scaffold in

the swollen condition. The experiment was conducted in triplicates (n = 3) under identical conditions and the percentage swelling was determined using the equation:

$$\% \text{ Swelling} = [(Ws - Wd)/Wd] \times 100$$

where, Ws is the swelled weight and Wd is the dry weight of the scaffolds (mg).

3.2.7 *In vitro* degradation pattern of the scaffolds

The *in vitro* degradation of the scaffolds was studied using protease XIV enzyme from *S. griseus* possessing an activity of ≥3.5 U/mg [299]. Scaffolds were treated with 2 U/mg protease enzyme in 1 mL of PBS and incubated at 37 °C. The enzyme solution was changed after every 3 days. Sodium azide (0.05 wt%) was supplemented to the solution in order to prevent microbial growth. For control, the samples treated in PBS without enzyme under similar conditions were used. The experiment was conducted in triplicates (n = 3) under identical conditions and the weight loss was determined using the equation:

$$\% \text{ Degradation} = [(W_0 - W_1)/W_0] \times 100$$

where, W_0 is the initial weight of the scaffold (mg) and W_1 is the final weight of the scaffold (mg).

3.2.8 Mechanical testing

Mechanical properties of fiber-reinforced composite scaffolds (n=3) were analyzed using a Universal Testing Machine (UTM, Instron 5944, USA) fitted with a 100 N load cell. Compression tests were conducted under hydrated conditions in a BioPuls temperature-controlled bath containing PBS at 37 ºC. A displacement control mode with a crosshead speed of 1 mm/min was used. A line was drawn parallel to the initial linear region of the stress–strain curve with an offset of 0.5% and the compressive modulus was calculated as the slope of the curve. The compressive modulus was determined using Bluehill version 3.66 software.

3.2.9 Isolation and culture of porcine chondrocytes

Auricular chondrocytes were harvested from the ear of freshly slaughtered pig obtained from a local abattoir, as described previously [291]. Briefly, the ear was cleansed and dissected free of skin. The obtained cartilage was cut into small fragments and treated with 1% antibiotic-antimycotic solution followed by sequential digestion with protease and collagenase enzyme for overnight at 37 °C with 95% relative humidity and 5% CO_2. Auricular chondrocytes were collected by centrifugation (2000 rpm for 5 min) with the resultant cell pellet washed 2-3 times with DMEM media. Trypan blue exclusion test was done to assess the viability of cells before cell seeding.

3.2.10 Cell seeding and culture

Each scaffold (6 mm in diameter and 2 mm thick) was carefully seeded with 0.5 million cells in 24 well plate and kept at 37 °C in a humidified incubator with 5% CO_2 to allow the cells to diffuse into and adhere to the scaffold. After 2 h, 1 mL of chondrogenic media containing DMEM, 10% FBS, 1% antibiotic-antimycotic solution, 100 nM dexamethasone, 40 µg/mL proline, 50 mg/mL ascorbic acid and 1X ITS+3 (comprising of 1.0 mg/mL insulin from bovine pancreas, 0.55 mg/mL human transferrin, 0.5 µg/mL sodium selenite, 470 µg/mL oleic acid, 470 µg/mL linoleic acid and 50 mg/mL bovine serum albumin) was added to each well. Spent media was replaced after every 3 days and scaffolds with cultured cells were harvested after 4 weeks. For biochemical assessment, the spent media was collected and stored at -20 °C until its assessment. Normal DMEM media supplemented with 10% FBS and 1% antibiotic-antimycotic solution was used for cell viability and proliferation assays.

3.2.11 Cell proliferation assay

Cell proliferation was examined by alamar blue dye reduction assay according to manufacturers' protocol. Briefly, cell seeded composite scaffolds were incubated in high glucose DMEM media containing 10% (v/v) alamar blue dye at 37 ºC incubator for 3 h. 200 µL of dye containing medium from each sample was taken and absorbance was recorded at 570 nm and 600 nm using a multiplate reader (Tecan Infinite M200Pro, Switzerland). For control, non-seeded scaffolds supplemented with 10% alamar blue dye were used. The obtained values were normalized and plotted using OriginPro 8 (OriginLab, USA).

3.2.12 Fluorescence imaging

In vitro analysis of chondrocyte attachment and viability was performed using calcein-AM based staining. Briefly, a working staining solution containing 4 µM calcein-AM (stains live cells) were prepared in PBS (pH 7.4). The chondrocyte seeded composites were incubated in the staining solution for 15-20 min at 37 °C. The samples were prewashed with PBS (pH 7.4) prior to visualization using an excitation filter of 450–490 nm under fluorescence microscope (EVOS FL, Life Technologies, USA).

3.2.13 Biochemical analysis

The chondrocyte cultured scaffolds were biochemically assayed for quantification of DNA content, sGAG and collagen content. For measuring DNA and sGAG content, the samples were

digested using papain solution (125 µg/mL papain, 5 mM L-cysteine, 100 mM Na_2HPO_4, and 5 mM EDTA, pH 6.2) at 60 °C for 16 h. Following digestion, the samples were centrifuged and DNA content was estimated in the supernatant using a PicoGreen DNA assay kit following the manufacturer's protocol. Briefly, 25 µL of supernatant was taken in a 96 well-plate having 75 µL of 1X TE buffer. To this, 100 µL of Quant-iT PicoGreen reagent (1:200 dilution) was added, and fluorescence was measured using a microplate reader (Tecan infinite M200Pro, Switzerland) at excitation and emission wavelengths of 480 nm and 528 nm, respectively. Lambda phage DNA (0−10 µg/mL) was used to prepare the standard curve. For estimation of sGAG content, 1,9-dimethylmethylene blue (DMMB) assay was used [255]. For this, 50 µL of a papain-digested sample was added to 200 µL of DMMB reagent and absorbance was recorded at 525 nm. Additionally, sGAG secreted in media was assessed using similar protocol. Chondroitin sulfate (Sigma-Aldrich, USA) in the range of 0−100 µg/mL was used to prepare the standard for sGAG estimation. Collagen content was estimated using Hride Tullberg-Reinert method [256]. Briefly, the samples were digested using pepsin solution (1 mg/mL, pH 3.0) at 4 °C for 48 h, centrifuged and the supernatant was dried at 37 °C for 24 h. Further, 100 µL of a Sirius red dye solution (1 mg/mL, prepared in picric acid-saturated solution) was added to the wells and kept for 1 h with mild shaking. The wells were washed with 0.01 normality HCl and the dye sample complex was resolved using 0.1 normality NaOH. The absorbance was recorded at 550 nm. Rat tail collagen type I (0−1 mg/mL, Sigma-Aldrich, USA) was used to generate the standard curve for collagen estimation. In order to avoid disparity due to scaffold sizes and cell numbers, sGAG and collagen values were normalized against scaffold weight and DNA content.

3.2.14 Histological and immunohistochemical (IHC) assessment

For histological analysis of the chondrocyte seeded scaffolds, they were fixed in 10% neutral buffered formalin (NBF) followed by dehydration, clearing and embedding in paraffin wax. Cross-section of 5 µm thickness were prepared using a microtome (Leica, Germany) and stained with hematoxylin and eosin (H&E, Sigma-Aldrich, USA) for chondrocyte distribution and 1% alcian blue (prepared in 3% acetic acid solution, pH 2.5) for sulfated proteoglycan. For IHC analysis, the slide with scaffold sections were deparaffinised, cleared, rehydrated and immunostained for the detection of collagen type II using Vectastain Elite Universal kit (Vector Laboratories) following manufacturer's protocol. Briefly, sections were incubated with blocking serum for 20 min and treated with monoclonal antibody against collagen type II (1:300) for 30 min followed by

incubation with biotinylated universal secondary antibody. Stained sections were developed using DAB peroxidase (HRP) substrate kit (Vector Laboratories) to get a brown reaction product. The stained sections were observed using bright-field microscope (EVOS FL, Life Technologies, USA).

3.2.15 Digital image analysis

A color deconvolution technique was used for semi-automated digital analysis of alcian blue and IHC stained images [291, 292]. Briefly, the different alcian blue and DAB-stained zones were identified and image thresholding was done in order to create a complementary image. The pixel intensities ranged from 0 to 255, where 0 represented the darkest shades of the color and 255 represented the lightest shade. The obtained histogram profile represents the number of pixels of a specific intensity value for their respective intensity of every image. Depending on the color intensity, an automated score was assigned to each image and designated as high positive, positive, low positive and negative. Standard ImageJ 1.48v (NIH, USA) program with color deconvolution and IHC profiler plugins were used for analysis.

3.2.16 Gene expression analysis

RNA was harvested from the chondrocyte cultured scaffolds using trizol-chloroform-isopropanol extraction method [300] after 4 weeks of culture. Briefly, chondrocytes cultured scaffolds were fragmented and transferred to tubes containing 1 mL TRIzol. After 30 min of incubation, the fragmented scaffolds were centrifuged at 13,000 rpm for 10 min at 4 ºC. The obtained supernatant was transferred to a fresh tube containing 200 µL of Chloroform and incubated for 15 min. The solution was centrifuged at 13,000 rpm for 15 min and the upper aqueous layer containing RNA was transferred carefully to a new tube containing 500 µL of Isopropanol (Sigma-Aldrich, USA). Post 30 min of incubation, the RNA precipitate was obtained using centrifugation. Finally, the pellet was washed with 70% ethanol and stored at -20 ºC in 20 µL RNase-free water. The isolated RNA was reverse transcribed into cDNA using reverse transcription kit (Applied Biosystems). Real-time PCR reactions were performed using the SYBR Green PCR mastermix in an ABI 7500 fast real-time system (Applied Biosystems). A reaction volume of 20 µL was prepared using SYBR Green mix, forward primer, reverse primer, cDNA and PCR-water. The level of expression of each target gene was further calculated using primers listed in **Table 3.1**. For all the genes, the PCR conditions were as follows: pre-denaturation at 95 °C for 2 min, denaturation at 95 °C for 15 s and

annealing/extension at 60 °C for 60 s, for 40 cycles. PCR products were quantified by the cycle threshold (Ct) value. Differential expression (fold change) of marker genes was calculated according to the $2^{-\Delta\Delta Ct}$ method.

Table 3.1. Primer sequences used in real-time PCR.

Genes	Primer Sequences (Forward & Reverse)	Accession no.
Aggrecan	F: 5'- CCCAACCAGCCTGACAACTT -3' R: 5'- CCTTCTCGTGCCAGATCATCA -3'	NM_001164652.1
Sox-9	F: 5'- TTCCGCGACGTGGACAT -3' R: 5'- GGCGGCAGGTACTGGTCAAACTC -3'	NM_213843.1
Collagen-II	F: 5'- CAGGTGAAGGTGGGAAACCA -3' R: 5'- ACCCACGAGGCCAGGA -3'	AF201724.1
GAPDH	F: 5'- TCGGAGTGAACGGATTTGG -3' R: 5'- CCAGAGTTAAAAGCAGCCCT -3'	NM_001206359.1

3.2.17 Macrophage stimulation and TNF-α release

For macrophage stimulation, the murine macrophage cell line RAW 264.7 was grown in DMEM containing 10% FBS, 1% antibiotic-antimycotic solution at 37 °C and 5% CO_2. Macrophages were plated at 1×10^5 cells per well in 12-well plate and incubated overnight followed by the placing of scaffolds to the wells. After 12 h of incubation, the medium was collected and the TNF-α release was estimated. Lipopolysaccharide (1000 ng/mL) (LPS from *Escherichia coli*, Sigma-Aldrich, USA) was taken as a positive control and medium without scaffolds was used as negative control. The released TNF-α was measured by enzyme-linked immunosorbent assay (ELISA) according to the manufacturer's protocol (Invitrogen, USA). Briefly, the diluted samples (4-fold with standard diluent buffer) were taken in an 8-well strip and 50 µL of biotinylated secondary antibody was added to it followed by incubation for 90 min at room temperature (RT). The wells were washed 4 times and 100 µL of strepavidin-HRP working solution was added to it followed by its incubation for 30 min at RT. The wells were washed and 100 µL of stabilized chromogen solution was added to each well and incubated for 30 min under dark conditions. The terminating step includes the addition of 100 µL of the stop solution and reading the absorbance at 450 nm. A standard curve was plotted in the range of 0−1000 pg/mL TNF-α for the determination of TNF-α released.

3.2.18 Statistical analysis

The data were represented as mean ± standard deviation (SD) (n = 3). Statistical analysis was performed by a one-way analysis of variance (ANOVA) using Sigma Plot 11.0 and a Holm−Sidak test was carried out to assess variance across groups. The differences between groups of $*p \leq 0.05$ were considered statistically significant and $**p \leq 0.01$, and $***p \leq 0.001$ as highly significant.

3.3 Results

3.3.1 Microarchitecture and porosity of the scaffolds

The micro architecture of the scaffolds visualized by FESEM images revealed an interconnected porous structure (**Figure 3.2**). The fiber-reinforced composite scaffolds exhibited comparatively smaller and heterogeneous pore sizes ranging from 20-80 μm compared to pure solution-based scaffolds. The fibers were seen to be well integrated with the solution matrix without any phase separation. The size of reinforced fibers was ~10 μm in diameter and 0.5-2.5 mm in length. In contrast, BS scaffolds showed pore size of 90 ± 12 μm compared to that of AS which was 130 ± 18 μm under similar fabrication conditions. The porosity percentage of the scaffolds ranged from 86-95% as shown in **Table 3.2**. The BSBF composite showed porosity of 86.5 ± 3.0% and the ASAF composite showed porosity of 87.8 ± 3.2%. The pure solution scaffolds showed a porosity of 93.6 ± 2.4% and 94.3 ± 1.1% for BS and AS, respectively.

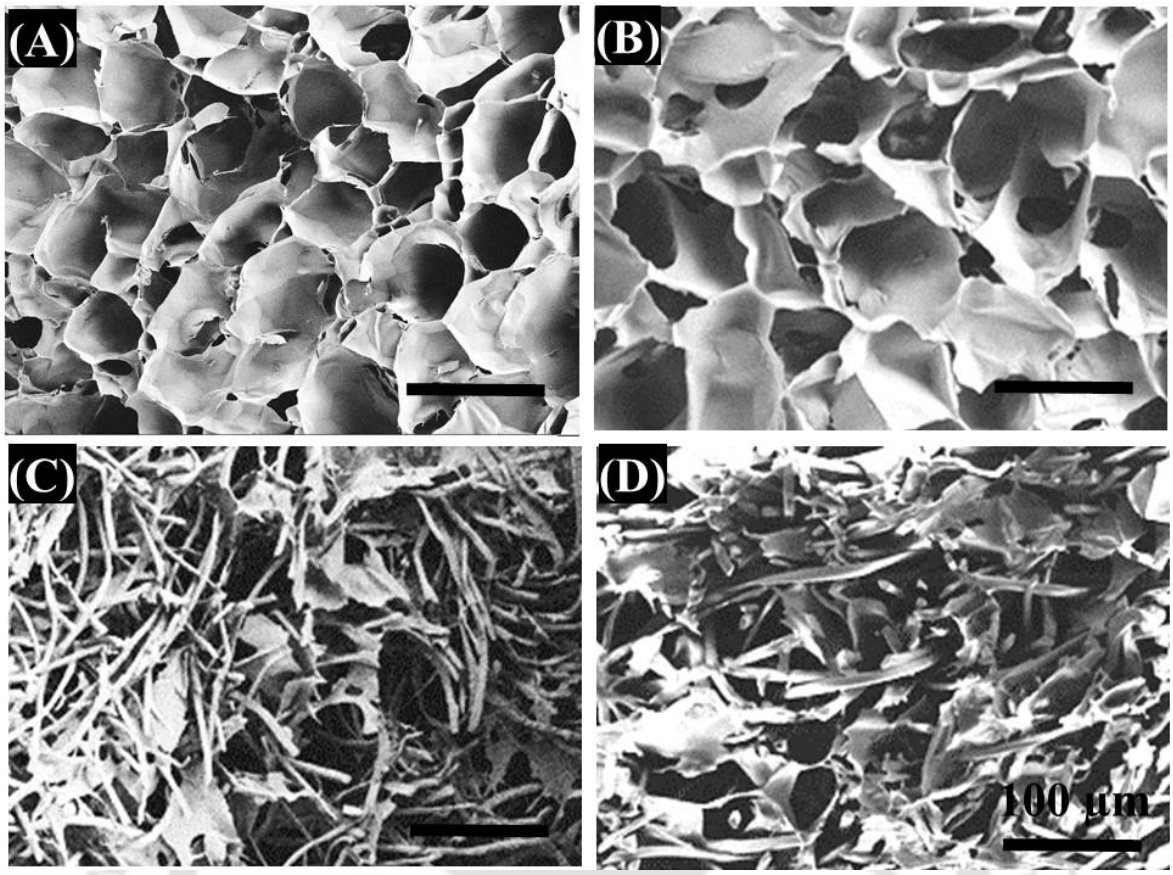

Figure 3.2. *Field emission scanning electron micrographs of scaffolds reinforced with silk microfibers. The microarchitecture of freeze-dried scaffolds: (A) BS scaffold, (B) AS scaffold, (C) BSBF fiber-reinforced composite and (D) ASAF fiber-reinforced composite. Scale bar represents 100 µm.*

Table 3.2. Porosity of different types of scaffolds.

Scaffold type	Porosity %
B. mori solution, *B. mori* fiber (BSBF)	86.5 ± 3.0
A. assamensis solution, *A. assamensis* fiber (ASAF)	87.8 ± 3.2
B. mori solution (BS)	93.6 ± 2.4
A. assamensis solution (AS)	94.3 ± 1.1

3.3.2 Swelling and degradation behaviour of the scaffold

Swelling behaviour of the composites was determined by immersing the scaffolds in PBS (pH 7.4) and weighing at defined time points. The scaffolds imbibed liquid within 15 min and reached swelling equilibrium within 90 min (**Figure 3.3A**). All the scaffolds showed swelling behaviour however, the pure solution scaffolds swelled significantly more (~2.4 times) than the fiber-reinforced composites ($p \leq 0.01$). The swelling ratio of BSBF and ASAF composites were ~25% and ~30%, respectively. The swelling study results underlined the liquid retention ability of scaffolds with the potential to serve as a nutrient reserve for the cells when seeded on the scaffolds. The *in vitro* degradation study showed that the BSBF composite scaffolds lost ~30% of the mass whereas the ASAF composite scaffolds showed ~10% mass loss after 28 days of protease treatment. The BS and AS scaffolds without any fiber-reinforcement showed higher degradation with 90% and 45% of mass loss, respectively. There was insignificant weight change observed with scaffolds incubated in PBS (**Figure 3.3B**).

3.3.3 Mechanical properties

To assess the intrinsic mechanical properties of the composites, the compressive modulus was analyzed and compared to the pure solution scaffolds (**Figure 3.3C**). The pure SF solution scaffolds showed a lower compressive modulus of ~5 kPa and ~10 kPa for BS and AS scaffolds, respectively. The silk fiber-reinforced composite scaffolds showed significantly higher compressive modulus as compared to pure solution scaffold ($p \leq 0.001$). The BSBF and ASAF composite scaffolds showed a compressive modulus of ~38 kPa and ~65 kPa, respectively. The ASAF composite scaffolds showed significantly higher modulus (~1.7 fold) than BSBF ($p \leq 0.01$). Thus, the reinforcement of silk fiber to the porous silk solution matrix increased the compressive modulus of the scaffolds nearly 8-fold in BSBF and nearly 6.5-fold in ASAF.

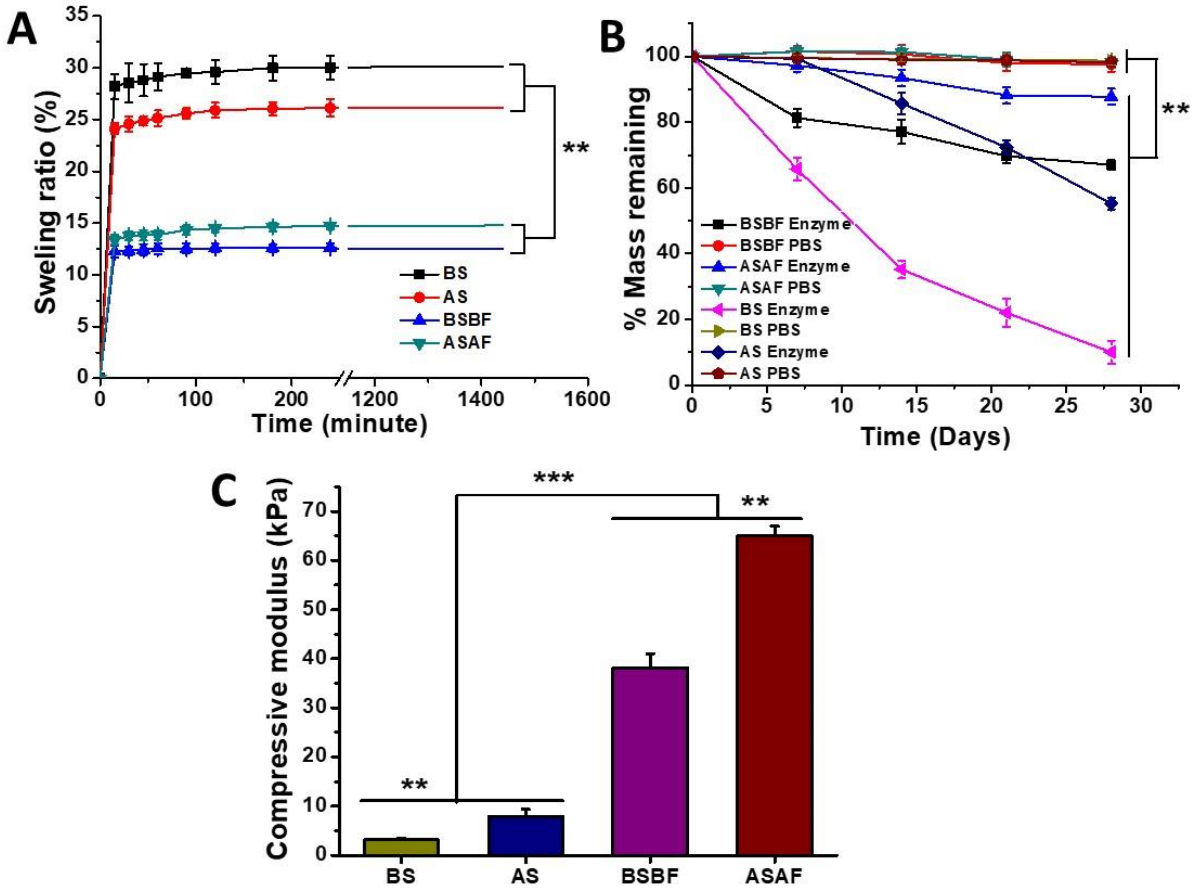

Figure 3.3. *(A) Swelling ratio, (B) degradation behaviour and (C) compressive modulus of the different types of scaffolds. Data are plotted as mean ± SD (n = 3). *** and ** shows significant differences between groups at p ≤ 0.001 and p ≤ 0.01, respectively.*

3.3.4 Chondrocyte proliferation and viability within the scaffolds

In order to study the cell proliferation on composite scaffolds, alamar blue assay was performed at different time points for a period of 28 days. Reduction in alamar blue corresponds to cell metabolism which co-relates directly to the number of cells. Throughout the culture period, all the scaffolds showed enhanced chondrocyte proliferation with time, which was significantly higher in ASAF as compared to BSBF ($p \leq 0.01$) (**Figure 3.4A**). The fiber-reinforced composite scaffolds showed significantly higher chondrocyte proliferation as compared to the solution scaffolds ($p \leq 0.01$). Among the pure solution scaffolds, AS showed significantly higher proliferation as compared to BS ($p \leq 0.05$). Calcein-AM dye was used to assess the viability of chondrocytes. Calcein-AM penetrates and retain into the cytoplasm of living cells giving bright green fluorescence. All the scaffolds-maintained cellularity and demonstrated homogenous chondrocyte

distribution throughout the culture period. Representative images of the stained cells from culture are shown in **Figure 3.4B**. The results showed that most of the cells were attached along the fiber surfaces in case of the composite scaffolds.

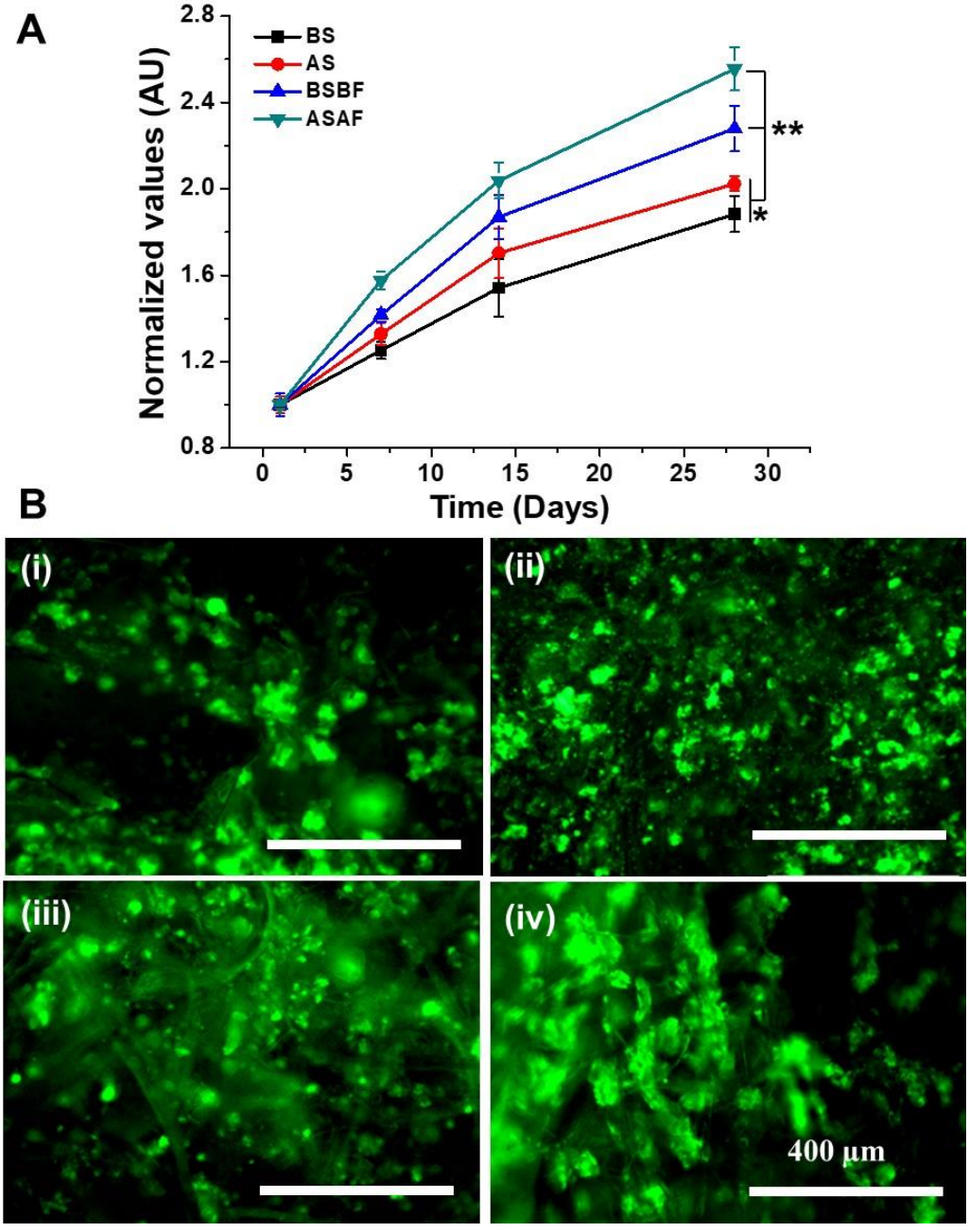

Figure 3.4. *(A) Alamar blue assay showing proliferation of primary porcine chondrocytes on different scaffold types for 28 days. (B) Calcein-AM staining of the chondrocytes in the scaffolds (i) BS scaffold, (ii) AS scaffold, (iii) BSBF fiber-reinforced composite and (iv) ASAF fiber-reinforced composite. Data are plotted as mean ± SD (n = 3). ** and * represent significant differences between groups at p ≤ 0.01 and p ≤ 0.05, respectively. Scale bar represents 400 µm.*

3.3.5 Biochemical assessment

3.3.5.1 DNA content of the construct

The DNA content of the constructs increased ~2.5 fold after 28 days of culture in chondrogenic medium when compared against day 1 ($p \leq 0.01$) (**Figure 3.5A**). The fiber-reinforced composites showed significantly higher DNA content as compared to the pure solution scaffolds ($p \leq 0.01$). Among the composites, the ASAF (~180 ng) showed markedly higher DNA content than BSBF (~165 ng) ($p \leq 0.01$). Similarly, among the pure solution scaffolds, AS exhibited significantly higher DNA in comparison to BS ($p \leq 0.05$). Similar trend was observed upon normalization of total DNA content with the scaffold mass.

3.3.5.2 Sulphated glycosaminoglycans (sGAGs) content

The total sGAG content as assessed in scaffolds and released in media showed increment in all scaffolds on day 28 in comparison to day 1 ($p \leq 0.01$) (**Figure 3.5B**). The fiber-reinforced composites showed significant increase ($p \leq 0.01$) in total sGAG content after 4 weeks of culture. Among the composites, the ASAF (~70 µg) exhibited significantly higher sGAG content as compared to BSBF (~55 µg) ($p \leq 0.05$). On normalization with DNA content, the sGAG content showed a similar trend with the fiber-reinforced composites with significantly higher sGAG production as compared to the pure silk solution scaffolds ($p \leq 0.01$). Upon normalization with scaffold mass, the composites showed significantly higher sGAG content in comparison to the pure solution scaffolds ($p \leq 0.05$).

3.3.5.3 Collagen content

The total collagen content in all the scaffolds was seen to be significantly higher on day 28 in comparison to day 1 ($p \leq 0.01$) (**Figure 3.5C**). The fiber-reinforced composites showed significantly higher collagen content in comparison to the pure solution scaffolds ($p \leq 0.01$). Among the composites, ASAF (~175 µg) showed significantly higher collagen content when compared to the BSBF (~160 µg) ($p \leq 0.05$). Among the pure solution scaffolds, AS showed significantly higher collagen content in comparison to BS ($p \leq 0.01$). Collagen content normalized with DNA content increased ~1.2 fold in composites on day 28 in comparison with pure solution scaffolds. Upon normalization with scaffold mass, the collagen content showed ~1.2-fold increment in composite scaffolds as compared to the pure solution scaffolds ($p \leq 0.01$). Among

the pure solution scaffolds, AS displayed significantly higher collagen content as compared to the BS ($p \leq 0.05$).

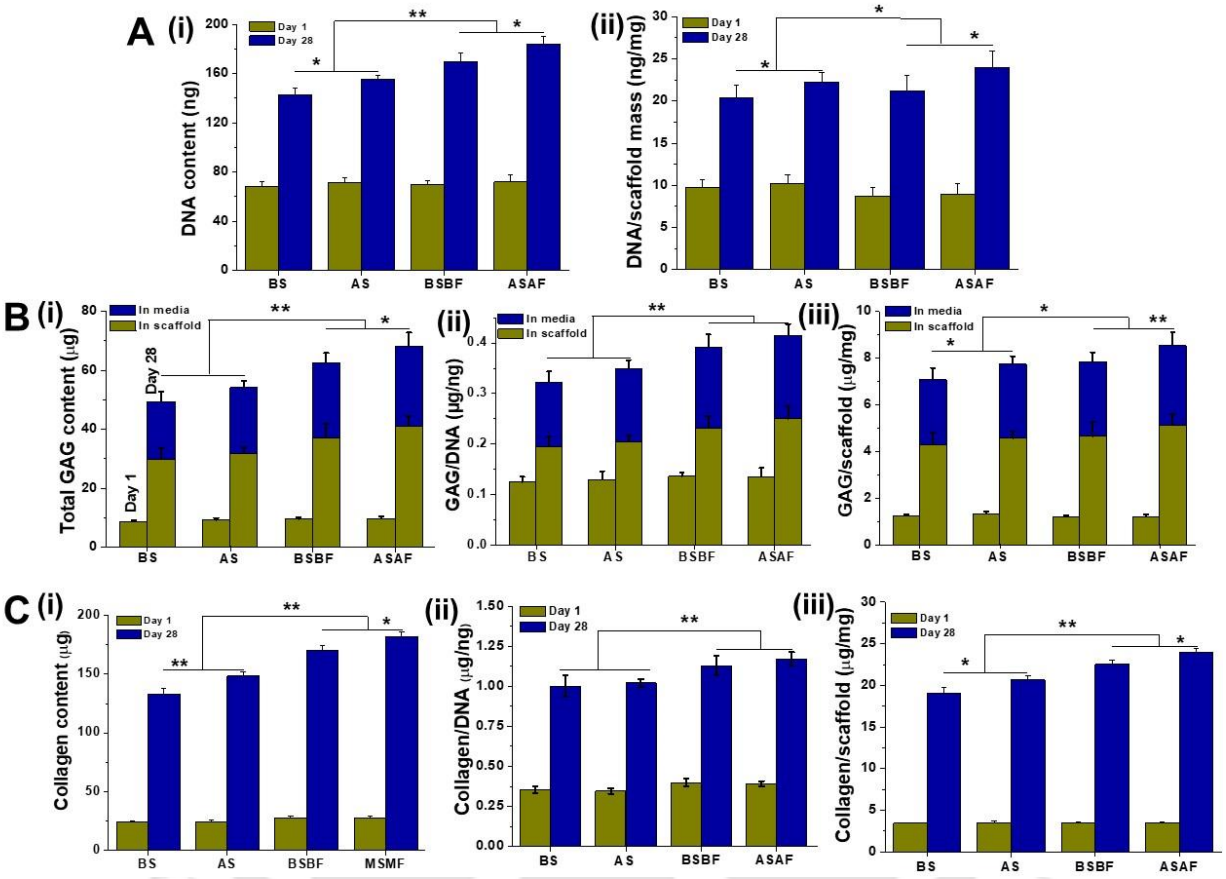

Figure 3.5. *Biochemical assay results showing (A) DNA content [i. total DNA, ii. DNA/scaffold mass); (B) GAG content [i. total GAG, ii. GAG/DNA, iii. GAG/scaffold mass] and (C) collagen content [i. total collagen, ii. collagen/DNA, iii. collagen/scaffold mass] in scaffolds seeded with primary porcine chondrocytes in chondrogenic medium after day 1 and 28. Data represents mean ± SD (n = 4). ** and * represent significant differences between groups at $p \leq 0.01$ and $p \leq 0.05$, respectively.*

3.3.6 Histology, IHC and digital image analysis

H&E-stained images showed homogenous distribution of chondrocytes in all constructs with the nuclei-stained blue by hematoxylin (**Figure 3.6A-D**). The ASAF composites showed the highest intensity of H&E staining indicating maximal presence of chondrocytes. AS scaffolds showed higher intensity-stained images as compared to BS scaffolds. Alcian blue staining of the sectioned scaffolds revealed abundant deposition of cartilage specific ECM component sGAG (**Figure 3.6E-H**). The composite scaffolds revealed higher sGAG deposition than the pure solution scaffolds.

Among the composites, ASAF showed more intense staining for alcian blue when compared to BSBF. AS scaffolds showed more intense staining for sGAG when compared to BS scaffolds. IHC showed the homogenous localization of collagen type II in the ECM (**Figure 3.6I-L**). Similar to sGAG profile, the composites revealed higher collagen type II deposition as compared to the solution scaffolds. The ASAF composites, showed the highest collagen type II localization as evident from the immunohistochemical staining. The AS scaffolds showed more intense immunostaining for collagen type II as compared to BS scaffolds.

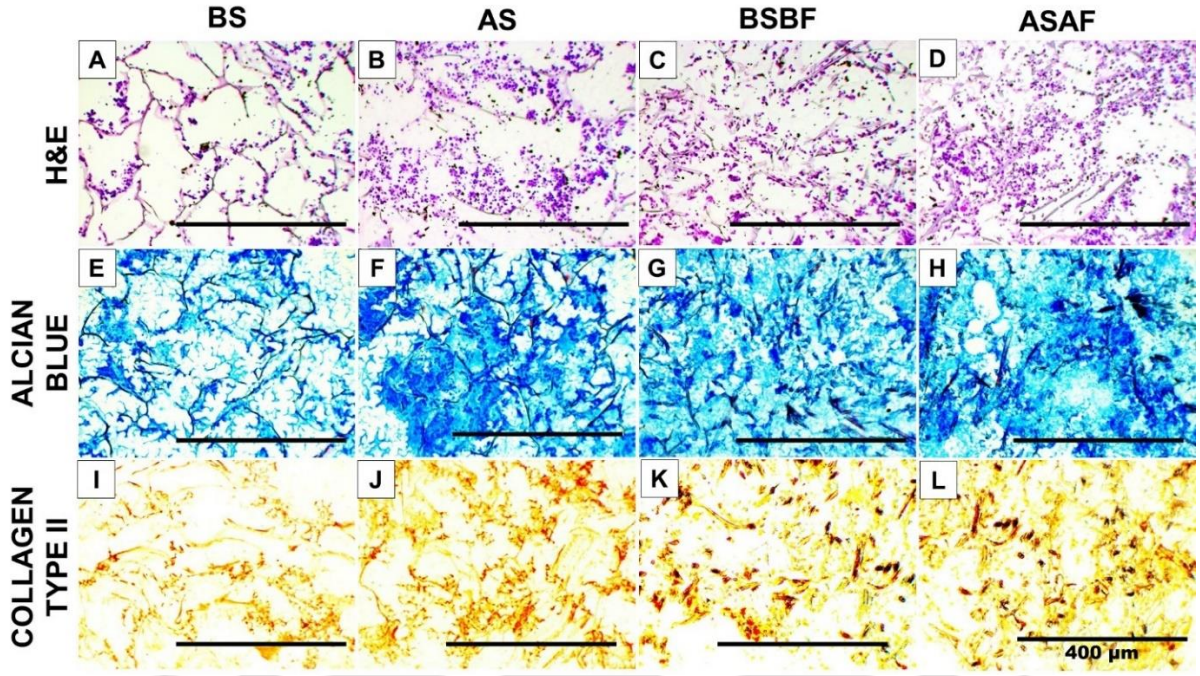

Figure 3.6. *H&E staining of scaffolds showing the distribution of chondrocytes (A-D), alcian blue staining for glycosaminoglycan deposition (E-H) and immunohistochemical staining of the scaffolds for localization of collagen type II (I-L), post 28 days of culturing the constructs. Scale bar represents 400 µm.*

Additionally, the color deconvolution plugin of ImageJ 1.48v software was used for data analysis of alcian blue and IHC stained images. The analysis revealed the histogram profile of pixels against the intensity of alcian blue or IHC stained images and their respective scores. The analysis of alcian blue stained images (**Figure 3.7**) revealed a low positive score for BS, positive score for AS, low positive score for BSBF and high positive score for ASAF. The high positive score for ASAF composite showed high intensity alcian blue staining for the composite. On the other hand, the analysis of IHC stained images (**Figure 3.8**) revealed a positive score for BS and high positive score for AS, BSBF and ASAF.

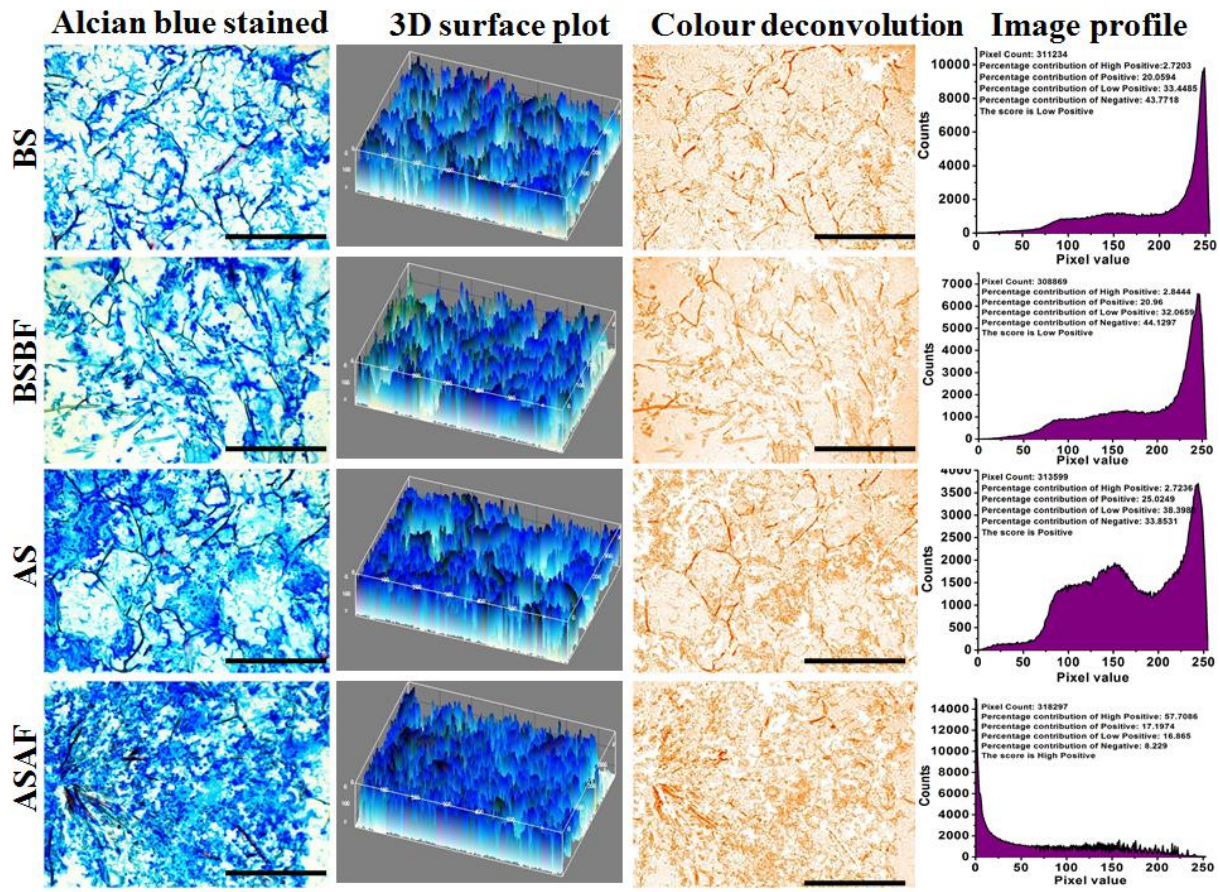

Figure 3.7*. Micrographs showing Alcian blue stained chondrocyte seeded scaffolds after 28 days of culture. The blue colour shows deposition of glycosaminoglycans in the extracellular matrix. Scale bar represents 400 µm. The 3D image analysis was performed using the Image J (NIH, USA) software.*

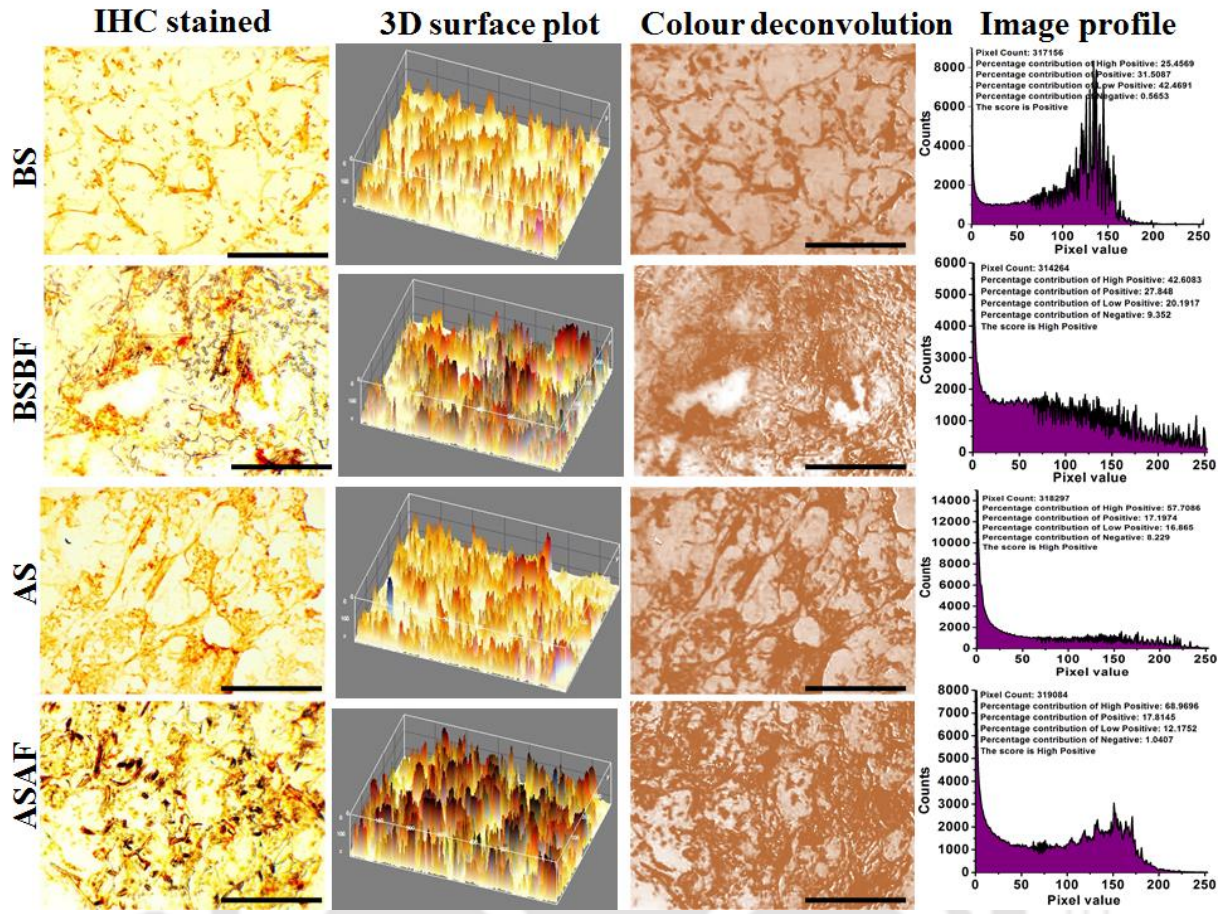

Figure 3.8*. Micrographs showing IHC stained chondrocyte seeded scaffolds after 28 days of culture. The brown colour shows localization of collagen type II in the extracellular matrix. Scale bar represents 400 µm. The 3D image analysis was performed using the Image J (NIH, USA) software.*

3.3.7 Gene expression analysis

Gene expression study was done using real-time PCR to validate the chondrogenic differentiation of cultured chondrocytes in the scaffolds. Herein, we assayed three different cartilage specific genes namely collagen type II, aggrecan, and early chondrogenic transcription factor sox-9. The results showed that the chondrogenic genes were up-regulated in all the scaffolds (**Figure 3.9**). The composites ASAF and BSBF showed significantly higher expression levels of all the three genes in comparison to pure silk fibroin scaffolds after 4 weeks culture period ($p \leq 0.01$ and $p \leq 0.05$). The composite scaffolds showed ~1.5 fold up-regulation of cartilage specific aggrecan gene when compared with the pure solution scaffold ($p \leq 0.01$). Among the composites, ASAF showed significant higher fold change of aggrecan as compared to the BSBF ($p \leq 0.05$). The collagen type II gene showed a ~1.5 fold up regulation in case of the composites as compared to the pure solution

scaffolds ($p \leq 0.01$). Similarly, the expression of sox-9 showed a ~1.2 fold up regulation in case of the composites as compared to the pure solution scaffolds ($p \leq 0.05$).

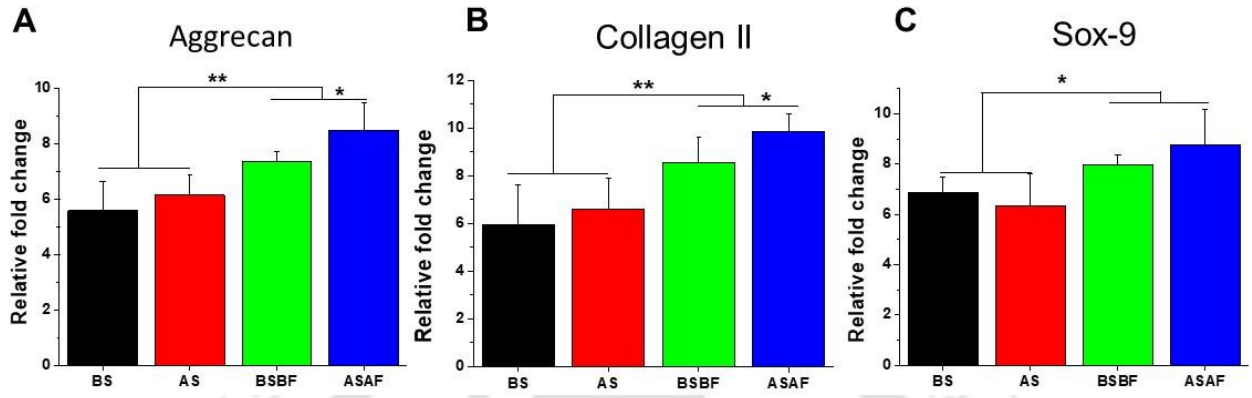

Figure 3.9. *Gene expression results showing transcript levels of cartilage-related genes after 4 weeks of chondrocyte culture on the scaffolds (a) aggrecan, (b) collagen type II, and (c) Sox-9. The genes were normalized to GAPDH and expressed as relative values to day 1. Data are represented as mean ± SD (n = 3). ** and * represent significant differences between groups at $p \leq 0.01$ and $p \leq 0.05$, respectively.*

3.3.8 Macrophage stimulation and detection of TNF-α release

The immunogenicity of the fabricated scaffolds was assessed *in vitro* by detection of TNF-α released by stimulated murine macrophage RAW 264.7 cells. After co-incubation of macrophage cells and scaffolds for 12 h, all the scaffolds showed significantly lower (~2.5 fold) secretion of TNF-α compared to that of the positive control lipopolysaccharide (LPS) ($p \leq 0.01$) (**Figure 3.10**). Secretion of TNF-α for the composite scaffolds was comparable to the values obtained with pure solution scaffolds and the negative control TCP.

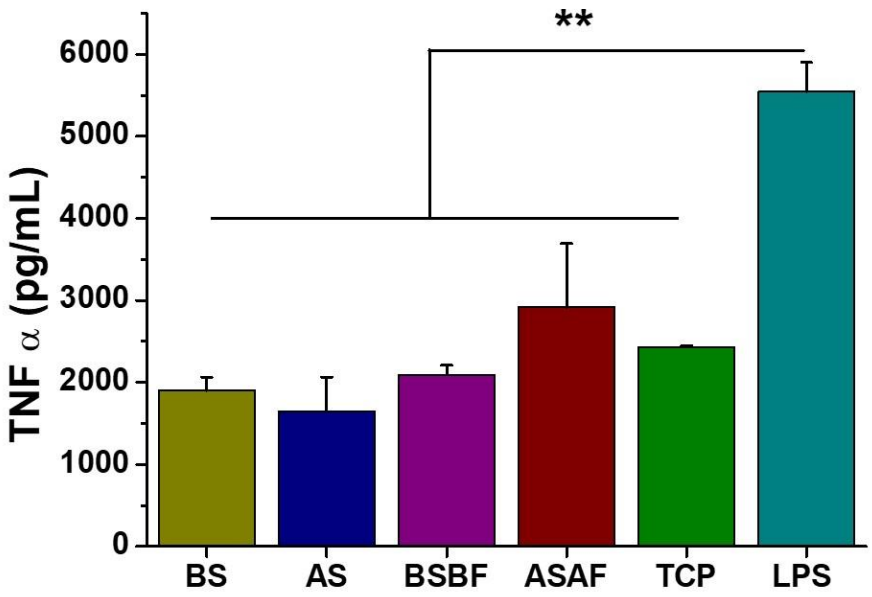

Figure 3.10. *Detection of TNF-α release from murine macrophage cell line RAW 264.7 induced by different types of scaffolds. Tissue culture plate (TCP) and lipopolysaccharide (LPS, 1000 ng/mL) were used as negative and positive controls, respectively. Data are represented as mean ± SD (n = 3).* ***represents significant difference between groups at* $p \leq 0.01$.

3.4 Discussion

The overall success of cartilage tissue engineering essentially relies on three elements; a safe and suitable cell source, a regulated environment for cell culture and scaffold (matrix) that is biocompatible and biodegradable. An efficient scaffold must possess desired structural attributes for cell attachment, proliferation and chondrogenesis [301]. In addition, scaffolds should be designed in a way to provide load bearing capacity and integration ability with the host tissue for formation of functional cartilage constructs [302]. Biomimetic scaffolds have therefore been developed to augment chondrogenesis by fine tuning their chemical and physical components. Accordingly, natural biomaterials are gaining prominence as their biochemical activities are in sync with a variety of cellular processes.

Silk as a natural fibrous protein is inherently bioactive and offers the advantages of biocompatibility, biodegradability, minimal immunogenicity, and ease of aqueous-based solvent matrix fabrication. SF from *B. mori* silkworm is extensively studied for various regenerative medicine applications; however, SF from *A. assamensis* silkworm is relatively lesser explored. Earlier, we explored the use of silk fibroin/agarose blend hydrogel derived from *A. assamensis*

silkworm for its potential utilization in cartilage tissue engineering [291]. In cartilage tissue engineering, porous SF scaffolds of are widely studied format; however, its utility are limited due to their low mechanical strength [230, 272, 297]. Thus, there is an exigency to engineer a mechanically proficient cartilage with a suitable microenvironment. In this context, the present study is conducted to typify the formation of cartilaginous tissue by primary porcine chondrocytes cultured on silk fiber-reinforced composite scaffolds.

The scaffolds serve to mimic the *in vivo* microenvironment where the pore size and porosity govern the vital triad of integrity, nutrient supply and cellular invasion that are responsible elements for the functional actualization of the fabricated tissue construct [303]. The composite scaffolds fabricated in the present study were porous with pore size ranging between 20-80 μm. As revealed by FESEM images, the reinforced fibers were dispersed throughout the porous silk matrix with formation of highly interconnected structure. These results are in line with those previous reports where the scaffolds with interconnected pores in this range supported higher chondrocyte attachment, proliferation and ECM component secretion [304-306]. Interestingly, pure solution scaffolds of *A. assamensis* showed larger pore size as compare to the *B. mori* silk fibroin. This deviation could have arisen due to differential presence of hydrophilic and hydrophobic amino acids in mulberry and non-mulberry silk, which interact differently with water molecules in the course of freeze drying [247]. Further, porosity analysis reaffirmed the highly porous nature of these composite scaffolds (~90% porosity). Moreover, the composite scaffolds maintained the porosity even after fiber reinforcement. The porosity in this range has previously been reported to be optimal for chondrocyte attachment and proliferation [115, 307].

The water retention capacity and degradability are essential factors of scaffolds for its applicability in tissue engineering. The higher water adsorption capacity tends to prevent the loss of body fluid and nutrients when the scaffold is implanted *in vivo*. Significant difference in swelling was observed between the scaffolds with and without fiber reinforcement. The silk solution scaffolds swelled more as compared to the fiber-reinforced scaffolds. Incorporation of fibers in scaffolds lowers the water uptake capability, but at the same time it improves the mechanical and chondrogenic properties, more important requirements for cartilage tissue engineering. Though fiber reinforcement had resulted in reduced swelling properties, it still remained within the range required to facilitate desired nutrient and waste transport for enhanced cell growth. These findings

were in accordance with the prior reports where incorporation of fibers has been reported to reduce water absorption of matrices [296, 308]. Furthermore, in order to assess the degradability of the composite scaffolds, protease XIV enzyme treatment was adopted. Degradation of the polymeric implant with time obliterates the need of surgical intervention for its removal at the end of its functional life. Moreover, the rate of degradation should match the rate of native tissue formation, and hence requires tunable biodegradation. Since, protease XIV enzyme cleaves silk non-discriminately at multiple locations along the length of the protein [262], in addition to earlier reports [263, 291], supported its choice for degradation study. The results of our study showed that *B. mori* scaffolds degraded faster than that of *A. assamensis* scaffolds which might be due to the difference in amino acid profile between the two silk varieties [250, 291]. The composite scaffolds showed lower degree of degradation than pure solution scaffolds as the incorporation of fiber imparted stability to the scaffolds and slowed down the degradation rate. The results were in agreement with a recent report by Li *et al.* where the *in vitro* proteolytic degradation showed that the 1% silk microfiber-reinforced membranes lost 90% weight after 5 days, a longer time frame than control plain silk membrane [295].

For articular cartilage to serve its function as a biomechanical structure, it is imperative that the implanted scaffold should withstand *in situ* physiological pressures until the nascent matrix is strong enough to resist the pressures to a variety of forces such as hydrostatic pressure, compression and shear forces [309]. Earlier Mandal *et al.* reported that micron-sized silk fibers (10–600 μm) obtained by alkali hydrolysis when reinforced in silk solution matrix to form a composite showed high compressive strength and no visible degradation over time [238]. Accordingly, our data depicted that the reinforcement of silk fibers in porous scaffolds resulted in ~8-fold increment in compressive modulus. This can be attributed to the physical outcome of fibers occupying spaces inside the porous solution scaffold forming a stiff, fibrous matrix.

This result demonstrated that incorporation of fragmented fibers into silk solution scaffolds could enhance mechanical properties of matrices by increasing the weight ratio of fibers in composites. Factors such as fiber content, fiber length, fiber–matrix interfacial bond strength, and fiber orientation affect the mechanical strength of fiber-reinforced composites [310]. Yodmuang *et al.* investigated the influence of different silk microfiber lengths on mechanical properties of fiber–hydrogel composites. They reported that composites made from all fiber lengths (200, 500 and >500 mm) displayed greater moduli coalesced with silk hydrogel alone [99]. Therefore, the

reinforcement of fibers not only mimic the structure of native ECM, but also it mimics the function of collagen fibers in adjusting the mechanical properties of tissue. With enhanced mechanical strength these composite scaffolds showed great promise in cartilage tissue engineering application.

Successful tissue development requires the use of a biomaterial that stimulates cellular adhesion, subsequent proliferation and differentiation to positively influence the final construct of tissues replacement [311]. Sufficient mass transport throughout scaffolds, both with and without fiber reinforcement was assessed from the homogeneity of viable chondrocytes distribution. In fact, uniform distribution of viable cells within both pure and composite scaffolds denotes that proper mass transport takes place throughout the constructs. Furthermore, chondrocytes maintained their round morphology into matrices. The evaluation of cell proliferation assay yielded higher proliferation of chondrocytes in case of the fiber-reinforced composites as compared to the pure solution scaffolds. It might be attributed to enhanced surface area for cell attachment, highly interconnected porous structure, and superior mechanical strength imparted by the microfibers to the composites. Subramanian *et al.* reported enhancement of growth and proliferation of articular canine chondrocytes with higher substrate stiffness [286]. The higher proliferation in ASAF composites might be due to the presence of intrinsic integrin binding RGD tripeptide present in *A. assamensis*. The results were in agreement with previous reports where attachment, growth and proliferation of articular chondrocytes was better in non-mulberry based SF scaffolds [292, 296]. The cartilage matrix is largely made up of sparsely dispersed chondrocytes embedded within a dense and hydrated ECM, which further is responsible for the load bearing function of cartilage [312]. The matrix is comprised mainly of proteoglycan and collagen fibers, which also generates the crucial microenvironment to support the embedded population chondrocytes. Herein, biochemical analysis results indicated significantly higher DNA, sGAG and collagen content in the fiber-reinforced composites than pure solution scaffolds. Among the composites, ASAF produced higher ECM components than that of BSBF. The differential deposition and accumulation of ECM might be due to difference in structural morphology and chemical composition of different types of scaffolds. This was in agreement with earlier reports showing that chondrocytes in the fiber-hydrogel composite material produced greater levels of sGAG and total collagen compared to hydrogel alone [313]. In another study, chondrocytes cultured on silk fiber-gel composite scaffolds allowed enhanced production of sGAG and collagen content as

compared to the no-fiber silk hydrogel [99]. Bhardwaj *et al.* in a recent endeavour demonstrated significantly elevated levels of sGAGs and collagen production in *A. assamensis* silk fibroin scaffolds compared to that of *B. mori* scaffolds [292].

The histological assessment of the composites revealed higher deposition of GAG and IHC staining showed localization of collagen type II around the fibers, suggesting the formation of new ECM. In both the staining, the fiber-reinforced composites showed more intense staining as compared to the pure solution scaffolds. Yodmuang *et al,* showed that chondrocytes cultured on fiber–gel composite silk scaffolds allowed fibers to be enveloped by ECM localized deposition that was GAG and collagen abundant [99]. Furthermore, the color deconvolution of the alcian blue and IHC stained images revealed a high positive score for composites compared to the pure solution scaffolds indicating enhanced ECM formation. The results were in accordance with the chondrocyte proliferation and biochemical evaluation studies indicating that the composite scaffolds supported chondrogenesis. Correspondingly, the ECM formation by chondrocytes on composite scaffolds were consistent with the upregulation of cartilage marker genes namely collagen-II, sox-9 and aggrecan. The transcript levels of these genes were significantly upregulated in fiber-reinforced composite scaffolds after 4 weeks of culture period which was similar to the biochemical and other cell metabolism study results. The results were in line with a previous study which reported an up-regulation of these genes in the fiber scaffolds as compared to the 3 days in pellet culture [314].

TNF-α is vital to immunity and inflammation regulation; as macrophages and other immune cells secrete it as a response to infectious and invasive stimuli. Macrophages are the first cells to identify an invading pathogen and respond by release of cytokines such as TNF-α. The results of our study indicated a minimal *in vitro* immune response for our fabricated composites, as the levels of released TNF-α by murine macrophages were comparable to the negative control TCP and ~2.5 fold lower than the positive control LPS. The results obtained clearly point out the low immune reaction and therefore the minimal inflammatory nature of the fabricated composites and similar to earlier reports [174, 251, 291]. Thus, it may be assumed that silk fiber-reinforced composites should prove to be a viable alternative biomaterial for cartilage tissue engineering.

3.5 Significant findings

1. This study investigated the potential of silk fibroin sponges versus silk fiber-reinforced composites based of mulberry (*B. mori*) and non-mulberry (*A. assamensis*) silk types for their individual impact in cartilage tissue engineering.
2. The fiber reinforcement within the silk solution enhanced the microarchitecture, porosity, swelling, degradation and compressive modulus characteristics of the scaffolds.
3. The live-dead assay and cell proliferation indices were uniformly higher for *A. assamensis* composites. This in turn was augmented and confirmed by biochemical, histological, immunohistological and gene expression analysis.
4. Finally macrophage simulation and detection of TNF-α data reinforced the biocompatibility of the fiber composite.
5. All the results derived from our assessment of various parameters pointed to the high potential of the composite scaffold, particularly of *A. assamensis.*
6. Therefore, the non-mulberry fiber-reinforced silk composite offers great promise to provide structural support, delivery of cells and, possibly refill the damaged tissue void by *in vivo* neo-tissue formation post transplantation.

Chapter 4

Hierarchically Structured Seamless Silk Scaffolds for Osteochondral Interface Tissue Engineering

The structural complexity of the osteochondral joint makes it a challenging job to fabricate a single construct mimicking its properties. In this study, we used a facile approach to fabricate an all-silk continuous hierarchical scaffold using the endemic silk varieties. The biphasic scaffold composed of an upper spongy phase for cartilage and a lower fiber-reinforced phase for bone tissue with distinct pore sizes and interconnectivity. After successful *in vitro* characterization, the biphasic scaffold was implanted *in vivo* in a rabbit model to assess the analogous and concurrent region-specific reconstruction of bone and cartilage.

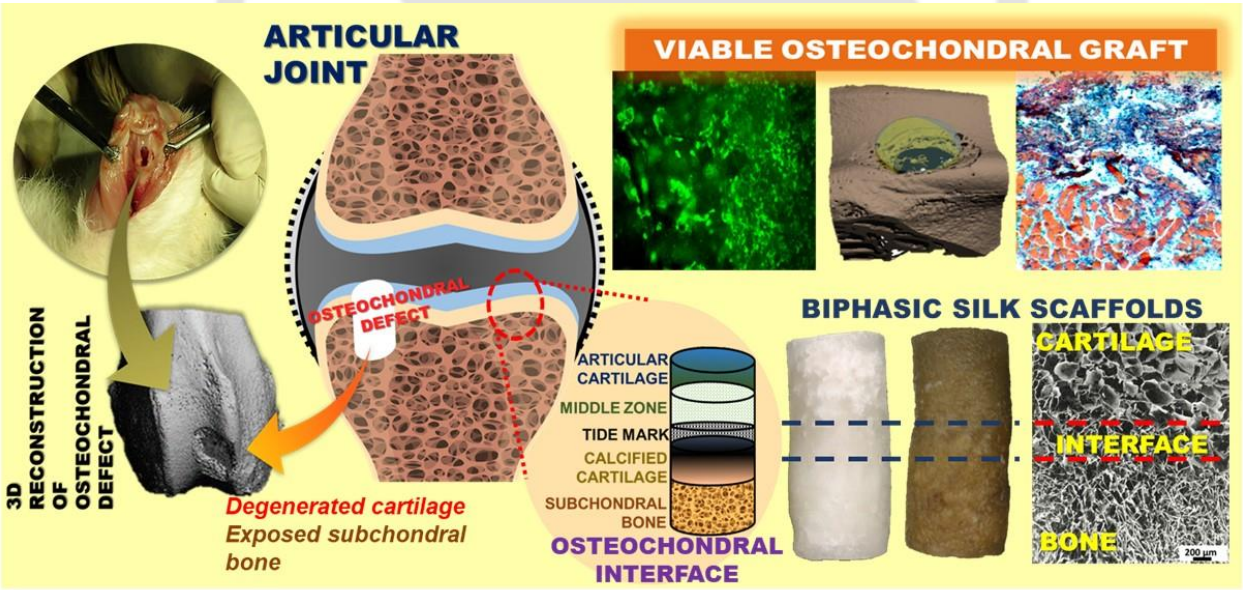

The work embodied in this chapter is published as follows:

Yogendra Pratap Singh, Joseph Christakiran Moses, Bibhas K. Bhunia, Samit Kumar Nandi, and Biman B. Mandal. "Hierarchically structured seamless silk scaffolds for osteochondral interface tissue engineering." ***Journal of Materials Chemistry B*** 6(36), 2018: 5671-5688.

ABSTRACT

The osteochondral healthcare market is driven by the increasing demand for affordable and biomimetic scaffolds. To meet this demand, silk fibroin (SF) from *Bombyx mori* and *Antheraea assamensis* is used to fabricate a biphasic scaffold, with fiber-free and fiber-reinforced phases, stimulating cartilage and bone revival. The fabrication is a facile reproducible process using single polymer (SF), for both phases, designed in a continuous and integrated manner. Physicochemical and mechanical scaffold characterization, display interconnected pores with differential swelling and tunable degradation. The compressive modulus values, extend to 40 kPa and 25%, for tensile strain, at elongation. The scaffold support, for growth and proliferation of chondrocytes and osteoblasts, for respective cartilage and bone regeneration, is verified from *in vitro* assessment. Up-regulation of alkaline phosphatase (ALP) activity, extracellular matrix secretion and gene expression are significant; with acceptable *in vitro* immune response. Upon implantation in rabbit osteochondral defects for 8 weeks, the histological and micro-CT examinations show biphasic scaffolds significantly enhance regeneration of cartilage and subchondral bone tissues, as compared to monophasic scaffolds. The regenerated bone mineral density (BMD) ranges from 600-700 mg hydroxyapatite (HAp)/cm^3. The results, therefore, showcase the critically positive characteristics of *in vitro* ECM deposition, and *in vivo* regeneration of osteochondral tissue by this heirarchically structured biphasic scaffold.

4.1 Introduction

The osteochondral (OC) interface in the human knee, is an area strikingly predisposed to osteoarthritis (OA) and traumatic injuries [315]. The near epidemic proportions of OA disables nearly half of the world's 65 plus population [277]. Orthopedic challenges of the OC health management, are aggravated by the complex osteochondral architecture and intrinsic limited healing potential of cartilage [218]. Both extant clinical practices and alternative restorative methods suffer from multiple impediments; thus, options of abrasion arthroplasty, microfracture, autografts, allografts, and autologous chondrocytes implantation, remain inadequate in OC health regeneration. In addition, the undeniable possibilities of fibrocartilage formation, donor site morbidity and the dearth of donor supply may actualize a substantive time lag that counteracts tissue healing and therapeutic advantages [316]. Therefore, the evolution of scaffold-based osteochondral tissue engineering strategies is strongly driven by the unabated clinical need for across-the-board restorative therapies. However, critical to any design of an effective template, is assimilating the synergy and topography of the upper cartilage and basal subchondral bone within the complex OC. The calcified upper cartilage with predominant chondrocytes is responsible for anchorage of the cartilage layer to the underlying subchondral bone [317]. The basal subchondral bone has collagen type I, hydroxyapatite and water as its principal constituents, which in turn sustain its mandatory levels of stiffness and compressive strength [16]. Therefore, the tissues of the bone-cartilage interface have unique cellular organization and chemical signatures, which is reflected in their individual physiological and load bearing properties.

A significant predicament in development of biomaterials for OC application is the adequate replication of the natural OC tissue gradient with its distinct yet homogenous layer integration. While an initial degree of success in repairing OC, defects has been achieved using biphasic scaffolds, several factors still limit their widespread implementation. Production of most extant biphasic constructs involve the use of separate materials to fabricate two scaffolds, one dedicated to cartilage regeneration and the other to bone reconstruction; conjoined by appropriate sealants [318]. Unfortunately, this heterogeneous fabrication hinders seamless cellular infiltration and makes the design prone to mechanical disintegration [319, 320]. This instability could arise from the individual fabrication of the two phases and their subsequent physical integration, creating fault lines that may open under pressure. Even in the alternative remedy of cell-substratum contact, the interphase shear force would continue to weaken the contact area after it is *in vivo* implantation

and during natural degradation [321]. In comparison to chondral only grafts; enhanced anchorage is acquired by press fitting OC constructs into pre-drilled cavities and subsequent reduction in exposure and disruption by shear forces [319]. In the final prognosis, the vital role of robust subchondral bone in voluntary cartilage repair/regeneration cannot be negated [322]; thus necessitating simultaneous reconstruction of both subchondral and cartilage layers.

The biomaterials used for fabrication of matrices in tissue engineering determines the lifespan of the implant and exerts a definite influence on tissue response. The catalog includes natural materials like collagen, agarose, glycosaminoglycan, hyaluronic acid, chitosan, silk fibroin and alginate; and synthetic materials such as poly(caprolactone) (PCL), poly(lactic acid) (PLA), poly(glycol alcohol) (PGA) [285, 323-326]. Though natural materials, stimulate host tissue interaction, the clinical prospects are dependent on using current technology to match native cartilage characteristics, by scaling up their lower mechanical prowess and stability [327]. In this context, silk fibroin (SF), occupy a special niche, as they are natural protein polymers, endowed with sterling advantages of biocompatibility, biodegradability, mechanical durability and minimal immune responses [238, 328, 329]. In addition, their water-soluble attributes leverage natural processing potential and cross-linking by requiring only mild solvents and proscribing toxic crosslinking agents [75]. SF has been widely explored for repair and regeneration in bone [238], cartilage [68], vascular [330], and neural tissues [331]. SF from mulberry silkworm *B. mori* has been studied extensively, whereas the biomedical efficiency of silk fibroin from non-mulberry silkworms is relatively less explored. The SF from Indian non-mulberry silkworm *A. assamensis* has the structural advantage over mulberry SF in possessing tripeptide Arg-Gly-Asp (RGD) sequence [247]. The RGD is an integrin binding cell attachment site, enhancing both cellular proliferation and differentiation [182]. Previous studies have reported promising results using biphasic scaffolds made of silk composites for osteochondral repair [59, 110, 332].

Addressing the drawbacks from previous fabrication strategies we resorted in using a facile approach for fabricating biphasic scaffolding matrices with a seamless interface using a single biopolymer – silk fibroin. Higher β-sheet content in the silk fibroin fibers presents a stiffer matrix suitable for osteoblasts whereas lower β-sheet content in the regenerated silk fibroin sponges presents a comparatively less stiff matrix amiable for chondrocyte survival and maturation. We explored this feasibility of differential presentation of biophysical cues for osteoblast and

chondrocyte maturation preferentially, using our minimalistic fabrication strategy. Additionally, we further tried to study the effects of use of different silks (non-mulberry and mulberry silk) in the cellular behaviour, as these two silks have differential amino acid sequences exhibiting different physico-chemical traits. The developed continuous biphasic scaffold has a porous, fiber-free part that mimics the cartilage tissue, and a silk fiber-reinforced stiffer part that resembles the bone. The biphasic constructs were characterized by their physicochemical properties of pore diameter, porosity, degradation, swelling behavior and mechanical properties. Furthermore, the competence of the biphasic constructs to holistically enhance the growth of chondrocytes and osteoblasts was assessed by a simulated *in vitro* system, where primary porcine auricular chondrocytes and human osteoblast cells (MG-63) were co-cultured [333]. The corresponding cellular, biochemical, histological and gene expression data were evaluated to affirm efficiency of the scaffolds as viable matrices. Promising post-injury management of OC regeneration, by the biphasic construct, was evidenced *in vivo* by using a rabbit model.

4.2 Materials and methods

4.2.1 Materials

Cocoons of *B. mori* silkworm and matured 5th instar larvae of *A. assamensis* silkworm were acquired from local silk farms, Assam, India. Lithium bromide (LiBr), protease XIV from *Streptomyces griseus*, sodium azide, collagenase (type I-A), 1, 9 dimethylmethylene blue (DMMB), alcian blue, alizarin red, Hoechst 33342, dexamethasone, lipopolysaccharide, calcein-AM and 12 kDa dialysis membrane were obtained from Sigma-Aldrich, USA. Cell culture reagents such as Dulbecco's modified Eagle's medium (DMEM), trypsin–EDTA, fetal bovine serum (FBS), antibiotics and amphotericin B were acquired from Gibco BRL Rockville, USA. PicoGreen dye, SYBR Green, alamar blue and, tumor necrosis factor alpha (TNF-α) kit were obtained from Invitrogen, USA. Vectastain universal elite kit and DAB substrate (Vector Laboratories), anti-collagen II monoclonal antibody (Abcam), and other reagents used were of analytical grade.

4.2.2 Isolation of silk fibroin solution and silk fibers

SF solution was extracted from the cocoons of mulberry *B. mori* silkworm and silk glands of non-mulberry *A. assamensis* silkworm as per earlier published protocol [76]. In brief, *B. mori* cocoons were cut into pieces and boiled in 0.02 M Na_2CO_3 solution for 30 min followed by its dissolution in 9.3 M LiBr at 60°C. The obtained solution was extensively dialyzed against milli-Q water using

dialysis membrane (MWCO 12 kDa). The SF protein of *A. assamensis* was extracted from the silk gland of fifth-instar matured larvae of silkworm according to previously published protocol [254]. The fibroin protein was squeezed out from the glands, dissolved in 1% (w/v) SDS and dialyzed extensively against milli-Q water. Conventional gravimetric method was used to determine the concentration of regenerated silk solution. The silk fibers from both mulberry and non-mulberry silkworms were obtained by degumming the cocoons in a boiling 0.02 M Na_2CO_3 as described above. The fibers were washed, air dried and finely chopped prior to use. Bright field microscopy showed that the chopped fibers had a heterogeneous distribution in their length ranging from 0.5 to 2.5 mm [334].

4.2.3 Fabrication of biphasic scaffolds

The biphasic scaffold was prepared by placing the finely chopped silk fibers into half space of the mold (10 mm X 10 mm) and adding SF solution in the ratio of 2:1 (w/w, 40 mg of silk fibers to 20 mg of regenerated silk). This set up allowed one half of the construct to contain only solution while the other half to have fibers reinforced in silk solution. The construct was pre-freezed at -20 °C for 12 h followed by lyophilization in a freeze drier (Christ ALPHA 1-4 LD plus) for 24 h. The lyophilized scaffolds were treated with 70% ethanol for 4-6 h to induce β-sheet. In the fabricated scaffold, the spongy porous part represents the prospective chondral phase while the fiber reinforced tough part as the bony phase. A single-phase spongy scaffold made of SF solution and a single-phase fiber-reinforced scaffold were used as a control for the study. The fabricated scaffolds were designated as BMS (*B. mori* solution), AAS (*A. assamensis* solution), BMF (*B. mori* fiber-reinforced), AAF (*A. assamensis* fiber-reinforced), BMI (*B. mori* interfacial), and AAI (*A. assamensis* interfacial).

4.2.4 FESEM observation and porosity measurement

The surface morphology, pore size, and interconnectivity of pores were examined using field emission scanning electron microscope (FESEM, Zeiss, Germany). The dry scaffold sections were sputter coated with gold and then scanned at 2.5 kV. Pore size was determined by taking 25 random pores and then analyzing using ImageJ (Wayne Rasband, National Institute of Health). The porosity of the scaffolds was measured using hexane displacement method as previously described [335]. Briefly, the scaffolds were dipped in a cylinder containing a known volume of hexane (V_1). The volume of the scaffold dipped hexane was recorded as (V_2). Post removal of hexane

impregnated scaffolds, the residual hexane volume was recorded as (V_3). The porosity was calculated using the equation:

$$\% \ Porosity = [(V_1-V_3)/(V_2-V_3)] \ X \ 100$$

4.2.5 Swelling behaviour

Swelling property of the scaffold was studied using the conventional gravimetric method [336]. Briefly, the dry weight of the scaffolds was recorded before immersion in phosphate buffered saline (PBS, pH 7.4) at room temperature till they attained equilibrium. The swelled weight of scaffolds was taken at various time intervals. The experiment was conducted in sets of three under identical conditions. The percent swelling was calculated using the equation:

$$\% \ Swelling = [(Ws - Wd)/Wd] \ X \ 100$$

where *Ws* is the swelled weight, and *Wd* is the dry weight of the scaffold.

4.2.6 *In vitro* enzymatic degradation

The *in vitro* enzymatic degradation of the scaffold was evaluated using protease XIV from *S. griseus* with an activity of ≥3.5 units/mg using previously published method [337]. The scaffolds (6 mm X 2 mm) were immersed in 1 mL PBS (pH 7.4) containing 2U of protease enzyme and were incubated at 37 °C. The enzyme solution was replaced every three days for 28 days. Samples in PBS without the protease enzyme were taken as control. The experiment was repeated three times under identical conditions, and the weight loss was calculated using the equation:

$$\% \ Mass \ remaining = [(W_0 - W_1)/W_0] \ X \ 100$$

where W_0 is initial dry weight of scaffold, and W_1 is the final dry weight of the scaffold.

4.2.7 Mechanical testing

Mechanical properties of scaffolds were tested using Universal Testing Machine (Instron 5944) equipped with a 100 N load cell at 37 °C under aqueous conditions. Scaffolds were pre-soaked in PBS for 10 min and examined at a crosshead speed of 1 mm/min. 4 cm long and 1 cm wide scaffolds were used to determine the tensile strength, elongation at break and modulus. The gauge length between two clamps was set at 2 cm. Tensile strength was examined at a crosshead speed of 1 mm min^{-1}. The tensile strength and elongation at initial break (%) of biphasic scaffolds were derived from the obtained stress-strain curve. For compressive strength, the biphasic scaffold (10 mm diameter X 16 mm thickness) was placed vertically between the plates and modulus was calculated from the slope of a stress-strain curve by drawing a line parallel to the initial linear

region with an offset of 0.5%. Bluehill version 3.66 software was used to analyze the compressive modulus.

4.2.8 Cell isolation and culture

The chondrocytes for the chondral phase were isolated from porcine source according to earlier established protocol [336]. Briefly, the obtained cartilage was cut into small fragments and digested using 0.2% protease and 0.05% collagenase. The digested tissue was centrifuged forming cell pellet and washed 2-3 times with DMEM containing 10% FBS and 1% antibiotic-antimycotic solution. MG63 cells (human bone osteosarcoma) were used for the bony phase. The cells were cultured in high glucose DMEM, similar to that for chondrocytes. The scaffolds were seeded with 5×10^5 cells/scaffold (2.5×10^5 cells each of chondrocytes and MG63). The cell-seeded scaffolds were kept in a 37°C humidified incubator with 5% CO_2 for 3 h to allow the cells to diffuse into and attach to the scaffold. After initial cell attachment, the scaffolds were transferred to new culture plates, and osteochondral media was added to it. The osteochondral media used for co-culture comprises of high glucose DMEM, 10% FBS, 1% antibiotic-antimycotic solution, 4 μg/mL sodium pyruvate, ITS (1X), 5 mM glycerol-2-phosphate, 10 mM dexamethasone, 40 μg/mL L-proline and 50 μg/mL L-ascorbic acid.

4.2.9 Cell viability and proliferation assay

The viability of both chondrocytes and MG-63 cells was assessed using live/dead assay. Briefly, the cell-seeded scaffolds were washed with PBS (pH 7.4) and treated with a staining solution containing 4 μM calcein-AM and 2 μM ethidium homodimer-1 (prepared in PBS, pH 7.4) for 15-20 min at 37°C. The treated scaffolds were washed with PBS and visualized under fluorescence microscope (EVOS FL, Life Technologies, USA). Further, to visualize cellular arrangement, nuclei were stained with Hoechst 33342 for 30 min under dark condition followed by imaging under a fluorescent microscope. Alamar blue reduction assay was performed to assess cell proliferation following manufacturers' protocol. Briefly, cell-seeded scaffolds were exposed to media containing 10% (v/v) alamar blue dye. Post 3 h of incubation at 37 ºC, absorbance was taken at 570 nm and 600 nm using a multiplate reader (Tecan Infinite M200Pro, Switzerland). Scaffolds without cell seeding were used as control. Acquired values were normalized and plotted using OriginPro 8 (OriginLab, USA).

4.2.10 Biochemical analysis

Quantification of alkaline phosphatase (ALP) activity

Alkaline phosphatase activity was assessed using colorimetric ALP kit (Abcam, UK) following manufacturer's protocol. Briefly, spent media from the cells cultured on the scaffolds for 14 days was collected and 80 µL of it was incubated with 50 µL of p-nitrophenyl phosphate (pNPP, 5 mM) solution at 37 ºC for 1 h in the dark. Post incubation, enzyme activity was terminated by adding 20 µL of stop solution. A standard curve was prepared using pNPP values ranging from 0 to 0.02 µmol/well. The amount of p-nitrophenol produced, corresponded to the ALP activity and was determined by monitoring absorbance at 405 nm. Obtained results were represented as U/L/DNA content.

DNA and sulphated glycosaminoglycan content

The scaffolds for estimation of DNA and GAG were digested with papain solution (125 µg/mL papain, 5 mM L-cysteine, 100 mM Na_2HPO_4, and 5 mM EDTA, pH 6.2) at 60 °C for 16 h. DNA content was measured according to manufactures protocol using PicoGreen DNA assay kit. Briefly, 25 µL of the digested sample was taken, and 75 µL of 1X TE buffer was added to it. To this, 100 mL of Quant-iT PicoGreen reagent (1:200 dilution) was added and measured using a fluorimeter (Excitation/emission maximum 480/528 nm). For total sulfated GAG (sGAG), 1,9-dimethylmethylene blue (DMMB) assay was used [255]. Briefly, 50 µL of papain digested sample or secreted media was added to 200 µL of DMMB reagent and absorbance was measured at 525 nm.

Total collagen estimation

For determination of collagen content, the samples were digested with pepsin cocktail (1 mg/mL pepsin, pH 3.0) at 4 °C for 48 h and quantified using a modified Hride Tullberg-Reinert method [256]. Briefly, the digested samples were dried at 37 °C for 24 h and to it, 100 µL of Sirius red dye solution (prepared in picric acid–saturated solution to a final concentration of 1 mg/mL) was added and incubated for 1 h with mild shaking. The samples were washed three times using 0.01 normality HCl and the dye sample complex was resolved using 0.1 normality NaOH. The absorbance was recorded at 550 nm. Rat tail collagen type I (Sigma-Aldrich, USA) was used to prepare the standard curve. Scaffolds without cells were used as control. GAG and collagen

contents were normalized against total scaffold weight and cell numbers (represented by the total DNA content) to negate the variations from scaffold sizes and cell numbers.

4.2.11 Histology

The cell-seeded scaffolds were fixed in 4% neutral buffered formalin (NBF) for 24 h; dehydrated, cleared and embedded in paraffin wax. The paraffinized scaffolds were sectioned (5 μm thick) using microtome (Leica Biosystems). The sections were processed and stained using hematoxylin and eosin (H&E, Sigma-Aldrich, USA) for cell morphology, 1% alcian blue (prepared in 3% acetic acid solution, pH 2.5) for sulfated proteoglycan and 2% (w/v) alizarin Red S stain (pH 4.1) to assess the calcium deposition. Stained sections were visualized by photo-microscopy (EVOS FL, Life Technologies, USA).

4.2.12 Gene expression studies

The total RNA from the cell-seeded scaffolds was isolated using TRIzol reagent (Sigma-Aldrich, USA) after 14 days of culture. The obtained RNA was quantified using Nanodrop (Eppendorf) and further cDNA was prepared using high-capacity cDNA reverse transcription kit (Applied Biosystems) in PCR thermal cycler (TaKaRa, Japan). Real-time PCR was performed using SYBR Green dye (Invitrogen) in a 7500 real-time PCR system (Applied Biosystems). SYBR Green mix, forward primer, reverse primer and cDNA was added to make a final reaction volume of 20 μL and run under the set conditions of holding stage (2 min at 50 °C, 10 min at 95 °C) and cycling stage (40 cycles of 95 °C for 15 s, and 60 °C for 45 s). Aggrecan (ACAN), Sox-9, osteopontin, and RunX2 were quantified and normalized to an endogenous housekeeping gene glyceraldehyde-3-phosphate-dehydrogenase (GAPDH). The obtained results were analyzed through comparative Ct method ($2^{-\Delta\Delta Ct}$) in triplicates.

4.2.13 Macrophage stimulation and determination of TNF-α release

Scaffolds (6 mm X 2 mm) were added to the cell (murine macrophage cell line RAW 264.7) containing wells. After 24 h of co-incubation, the resultant medium was tested for TNF-α release while medium without scaffold was used as negative control and lipopolysaccharide (LPS from *E. coli*) (500 ng/mL) was taken as positive control. ELISA was used for quantification of TNF-α as per manufacturer's protocol. Diluted samples with 50 μL of biotinylated secondary antibody were incubated for 60 min at RT. Post incubation, the wells were washed, and 100 μL of streptavidin-HRP working solution was added (incubated for 30 min at RT). Subsequently, to each well, 100

μL of stabilized chromogen solution was added and incubated in dark for another 30 min. To stop the incubation, 100 μL of stop solution was added, and TNF-α level was recorded at an absorbance of 450 nm. A murine TNF-α standard curve with a range of 0-1000 pg/mL was used to derive the secreted volume.

4.2.14 *In vivo* assessment of biphasic scaffold

All *in vivo* studies were approved by the Institutional Ethical Committee (IAEC), West Bengal University of Animal and Fishery Sciences (WBUAFS) Project License approval (Permit No. Pharma /IAEC /168 dated 01.12.15). Throughout the experiments, rabbits were being housed in their cages, with proper hygiene and a standard balanced diet. Total 28 White New Zealand rabbits of either gender with average 1.5-2 kg body weight were assigned randomly. The animals were anesthetized using an intramuscular injection of xylazine hydrochloride (Xylaxin®, Indian Immunologicals, India) and ketamine hydrochloride (Ketalar®, Parke-Davis, India) at the dosage of 5 mg/kg body weight and 25 mg/kg body weight respectively. The animals were divided into 7 groups (4 control groups- BMS, AAS, BMF and AAF, 2 experimental groups- BMI and AAI, and 1 non-treatment group) with 4 animals per group and the experiment was continued for 8 weeks. The *in vivo* experiment was initiated by creating defects involving the articular cartilage and its underlying bone of femoral intercondylar notch with the help of a motorized dental drill. The acellular implants (4 mm X 4 mm) were press-fitted into the defects of the control and experimental groups and the surgical site was sutured in a layering pattern. The non-treatment group was subjected to the same defects; however, no scaffold was implanted. Post-surgery, the animals were given one dosage (10 mg/kg body weight) of intramuscular injection of cefotaxime sodium (Mapra, India) every 12 h for 5 days and one dosage (0.2 mL) of meloxicam every 24 h for initial 3 days. Animals were sacrificed upon completion of appropriate time points. The implants along with surrounding tissues were collected for further study (macroscopic observations, histology, and micro-CT).

4.2.15 Micro-CT scanning

Microcomputed tomography (micro-CT) was carried out using a Scanco Medical 50 Micro CT system (Scanco Medical, Switzerland) with 70 kV X-ray energy source and 114 μA intensity. Scans were performed using isotropic and medium resolution mode of 17.2 μm. The defect region was recognized and a cylindrical volume of interest (VOI), 3.5 mm wide × 3.5 mm deep, was

demarcated to assess subchondral bone healing. The 3-dimensional reconstructions of the tissues were carried out using a threshold of 350 mg HAp/cm^3 in a scale from 0 to 1000. A constrained Gaussian filter was used to partly suppress noise (filter width: 0.8 and filter support: 1). The subchondral bone healing was expressed as percentage bone volume over total volume (% BV/TV) and bone mineral density of bone volume (mg HAp/cm^3 BMD of BV). The data was analyzed using IPL (Image Processing Language) V5.42, SCANCO Medical AG.

4.2.16 Statistical analysis

Data are presented as means ± standard deviation (n=3). Statistical analysis was performed by one-way analysis of variance (ANOVA) using Sigma Plot 11.0 and a Holm–Sidak test was carried out to assess variance across groups, and statistical significance was set at $p < 0.05$. The differences between groups of $^{\#}p \leq 0.05$ were considered statistically significant and $^{\#\#}p \leq 0.01$ as highly significant.

4.3 Results

4.3.1 Analysis of scaffold architecture

FESEM examination of the biphasic scaffold revealed two phases with distinct pore morphology, homogenously meshed at the interface. The cartilage portion was characterized by the fiber-free silk scaffold at the upper end of the biphasic scaffold (**Figure 4.1A, D**), while the fiber reinforced scaffold characterized the bone portion at the lower end (**Figure 4.1C, F**). The interface region displayed a merger of the structural properties of the two phases (**Figure 4.1B, E**). It is interesting to note that, though the cartilage phase exhibited pore sizes of 160–200 µm against 40–60 µm for bony fiber-reinforced scaffolds; yet both scaffolds showed high porosity and interconnectivity. The porosity of the all the scaffolds examined (control and experimental) ranged from 80-94% (**Table 4.1**). Among the silk varieties, the scaffold constituted of *A. assamensis* displayed larger pore size as compared to its counterpart *B. mori*.

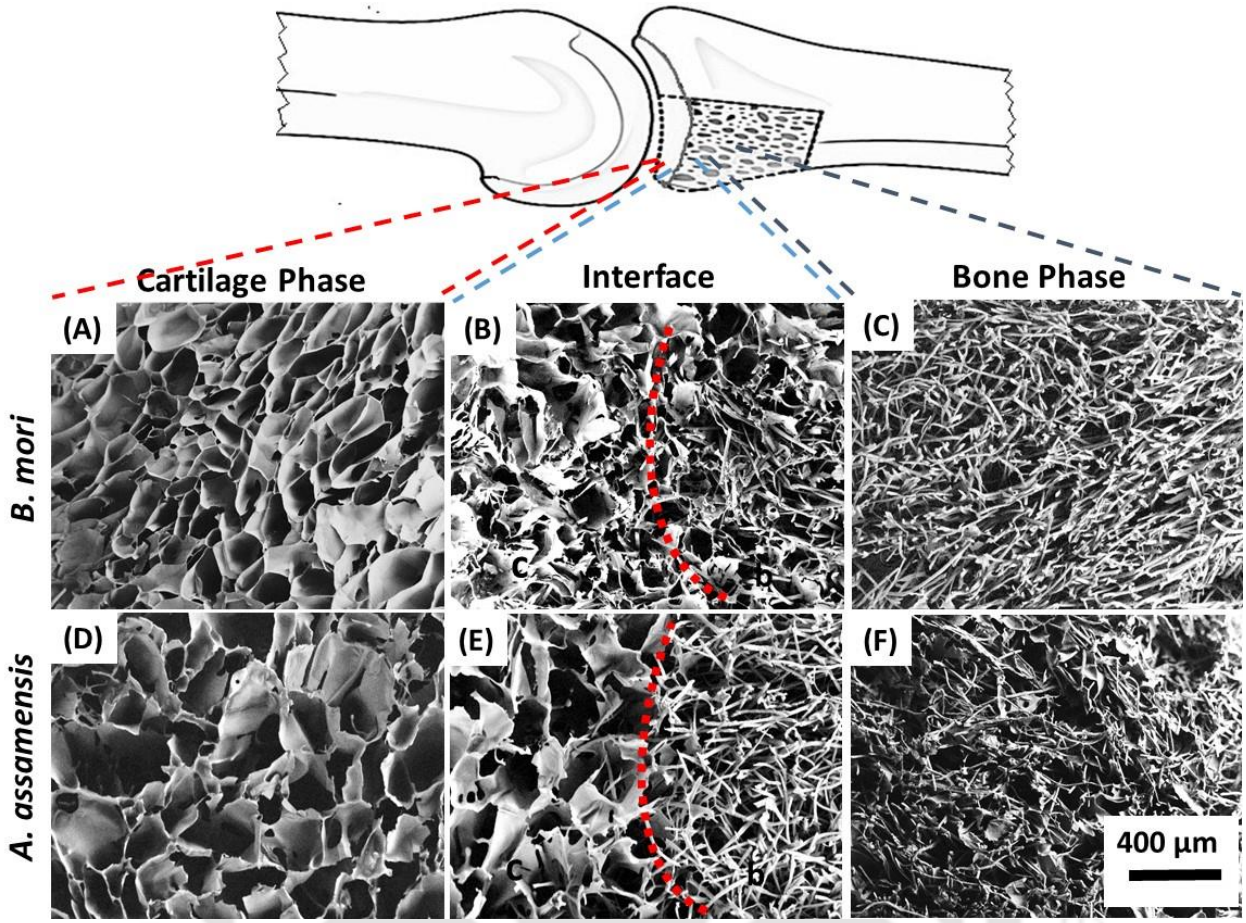

Figure 4.1. *Field emission scanning electron micrographs of the biphasic scaffold showing (A, D) cartilage phase, (B, E) interface region (c-cartilage, b-bone phase) and (C, F) bone phase. Scale bar = 400 µm.*

Table 4.1. Porosity of the scaffolds as determined by liquid displacement method.

Scaffold type	**Porosity %**
B. mori solution (BMS)	90.32 ± 2.31
A. assamensis solution (AAS)	93.53 ± 2.12
B. mori fiber-reinforced (BMF)	80.51 ± 1.36
A. assamensis fiber-reinforced (AAF)	82.41 ± 1.65
B. mori Interfacial (BMI)	87.43 ± 2.03
A. assamensis Interfacial (AAI)	89.49 ± 3.41

4.3.2 *In vitro* swelling and degradation assessment

All the scaffolds showed swelling behavior under PBS (pH 7.4) simulating physiological like conditions. The swelling equilibrium was reached in 4-5 h with rapid maximal swelling in the first 30 min, finally attaining a swelling ratio of 28. The fiber-reinforced composite silk scaffolds (BMF and AAF) showed reduced swelling ratio when immersed in PBS as compared to fiber-free scaffolds (BMS and AAS). The swelling ratio of biphasic scaffolds (BMI and AAI) showed moderate swelling between the fiber-reinforced and the fiber-free scaffolds (**Figure 4.2A**). Among the silk varieties, *B. mori* silk scaffolds showed higher swelling as compared to the *A. assamensis* silk scaffolds. The BMS scaffold showed the highest swelling ($p \leq 0.01$) compared to other scaffolds. Similarly, AAS and BMI showed significantly higher ($p \leq 0.05$) swelling as compared to BMI, BMF, and AAF.

In vitro degradation study using protease enzyme, was performed by monitoring the loss in weight of scaffolds during its incubation for 21 days. For control, scaffolds were treated with only PBS (pH 7.4). The control scaffolds kept in PBS showed no significant degradation over 21 days. However, on incubating with protease, the scaffolds underwent significant degradation ($p \leq 0.01$) as evident from the loss of mass (**Figure 4.2B**). After 21days of enzymatic treatment, the BMS and AAS showed 76% and 55% mass loss respectively. The fiber-reinforced scaffolds BMF and AAF showed 62% and 46% mass loss respectively. The biphasic scaffolds, BMI and AAI showed 56% and 47% mass loss respectively. The *B. mori* silk scaffolds showed higher degradation compared to *A. assamensis* type.

4.3.3 Mechanical testing

The mechanical profile of the biphasic scaffold under compression was displayed by its stress-strain curve (**Figure 4.2C**). The initial linearity of the curve was replaced by a plateau, indicating elastic deformation followed plastic deformation, in the course of yielding, in the fiber-free silk scaffold. Subsequently, silk scaffold densification with compressive load transfer to the fiber-reinforced scaffold was observed. The fiber-reinforced scaffold exhibited remarkable load-bearing ability, clearly delineated by the extensive area under the relevant section of the stress-strain curve. At the end of compression testing, no signs of structural deformation between the phases were seen in the scaffolds indicating that the biphasic scaffold maintained its structural integrity. The compressive modulus values of 3 ± 0.5 kPa, 7 ± 1 kPa for the BMS and AAS scaffolds, and 57 ± 4 kPa and 81 ± 5 kPa for the BMF and AAF scaffolds were observed, respectively. The biphasic

scaffolds displayed an intermediate compressive modulus of 17 ± 3 kPa and 39 ± 4 kPa for BMI and AAI, respectively (**Figure 4.2D**).

Further, biphasic scaffolds were tested in tension to determine the interfacial bonding strength between the two phases (**Figure 4.2E-F**). As the biphasic scaffold was pulled in tension, an incipient elastic deformation was observed continuing till the yield point, which was followed by plastic deformation until the breaking point. The breakage was visible in the fiber-free region of the biphasic scaffold in all samples (**Figure 4.2G**). It is penitent to note that the biphasic scaffolds did not yield at the interface, indicating a robust interfacial binding and visibly no delamination between the two phases. The tensile extension at maximum load was found to be 17 ± 2 kPa and 26 ± 2 kPa for BMI and AAI, respectively; while the tensile strain at elongation was found to be 16.65 ± 1.90% and 25.66 ± 1.57%, respectively. **Table 4.2** summarizes the mechanical behavior of the biphasic scaffolds.

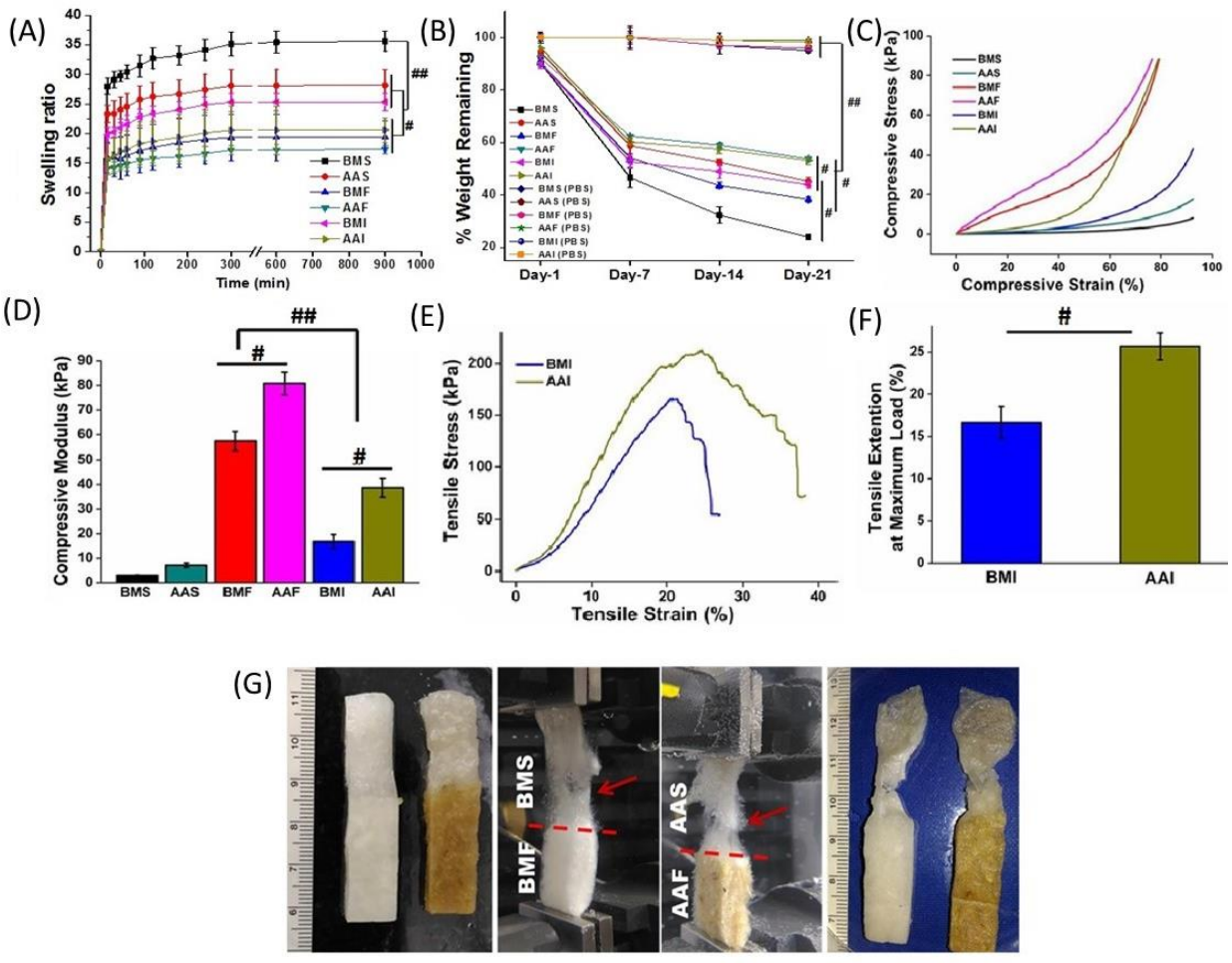

Figure 4.2. *(A) Water retention capability of scaffolds, (B) degradation profile of various scaffolds in the presence of protease enzyme/PBS. Mechanical behavior of the scaffold was determined in compression and tension, where (C) compressive stress-strain curve, (D) compressive modulus, (E) tensile stress-strain curve, (F) tensile extension at maximum load, and (G) gross morphology of the biphasic scaffolds undergoing deformation in tension. Data are represented as mean ± standard deviation ($^{\#}p \leq 0.05$ and $^{\#\#}p \leq 0.01$).*

Table 4.2. Mechanical properties of the biphasic scaffold.

Sample	Compressive Modulus (kPa)	Young's Modulus (MPa)	Tensile Stress at Yield (MPa)	Tensile Strain at Elongation (%)
BMI	16.87 ± 2.81	1.27 ± 0.28	0.12 ± 0.02	16.65 ± 1.90
AAI	38.69 ± 3.81	5.61 ± 0.13	0.23 ± 0.05	25.66 ± 1.57

4.3.4 Cell viability and proliferation

Chondrocyte and osteocyte viability, proliferation, localization status were tested in the scaffolds using live/dead assay. The fluorescent images obtained showed live (green) cells when cultured on scaffolds over a period of 14 days (**Figure 4.3A**). All scaffolds showed uniform cellular distribution and displayed their characteristic morphology throughout the culture conditions. The *A. assamensis* silk scaffolds displayed higher live cell density in comparison to the *B. mori* scaffolds. No cell death was observed within scaffolds evident from the absence of dead red cell population. The uniform cellular distribution was further confirmed by Hoechst 33342 staining, which stains the nucleus (**Figure 4.3B**). The biphasic scaffold shows a clear interface where the fiber-free and the fiber-reinforced phases formed a mesh.

Alamar blue assay was performed to assess cellular proliferation on the scaffolds after 14 days. The scaffolds seeded with cells showed a reduction in alamar blue corresponds to cell metabolism which can be correlated with cell population. The control scaffolds were seeded independently with either chondrocytes or osteoblasts while the biphasic scaffolds were co-cultured with both the cell types. Higher proliferation was observed in all the scaffolds on day 14 as compared to day 1 (**Figure 4.3C)**. The culture of chondrocytes showed significantly higher proliferation ($p \leq 0.01$) in the *A. assamensis* scaffolds as compared to the *B. mori* counterpart while the culture of osteoblasts

indicated significantly higher proliferation ($p \leq 0.01$) in the fiber-reinforced scaffolds as compared to the fiber-free scaffolds. The co-culture of chondrocytes and osteoblasts on the biphasic scaffolds showed significantly higher cellular proliferation in the *A. assamensis* composite and compared to the *B. mori* type. Thus, it was observed that the chondrocytes preferred the fiber-free scaffolds while osteoblasts showed enhanced proliferation on the fiber-reinforced scaffolds.

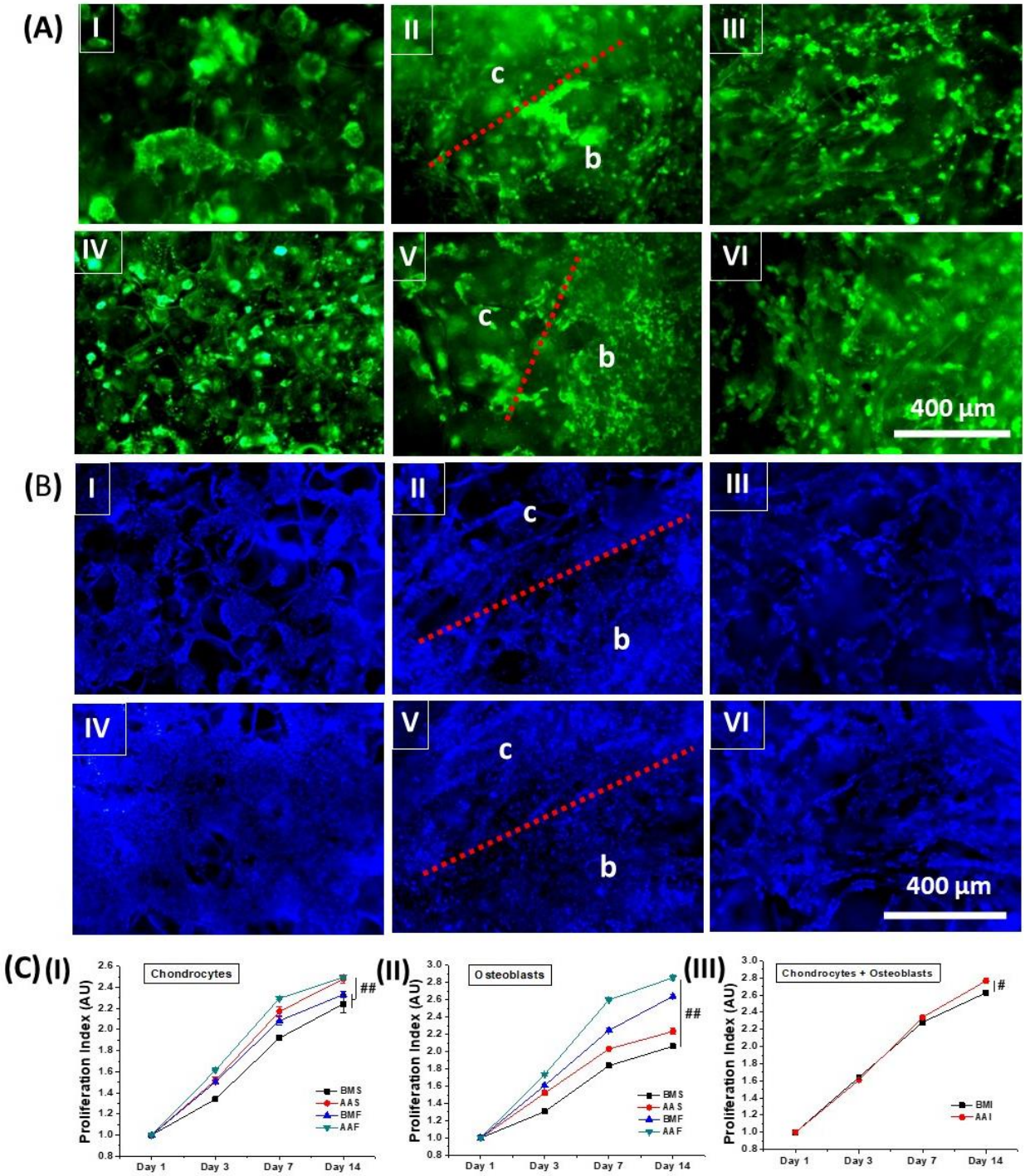

Figure 4.3. *(A) Live/dead fluorescence images and (B) Hoechst staining showing the viability of chondrocytes and osteocytes on the scaffolds after 14 days. (I-BMS, IV-AAS) Cartilage phase, (II-BMI, V-AAI) interface region (c-cartilage, b-bone phase) and (III-BMF, VI-AAF) bone phase. Scale bar = 400 µm. (C) Proliferation graph of (I) chondrocytes (II) osteoblast and (III) co-culture of chondrocyte and osteoblast at various time points determined by alamar blue assay. Data are represented as mean ± standard deviation ($^{\#}p \leq 0.05$ and $^{\#\#}p \leq 0.01$).*

4.3.5 Biochemical assessment

ALP, a primary osteogenic phenotype marker, also shows clear involvement in the primary steps of bone extracellular matrix mineralization [334]. The functional activity of osteoblast cells on scaffolds was determined by quantifying their ALP activity (**Figure 4.4A I**). In our study, higher ALP activity was observed in all scaffolds on day 14 as compared to day 1. Interestingly, the quantum hike in ALP activity for *B. mori* silk scaffolds showed a significant increase in all cases ($p \leq 0.05$) as compared to the *A. assamensis* silk scaffolds.

DNA content increased significantly in all the scaffolds on day 14 (~3 fold) as compared to day 1 ($p \leq 0.01$) (**Figure 4.4A II**). No significant difference in the DNA content of the monophasic scaffolds (BMS, AAS, BMF, and AAF) was observed; however, among the biphasic scaffold, AAI showed significantly higher DNA content as compared to BMI ($p \leq 0.05$). Concurrently, the total sGAG content (in secreted media and scaffold) increased on day 14 as compared to day 1 ($p \leq 0.01$). On day 14, the sGAG content of the fiber-reinforced scaffolds was higher compared to that of the fiber-free scaffold ($p \leq 0.01$). The sGAG content of the biphasic scaffolds was significantly higher than other scaffolds ($p \leq 0.01$). Among the biphasic scaffold, AAI scaffold showed higher (~1.2 fold) secretion of sGAG compared to that of BMI ($p \leq 0.05$). sGAG in medium constituted 25–30% of the total secreted sGAG (**Figure 4.4B**). The discrepancies due to cell seeding were minimized by normalizing total sGAG per unit of DNA, which showed an increment on day 14 compared to day 1. On day 14, sGAG content per DNA in biphasic scaffolds was significantly higher compared to other monophasic scaffolds ($p \leq 0.01$). Individual scaffold mass effect on the growth and maturation of chondrocytes was assessed by normalizing total sGAG content with scaffold mass. sGAG content normalized to scaffold mass showed a similar trend, where biphasic showed significantly higher content compared to all other monophasic scaffolds ($p \leq 0.01$). Overall, the biphasic scaffolds, particularly AAI, showed sGAG content significantly higher than other scaffolds. The total collagen content in all scaffolds increased on day 14 (~6 fold) as

compared to day 1 ($p \leq 0.01$). Collagen content in biphasic scaffolds was significantly higher (~1.3-fold) compared to all other monophasic scaffolds (**Figure 4.4C**) ($p \leq 0.05$). Among the biphasic scaffolds, no significant difference was observed. Normalized collagen content per DNA and scaffold mass showed a similar trend, where the biphasic scaffolds exhibited significantly higher collagen content than the other scaffolds ($p \leq 0.05$). No significant difference among the monophasic scaffolds was observed.

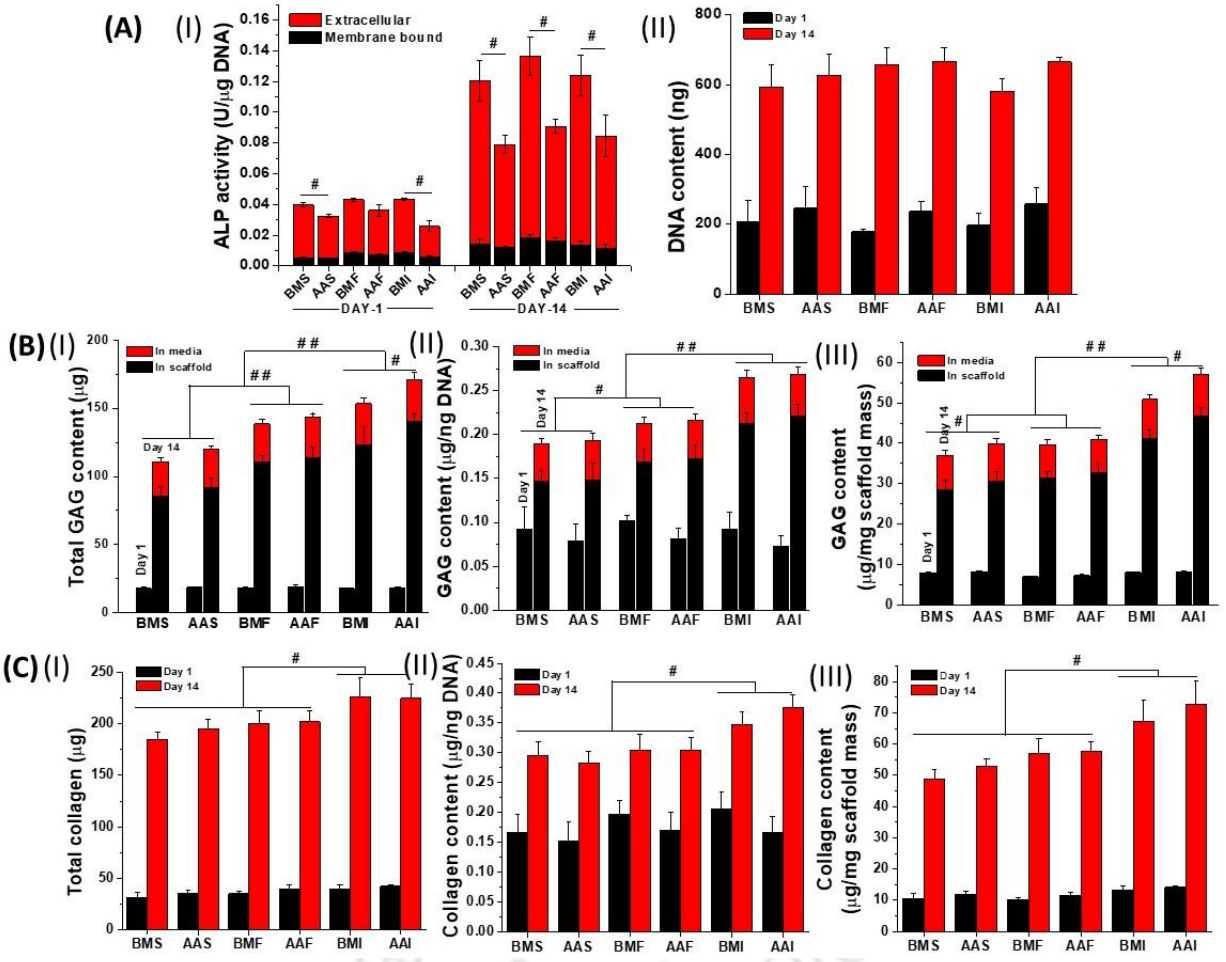

Figure 4.4. *Biochemical assessment of constructs showing (A) [(I) ALP activity and (II) DNA content], (B) [(I) total GAG, (II) GAG per DNA, and (III) GAG per scaffold mass], and (C) [(I) total collagen, (II) collagen per DNA, and (III) collagen per scaffold mass]. Data are depicted as mean ± standard deviation, n = 3 ($^{\#}p \leq 0.05$, $^{\#\#}p \leq 0.01$).*

4.3.6 *In vitro* histological assessment

After 14 days of culture *in vitro*, histological profile was assessed with relevant stains. H&E staining used to study for cell attachment and distribution showed that the stained transverse sections presented a homogenous distribution of cells in the scaffolds. ECM deposition on the

scaffolds were located using cell-specific stains; thus alcian blue was used to detect sGAG secreted by chondrocytes and alizarin red for calcium deposited by osteoblasts (**Figure 4.5A**). The BMF and AAF scaffolds displayed red areas of mineral deposits which were meshed well inside the matrix. The biphasic scaffolds attested differential and spatial support of both the cell types at distinct regions, as indicated by the differential stain uptake, of deep red colorant in the fiber-reinforced section and solid blue intensity in the fiber-free section.

4.3.7 Gene expression analysis

Real-time PCR studies were employed 14 days after cell culture on scaffolds, to study the expression of cartilage and bone-specific genes. Greater up-regulation of cartilage-specific genes *ACAN* and *Sox-9* (**Figure 4.5B I-II**) was observed in cells seeded on biphasic scaffolds (~2-fold increase in sox-9 expression and ~2.3-fold increase in *ACAN*) in comparison to other scaffolds ($p \leq 0.05$). Concurrently, up-regulation of bone-specific gene osteopontin (**Figure 4.5B III**) increased in cells seeded on biphasic scaffolds in comparison to monophasic scaffolds. The expression of osteopontin in case of cells seeded on biphasic scaffolds was significantly higher (~5 fold) than the fiber-free scaffolds ($p \leq 0.05$). In case of *RunX2* (**Figure 4.5B IV**), the expression for biphasic scaffolds was ~3 folds higher than fiber-free scaffolds ($p \leq 0.05$). When expression of bone-specific genes was compared, the resultant values were insignificant. It is important to note that heightened expression of both chondrogenic and osteogenic genes was recorded from cells cultured in biphasic silk scaffolds and not from monophasic silk scaffolds.

4.3.8. Macrophage stimulation and determination of TNF-α release

Macrophages are the primary source of pro-inflammatory mediators like TNF-α which plays a crucial role in inflammation and regulation of the immune response. Thus, TNF-α release after a 24 h exposure of scaffolds to murine macrophage cells (RAW 267.4), was used as an *in vitro,* quantifiable assay for scaffold immunogenicity. **Figure 4.5C** data confirmed that the scaffold immune response was not only much lower than positive controls but compared favorably with the TCP of negative controls. This marked the scaffolds as ready for use, non-immunogenic constructs that could be successfully transplanted *in vivo*.

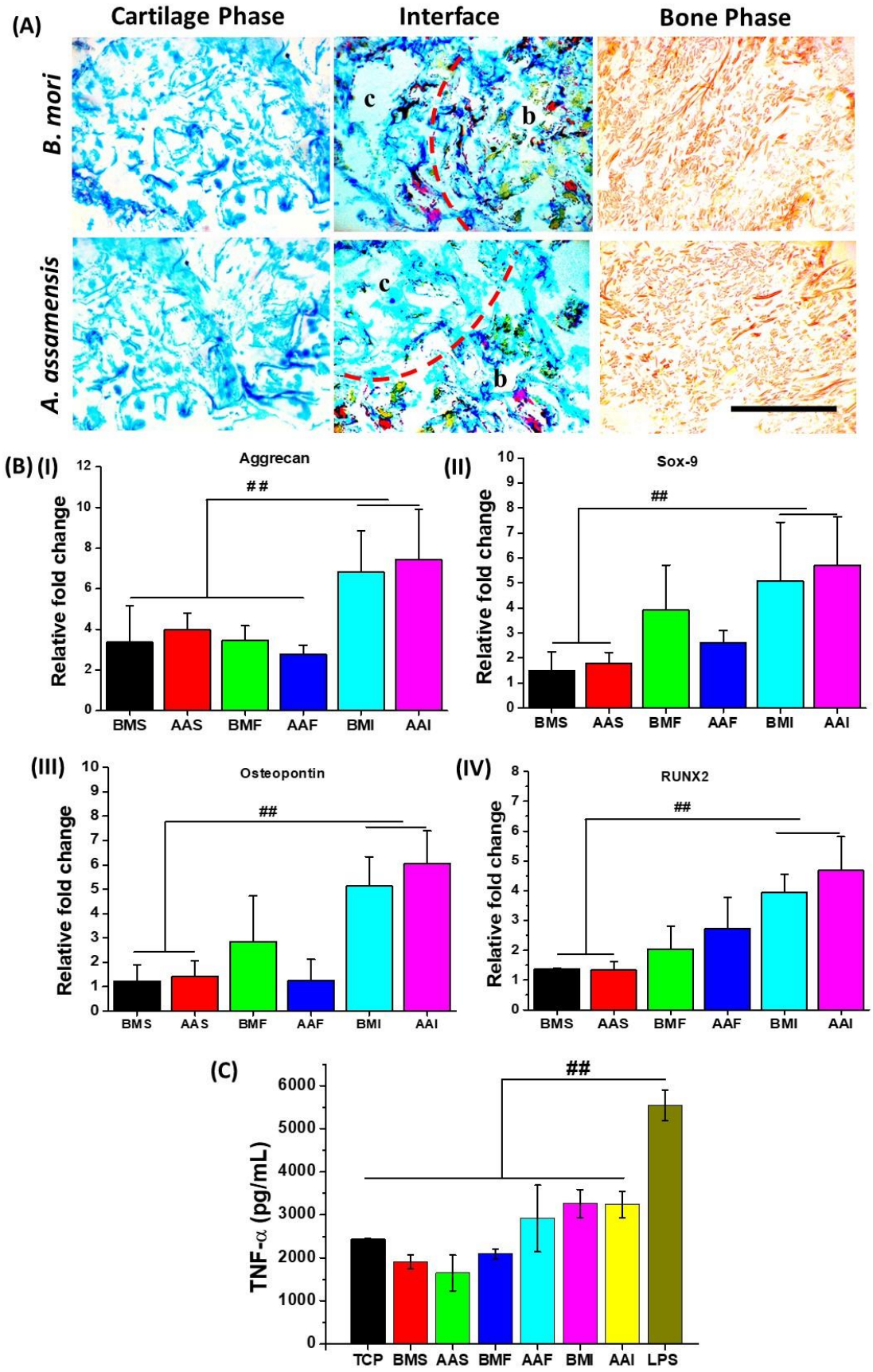

***Figure 4.5**. (A) In vitro histological study showing differential staining of the scaffolds with alcian blue and alizarin red (c-cartilage, b-bone phase), Scale bar = 400 µm. (B) Gene expression analysis of cartilage and bone-specific genes after 14 days of culture where, (I) aggrecan, (II) Sox-9, (III) osteopontin and (IV) RunX2. (C) In vitro immune response assessment of scaffolds by measuring TNF-α release from murine macrophage RAW 264.7 cells after 24 h. Data are shown as mean ± standard deviation, n = 3 ($^{\#\#}p \leq 0.01$).*

4.3.9 *In vivo* assessment of biphasic scaffold

4.3.9.1 Macroscopic evaluation

The parameters such as inflammatory response, disability or deterioration were absent in all joints, as confirmed by macroscopic assessment. The regenerated tissues were observed to fill in the defective areas, with surface dents clearly visible (**Figure 4.6**). In the experimental group containing the biphasic scaffolds, no osteochondral composites detachment was found after 8 weeks of surgery. At 8 weeks post-surgery, the defect areas were evidently lower in comparison to neighboring areas of native cartilage. A clear neocartilage cover and comparatively smooth exterior were observed in the defects of the experimental groups.

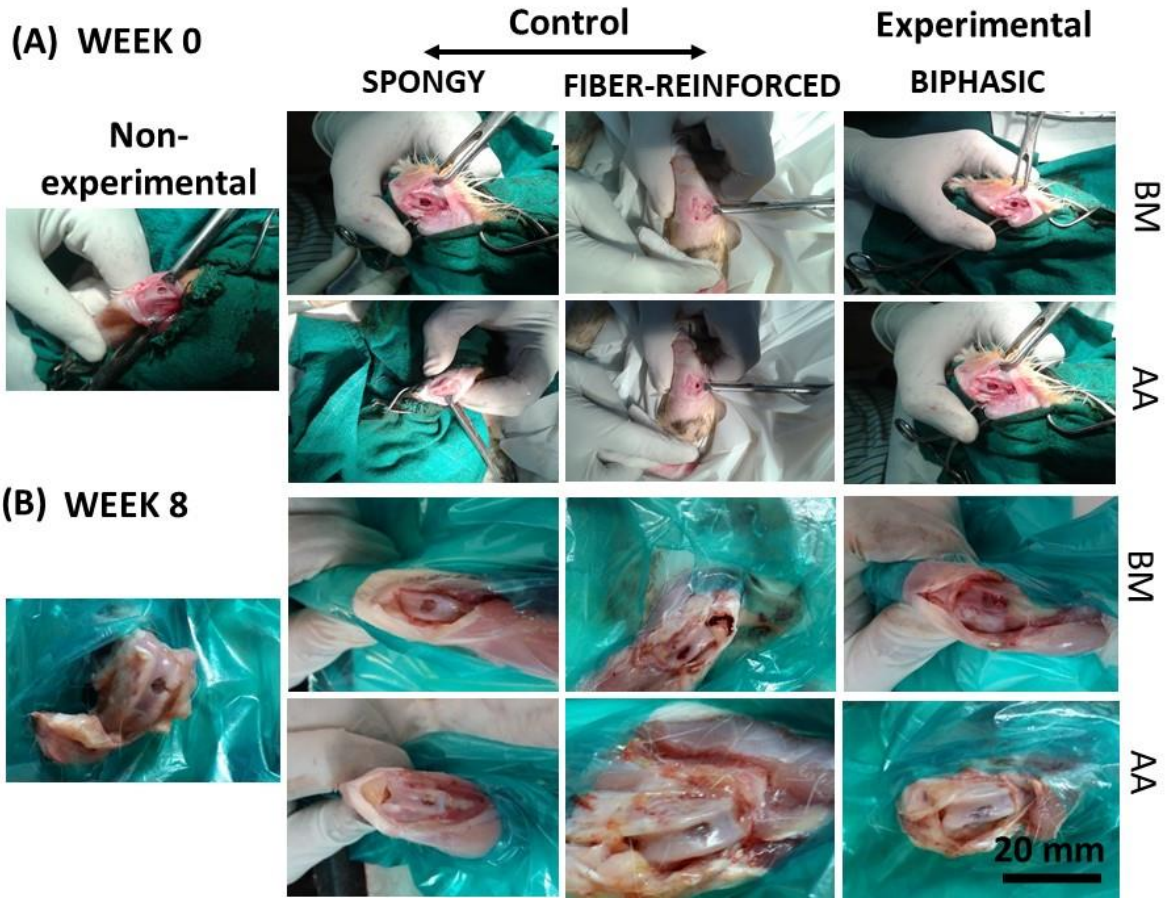

Figure 4.6. *Implantation surgery. An osteochondral defect (diameter = 4 mm; depth = 4 mm) was generated in the rabbit knee femoral intercondylar notch surface and the prepared biphasic scaffold inserted into the defect. The implanted scaffolds were assessed after 8 weeks. Scale bar = 20 mm.*

4.3.9.2 *In vivo* histology

All histological specimens were harvested successfully and subjected to H&E, alcian blue and alizarin red staining to confirm the presence of ECM components in the neocartilage. In less than 8 weeks of implantation, most of the biphasic scaffold materials were resorbed, and manifestation of regenerated osteochondral tissue was observed, with no evidence of deterioration seen at the defect site. Thus, histological and macroscopic evidence corroborated the superior qualities of the experimental group against the qualities of the control groups.

After 8 weeks of surgery, the H&E staining revealed the infiltration of cells in both the phases of the experimental group (**Figure 4.7A**). Further, the alcian blue stained cartilage area and the alizarin red bone area helped to establish a clear tissue demarcation. The control (non-treatment) group exhibited single tissue occupancy, mostly occupied by either of the cartilage or the bone tissue (**Figure 4.7B**) with no clear-cut interphase. The real effectiveness of the differential staining was visible in the experimental group with its clear demarcation of the unbroken osteochondral interface, attesting to the seamless integration of neocartilage, regenerated cartilage, and subchondral bone. Consequently, the even and homogenous neocartilage surface morphology confirmed the similarity of repaired tissue of the experimental group with the native articular tissue. Furthermore, the differential stain indicated a visible fusion of neocartilage with the regenerated cartilage and subchondral bone joined at a clear tidemark attesting the success of creation of an intact osteochondral interface.

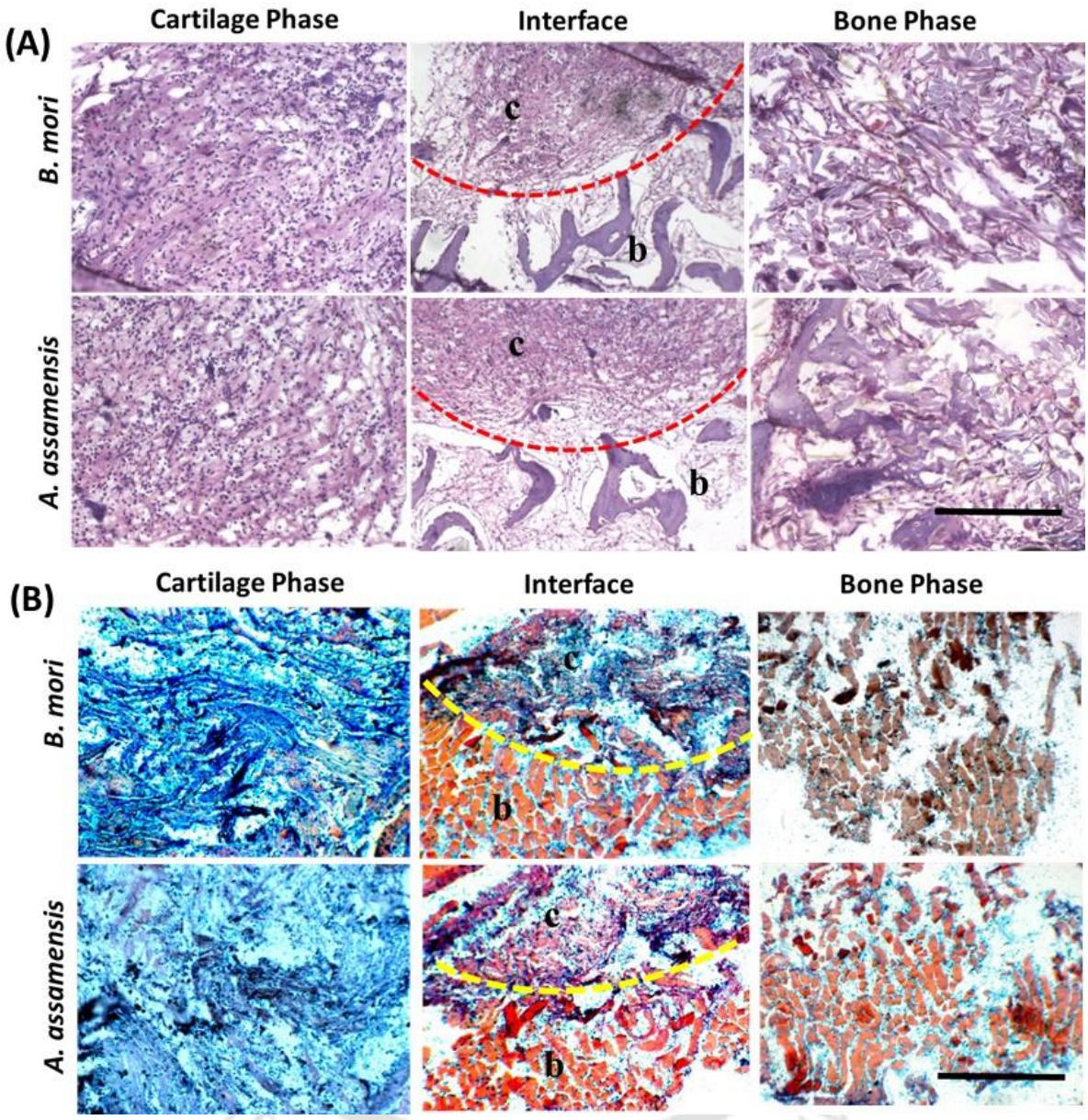

Figure 4.7. *Histological assessment of the constructs in vivo. (A) Haematoxylin & Eosin-stained images and (B) differential staining with alcian blue for the cartilage phase and alizarin red for the bone phase and presence of both at the interface region (c-cartilage, b-bone phase). Scale bar = 400 µm.*

4.3.9.3. Micro-CT evaluation

Evaluation of the extent of regeneration, post 8-weeks of surgery, was carried out by micro-CT scanning of individual regions of interest (ROI), derived from initial areas of injury. The obtained results of the micro-CT analysis showed extensive bone repair within the subchondral region of operated knees by 8 weeks post-surgery. **Figure 4.8A** shows the whole bone that was scanned

giving an overview of the location of the defect. **Figure 4.8B** shows a sub-volume around the defect. The yellow areas show the bone volume in the defect, the brown is the volume surrounding the bone, and the blue is the volume of interest (VOI) used for analysis. **Figure 4.8C** shows the actual new bone formed in the VOI. By this data, the BV/TV and BMD were calculated.

Evaluation of control versus experimental 3D reconstructions exhibited sparse, fresh bone regeneration in the former against robust bone formation in the latter. The regeneration showed definitive regional localization by being restricted to the subchondral region of the operated area and not reaching into the overlying cartilage. Concurrently, the control groups also showed proper regeneration of the subchondral bone, however, in their case the regenerated bone was not limited to the lower subchondral bone region but was distributed throughout the defect. Quantification of bone formation through bone volume/total volume (BV/TV) and bone mineral density (BMD) of the experimental and control groups are shown in **Figure 4.8D**. Among the control groups, the fiber-reinforced scaffolds exhibited higher BV/TV (12% for AAF and 10% for BMF) than those of the fiber-free scaffolds (8% for AAS and 7% for BMS). The experimental groups exhibited an intermediate BV/TV levels (10% for AAI and 8% for BMI). The BMD of the control and the experimental groups were in the range of 600-700 mg HAp/cm^3. The results indicate the regeneration of subchondral bone in the biphasic scaffolds to be most suitable for reconstruction of the damaged osteochondral joint.

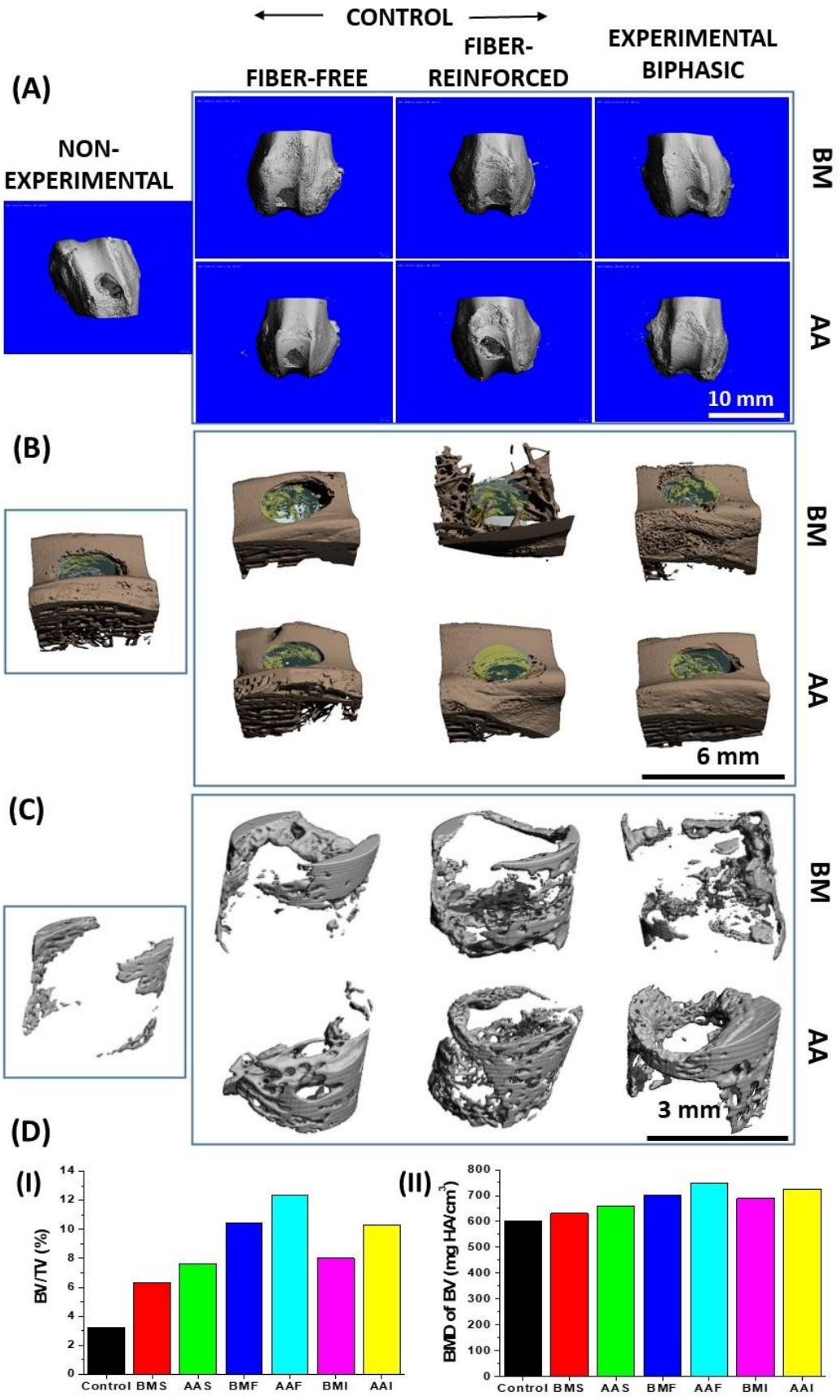

Figure 4.8. *Micro-CT generated representative images for the regeneration of subchondral bone after 8 weeks of implantion. (A) Morphological analysis showing the site of implant; (B) 3D reconstructed images of the area in and around the volume of interest (VOI); (C) the actual bone volume formed in the VOI; (D-I) BV/TV and (D-II) BMD results of the regenerated subchondral bone as quantified using micro-CT.*

4.4 Discussion

A range of strategies developed for repair of OC defects [321, 325], have contributed to the fabrication of biomimetic biphasic scaffolds [110, 338, 339]. Several factors like insufficient interphase integration, low adhesion at the implant site, delamination at the interface post-implantation, and immunogenic issues still limit the widespread implementation of the biphasic scaffolds [320, 340]. To target these deficiencies, we designed a scaffold, employing only silk protein and a simple, single step fabrication to actualize a continuous yet biphasic silk scaffolds. The biphasic scaffold was designed to mediate the spatially controlled development of cartilage phase in the fiber-free region and bone phase in the fiber-reinforced region. Its biomedical viability was strengthened by test implantation in a rabbit model as an acellular graft, and the consequent and significant repair of the OC defects.

Silk fibroin was the material of choice due to its high mechanical strength, easy compliance and adaptability in fabrication [76], proven competence for *in vitro* OC construct formation [333], augmented by *in vivo* stability, durability, and biocompatibility [59]. Our material of choice, for the cartilage phase, was endorsed by the well-documented efficiency of silk sponges in chondrogenesis [292, 336]. While the selection of silk fiber for the bone phase was dictated by the evolving hypothesis of chondrogenesis being mediated by the subchondral bone in the OC milieu [110] which in turn would be a vital anchor in cartilage repair. The previously developed silk fiber-reinforced scaffold [341], had proved an able match for the bony phase, with its microstructure configuring a high mechanical strength scaffold; a consequence of silk fiber reinforcement, which resulted in enhanced osteogenic potential. This chosen biphasic scaffold could, therefore, facilitate adequate restoration of the superficial cartilage and underlying subchondral bone in a load-bearing environment while simulating the structural and mechanical characteristics of OC joint. The advantage of using the same silk polymer in the construction of both scaffold phases was evident in the ease of interphase integration. This, in turn, facilitated production of biphasic scaffolds *via* a simple, reproducible and customizable procedure. Further, the dimensions of the scaffolds could

be customized to suit multiple site OC regeneration; expedited by easy and reproducible preparation that accommodated customizing proportions of biphasic and interface components.

The developed biphasic scaffold is a porous matrix with internal interconnected pores formed as a result of a simple freeze-drying approach. The increased interconnectivity between pores could enhance migration of cells toward internal pores. The FESEM studies displayed two distinct phases with markedly specific pore architecture and an obvious interface overlap, characteristic of a two-phase scaffold. The larger pore sizes of 160–200 μm with their high interconnectivity, observed in this silk scaffold, matched the reported pore size range, suitable for cartilage regeneration [258, 292, 336]. In contrast, the fiber-reinforced scaffold of the bone phase had smaller pore sizes of 40–60 μm coupled with high porosity and interconnectivity. Unfortunately, the data for ideal pore size vs. osteoblast activity is not yet unequivocal [342]. In general, scaffolds with pore sizes of about 20 to 1500 μm have been used [342-344]. In our study, we singled out a 40-60 μm pore diameter, based on positive reports linking this pore size with securing both vascularization and diminished non-fibrotic integration inside [108, 345-347]. It is pertinent to note that bone tissue should be highly vascularized, while the cartilage layer should have low vascularity as large pores have been found to lead to low vascularity [348]. Contingent on the silk variety chosen, scaffolds fabricated using *A. assamensis* showed larger pore sizes than the *B. mori*. This difference may be attributed to constituent amino acids of both hydrophobic or hydrophilic synergy and their consequent effect on freeze drying; which was also concurred by other reports [292, 333, 336]. The porosity of the scaffolds is another crucial scaffold parameter in tissue engineering; results of our study indicate porosity values of 90-93% for cartilage phase and 80-82% for bone phase. The obtained results are in accord with an earlier report, where 92% porosity in the cartilage layer and 77% porosity in the bone layer resulted in the best efficacy of the bilayer scaffold [349]. This range of porosity was derived by biomechanical mimicking of the well-hydrated native cartilage with its comparatively lower compressive modulus; whereas the subchondral bone is an area of low hydration, and consequent characteric higher compressive modulus [349].

The twin requirements for success in tissue engineering applications are the water retention and degradability competency of the scaffold. The former serves to minimize nutrients and fluid loss from scaffolds on implantation. The swelling ratio results of our study suggested differential water

uptake ability of the scaffolds were based on their composition. The fiber-free scaffolds for the cartilage phase swelled more while, incorporation of silk fibers in scaffolds for bone phase lowered water uptake capability. Though, fiber-reinforcement may reduce the water uptake capacity, however, it does improve vital mechanical and osteogenic profiles, crucial for bone tissue engineering [238]. These outcomes corroborated earlier investigations on scaffolds where reduction of matrix hydration had been achieved by fiber incorporation [308, 334]. The degradability of the scaffolds was assessed with protease XIV, to attenuate the implant degradation profile, to factor *in situ* degradation and rule out further surgical intervention. Biodegradation that can be tuned or controlled is required to synchronize the rate of new tissue generation with that of scaffold degradation. The indiscriminate and multiple locale silk protein cleaving propensity of protease XIV [262], rendered it ideal for biodegradation profiling. Our study exhibited the majority of degradation in the fiber-free scaffolds belonging to the cartilage phase against the much lower degradation in the fiber-reinforced scaffolds of the bony phase. The biphasic scaffolds showed an intermediate degradation behavior. This indicates that regenerated silk solution has faster degradation rates than native silk fibers. Fiber-reinforced scaffolds had comparatively lower degradation rate due to the presence of silk fibers. These results were consistent with a previous report by Li *et al.*[294].

Assessment of the mechanical properties of scaffold behavior under compression were indicative of their capacity to sustain loads in the osteochondral milieu. The compressive modulus of the fiber-reinforced scaffold displayed 10-fold (in case of *B. mori* scaffolds) and 8-fold (in case of *A. assamensis* scaffolds) increase in comparison to the fiber-free scaffolds. The biphasic scaffolds demonstrated stratified compressive properties and mechanical realignment, which were characteristic of a biphasic structure within the OC strata. The mechanical stability of an implanted scaffold is a significant contributory factor in its regenerative capability. When implanted, the surrounding native tissue is likely to bear the aggregate load; consequently, it must respond with deformation that conforms to the load on the neighboring tissue [350]. The cartilage phase of the biphasic scaffold showed large deformation, whereas the solid bone phase withstood large compressive stresses with minimal deformation while retaining its shape recovery ability upon hydration. The biphasic scaffold did not show any instability or delamination at the interface and matched requirements for tissue regeneration concurrent with loads encountered or developed in load-bearing conditions.

Subsequently, the interfacial bonding strength within the biphasic scaffold was examined under tension. As the scaffold was pulled in tension, the fiber-free soft cartilage phase displayed impairment. The tensile stress at yield was measured to be 0.12 ± 0.02 MPa and 0.23 ± 0.05 MPa for BMI and AAI scaffolds, respectively; while the strain at elongation was 16% and 25% for BMI and AAI scaffolds, respectively. The higher tensile strength and mechanical characteristics of *A. assamensis* scaffolds might be attributed to its higher poly-alanine repeats; whereas the higher poly glycine-alanine repeats of the *B. mori* silk do not seem to confer the same advantages [351]. The tensile properties of our biphasic scaffolds compared well with the yield strengths of other composite scaffolds [333, 352]. The higher interfacial bonding of our biphasic structure may be attributed to the fabrication procedure resulting in a continuous matrix made of a single polymer. This allowed sufficient interphase bonding and interphase resistance to shear stress in the joint under physiological conditions.

Articular cartilage and subchondral bone demand diverse microenvironments for cellular growth and development. The use of biphasic scaffold with unique micro spatio-architecture intended to provide a conducive environment for culture and maintenance of cells. Thus, as a biomimetic model, primary chondrocytes were used for the cartilage phase while osteoblast cells were used for the bone phase. The cellular co-culture model for the biphasic scaffolds is vital for tracking inter-cell activity and was examined using live/dead staining. The resultant cell attachment and multiplication, showed greater population of living cells within the *A. assamensis* scaffolds, in comparison to the *B. mori* scaffolds. Further, neither scaffold exhibited any apparent cytotoxicity. The co-culture system on the biphasic scaffolds promoted proliferation of both cell varieties, with no adverse effects observed over the period of 2 weeks. Further, the cell proliferation evidenced through alamar blue assay attested chondrocytes preferred the fiber-free cartilage phase while osteoblasts the fiber-reinforced bone phase. However, scaffolds fabricated using *A. assamensis* silk supported significantly higher cellular proliferation than that of *B. mori* variety. This could be attributed to the intrinsic tripeptides–RGD on the N and C terminals of glycine-rich G-motif in case of *A. assamensis* [247] [182].

Marker protein profiles were tested by biochemical analysis to evaluate the progression of chondrogenesis and osteogenesis. Concurrently. ALP activity is often evaluated in studies investigating the osteoconductive potential of a matrix. Our results showed increased bone

mineralization over the 2-week period. Also, it is of interest that, the *B. mori* silk scaffolds showed higher ALP activity compared to its *A. assamensis* counterpart. This could be an outcome of ALP secretion, stimulated by cessation of pre-osteoblasts proliferation. Subsequently, this stimulus triggers the formation of active osteoblasts enriched in ALP, and secretion of bone matrix proteins including collagen I and other non-collagenous proteins [353]. This was in agreement with the alamar blue assay that showed higher cellular proliferation in the *A. assamensis* silk scaffolds and consequently, lower ALP secretion. Again, the co-culture of chondrocytes and osteoblasts might have influenced this result. Additionally, a balance in ALP secretion is vital to bone formation and metabolism [354].

Sulphated GAG, a cardinal ECM cartilage component, secreted by chondrocytes, reflects the chondrogenic potential of the scaffolds. The sGAG varied significantly, with the fiber-reinforced scaffolds exhibiting higher levels in comparison to fiber-free scaffolds. The biphasic scaffolds, where the cells were co-cultured showed a higher increase in sGAG after 14 days. The biphasic scaffold fabricated using *A. assamensis* silk showed the highest content of sGAG. Chondrocytes often drive multiple integrin receptor families towards homeostasis; further, the high percentage of RGD tripeptide in the *A. assamensis* scaffolds may offer more integrin binding sites that in turn stimulate intracellular signaling and subsequent ECM production [355]. The terminal maturation of the OC tissue is characterized by an upward trend in the deposition of minerals for matrix formation, with a concomitant increase in deposition of collagen. Collagen levels peaked in the biphasic scaffolds during chondrocytes and osteoblasts co-culturing, concurrent with sGAG results.

The competence of the seeded cell constructs for chondrogenesis and osteogenesis was estimated by assaying marker genes- aggrecan and Sox-9 for chondrogenesis, and osteopontin and runx-2 for osteogenesis. The increased expression of Sox-9, an initial chondrogenic indicator, demonstrated the propensity towards chondrogenesis. Similarly, the increased level of expression of aggrecans matches the increased amounts of sGAG documented in the composite scaffolds. Aggrecans are vital in bringing together sGAGs and chondroitin sulfate for the cartilaginous matrix template, through functional cluster development *via* chondrocytes condensation [333]. Furthermore, higher up-regulation of bone-specific gene osteopontin and runx-2 were found in cell-seeded biphasic scaffolds compared to other monophasic scaffolds. High expression levels of

runx-2 attested to the fact that osteoblasts were potentially primed towards a differentiating phenotype while conserving their osteogenic fate. This was crucial in establishing a viable population of committed osteoblasts for better matrix turnover. Higher expression levels of osteopontin, an early-mid stage marker, is primarily expressed during the phase of active proliferation and helps in cell attachment and apatite nucleation initiation [334], which concurred with the runx-2 experiment findings. Therefore, the seeded cell types successfully exhibit the continuity of both chondrogenic and osteogenic phenotypes.

Cartilage degradation associated with chondrocyte catabolism and hypertrophy alone was initially thought to be the characteristic feature of OA [356]. However it is now recognized that in addition to the articular chondrocytes intricate crosstalk between other cell types such as the osteoblasts, osteoclasts, synovial cells and other tissue resident immune cells [44] also contributes to the pathological mechanism [32, 357]. Recent reports suggest that several critical signaling pathways and biological factors are key regulators and activate cellular and molecular processes in crosstalk in the articular joint microenvironment. Some of them including HIF-2α, OPG/RANK/RANKL, TGF-β and Wntβ-catenin may play regulatory roles in OA progression and homeostasis of the neighbouring tissues [357]. Sanchez *et al.* showed that in co-culture, sclerotic subchondral osteoblasts decrease Sox-9, Col-II, PTHrP and PTH-R gene expression by chondrocytes but increase that of OSF-1 indicating a transition in chondrocyte phenotype towards hypertrophic differentiation and subsequent matrix mineralization [358]. In the current study, we observed that the differential bulk matrix stiffness presented by the silk matrices enabled in differentially maintaining the chondrocyte and osteoblast maturation. Chondrocytes and osteoblasts are very sensitive to their pericellular matrix microenvironment and hence biophysical cues are of utmost importance which govern their cellular fate [359, 360]. Moreover, another plausible reason is the presence of RGD in non-mulberry matrices which could have led to the activation of Wnt/β-catenin pathway through integrin/FAK mechanism [361]. However, the complete understanding of this crosstalk at the bone–cartilage interface mediated through these silk matrices requires additional evidence at the molecular level using a more systems biology-based approach involving genomics, epigenetics, proteomics and metabolomics approaches.

Histological examinations were carried out to evaluate the *in vitro* ECM deposition on the matrices. The presence of both alcian blue and alizarin red at the surface of the biphasic scaffolds

indicate that co-culture of chondrocytes and osteoblasts produce an interphase similar to the osteochondral structure, at the region of interaction with the surface. The results also suggest that cells not only retain their phenotypes but also associate positively, in the course of being co-cultured. This interaction makes possible the release of factors by either osteoblasts or chondrocytes, which may impact the reaction of abutting cells and architecture of developing osteochondral interface [362]. Whether cell to cell reactions mediate these events or paracrine signaling, between neighboring populations of chondrocytes and osteoblasts direct operations, is not yet clear.

Any adverse immune response elicited by a biomaterial might lead to an acute response to inflammation, tissue destruction, obstruction in healing, and possible graft rejection [363]. Hence, as a measurable preliminary precaution to *in vivo* implantation, the levels of TNF-α secretion was monitored *in vitro* by exposing the scaffolds to murine macrophage cells. The results showed that all the scaffolds exhibited a negligible immune response, thereby negating disruption by unfavorable immune feedback. Thus corroborating the reports on *in vitro* immunocompatibility [333, 341], that evoked minimal *in vivo* immune response [59, 364]. This set the stage for preliminary adoption of the scaffold for *in vivo* implantation.

The *in vivo* results indicated that the fabrication of an all silk, seamless, biomimetic, biphasic construct for *in vitro* and *in vivo* osteochondral defect repair, had definite advantages, unavailable in contemporary constructs. Driven by our hypothesis that the biphasic scaffolds differentio-spatially dictated the maturation of chondrocytes and osteoblasts to achieve absolute osteochondral interface regeneration, simulating the native conditions. Histological results of the retrieved samples acknowledged the fast rate cell propagation in the experimental cohort within 8 weeks of implantation; in addition, the biphasic scaffold displayed both cartilage and bone phases, with a well-integrated interface. Further, the infiltrating cells seemed to take up specific regional morphologies, characteristics of chondrocytes in cartilage and osteoblasts in the bone region. Again, the formation of thick neocartilage and a clearly delineated bone trabecula in the joint, vindicate the increased neocartilage GAG and collagen levels and correlate it with the superior gross morphology results observed in the experimental group. The quantitative assessment by micro-CT analysis exhibited the ability of the biphasic scaffold to stimulate decidedly enhanced *in vivo* bone growth in comparison to controls and significantly, illustrated the confinement of the

regenerated bone to the subchondral zone. However, these are representative results of the micro-CT experiment, as the analysis was done only for one set of samples and further testing would be required to get statistically significant results. The success of the biphasic scaffolds was due to reasonable cellular proliferation in both the phases of the scaffold at the recipient site, especially in case of the *A. assamensis* biphasic scaffold. The designed layer-definitive mechanical and compositional scaffold characteristics, thus provide unequivocal advantages. Overall, this study demonstrates *in vitro* and *in vivo* proof of concept and the significant promise of utilizing these biphasic scaffolds for osteochondral defect repair.

4.5 Significant findings

1. Herein we report the development of a seamless biphasic scaffold made entirely of silk fibroin (*B. mori* and *A. assamensis*) with a layered structure distinct for cartilage and bone tissues that are conjoined along a homogenous and uninterrupted interface.
2. The fabricated biphasic constructs were porous, with optimal swelling and degradation attributes.
3. The scaffolds supported the simultaneous growth of chondrocytes and osteoblasts by providing a suitable environment for cell attachment, infiltration, and proliferation. The presence of intrinsic RGD motifs in *A. assamensis* silk enabled better cell attachment and proliferation as assessed by live/dead and alamar blue assay.
4. The biphasic scaffold exhibited positive mechanical attributes that sustained regeneration in the demanding load-bearing osteochondral workspace.
5. The biochemical assessments of cell-seeded biphasic constructs showed higher ECM secretion and deposition, where there was increased sGAG, collagen content and ALP activity when compared to control.
6. Gene expression studies within biphasic constructs also revealed upregulation of genes specific for cartilage and bone. Based on the scaffold design and the *in vitro* results we implanted the biphasic scaffold in a rabbit model.
7. The *in vivo* implanted biphasic scaffold triggered analogous and concurrent region-specific reconstruction of bone and articular cartilage as assessed by histology and micro-CT studies. The *A. assamensis* silk based biphasic construct performed better than the *B. mori* counterpart.
8. In conclusion, the *in vitro* and *in vivo* assessment establishes competence of an all silk, seamless, hierarchical, biphasic scaffolds for repair of osteochondral defects.

Chapter 5

Wild Silks Enable Controlled Gelation and Increase Silk Hydrogel Composite Performance

The aim of this study was to gain an understanding into the mechanisms, flow dynamics, and possible interactions generating composite high-performance hydrogels. The structural and thermal properties of various silk types including well-explored domesticated *Bombyx mori*, and unexplored wild type *Antheraea assamensis, Antheraea mylitta, and Philosamia ricini* were studied, and further the performance of the silk-silk blended hydrogels was investigated.

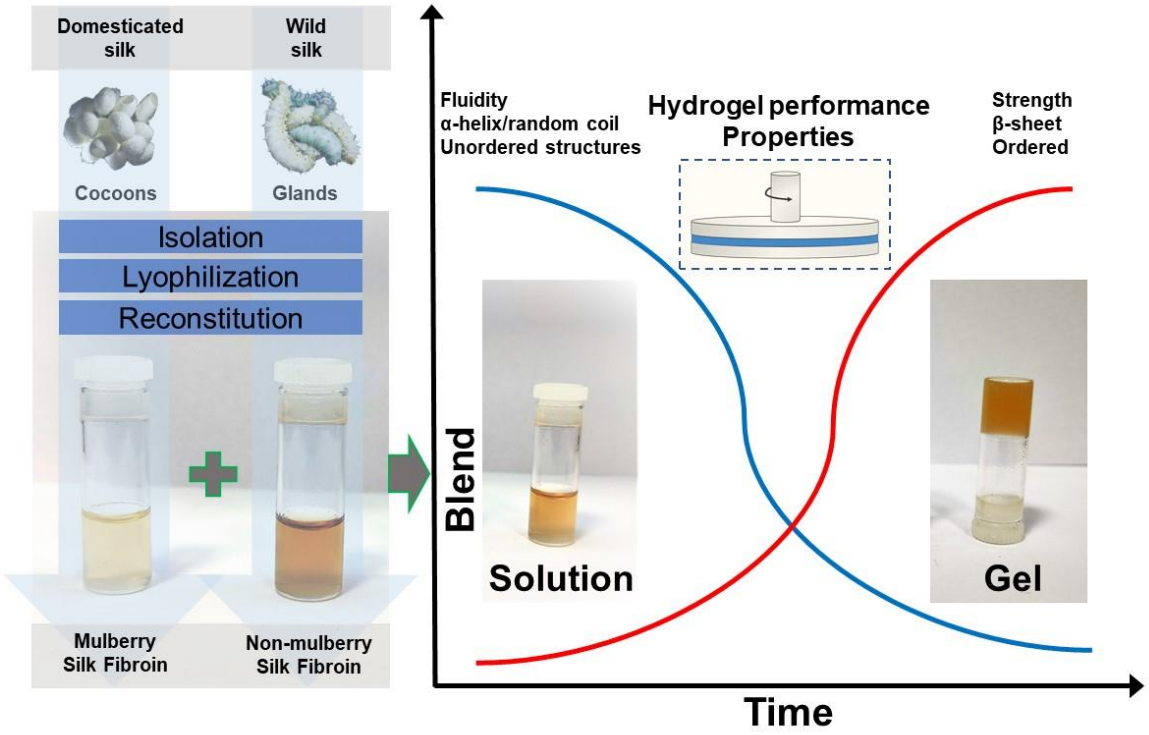

The work embodied in this chapter is submitted for publication as follows:

Yogendra Pratap Singh, Chris Holland, and Biman B. Mandal. "Wild silks enable controlled gelation and increase silk hydrogel composite performance." (*Manuscript under preparation*)

ABSTRACT

Silk fibroin (SF) has gained extensive attention owing to its superior material properties and diverse applications. The biomolecular self-assembly of SF is well studied, however much understanding is required into the molecular mechanisms, flow dynamics, and possible interactions generating these composite high-performance hydrogels. In the current study, we analyzed the structural and thermal properties of various silk types including well-explored domesticated *Bombyx mori,* and unexplored wild type *Antheraea assamensis, Antheraea mylitta, and Philosamia ricini,* and further investigated the performance of the silk-silk blended hydrogels. The individual regenerated SF showed varied characteristics where wild silks were suitable to potentially act as a nucleating agent towards creating more stable blends. The hydrogel dynamics assessed rheologically demonstrated blends with *P. ricini* to be the best activators as shown by the high crystallinity content. The blends with *A. mylitta* formed thermally sensitive hydrogels, which needed to be activated to gel completely, but eventually forming stronger gels; while other silk blends are thermally insensitive thus forming stable gels unaffected by the increased temperatures. The blends of wild-domesticated silk performed better than the wild-wild silk blends and this is majorly influenced by the self-assembly of peptides, driven by hydrogen bonds, physical entanglements, electrostatic interactions, metal-ion interactions, hydrophobic interactions, and tyrosine/phenylalanine stacking. The wild silk-based blending produces composites with increased performance. Thus, the study highlights not only the appropriate combinations of properties to potentially include in future crosslinker-free silk-silk composites but also how those materials self-assemble and develop matrices with tunable properties for tissue engineering applications with advantages of wild silks.

5.1 Introduction

Silk is a natural fibrous biopolymer that has gained worldwide attention and has been in use for centuries in diverse applications [170]. Silk protein is produced by members of the class Arachnida (spiders) and by several species of the order Lepidoptera, which includes silkworms, mites, butterflies, and moths. Among the silkworms, silk from the domesticated *Bombyx mori* (mulberry) of the Bombycidae family is found globally and is well studied, however, the Indian wild varieties (non-mulberry) such as *Antheraea assamensis* (commonly known as Muga), *Antheraea mylitta* (commonly known as Tasar), and *Philosamia ricini* (commonly known as Eri) of Saturniid family are relatively untapped. Structurally, silk is composed of two major proteins: the structural core protein SF (70–80 wt%) and the outer glue-like protein SS (20–30 wt%) which keeps the silk fibers together. For biocompatibility reasons, its processing requires removal of the sericin component, as the two components might be safe to use independently, but a combined silk fibroin-sericin structure can elicit adverse immune response [174, 365]. SF can be isolated directly from silk glands of the silkworms maintaining the native conformation of the protein or from cocoons using various established protocols [76, 366]. However, unlike the conventionally used chaotropic agents like LiBr to solubilize mulberry silk, the process of solubilizing wild silk cocoons is difficult and involves using harsh chemicals resulting in less effective isolation and low yield. Alternatively, SF isolation from glands has been the preferred method. The obtained regenerated silk fibroin (RSF) solution is, however, unstable at lower pH and higher temperature where it starts to gel. The gelation time reduces with decreasing the pH, increase in temperature and protein concentration, and with divalent ions [176]. The gelation of SF is accompanied by the rearrangement of SF molecules from a random coil conformation in the sol state to an antiparallel beta-sheet conformation in the gelled state [367]. In the current study, we have lyophilized the obtained SF solution and stored at lower temperatures, to be used later. Herein, we have shown an added advantage of RSF in terms of its increased shelf life or storage post-freeze-drying and availability as off-the-shelf ready to aqueously dissolve for various applications. This majorly helps manage the unwanted wastage of SF solution due to its untimely gelation.

Structurally, SF polymer is generally composed of repetitive protein sequences which play a crucial role in protective mechanisms such as cocoon formation. SF is majorly found in β-sheet conformation due to dominant hydrophobic domains that allow tight packing of stacked sheets. The presence of larger hydrophobic crystallite domains (composed of β-sheets) interspersed with

smaller hydrophilic amorphous domains (composed of α-helices) allows the assembly of SF and imparts silk its strength and resilience [368]. Silk is reported to display polymorphism, with a pre-crystallization glandular protein (silk I), the β-sheet rich spun state (silk II), and an assembled air/water interface state (silk III) [75]. The silk I state is water-soluble which is converted to silk II upon induction with stimulants such as methanol, ethanol, temperature, salts, and shearing. The SF from mulberry and non-mulberry vary in composition with specific repeating units and secondary protein structures imparting them with unique properties. Typically, SF is a semi-crystalline in nature where the crystallites are distributed in an amorphous milieu [26]. The chemical structure of these silks differs from each other and is highly influenced by the varying amino acid contents. The amino-acid composition of *B. mori* SF includes multiple repeats of $(Gly\text{-}Ala\text{-}Gly\text{-}Ser\text{-}Gly\text{-}Ala)_n$ conferring crystallinity to the structure [179]. Concurrently, the amino acid structure of non-mulberry silk consists of poly-alanine $(Ala)_n$ repeats and is responsible for the higher crystallinity in non-mulberry silks as compared to mulberry. Crystallinity is a vital parameter for the *in vivo* biodegradability of SF matrices, which can be tuned using various treatments. The wild silk has been reported to show improved physicochemical, thermal, and mechanical stability [180, 181]. Another advantage that the wild non-mulberry variety possesses over the mulberry silk is the presence of cell binding tripeptide Arg-Gly-Asp (RGD), which are integrin-binding receptors for cell adhesion mediating better cell-material interaction [182].

The ease of processing and ability of SF solution to be fabricated into various formats such as sponges, mats, hydrogels, films, and nanoparticles is another desired characteristic. Among others, its capability to form hydrogel is of particular interest due to its ability to mimic the native microenvironment along with being biocompatible and biodegradable for their use in biomedical applications [369]. The hydrophilicity and stability of the hydrogels allow them to swell, facilitating nutrients/waste exchange with impetus on water-requisite soft tissue regeneration applications. Silk hydrogels have been used for bioengineering a variety of tissues such as skin [370], pancreas [371], cartilage [336], and intervertebral disc [191]. The studies have reported successful tissue regeneration and shown promising attributes of silk hydrogels however, challenges such as lower mechanical strength and longer gelation time may still need addressing in standalone usage of SF. To do that, it is essential to better understand SF properties, their assembly, the gelation, and their tunability for the betterment. In nature, SF is synthesized in the posterior part of the silk gland which is then stored in the middle part at a high concentration and

then transported to the anterior segment before being spun into fibers [372, 373]. During the process of spinning in the air, the SF protein experiences a structural transition from a dominant α-helix and random coils into β-sheets forming solid fibers. Factors such as pH, metallic ions, and salts along with water content influence this transition [367, 374]. A similar process takes place *in vitro*, during the sol-gel transition and although the natural process is not yet completely recapitulated *in vitro*, these factors do manage and control the solubility and assembly of the protein. Factors such as increased concentration and temperature have been shown to alter the mechanical characteristics of silk hydrogel.

Towards understanding the gelation process and sol−gel transition of SF, various physical and chemical methods have been employed. Methods such as sonication, vertexing, changing pH and temperature and the use of toxic/harsh chemicals might help produce good gels however, they may not be suitable for use in clinical settings. Chemical crosslinkers often result in the lost properties of the involved individual components and may involve the use or release of toxic products which may lead to inflammation and tissue damage [375]. Concurrently, physical crosslinking methods such as chain entanglement, crystallite formation, and hydrophobic interactions and are often preferred due to the absence of possible cytotoxicity due to crosslinkers, the presence of stimuli-responsiveness, and the absence of permanent bonds yet sufficient interactions to form insoluble hydrogels. Towards this, the blending of polymers is an effective approach to form composites with tunable physicochemical properties. Recently, few studies from our group have reported the fabrication of a self-gelling hydrogel formed as a result of blending mulberry and non-mulberry SF [191, 370, 371]. These studies used the rapid gelling property of SF solution, upon blending of *B. mori* and *A. assamensis* for nucleus pulposus tissue engineering, skin regeneration, and islet encapsulation applications.

Taking cues from these reports, the current study focuses to understand the gelation processes and pathways involved upon blending the two silk types and the possible role of wild silk as nucleators in this system. First, the proteinaceous nature and functionality of the regenerated and reconstituted SF solution was established for all the individual silk types. Herein, we have used several structural-thermal protein characterization methods such as Fourier-transform infrared spectrometry (FTIR), sodium dodecyl sulfate-polyacrylamide gel electrophoresis (SDS-PAGE), UV-Visible spectrophotometer, dynamic light scattering (DLS), and dynamic scanning

calorimetry (DSC), to understand their structural-thermal properties along with analyzing the amino acid composition and their enzymatic degradation profiles. Next, the individual silk types were blended and their dynamic profiling was assessed using rheology to understand the possible physical and chemical interactions occurring during this gelation. Herein, the aim was to understand not only the appropriate combinations of biochemical, mechanical, and structural markers to potentially include in future silk-silk composites but also how we can make those materials self-assemble and develop matrices with tunable properties.

5.2 Materials and methods

5.2.1 Preparation of regenerated silk fibroin

Silk cocoons of mulberry/domesticated *Bombyx mori* silkworms and matured fifth instar larvae of non-mulberry/wild silkworms (*Antheraea assamensis, Antheraea mylitta, and Philosamia ricini*) were obtained from Mangaldoi Silk Farm, Assam, India. For isolation of SF solution, *B. mori* cocoons were cut into small pieces and degummed in boiling 0.02 M sodium carbonate, washed using milli-Q water, and air-dried. The degummed silk fibers were dissolved in a 9.3 M LiBr solution and dialyzed extensively against milli-Q water. In the case of wild silks, SF from silk glands was isolated in 1% (w/v) SDS and dialyzed using milli-Q water. The isolated regenerated silk fibroin (RSF) solution was then freeze-dried and stored until further use. For experimental purposes, the lyophilized silk was dissolved in water as per the required concentration and used. Silk films were fabricated on PDMS platforms by casting an SF solution and drying it overnight. The formed films had a thickness of 4-5 μm which were subsequently treated with 70-80% methanol (MeOH) to transition β-sheet content into them making them water-insoluble. The 4 individual silk types in the study are abbreviated as RBM (regenerated *B. mori*), RAA (regenerated *A. assamensis*), RAM (regenerated *A. mylitta*), and RPR (regenerated *P. ricini*).

5.2.2 Fourier transform infrared spectrometry (FTIR)

FTIR analysis of silk films was executed using Nicolet 380 (Thermo Scientific, USA) containing an attenuated total reflection (ATR) setup (Golden Gate, Specac, UK). To minimize the background absorbance, the optical path of the device was purged with dry air. Silk films were held to the ATR stage and a spectrum between 800 and 4000 cm^{-1} was recorded at 4 cm^{-1} resolution and 64 scans with applied corrections for background absorbance and sampling depth. To analyze

the secondary structures, the amide-I spectra (1700–1600 cm–1) were deconvoluted using the second derivative of the spectra and fitting Gaussian peaks using OriginPro 2019 software. The following bands in the spectra were assigned to secondary structures: aggregated strands (1605–1615 cm^{-1}), β-sheets (1616–1637 cm^{-1}), random coil (1638–1655 cm^{-1}), α-helices (1656–1662 cm^{-1}), and β-turns (1663–1696 cm^{-1}) as per previous studies [376, 377]. For each sample, the deconvoluted spectra were area-normalized and represented as a percentage of secondary structures. A general rule of mixture was used to derive the predicted β-sheets contents of the blends by averaging the values of the individual SF contents. The predicted values were compared to the measured values obtained using FTIR analysis.

5.2.3 Amino acid analysis

The amino acid composition was determined as per a previously reported and protocol used in the NEaar laboratory [378]. The total hydrolyzable amino acids (THAA) were formed using acid hydrolysis (100 µL of 7 M HCl per mg of powder) for 24 h at 110 °C. The samples were then dried overnight using a centrifugal evaporator, and rehydrated using the rehydration fluid containing 0.01 M HCl, 1.5 mM sodium azide) along with an internal spike of the non-protein amino acid l-homo-arginine. Following this, the samples were run in reverse-phase high-performance liquid chromatography (RP-HPLC) and fluorescence was detected as per the modified method of Kaufman and Manley [379]. The amount of racemization and hydrolysis for the amino acids was measured according to the concentrations of d- and l- enantiomers. Additionally, the amino acids asparagine and glutamine undergo rapid irreversible deamination to aspartic acid and glutamic acid respectively during the hydrolysis step, thus they are reported together as Asx and Glx. Furthermore, as per the method used, proline, hydroxyproline and cysteine amino acids were not detected.

5.2.4 Sodium dodecyl sulfate-polyacrylamide gel electrophoresis (SDS-PAGE)

The molecular weight of regenerated SF solutions was studied using SDS-PAGE. The stacking gel constitutes of 30% acrylamide, 10% SDS in 0.5 M Tris-HCl buffer (pH 6.8), and 10% ammonium persulfate (APS), while the separating gel constitutes of 30% acrylamide, 10% SDS in 1.5 M Tris-HCl buffer (pH 8.8), and 10% APS. The protein was run on polyacrylamide gel with a running buffer made up of 25 mM Tris-HCl, 0.1% SDS, 192 mM Glycine. Beta-mercaptoethanol (2-ME) was used for reducing conditions and a pre-stained protein ladder (Abcam, USA) was used as the

molecular weight marker. The resolved protein bands were visualized by staining with 0.25% Coomassie Brilliant Blue R-250 (Sigma-Aldrich, USA).

5.2.5 Absorbance, zeta potential, conductivity, and pH

The absorbance of the SF solution was measured using UV-300 UV/Vis Spectrometer (Thermo Spectronic, UK). The zeta potential measurement of the solution was performed using Zetasizer Nano ZS90 (Malvern, UK) at 90° angle light scattering for three measurements of automatically calculated time. The conductivity was measured using a standard electrical conductivity meter while the pH was measured using a pH meter.

5.2.6 Differential scanning calorimetry (DSC)

All tests were executed on a DSC 4000 instrument (PerkinElmer, USA), which was fully calibrated with the sample chamber purged with highly pure nitrogen at a flow rate of 20 mL/min. Standard mode DSC tests were performed on SF films placed in specialized aluminium sealed sample pans from 5 to 95 °C at a heating rate of 10 °C/min. The heat flow spectra as a function of temperature were recorded.

5.2.7 Rate of evaporation

The rate of evaporation of the silk solutions was assessed using moisture analyzer MX-50 (A&D Company, Limited, Tokyo, Japan). For testing, 1 mL of silk solution was placed on the sample pan and run at a rate of 2 °C/min. The generated data were plotted as the percent mass loss with the increase in temperature.

5.2.8 Thermogravimetric (TGA) analysis

The water content of SF films with temperature was estimated using thermogravimetry (TGA, NETZSCH, Germany). The samples in alumina (Al_2O_3) crucibles were heated at a continuous rate of 10 °C/min under an inert nitrogen atmosphere from 30 to 400 °C and the percentage mass remaining (TG) and derivative of mass remaining (DTG) was recorded as a function of temperature.

5.2.9 Enzymatic degradation

The *in vitro* enzymatic degradation of silk films was performed in the presence of 2 U/mL protease XIV from *Streptomyces griseus* (Sigma-Aldrich, USA) in phosphate-buffered saline (PBS) solution at 37 °C. For calculations, the initial dry weight (W*i*) of all films was noted and the enzyme

solution was replaced every third day to maintain the enzymatic activity during the whole time. At predefined time points, the samples were taken, cleansed gently with milli-Q water, dried, and weighed (W*t*). Silk films incubated in PBS solution without the enzyme served as control and the degradation was calculated as follows:

$$\% \text{ Degradation} = [(W_i - W_t)/W_i] \times 100$$

5.2.10 Rheology

Rheological measurements were carried out with a Discovery Hybrid Rheometer 2 (DHR-2) (TA Instruments, Delaware, USA) rheometer, fitted with a Peltier (heating and cooling) stage, and a cone plate geometry (CP50-2°; 50 mm radius and 2° opening angle). Regenerated silk fibroin solution, enough to fill the geometry, was placed on the plate (fixed) and the cone (driven) was lowered as per the gap setting. The geometry was then enclosed using an environmental chamber designed to fit around the cone and driveshaft without touching it, to avoid any drying out of the sample. The oscillatory experiments were carried out in stages. First, a time sweep was performed at a constant shear strain of 5% and frequency of 0.1 Hz for 2500 s at 37 °C. Next, a frequency sweep from 0.1-100 Hz at 37 °C and a constant strain of 5% was carried out to measure the elastic (i.e., storage) and viscous (i.e., loss) moduli (G' and G"). Next, a temperature ramp from 37-80 °C was performed at a constant shear strain of 5% and frequency of 0.1 Hz. Finally, another frequency sweep with the same specifications as the previous one was performed. The rheo-optical properties of the hydrogels were studied using Modular Microscope Accessory (MMA; TA Instruments, Delaware, USA) with simultaneous rheological measurements on a DHR-2 that enables complete flow visualization. A 40 mm parallel plate geometry was used and a time sweep was carried out for 1200s at 37 °C. The rule of mixture was used to derive the predicted modulus values of the blends by averaging the values of the individual SF solutions. The predicted values were compared to the measured values obtained using rheological tests.

5.3 Results

5.3.1 Structural properties - FTIR

The structural change and the identification of functional groups in the regenerated silk films were assessed by FTIR spectroscopy. The IR absorption spectra between 1700 and 1600 cm^{-1} are assigned to amide I (C═O stretching), 1600–1500 cm^{-1} to amide II (N—H bending), and 1300–1200 cm^{-1} to amide III (C—N stretching) [380]. The peaks at 1610–1630 cm^{-1} (amide I) and 1510–1520 cm^{-1} (amide II) are characteristic of silk II conformation [377], and the absorptions at 1648–1554 cm^{-1} (amide I) and 1535–1542 cm^{-1} (amide II) are indicative of random coil structures [381], or the silk I conformation [382]. In the current study, the amide I spectra peak was observed at 1637 cm^{-1} in the domesticated silk (RBM) and at 1650 cm–1 in the case of the wild silks (RAA, RAM, RPR), and the amide II spectra was observed at 1513 cm^{-1} in RBM and 1536 cm^{-1} in the wild silks suggesting the presence of α-helix/random coil conformation (**Figure 5.1A**). A low-intensity amide III band was also detected for all samples ranging from 1220-1240 cm^{-1}. Additional bands were observed at 1308 cm^{-1} and 1380 cm^{-1} in the non-methanol treated wild silks were assigned to bound water present in the wild silks.

Upon treatment with methanol (MeOH), a clear shift of the IR absorption peak to a lower wavenumber was observed with peaks at 1620 cm^{-1} (amide I), and at 1512 cm^{-1} (amide II) in all silk types indicating a transition to β-sheet structures (**Figure 5.3A**). This property of MeOH to increase the crystallinity of silk due to formation of β-sheets have been utilized for applications such as to retard the release of encapsulated vaccine from silk tips following *in vivo* implantation [383]. Further, the secondary structure composition of the samples was quantified by deconvolution of the amide I region between 1600 and 1700 cm^{-1}. The percentage of secondary structures before and after MeOH treatment is shown in **Figure 5.3B**. The visible shift in the amide I and amide II spectra of MeOH treated films is corroborated by the increased β-sheet content upon MeOH treatment. The higher β-sheet content in the wild silk (maximum in RPR) is attributed to the presence of polyalanine residues. Furthermore, the change in β-sheet content upon the blending of the silk types is shown in **Figure 5.3C**. Herein, the measured values (with and without MeOH treatment) were compared to the predicted ones derived as per the rule of mixtures. The results showed that the measured β-sheet content in the blends was higher than the predicted values indicating greater interaction among them. The blends of domesticated-wild silk (~40%) showed greater β-sheet content as compared to the wild-wild silk blends (~30%). The measured content of

the RBM-RPR blend (~36%) reached close to the maximal value i.e., due to MeOH treatment (~38%), indicating that the blending resulted in increased β-sheet content comparable to that of methanol treatment.

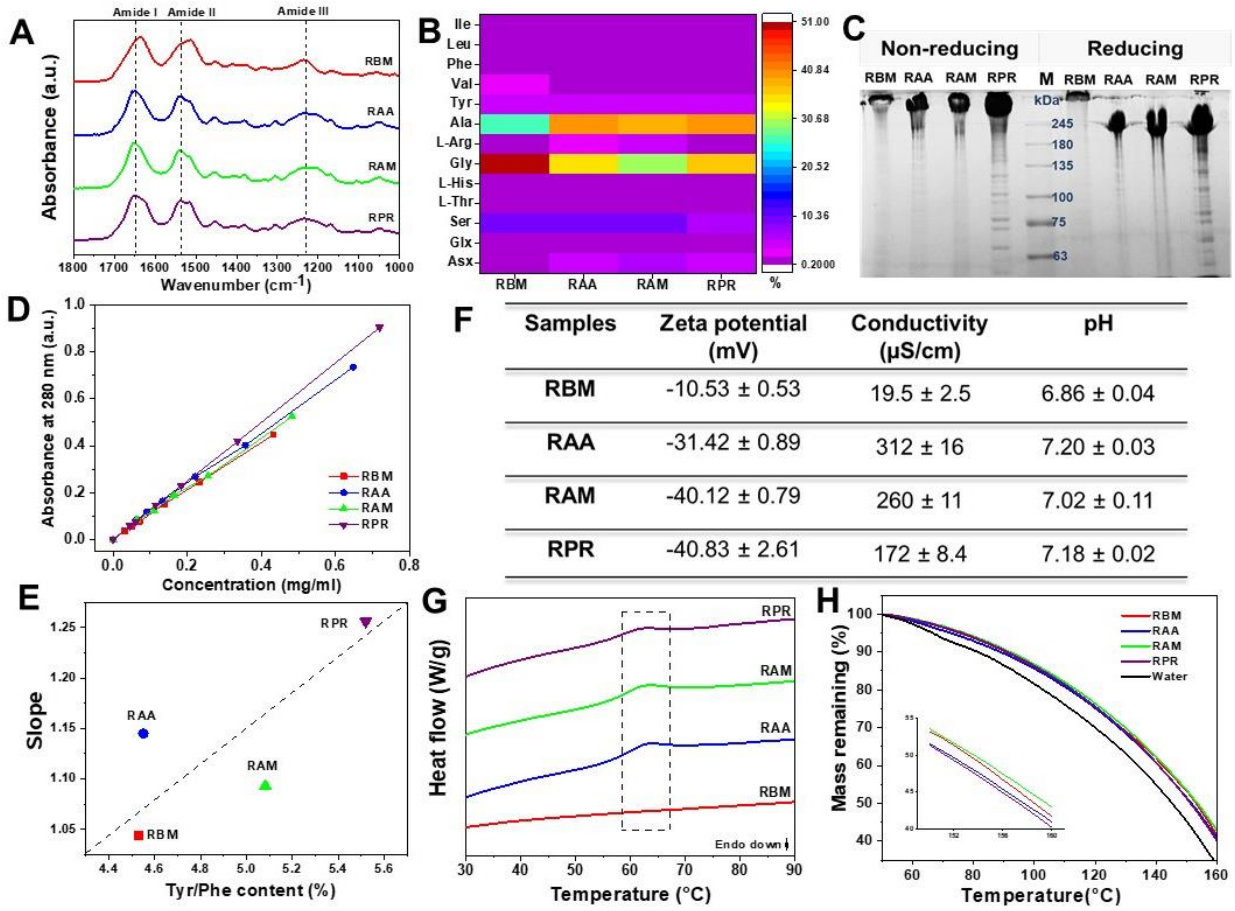

Figure 5.1. Structural-thermal properties of individual silk types. *(A) FTIR spectra showing the typical protein amide bands, (B) amino acid composition, (C) SDS PAGE analysis of the proteins under reducing and non-reducing conditions, (D) UV-Vis absorbance at 280 nm vs concentration of silk solution, (E) absorbance slope vs tyrosine/phenylalanine content, (F) table showing DLS measurements, conductivity and pH of silk solutions, (G) DSC spectra of silk films, and (H) rate of evaporation of the silk solutions.*

5.3.2 Structural properties - amino acid analysis

The amino acid configuration affects the material properties of different silk types. Thus, the amino acid composition of all the silk types was assessed by a methodology where the samples are first hydrolyzed, derivatized, and then run on the HPLC. The results the dominance of glycine, alanine, and serine residues in all silk types. These amino acids constituted about 87% in the domesticated silk, and about 83% in RAA/RPR, and 77% in RAM wild silks (**Figure 5.1B**). The wild silks

showed a higher proportion of alanine residues as compared to the domesticated silk (**Table 5.1**). Additionally, the wild silks showed a higher proportion of hydrophilic amino acids as compared to the domesticated mulberry variety (**Table 5.2**). The wild silks also had a higher basic/acidic amino acid ratio as compared to the domesticated variety. This leads to the varied surface property such as wettability of different regenerated silk-based biomaterials due to varying hydropathicity [384, 385]. Malay *et al.* reported that the differences in the amino acid sequence in silkworm silks (like the presence of polyalanine repeats in wild silks) could directly be correlated to their thermal stability and mechanical properties [172].

Table 5.1. Amino acid composition (%) of the silk types.

Amino acid	RBM	RAA	RAM	RPR
Ala	27.00	39.72	37.52	40.22
Gly	50.80	34.66	30.57	36.74
Ser	9.86	8.91	9.51	5.80
Tyr, Phe	4.53	4.35	5.18	5.52
Arg, Thr	1.20	2.83	4.50	2.47
Asx, His	1.78	6.14	7.66	5.10
Glx	1.11	1.41	1.64	1.46
Ile, Leu, Val	3.42	1.98	3.41	2.70

Table 5.2. Amino acid ratios of different silk proteins. *

Ratio	RBM	RAA	RAM	RPR
Hydrophilic/ hydrophobic	0.22	0.30	0.38	0.25
Basic/acidic	0.23	0.57	0.58	0.60
Glycine/alanine	1.88	0.87	0.81	0.91

**Basic amino acids*: arginine, lysine, histidine, tryptophan*; acidic amino acids*: aspartic acid, glutamic acid; *hydrophilic*: serine, threonine, aspartic acid, glutamic acid, tyrosine, arginine,

lysine, Histidine; *hydrophobic*: glycine, alanine, cysteine, proline, tryptophan, valine, isoleucine, phenylalanine, methionine, tryptophan.

5.3.3 Structural properties - SDS-PAGE

The chain length of SF molecules in the regenerated silk samples was assessed using SDS-PAGE. The native SF of *B. mori* constitutes of heavy (~391 kDa) and light (25 kDa) polypeptide chains, linked by a disulfide bond along with a glycoprotein, P25 (25 kDa). In the case of wild silks, 2 fractions of 220 kDa and 20 kDa have been reported for *A. assamensis*, homodimers of ~395 kDa (each monomer being ~197 kDa) for *A. mylitta*, and polypeptides of 97 kDa and 45 kDa, connected through a disulfide bond for *P. ricini* [181]. In the current study, all the silk types showed the presence of large polypeptides (>245 kDa) under non-reducing conditions (**Figure 5.1C**). Whereas, due to the cleavage of the disulfide bonds under reducing conditions, the migration of these polypeptides to the 200-240 kDa range in the RAA and RAM silks along with some additional bands in case of the RPR were observed. The intense band of RBM at the top of the gel consisting of the heavy chain did not show any change. Overall, the study showed the presence of larger polypeptide chains in the regenerated silks, indicating the possibility of chain interaction and physical entanglement when these are blended.

5.3.4 Structural chemistry - UV-visible spectroscopy

The UV-Visible spectroscopy was executed to understand the absorption spectra of the regenerated SF samples. The absorption spectra at 280 nm are assigned to π transitions in the aromatic amino acids such as tyrosine (Tyr), Phenylalanine (Phe), and Tryptophan (Trp) present in the SF molecular chain. In this study, **Figure 5.1D** shows the absorbance at 280 nm against the concentration of SF solution. The wild varieties showed a higher absorbance as compared to the domesticated silk, and this could be correlated to the presence of aromatic amino acids in the silks (**Figure 5.1E**). RPR and RBM show the highest and lowest absorbance, respectively. This can be attributed to the highest and lowest Tyr/Phe residues in the RPR and RBM, respectively. However, the RAA and RAM samples did not fit this correlation which might be due to the Trp residue which is not accounted for in the current study due to the amino acid detection method used. The presence of aromatic residues such as Tyr and Phe in the wild silks is advantageous in many ways. Tyr plays a crucial role in regulating the protein's structural conformations and also the self-assembly process where proteins self-assemble into cross-β-like fibers *via* hydrogen bonding and

π–π stacking between aromatic side chains [386]. By tuning these interactions, the properties of SF can be managed and understood in the sol to gel transition process. Additionally, dityrosine chemistry can be potentially used to enhance the mechanical properties of biomaterials [387].

5.3.5 Structural chemistry - charge, conductivity, and pH

The charge on the SF molecules in the solution was estimated by studying the zeta potential. The charge in the dispersed phase provides an understanding of the stability of the solution. The results of the current study showed a zeta potential of around -10 mV in the RBM silk type. The wild silk types showed a higher negative zeta potential of around -31 mV in RAA, -40 mV in RAM, and -41 mV in RPR (**Figure 5.1F**). The higher negative charge in the wild silks imparts them more stability in the solution. The theoretical isoelectric point (pI) for SF is around 4.37-5.05 [384]. At neutral pH (which is above the pI) of the RSF in the study, the surface of the SF protein is predominantly negatively charged. Additionally, SF proteins majorly consist of neutral amino acids such as glycine, alanine, and serine, however, wild silk has higher basic amino acids (**Table 5.2**) as compared to domesticated silk, making it feasible to donate a negative OH ion. This charge difference also imparts varied surface property to SF in terms of their interaction with the cells while being used as biomaterials derived from the regenerated SF [388]. Furthermore, the different processing methods of the wild and domesticated silks may also be contributing to this high difference in their charges. The van der Waals attraction and the electrostatic repulsion force are two major forces that contribute to the stability of a system. The electrostatic force is related proportionally to the particle zeta potential. Thus, a high zeta potential corresponds to a high repulsion force between particles, subsequently forming a more stable system. The near-neutral pH in all silk types makes it readily more soluble in an aqueous solution. The conductivity of the silk solution is another crucial factor indicating its stability and helps to understand the possible interactions of the molecules. The domesticated silk RBM measured conductivity of ~20 µS/cm, while the wild silk showed a higher conductivity of 312 ± 16 µS/cm in RAA, 260 ± 11 µS/cm, and 172 ± 8 µS/cm in RPR (**Figure 5.1F**). The higher conductivity in the wild silks indicates the abundance of metal ions in them, making them available for metal ion interactions. Recent work from our group has shown that silk interacts with metal ions and uses it to control the viscosity and gelation of silk *via* interaction with divalent metal ions or sticky reptations and we associate that with the presence of carbonyl groups and the availability of the protein to interact with metal ions [389, 390]. Tulachan *et al.* showed that *Antheraea mylitta* cocoon could conduct higher

current density as compared to the *B. mori* cocoons and owed this to the higher mineral contents in the wild type [391]. Higher conductivity in regenerated wild silks implies that it's interacting with more metal ions by sequestering them. This makes them good gelators because they will be able to create divalent metal ion bridges between chains which will increase the strength of any gel. So, the wild silks are better at interacting and creating salt bridges than the domesticated silk type.

5.3.6 Thermal stability

To study the thermal stability and hydration status of silk and investigate its denaturation and solidification, DSC was used. The results of the DSC spectra show the presence of ectotherms at ~62 °C in the wild silk films which is absent in the domesticated silk films (**Figure 5.1G**). Wild silk unlike domesticated silk shows clear crystallization as they go through denaturation, implies making more stable forms. Thus, the addition of wild silks in a mixture could stabilize the system where the wild silks could act as nuclei or stabilizers. The presence of peaks indicates the presence of a thermal switch, where they denature more readily and can undergo thermal transitions. The thermally active wild silks show that despite processing and fabricating them into films, they can rehydrate and dehydrate, which is lost in the case of the domesticated silk type.

The ability of silk to interact with water is another essential feature. The ability of silk films to be able to hold onto the water was studied using a moisture analyzer which is good for general bulk measurements. The results indicated that all regenerated silk behaves almost in a similar way (**Figure 5.1H**). Thus, TGA was used which is a more specialized technique to get a detailed understanding of the change in mass with temperature. The thermograms in the current study show significant mass loss in samples mainly in two phases over the temperature range of 30-400 °C (**Figure 5.2A**). The first phase of mass loss is at around 70-120 °C which indicates the removal of absorbed water or the loss of moisture. The results indicate that the wild silks hold on to more water and therefore can give off more water but at a relatively lesser temperature as compared to the RBM. This also establishes that RBM holds on to less water but it is tightly bound and thus requires a higher temperature to lose. Wild silks have a higher degree of hydration but their hydration shell is less stable which allows them to go into a solution state, and because the hydration shell is more unstable, they would readily fall out of solution and act as a nucleator for gelation in the blends making them probable nucleating agents in the system. The higher

hydrophilicity of the wild silks renders them to have higher moisture content. Additionally, the presence of positively charged amino acids in the wild silks contributes to enhancing cellular attachment and proliferation when used as a scaffold for tissue engineering applications [392]. Chouhan *et al.* recently showed that the wild-silk-based wound dressings were capable of higher water retention capacity which aid in wound healing [393]. The second phase ranges from 250 to 400 °C, which is majorly a result of the cleavage of peptide bonds and the breakdown of side-chain groups of amino acid residues [380]. The results indicate the denaturation peak at ~290 °C in RBM, which is higher in all the wild silk types reaching ~348 °C in RAA/RAM, and ~354 °C in the case of the RPR. This shows that the wild silks are more thermally stable compared to domesticated silk. Among the wild silks, RPR is most thermally stable. This majorly is due to the crystallinity domains present in the silk, which are more in the wild silks compared to the domesticated silk. This is attributed to the higher alanine content found in the wild silks. **Figure 5.2B** shows that the higher thermal degradation temperature in the wild silk can be attributed directly to the polyalanine content of the individual silk types. These findings are consistent with the previous reports of the thermal stability of these silk types [392, 394]. Malay *et al.* reported a similar outcome where *P. ricini* having the highest polyalanine residues showed highest thermal stability in comparison to other wild silk fiber types [172].

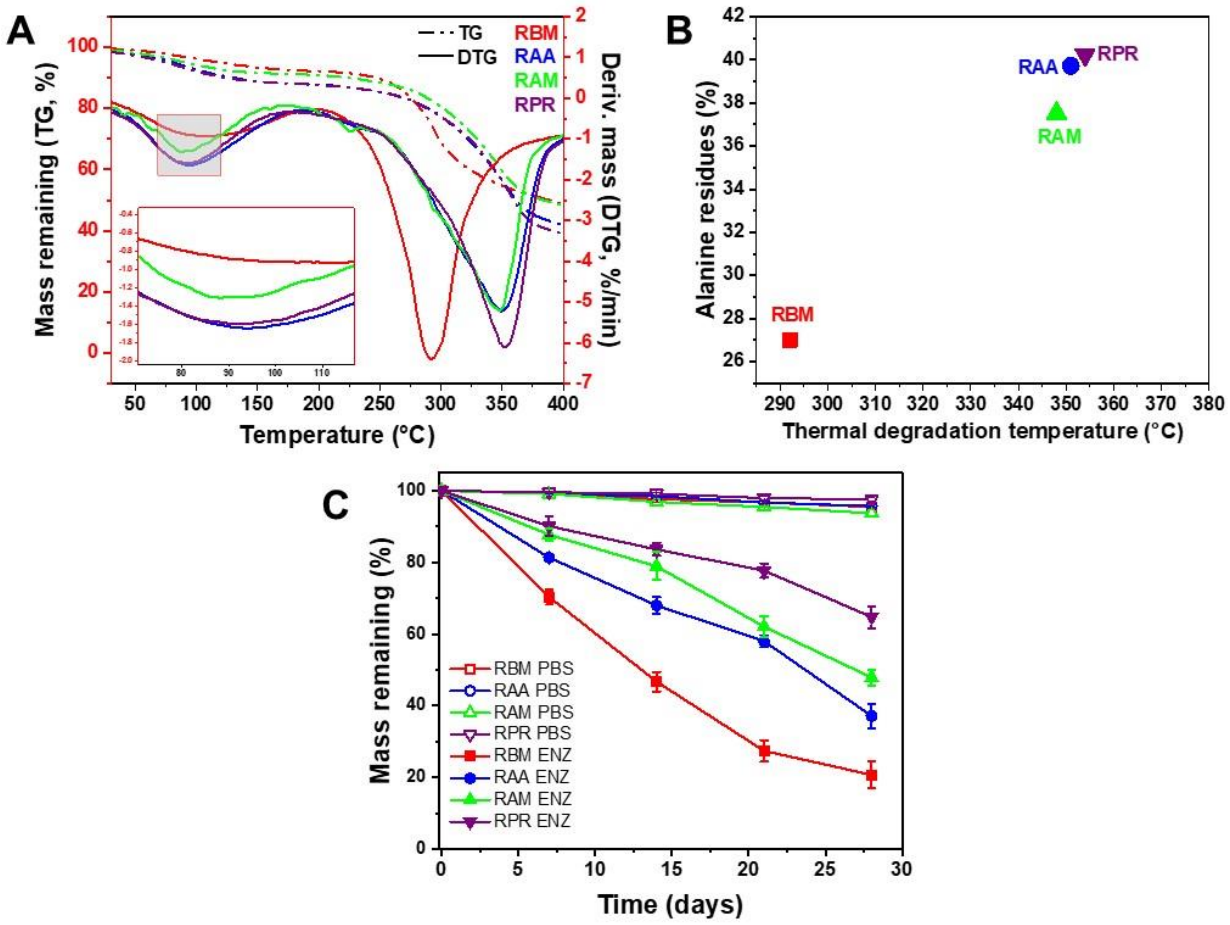

Figure 5.2. Thermogravimetric and degradation analysis. *(A) Thermogravimetric analysis, (B) the alanine residues vs thermal degradation temperature plot, and (C) enzymatic degradation of various silk types.*

5.3.7 *In vitro* enzymatic degradation

Crystallinity is also an important factor controlling the degradation of RSF-based materials *in vivo*. The extent of crystallinity of β-sheets can be tuned *via* various physical and chemical processes to modulate the biodegradability and the water stability of the SF biomaterials [395]. Evaluating the biodegradability of the silks is important to comprehend the stability, breakdown, and possible elimination of the matrix from the body. Upon implantation of any biomaterial matrix, its biodegradation should be at a rate consistent with the neo-tissue formation in the body. In the current study, the domesticated RBM showed a higher degradation (~80% mass lost) after 28 days of protease XIV enzymatic treatment. Concurrently, the wild silks showed a lesser enzymatic degradation with RAA showing ~62% mass loss, RAM ~50% mass loss, and RPR ~36% mass

loss (**Figure 5.2C**). The silk films maintained their stability in PBS over time with no degradation. The lower degradation of wild silks is again linked to their higher crystallinity making the cleavage site inaccessible to the enzymatic cocktail. The characteristic polyalanine repeats, high α-helix, and β-sheet contents, and compact crystalline structure makes wild SF more resistant to enzymatic degradation as compared to domesticated SF. The *in vitro* degradation was performed using a protease XIV cocktail with preferential cleavage sites between hydrophobic amino acids. Therefore, the low crystallinity and the higher available cleavage sites in the domesticated silk leads to their greater degradation as compared to the wild silks. The findings of the current study are in agreement with previous reports [264, 385].

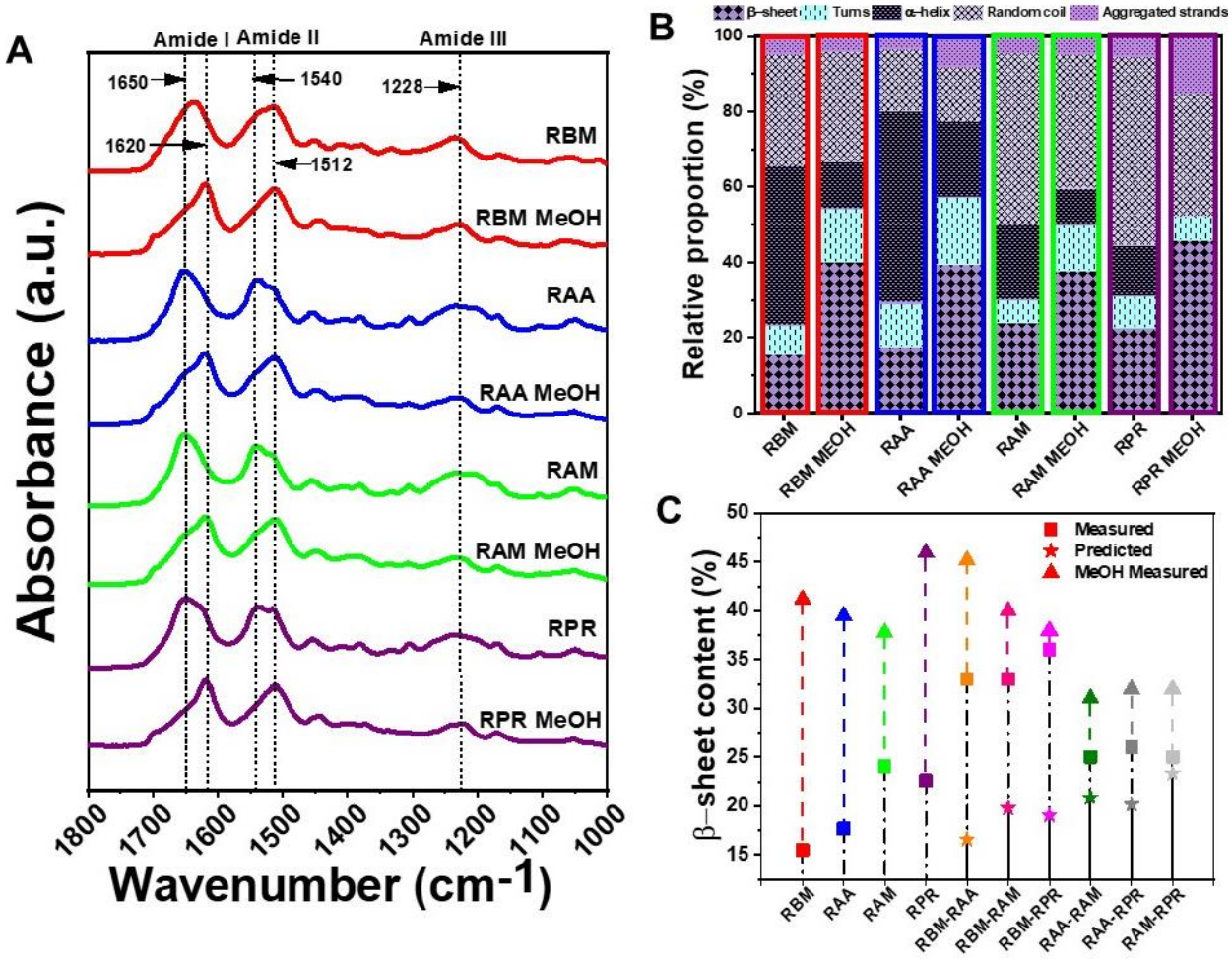

Figure 5.3. FTIR spectra of silk samples. *(A) Spectra of silk proteins with and without methanol (MeOH) treatment over the 1000-1800 cm^{-1} range, (B) deconvoluted amide-I showing contents of secondary structures of proteins, and (C) predicted and measured beta-sheet content in the samples.*

Overall, when assessed individually, the wild silks have increased functionality and performance range as they show the presence of a thermal switch, a higher degree of hydration with an unstable shell of hydration, and a high degree of crystallinity. So, they are better at holding on to water and they go into a solution more easily but due to a relatively unstable hydration shell, they fall out of the solution more readily and form more stable aggregates which is why they have higher thermal degradation temperatures. Thus, they can potentially act as nucleating agents. These factors will help in terms of tuning the rate and strength of gelation upon blending. Thus, the results of the current study showed that wild silks could be of immense interest because they have lots of active molecular switches that could help to interact with domesticated silk; and by introducing just a small quantity of wild silks, the properties of domesticated RBM could be improved. So, next, different silk types were mixed to form hydrogels.

5.3.8 Rheological and rheo-optical assessment

The rheological measurement helps us to characterize (structure-property relationship), understand the process performance (hydrogel stability, processing temperatures, etc.), and end-product properties such as the mechanical strength of the blend hydrogels. Considering the gel nature of the system and the variability in input parameters, storage modulus (G′) was used to assess the gel formation and relative gel strength. The assessment was performed in 4 phases. First was a time sweep at 37 °C for 2500 s, the second was a frequency sweep, third was a temperature sweep from 37-80 °C, and fourth was again a frequency sweep. The results showed that some blends start to gel quickly at 37 °C indicated by the increasing G′, where the RBM-RPR blend was quickest to gel followed by RBM-RAA (**Figure 5.4A**). These blends gel at 37 °C and their storage modulus do not change even with the temperature rise, indicating their complete gelation and formation of a stable gel. The G′ of the frequency sweep before the temperature sweep was constant with the change in frequency. The blends such as RBM-RAM and RAA-RPR, start to gel at 37 °C but do not completely gel, and require temperature stimulus to gel completely. Among the individual proteins, only the RAA starts to gel in ~18 min time as shown by the increased G′. Furthermore, some blends such as RAA-RAM and RAM-RPR need additional activation such as temperature stimulation even to start the process of gelation and eventually gelling completely (**Figure 5.4B**). The final frequency sweep following the temperature sweep also showed constant G′ with frequency. Possible interactions during the gelation process include physical entanglement and Tyr stacking at 37 °C, where the wild silks act as chemical nucleators in the blend. The other is the

results of a crystallization event that occurs as a result of increasing the temperature eventually reaching the crystallization temperature i.e., around 60 °C as seen from the DSC results. The results indicated that a wild-domesticated silk-blend gelled early and maintained a stable G′, except for blends with RAM. All the blends containing RAM silk needed to be stimulated thermally to gel completely. However, upon complete gelation, the RAM-based gels form a stronger gel as compared to other wild silks. These hydrogels harness the energy from thermal sources to enhance intermolecular interaction in the hybrid gels, on account of thermal energy being transformed into an electron flow that powers a chemical reaction, where the wild silks act as nucleation point to remodel this crosslinking in the gels. Physical cues such as temperature, pH, and vibrations have been reported to affect the gelation and mechanical properties. Recently Wang *et al.* reported the strengthening of a composite soft gel matrix due to vibrations. The matrix composed of methylcellulose, and dynamically reactive materials with piezoelectric ZnO. Vigorous shaking of this composite makes it almost 66 times stronger with less chances of deformation as compared to the composites without exposure to these vibrations [396]. Concurrently, the light intensity reduced upon gelation in some blends with maximum reduction was observed in RBM-RAA and RAA-RPR, followed by RBM-RAM and RBM-RPR. The decrease in light intensity in these blends was consistent with the increase in storage modulus and gelation process. This decrease due to the processes occurring during gelation could be attributed majorly to interactions such as chain entanglements and desolvation due to phase separation in the gel among others. Owing to its tunability in terms of transparency and biocompatibility, silk fibroin film from non-mulberry *Antheraea mylitta* has been used for corneal regeneration [397].

Furthermore, the measured and predicted G′ before and after temperature sweep was assessed to understand the change in G′ due to temperature. Corroborating the abovementioned results, the wild-wild silk blend (RAA-RPR) and the RAM SF containing blends (RAA-RAM and RAM-RPR) showed a higher increase in G′ after temperature treatment as compared to other blend hydrogels. Additionally, the measured G′ was higher than the predicted G′ (except for RBM-RAA), implying that this is a good composite because the amount of G′ is increased. The decreased amount of measured G′ in the RAA-containing blend as compared to the individual RAA SF indicates lower interactions among the silk types.

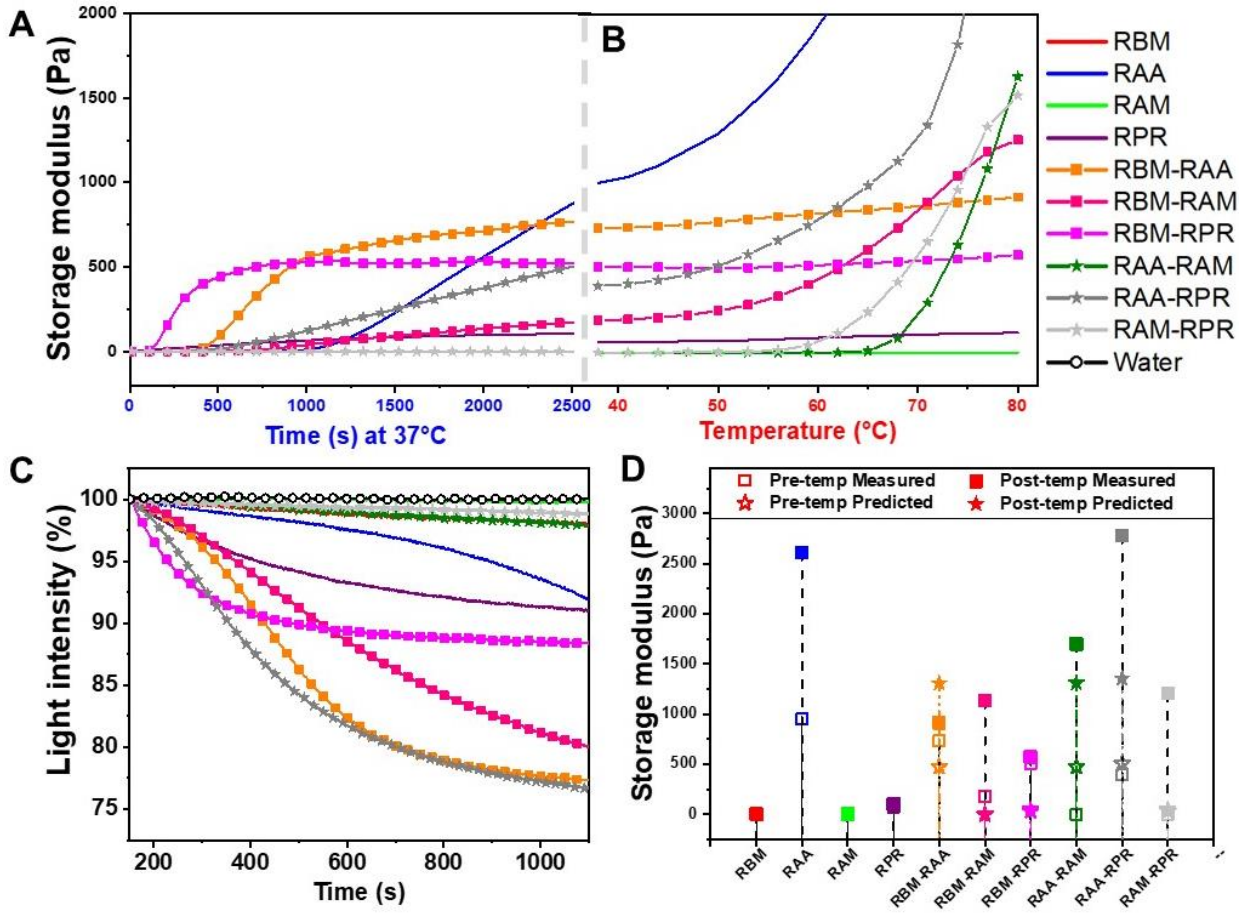

Figure 5.4. Rheological properties of hydrogels. *The storage modulus of the hydrogels during (A) time sweep at 37 °C, (B) temperature sweep (37-80 °C), (C) rheo-optical light intensity analysis, and (D) the measured and predicted storage modulus before (pre-temp) and after (post-temp) temperature sweep.*

5.4 Discussion

Silk exists in its water-insoluble (silk-II) form in the spun cocoons and needs to undergo processing using techniques such as degumming (with basic salts) and dissolution (with chaotropic solvents), as reported in several previous studies [76, 297]. Concurrently, the protein from the silk glands of the silkworms can be isolated and dissolved in aqueous detergents [254, 385]. The resulting SF solution is not stable for long at room temperature and tends to gel. Therefore, in the current study, the SF solution was lyophilized, stored for longer time durations, and eventually reconstituted in water for usage. The reconstituted proteins were first studied individually to confirm the functionality of the protein. The structural and thermal properties of the individual silk types were assessed using various characterization techniques. Further, the wild and domesticated SF

solutions were blended to form self-assembled silk hydrogels. The performance and gelation mechanism of these blend hydrogels were then investigated by studying their dynamic interactions *via* rheology.

Possible interactions and gelation mechanism: An increase in G′ and decrease in light intensity was observed in the silk blend hydrogels and this is linked to the change degree of hydration and increased interactions due to different switches such as metal ion bridges, chemical Tyr stacking, chain physical entanglement, potential crystallization with the poly-alanine segment or beta-sheet formation. The results indicated that among the wild silks, RPR is the best activator that stimulates others to gel probably owing to its highest alanine content and high crystallinity followed by RAA. The blends of RAM on the other hand need thermal stimulation to form a complete gel but the formed final gels are stronger than others. Thus, each wild silk has a different level of interactions and switches to explore and these could be tuned for various applications. The individual regenerated SF proteins show their characteristic features which would help understand their interactions upon their blending (**Figure 5.5A**). The blending of the wild and domesticated silks could be linked to various possible interactions in the formed hydrogels. Towards this several gelation pathways have been hypothesized (**Figure 5.5B**). The high difference in the conductivity among the wild and domesticated silks indicates the involvement of metal-ion interactions or salt bridging, where no specific binding sites are required. Another potential mechanism for inter-fibroin chain interactions is electrostatic interactions considering the high difference in the zeta potential or charges between the wild and domesticated silks. A similar charge among the wild silks might lead to electrostatic repulsion as opposed to the varied charges in the wild and domesticated silks in the blends allowing greater electrostatic interactions and making better gels. The presence of lengthy chains in the hydrogels indicates possible physical entanglement aiding the process of gelation. Further, the differing hydropathicity of the RSFs in an aqueous hydrogel environment necessitates hydrophobic interactions in the system. The interactions between aromatic–aromatic amino acid side chains are additional crucial non-covalent forces that have been widely explored in the milieu of protein folding, molecular recognition, stability, and the process of self-assembly [387]. The presence of higher aromatic residues such as Tyr, Phe in wild SF proteins suggests hydrogen bonding and π–π stacking between aromatic side chains leading to greater gelation. The presence of hydrophobic aromatic Tyr residue favors the formation of silk II structure [179]. Another desired fabrication strategy is the process of self-assembly, where

components assemble to form ordered and hierarchical structures without external interventions. Proteins possess this capability to self-assemble with an initial drive force provided by non-specific interactions such as hydrophobic forces, followed by more specific interactions, such as hydrogen bonding. Silk fibroin being amphiphilic drives its self-assembly into spherical micellar structures in the silk glands as well as the process of its spinning where a transition from the soluble state (silk-I) to an insoluble state (silk-II) takes place leading to the development of self-assembled hierarchically arranged silk fibers [398]. This understanding of the natural spinning process has inspired the research to fabricate silk fibers *via* artificial spinning using aqueous-based greener approaches [170, 399].

There is a molecular rearrangement taking place in the hydrogels with a transition from an unordered state in the solutions to ordered structures in the gelled state through an intermediate state (**Figure 5.5C**). In terms of secondary structures of the proteins, the solution predominantly consists of α-helices and random coils which starts to transition into orderly β-sheet with time during the normal gelation process, and finally, a highly ordered structure with increased β-sheet content could be hypothesized when the hydrogels are thermally activated to reach a fully gelled condition. The formation of thermodynamically stable β-sheets stabilizes the hydrogels *via* physical cross-linking processes and are essentially irreversible in physiological settings unless degraded using oxidative or enzymatic methods. The ordered structures may be created by the formation of crystals first due to the polyalanine-rich domains and then using other interactions such as Tyr stacking to stabilize the chains, where the wild silk act as nucleators.

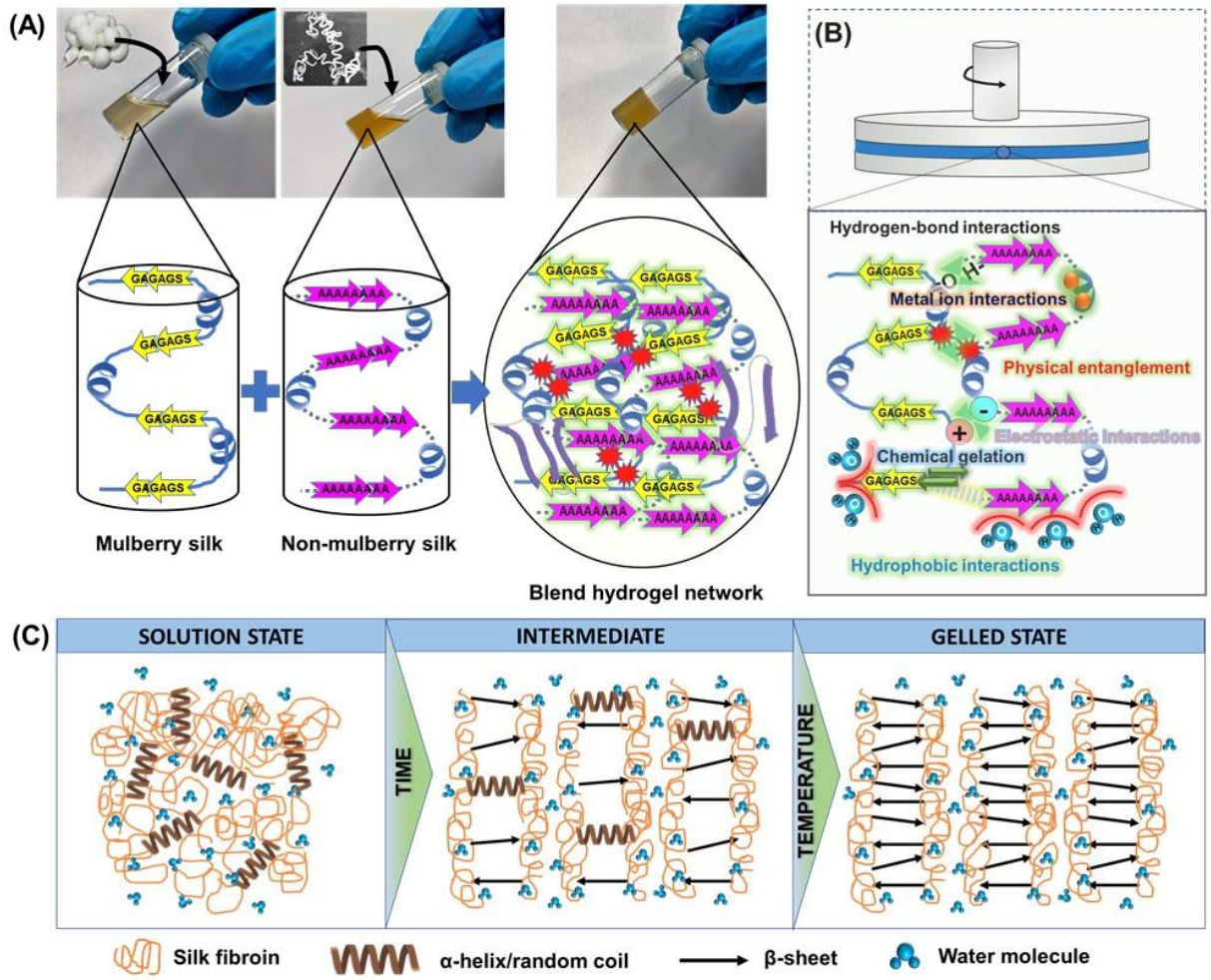

Figure 5.5. Schematics of the possible interactions involved in the sol-gel transition. *(A) Scheme illustrating the blending of mulberry and non-mulberry silk to form a self-gelling hydrogel network, (B) the hypothesized molecular interactions in the blended gelled hydrogels, and (C) scheme showing the rearrangement in the protein secondary structures form unordered to ordered during the process of gelation.*

Potential applications: The understanding of the gelation mechanisms and properties of the hydrogels would find application in numerous domains. For instance, they can be used for the fabrication of hydrogel scaffolds or matrices for the delivery of cells, drugs, or therapeutics in the various soft tissue to hard tissue engineering applications. The capability of these hydrogels to gel without any external stimulus and further demonstration of gel strengthening upon the increase in temperature (the RAM blends) could place them as thermally responsive hydrogels. This makes these blend hydrogels attractive for the delivery of cells and macromolecules However, as opposed to most thermoresponsive hydrogels this gelation is irreversible as the insolubility in the gelled state does not revert to soluble conditions upon a decrease in temperature. With the increase in

temperature, the hydrophobic forces become strengthened while the hydrogen bonding becomes weaker, leading to stronger gelation in these thermosensitive hydrogels. These could be used as injectable technologies for the non-invasive delivery of cargo to the targeted site. The produced thermally stable hydrogel may also be used in high-temperature food processing and templating of composite materials. Additionally, its conductive nature and the ability to be fabricated into thin films could have potential application in flexible electronics and bioelectronics.

5.5 Significant findings

1. The current study explored the functionality and performance of hydrogels formed by blending various silk types. To understand the self-gelation mechanism of these blends, first, the structural and thermal properties of individual silk types were studied.
2. The regenerated SF proteins showed the characteristic amide peaks, had varied amino acid composition, chain length, charge, and conductivity along with distinct thermal stability and degradation.
3. The wild silks are better at holding on to water so they go into a solution more easily but the hydration shell is less stable so they fall out of the solution more readily, allowing them to potentially act as nucleating agent thus creating more stable aggregates indicated by a higher thermal degradation temperature.
4. The different silk types were then blended to form hydrogels and assessed rheologically for their dynamics. The content of β-sheet measured in the blends was higher than the predicted value implying the formation of a good composite because of the increased amount of crystallinity.
5. The blends with *P. ricini* (RPR) were the best activators as shown by the high crystallinity in their blends nearing the methanol-treated levels.
6. The blends with *A. mylitta* (RAM) form thermally sensitive hydrogels, which require to be activated to gel completely but they eventually form stronger gels, while others are thermally insensitive forming stable gels unaffected by the increased temperatures.
7. The blends of wild-domesticated silk performed better than the wild-wild blends.
8. The gelation process is majorly due to peptide self-assembly, driven by hydrogen bonds, physical entanglements, electrostatic interactions, metal-ion interactions, hydrophobic interactions, and tyrosine/phenylalanine stacking.
9. The wild silk-based blending produces composites with increased performance.
10. This understanding of the performance of wild silk-blend hydrogels might be valuable in developing various silk-based composites for non-invasive delivery of cargo for different soft and hard tissue engineering applications, high-temperature food processing, templating composite materials, and bio-flexi-electronics.

Chapter 6

3D Bioprinting using Cross-Linker Free Silk-Gelatin Bioink for Cartilage Tissue Engineering

The present study aims to develop a cross-linker free silk-gelatin based bioink formulation for cartilage regeneration. The ink was prepared by first blending two different varieties of silk, i.e., *B. mori* and *P. ricini*, and adding gelatin to it. The silk polymers start to self-gel when the two silk types are mixed. To this gelling silk matrix, gelatin is entrapped forming a viscoelastic ink that is optimal for bioprinting. Further, porcine primary chondrocytes were encapsulated in ink to create the bioink and investigated for its printability, print fidelity, biological and functional assessment, and *in vitro* and *in vivo* biocompatibility for cartilage tissue engineering applications.

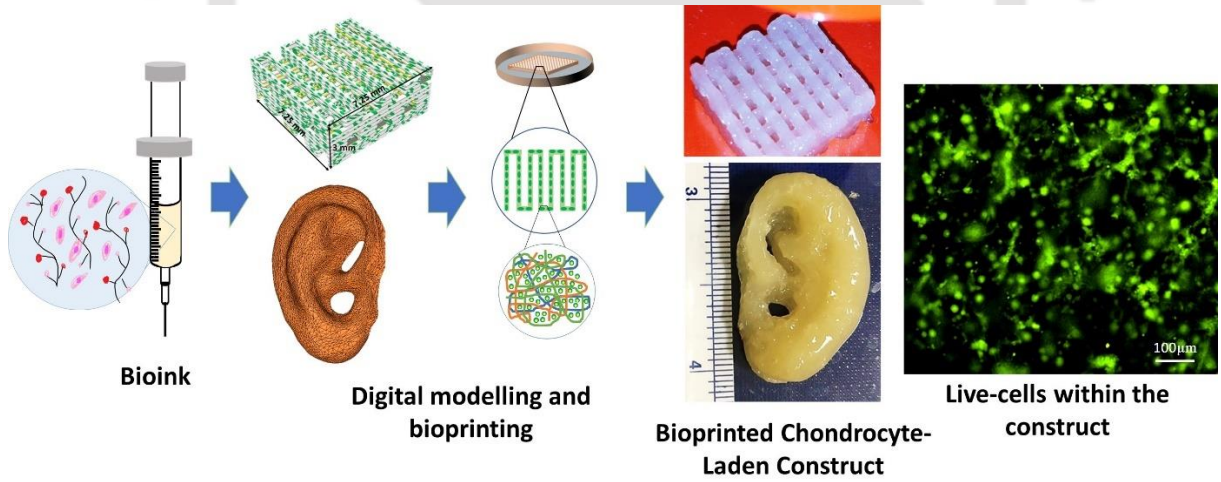

The work embodied in this chapter is published as follows:

Yogendra Pratap Singh, Ashutosh Bandyopadhyay, and Biman B. Mandal. "3D bioprinting using cross-linker-free silk–gelatin bioink for cartilage tissue engineering." ***ACS Applied Materials & Interfaces*** 11(37), 2019: 33684-33696.

ABSTRACT

Cartilage tissue is deprived of intrinsic self-regeneration capability; hence its damage often progresses to a chronic condition which reduces the quality of life. Towards the fabrication of functional tissue substitutes, 3D bioprinting has progressed vastly over the last few decades. However, this progress is challenged by the difficulty in developing suitable bioink materials as most of them require toxic chemical crosslinking. In this study, our goal was to develop a crosslinker free bioink with optimal rheology for polymer extrusion, aqueous and non-toxic processing and offers structural support for cartilage regeneration. Towards this, we use the self-gelling ability of silk fibroin blends (*Bombyx mori* and *Philosamia ricini*) along with gelatin as a bulking agent. Silk and gelatin interact with each other through entanglement and physical crosslinking. The ink was rheologically and structurally optimized for printing efficiency in printing grid-like structures. The printed 3D constructs show optimal swelling capability, degradability, and compressive strength. Further, the construct supports the growth and proliferation of encapsulated chondrocytes and formation of cartilaginous extracellular matrix as indicated by the increased sulfated glycosaminoglycan and collagen contents. This was further corroborated by the upregulation of chondrogenic gene expression with minimal hypertrophy of chondrocytes. Additionally, the construct demonstrates *in vitro* and *in vivo* biocompatibility. Notably, the ink demonstrates good print fidelity for printing anatomical structures such as human ear enabled by optimized extrudability at adequate resolution. Altogether, the results indicate that the developed crosslinker free silk-gelatin polymer-based bioink demonstrated high potential for its 3D bioprintability and application in cartilage tissue engineering.

6.1 Introduction

Cartilage is a highly specialized connective tissue that possesses limited self-regeneration capability as it is devoid of blood vessels, lymphatic system, and has low cellular density [1]. Thus, any injury to this tissue is retained over the years, degenerating further and eventually leading to degenerative diseases such as osteoarthritis causing impaired joint function with a reduced quality of life. Current treatment strategies include microfracture, mosaicplasty, osteochondral grafts, and autologous chondrocyte implantation (ACI) [400]. These methods have substantially improved the outcomes of defect repair, however they are not long-term clinical solutions and frequently result in the formation of low-performance cartilage, which only postpones the onset of tissue degeneration and subsequent osteoarthritis [401]. Therefore, there is a dire need for potential alternative methods of treatment.

Additive manufacturing of composite tissue constructs through 3D printing has garnered rising popularity in tissue engineering due to its rapid prototyping capabilities and creating complex formulations [402, 403]. This drive is fueled by increased access to affordable printers and general public interest due to its ability to fabricate patient-specific anatomical structures catering to personalized regenerative medicine. The printing device (bioprinter) and the ink (biological ink or bioink) are the two main components of the bioprinting technology. 3D bioprinting permits the dissemination of the bioink (cells in a supporting matrix) in advanced ways with higher spatial resolution so as to mimic the microarchitecture of native tissues [404]. Selection of suitable biomaterials for the bioink is crucial for successful bioprinting. Among the several essential criteria that a bioink need to fulfil are appropriate viscosity that is used to govern the flexibility in creating free-standing constructs during bioprinting and preservation of architectural integrity post bioprinting. Besides, shear thinning for the extrusion of the bioink at low nozzle pressures to guard the cells against physical stressors and smooth printability with high resolution are other essential attributes. Finally, its biocompatibility for immune acceptance, biodegradability to allow integration of the newly formed tissues and biomimetic properties along with its structural and mechanical stability are equally vital criteria [405]. Various physical and chemical crosslinking mechanisms have been used to impart long-term stability to the printed constructs [406]. Among other formats, hydrogels, which form 3D crosslinked hydrated and mechanically supportive niche, are most commonly used as a cell carrier in bioink during 3D bioprinting.

Both natural and synthetic biomaterials have been explored for bioink development. The synthetic polymers have the advantage of robust mechanical properties, better architectural control, and accessibility through simple processing and modifications. However, drawbacks such as immune reaction, high chances of infection, and the effect of degradation by-products have limited their use [407]. These drawbacks can be overcome by using natural polymers, though its controlled printability would still require optimization. In the current study, silk fibroin and gelatin, both natural polymers were chosen as biomaterials for the preparation of bioink. Silk fibroin (SF) is a natural fibrous protein polymer that is extensively studied for various tissue engineering applications owing to its well-defined mechanical properties, biocompatibility, tunable degradation, ease of processing and effectively support cell functionality [408-410]. SF from *Bombyx mori* (mulberry silk) is the most common and well-explored variety. Lately, SF from various non-mulberry wild species such as *Philosamia ricini* (commonly known as Eri) has gained attention due to the superior mechanical properties in comparison to mulberry silk and intrinsic presence of cell binding RGD tripeptide [411]. The primary structure of Eri silk is composed of approximately 100 repeats of alternating polyalanine and glycine domains. Its basic repeating unit is $(alanine)_{12\text{-}13,}$ which is similar to major ampullate silk of spider that contains $(alanine)_{5\text{-}7}$ as repeating unit [412]. The presence of poly-alanine sequence imparts Eri with enhanced mechanical properties. The aforementioned properties establish both *B. mori* silk and Eri silk as suitable polymers for bioink formulations. Blended silk has been used as a biomaterial for creating suitable bioink for 3D bioprinting for various tissues [413-415]. Unfortunately, unassisted bioprinting of silk alone is difficult as it has low viscosity or causes frequent clogging as a result of shear-induced β-sheet crystallization. In addition, slow silk gelation mechanisms to form a hydrogel construct are impediments unless crosslinked with cytotoxic chemicals or pre-gelled prior to printing. Blending of SF from *B. mori* and *A. assamensis* shows self-assembly and induction of β-sheet transitions that result in hydrogel formation [191, 370, 371]. Taking cues from these mulberry and non-mulberry blends, in the current study, we blended silk fibroin from *B. mori* and *P. ricini*, to form a self-blended hydrogel in a cross-linker free approach.

Gelatin, another commonly used polymer is a partial derivative of collagen and is benefitted by superior biocompatibility and relatively lower antigenicity in comparison to collagen. Furthermore, it inherits the favorable properties of collagen to endorse cellular adhesion and chondrogenic differentiation. However, drawbacks such as fast degradation and inferior

mechanical strength limit its exclusive usage. The blending of gelatin with silk would match the required scaffolding properties for cartilage tissue engineering while serving as a bulking agent to produce the optimized printed structure. Silk fibroin component of the blend acted as a structural matrix and provided tunable degradation and enhanced mechanical properties of the gel. The added advantage of using gelatin is its temperature-controlled phase transition in physiological conditions to fabricate three-dimensional structures.

Recently, blends of gelatin and silk from *B. mori* have been reported for extrusion-based 3D printing [416-418]. However, the use of different crosslinking mechanisms in these studies have resulted in inferior printing resolution [419], and while they were suitable for smaller structures, they would prove inadequate for larger constructs that require stability during their lengthier printing time. We believe that it is preferable to avoid crosslinkers since these have various adverse effects such as toxicity to cells, structural alteration to polymers, and cost escalation. Additionally, in the long term, it may lead to heightened cytotoxicity due to the release of residual crosslinker from the implant.

Therefore, the present study aims to develop a cross-linker free silk-gelatin based bioink formulation for cartilage regeneration. The ink was prepared by first blending two different varieties of silk, i.e., *B. mori* and *P. ricini*, and adding gelatin to it. The silk polymers start to self-gel when the two types are mixed. To this gelling silk matrix, gelatin is entrapped forming a viscoelastic ink that is optimal for bioprinting. Further, porcine primary chondrocytes were encapsulated in ink to create the bioink and investigated for its printability, print fidelity, biological and functional assessment, and *in vitro* and *in vivo* biocompatibility for cartilage tissue engineering applications.

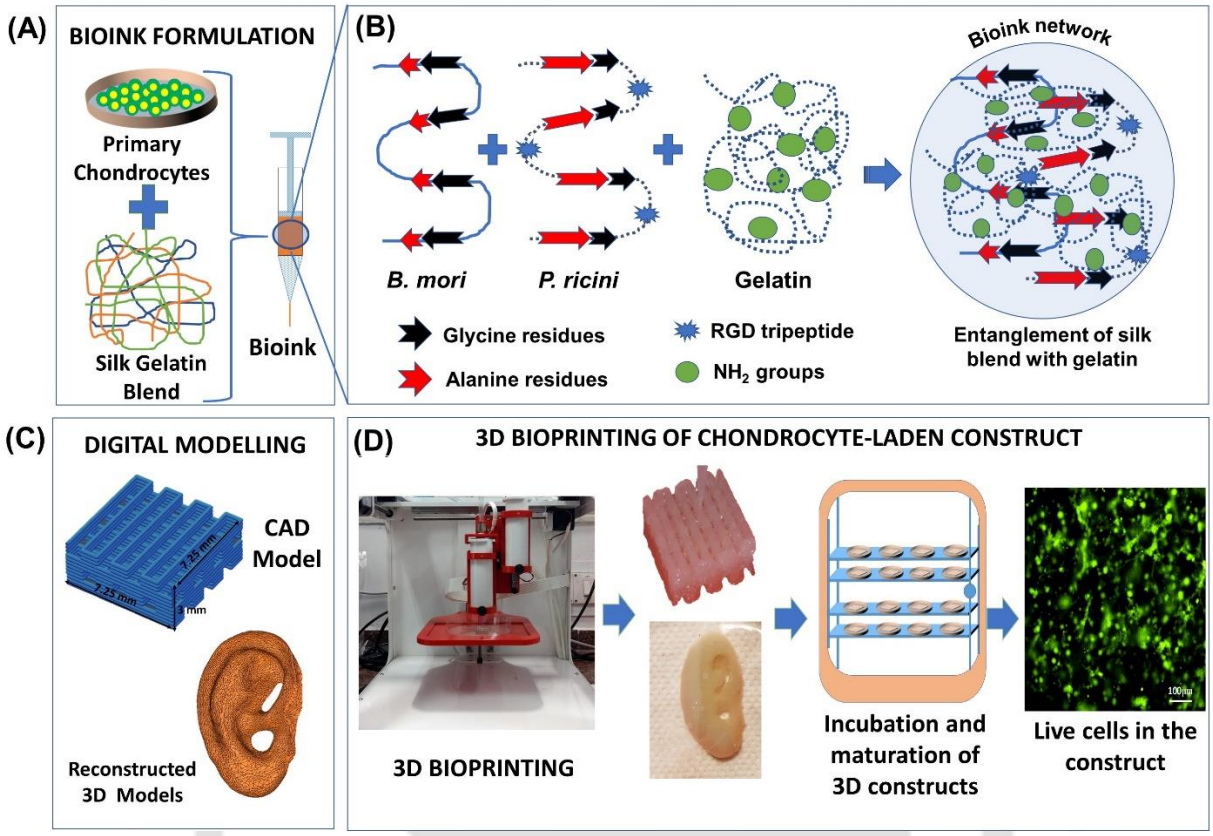

Figure 6.1. *Scheme of the study showing (A) bioink formulation, (B) entanglement and interaction of biopolymers, (C) digital modeling, and (D) 3D bioprinting and maturation of cell-laden construct.*

6.2 Materials and methods

6.2.1 Materials

Silk cocoons of domesticated *B. mori* and matured 5th instar larvae of wild type *P. ricini* were collected from Mangaldoi Silk Farm, Assam, India. Gelatin powder (bovine type B), lithium bromide (LiBr), protease XIV (from *Streptomyces griseus*), 1, 9-dimethylmethylene blue (DMMB), collagenase type I, TRI reagent, chloroform, shark chondroitin sulfate, lipopolysaccharide, neutral buffered formalin (NBF) were acquired from Sigma-Aldrich, USA. Reagents for cellular culture such as Dulbecco's modified Eagle's medium (DMEM), trypsin–EDTA, fetal bovine serum (FBS), penicillin-streptomycin (antibiotic-antimycotic) solution and amphotericin B were acquired from Gibco BRL Rockville, USA, PicoGreen dye, SYBR Green, and IL-1β kit were acquired from Invitrogen. Anti-CD68 antibody (Abcam), calcein-AM (Molecular Probes), and other chemicals used were of analytical grade.

6.2.2 Preparation of silk fibroin solution

The extraction of silk fibroin from the cocoons of *B. mori* was done as per a modified previous protocol [76]. In brief, the whole cocoons were trimmed to smaller fragments and degummed using 0.02 M Na_2CO_3 solution for 20-30 min under boiling conditions. The obtained fibers were cleaned and subjected to a 4 h dissolution at 60 °C using 9.3 M LiBr. The resulting solution was dialyzed using distilled water for 4 h. Silk fibroin from *P. ricini* was isolated from matured 5^{th} instar larvae of *P. ricini* silkworm according to previously reported protocols [254]. Briefly, the protein was extracted out of the silk glands, rinsed in distilled water, dissolved using 1% (w/v) SDS and dialyzed against distilled water.

6.2.3 Preparation of bioink and bioprinting

6.2.3.1 Preparation of silk-gelatin blend and its printability

For the preparation of silk-gelatin blended ink, silk fibroin (from *B. mori* and *P. ricini*) was used in the concentrations range of 0.5-2% (w/v) and gelatin in the range of 1-9% (w/v). The components were blended at various concentrations for optimization. All constituents were UV sterilized. The blends were loaded into a 10 mL syringe and incubated at RT for 20 min, followed by 20 min incubation at 4 °C. The formed blends were checked for printability by extruding it through the extruder of the bioprinter.

6.2.3.2 Cell isolation and expansion

Porcine ear was acquired from a local abattoir, and primary chondrocytes were harvested as reported earlier [420]. In brief, the porcine ear was cleansed, skin removed, cut into small fragments, and rinsed using phosphate buffered saline (PBS, pH 7.4). The pieces were digested using 0.2% protease type XIV (activity of ≥3.5 U/mg) and 0.05% collagenase type IA (≥125 collagen digestion units/mg). The chondrocytes were acquired by centrifuging the digests at 2000 rpm for 5 min. The cells were maintained and expanded using DMEM with 10% (v/v) FBS and 1% (v/v) antibiotic-antimycotic solution.

6.2.3.3 CAD designing

The grids were designed using AutoCAD (Autodesk) to generate the required input file for slicing. Further sliced CAD model GCODES were fed to the 3D bioprinter. The grid-like structures were

printed using the developed silk-gelatin bioink with a 27G needle having an inner nozzle diameter of 250 μm and other specifications, as mentioned in **Table 6.1**.

For the human ear structure, the stereolithography (STL) file was retrieved from an open-source web reference (**https://www.thingiverse.com/thing:304657**). The obtained STL file was then sliced using Slic3r, and the required G-code was obtained. The specifications and dimensions of the ear are mentioned in **Table 6.1**.

Table 6.1. Parameters of the designed construct and 3D bioprinting.

Parameters	Grid	Ear
Nozzle diameter	27 G (250 μm ID)	27 G (250 μm ID)
Layers	12	24
Dimensions (LxWxH)	7.25x7.25x3 mm^3	33x20x12 mm^3
Inter filament distance	0.75 mm	0.10-0.30 mm
Inter layer increment	0.25 mm	0.25 mm
Printing speed	6-8 mm/s	6-8 mm/s
Printing pressure	15-25 kPa	15-25 kPa

6.2.3.4 3D bioprinting using bioink

The printing was performed using Biobot 1 (Allevi, USA) microextrusion bioprinter. The obtained G-codes of the grid-like structure and human ear were communicated to the 3D bioprinter through a PC interface connection. For bioink preparation, chondrocytes were counted and added into the optimized silk-gelatin blended ink at a concentration of 10^6 cells/ml of bioink. The bioink solution was loaded into a 10 mL syringe and kept at room temperature (RT) for 20 min, followed by incubation at 4 °C. The instructed designs were then printed under sterilized conditions at a speed of 6-8 mm/s and pressure of 15-25 kPa. **Figure 6.1** depicts the scheme of the study showing the process of bioink development and its bioprinting.

6.2.4 Physicochemical characterization

6.2.4.1 Rheological characterization

Rheological characterization of bioink was performed using rheometer (Anton Paar MCR 302) fitted with 25 mm diameter parallel plate with a set gap of 1 mm. For each measurement, 1 mL of

bioink was placed on the temperature-controlled testing platform of the rheometer. Temperature based viscosity and modulus was assessed in the range of 4 °C – 45 °C to study their behavior with respect to temperature. The amplitude sweep was performed in the range of 0.01-100% strain (γ) at 25 °C to obtain the yielding point and the linear viscoelastic range (LVER) for the bioink. The frequency sweep was performed within the LVER obtained from the amplitude sweep and by varying the angular frequency from 0.1-100 rad/s at 25 °C. Three interval thixotropy test (3ITT) was carried out by exposing the ink to a sequential low shear (Interval I, strain 0.05%), high shear (Interval II, stain 30%) and again low shear (Interval III, strain 0.05%) intervals to study the deformation and regeneration capability of the bioink.

6.2.4.2 Fourier transform infrared spectroscopy (FTIR)

Structural analysis of the ink was performed using FTIR spectroscopy (Spectrum Two, PerkinElmer) in ATR mode. The samples of pure silk fibroin, pure gelatin, and blend bioink were prepared by freeze-drying. The transmittance readings were measured by accumulating 32 scans at a resolution of 4 cm^{-1} in the spectral region of 4000–600 cm^{-1}.

6.2.4.3 Field emission scanning electron microscopy (FESEM)

The morphology of the 3D printed grid structure, its pore size, and pore distribution was determined using FESEM (Zeiss, Sigma, USA). The printed constructs were lyophilized and sputter coated with gold followed by scanning under FESEM. The micrographs were analyzed with Image J (Wayne Rasband, NIH) software. Further, ImageJ based pore-size distribution, and representative porosity of the constructs was calculated using the particle-size plugin on different FESEM images from the horizontal cross-section of the printed constructs. The porosity distribution has been calculated by evaluating the percentage area of the scaffold surface occupied by the pores as compared to the total visible cross-sectional area of the image.

6.2.4.4 Swelling study

The water retaining property of the 3D printed constructs was assessed using a conventional gravimetric method. For this, the initial dry weight (*Wd*) of constructs was noted, followed by their immersion in PBS (pH 7.4) at 37 °C. At predefined time points, the wet constructs were taken, the excess surface liquid was cleared using filter paper, and the swelled weight (*Ws*) was recorded. The study was conducted under identical conditions in triplicates, and swelling ratio (SR) was obtained by using the equation: $SR = (Ws - Wd)/Wd$

6.2.4.5 Degradation study

The degradation study was performed using protease XIV enzyme (≥3.5 units/mg activity) as per earlier reported protocol [420]. Briefly, the printed construct was treated with 2 U/mL of protease XIV enzyme in PBS and kept at 37 °C. Throughout the study (28 days), the enzyme solution was replaced every three days. Constructs immersed in PBS (without enzyme treatment) were observed parallelly for its stability. The mass remaining (%) was calculated using the formula:

$$\% \text{ Mass degraded (MD)} = [(Wi - Wd)/Wd] \; X \; 100$$

$$\% \text{ Mass remaining} = (100\text{-MD})$$

where, *Wi* is the initial dry weight of construct, and *Wd* is the final dry weight of the construct.

6.2.4.6 Compressive strength

Unconfined compressive strength of the bioprinted constructs was assessed by Instron 5944 (Norwood, MA, USA) fitted with a load cell 100 N. Constructs were placed on the testing platform and studied in displacement control mode at a 5 mm/min rate. For comparison, the non-printed ink fabricated using a mold of the same dimension was used. The stress-strain curve was analyzed and plotted depending on the cross-sectional area and height of the constructs. The compressive modulus of the constructs was determined within the linear region. For cyclic mechanical testing, compressive loading/unloading on the ink was performed to the axial strain of 20% for 20 cycles at a 5 mm/min rate. The hysteresis loop of compressive stress-strain was plotted to determine the deviation in the strength and stress profile of the printed construct and the non-printed hydrogel.

6.2.5 *In vitro* biological assessment

6.2.5.1 Cell viability assessment

The viability of chondrocytes was assayed using calcein-AM staining. The 3D bioprinted constructs with encapsulated chondrocytes were incubated in 4 μM calcein-AM at 37 °C for 20-30 min. Post incubation, the bioprinted constructs were washed using PBS and visualized under a fluorescent microscope (EVOS FL, Life Technologies).

6.2.5.2 *In vitro* histology

Post 14 days of culture, the bioprinted constructs were fixed using 10% neutral buffered formalin (NBF) for 24 h, followed by cryoprotection processing in 15% (w/v) sucrose and 30% (w/v) sucrose solution for 6 h and 12 h respectively. The sucrose fixed constructs were embedded in

Tissue Freezing Medium (Leica Biosystems) and snap-frozen before sectioning. The constructs were sectioned (10-12 μm thick) using cryomicrotome (Leica Biosystems) and stained by 4′,6-diamidino-2-phenylindole (DAPI) and hematoxylin and eosin (H&E) to observe cellular presence and morphology. The imaging of the stained sections was done using a microscope (EVOS FL, Life Technologies, USA).

6.2.5.3 Biochemical analysis

The bioprinted constructs for quantification of DNA and GAG content were digested at 60 °C for 16 h with papain solution (125 μg/mL papain). The content of total DNA was quantified as per manufacturer's protocol using PicoGreen DNA assay kit. In brief, the papain digests were diluted using 1X TE buffer and treated with diluted (1:200) PicoGreen reagent. The resulting fluorescence was recorded at a wavelength of 480/528 nm (excitation/emission). Sulfated GAG (sGAG) was quantified using 1,9-dimethylmethylene blue (DMMB) assay where papain digests (for sGAG in construct) and spent culture medium (for secreted sGAG) was treated with DMMB and the absorbance was taken at 525 nm. The content of total collagen was quantified as per an adapted Tullberg-Reinert method [256]. In brief, the digestion of the constructs was done at 4 °C for 48 h using pepsin (1 mg/mL) and dried in a 96-well plate. Sirius red dye solution (1 mg/mL) was added and incubated with mild shaking for 1 h. The wells were washed with 0.01 normality HCl, the dye-protein complex was resolved using 0.1 normality NaOH and absorbance taken at 550 nm. The printed acellular construct was used as blank for the assay, and its values were negated from the experimental value. To negate discrepancies due to cell numbers and construct sizes, the sGAG and collagen contents were normalized by DNA content and construct weight.

6.2.5.4 Gene expression study

For gene expression studies using real-time PCR, the RNA was isolated by TRI reagent-chloroform method and reverse transcribed to cDNA by reverse transcription kit (Applied Biosystems) using thermal cycler (Takara). Real-time PCR (7500 Real-Time PCR system, Applied Biosystems) was performed using a reaction mixture consisting of cDNA, SYBR Green mix, forward primer, and reverse primer. The run conditions of holding stage (2 min at 50 °C, 10 min at 95 °C) and cycling stage (40 cycles of 95 °C for 15 s, and 60 °C for 45 s) were set. Genes such as collagen type II (*Col-II*), SRY-(sex determining region)-box-9 (*Sox-9*), aggrecan (*ACAN*) and collagen type X (*Col-X*) were assessed and normalized to glyceraldehyde-3-phosphate

dehydrogenase (*GAPDH*). The analysis was done in triplicates using the comparative Ct method ($2^{-\Delta Ct}$). **Table 6.2** lists the details of the primers used.

Table 6.2. Details of primers used for real-time PCR study.

Gene	Sequence	Accession No.
Aggrecan	F 5′-CCCAACCAGCCTGACAACTT-3′ R 5′-CCTTCTCGTGCCAGATCATCA-3′	NM_001164652.1
Sox-9	F 5′-TTCCGCGACGTGGACAT-3′ R 5′-GGCGGCAGGTACTGGTCAAACTC-3′	NM_213843.1
Collagen II	F 5′-CAGGTGAAGGTGGGAAACCA-3′ R 5′-ACCCACGAGGCCAGGA-3′	AF201724.1
Collagen X	F 5′-ACGGGCAACAGCACTATGACC-3′ R 5′-GCACTCCCTGAAGCCTGATCC-3′	NM_001005153.1
GAPDH	F: 5′-TCGGAGTGAACGGATTTGG-3′ R: 5′-CCAGAGTTAAAAGCAGCCCT-3′	NM_001206359.1

6.2.5.5 *In vitro* immunocompatibility

The immunocompatibility of the acellular printed constructs was assessed by exposing the constructs to murine macrophage cell line (RAW 264.7) for 24 h. The spent medium after 24 h incubation was taken and tested for the presence of IL-1β using IL-1β ELISA kit [410]. Briefly, the medium was incubated for 1 h at RT using biotinylated secondary antibody. Then the wells were washed and incubated with streptavidin–HRP solution for 45 min. Further, stabilized substrate reagent was supplemented and kept for 30 min under dark conditions. To end, a stop solution was used, and the amount of IL-1β was estimated by measuring the absorbance at 450 nm. Culture medium with LPS (lipopolysaccharide from *E. coli*) (500 ng/mL) treatment was used as a positive control and without the constructs was used as a negative control.

6.2.6 *In vivo* biocompatibility assessment of acellular ink

In order to assess the immunocompatibility furthermore, *in vivo* macrophage response was evaluated by subcutaneous injection of the ink in female Swiss inbred mice of 30–35 g body weight. The protocols for animal handling were reviewed and sanctioned by the IAEC, WBUAFS, Kolkata, India. The ink was implanted in the subcutaneous pockets of the mice in quadruplets for each time point. The implanted site was monitored for inflammatory responses with no animal death during the duration of the experiment. At predefined time points of day 7 and day 14, animals

were sacrificed by cervical dislocation, and the tissue containing the implanted samples were retrieved and taken for histological processing.

For histological analysis, retrieved ink was fixed using 10% NBF and 30% (w/v) sucrose followed by embedding in Tissue Freezing Medium (Leica Biosystems) and sectioning (10-12 μm thick) using cryomicrotome (Leica Biosystems). Cryosections were stained using H&E to observe cellular infiltration and immuno-stained for CD68 marker with mouse monoclonal antibody to CD68 (1:400 dilutions) using Vectastain universal elite kit and DAB substrate (Vector Laboratories) to observe the infiltration of macrophages within the implanted ink. Stained sections were imaged using an inverted fluorescence and bright-field microscope (EVOS FL, Life Technologies, USA). Further, the digital analysis of IHC stained images was performed using Image-J IHC profiler to give 3D surface plots.

6.2.7 Statistical analysis

The experiments were performed in triplicates (unless otherwise mentioned), and the results are presented as mean ± standard deviation. The data of results from each sampling were analyzed through one-way analysis of variance (ANOVA) *via* Tukey's test (Origin 2019, OriginLabs, USA) and analysis if fulfilling the null hypothesis at $p \leq 0.05$ was considered as statistically significant (#), while at $p \leq 0.01$ as highly significant (##).

6.3 Results

6.3.1 Characterization of the bioink

6.3.1.1 Printability

Printability of the bioink was found to be ideal when the gelatin concentration was raised ≥5% (w/v), and the silk fibroin concentrations of *B. mori* and *P. ricini* were ≥1.5% (w/v) (**Figure 6.2A**). However, gelatin concentrations above 9% and silk fibroin concentrations above 2% in the blend yields a highly viscous bioink and requires higher printing pressures that would contribute to the attenuation of encapsulated cell viability. Printability was also hindered when the gelatin concentration was lowered below 5% (w/v) in ink resulting in low viscosity. Similarly, when the concentration of silk-fibroin lowered below 1% (w/v), the ink was found to be losing the printability due to slow gelation. Thus, a printing range of 5-9% for gelatin and 1-2% for silk fibroin was found to be optimal for cell-laden bioprinting.

6.3.1.2 Rheology

Rheological assessment of the ink was done to study its flow properties (**Figure 6.2B-F**). First, the viscosity of the ink was assessed over a temperature range between 4 ℃ and 45 ℃. The results showed a decrease in the complex viscosity with the increasing temperature reaching the lowest point at 31 ℃, and thereafter the complex viscosity increased with the temperature. Therefore, the complex viscosity of the bioink was lowest at 25℃-35 ℃. Further, the temperature sweep gave the modulus of the bioink over the same temperature range. The storage modulus (G′) represents the elastic nature, while the loss modulus (G″) represents the viscous nature of the bioink. In the temperature range of 4-25 ℃ and 35-45 ℃, the G′ was higher than G″ indicating the gel-like nature while the in-between temperature range of 25-35 ℃ showed a higher G″ than G′ indicating a liquid nature dominance. Next, amplitude sweep was performed to assess the linear viscoelastic range (LVER) of the bioink. The ink showed dominant storage modulus (G′ ~1.5 kPa), indicating their gel-like character. The LVER value shows stability in terms of preventing sedimentation in the sample and determines the limit at which the structure of the construct gets deformed. An LVE range was observed between 0.01-1% strains. The ink began to permanently deform once the range exceeded the yield point seen as the point where G' and G" cross-over happens. After this, the ink flowed like a liquid, as indicated by the higher G". Further, the results of frequency sweep showed a stable ink with dominating G' values over G" at all frequencies. 3ITT test was used to determine the effect of instant shear stress or shear rate coupled with different shear time on deformation and regeneration ability of the ink. In interval I (low shear), the G′ of ~625 kPa was recorded, which reduced to ~5 kPa under high shear (Interval II). Upon returning the shear to the lower level (Interval III), the G′ regained to a value of ~100 kPa. The higher G′ and low G″ in interval I indicate a gel-like nature of the ink which deformed to liquid-like nature in interval II as indicated by the at par modulus, and finally, the ink regained its gel-like nature in interval III indicated by the higher G′. However, as expected the regenerated G′ did not reach the initial values due to the high shear stress-related damage.

6.3.1.3 Structural analysis

Structural analysis of the individual proteins and the transition in the ink due to the blending of silk fibroin and gelatin was analyzed by FTIR spectroscopy (**Figure 6.2G**). The physical crosslinking of ink and the effects of blending on protein secondary structure was analyzed. In case of silk fibroin, the β-sheet structure is characteristically indicated by peaks between 1616–

1637 cm^{-1}, whereas amorphous elements such as α-helices and random coils show peaks between 1638–1662 cm^{-1} [377]. The spectra of the lone silk fibroins and lone gelatin showed intense peaks around 1645 cm^{-1} (amide I), 1530 cm^{-1} (amide II), and 1235 cm^{-1} (amide III), which are the characteristic absorption peaks of proteins. However, a slight shift in the amide I peak of the silk-gelatin blend to 1622 cm^{-1} was observed.

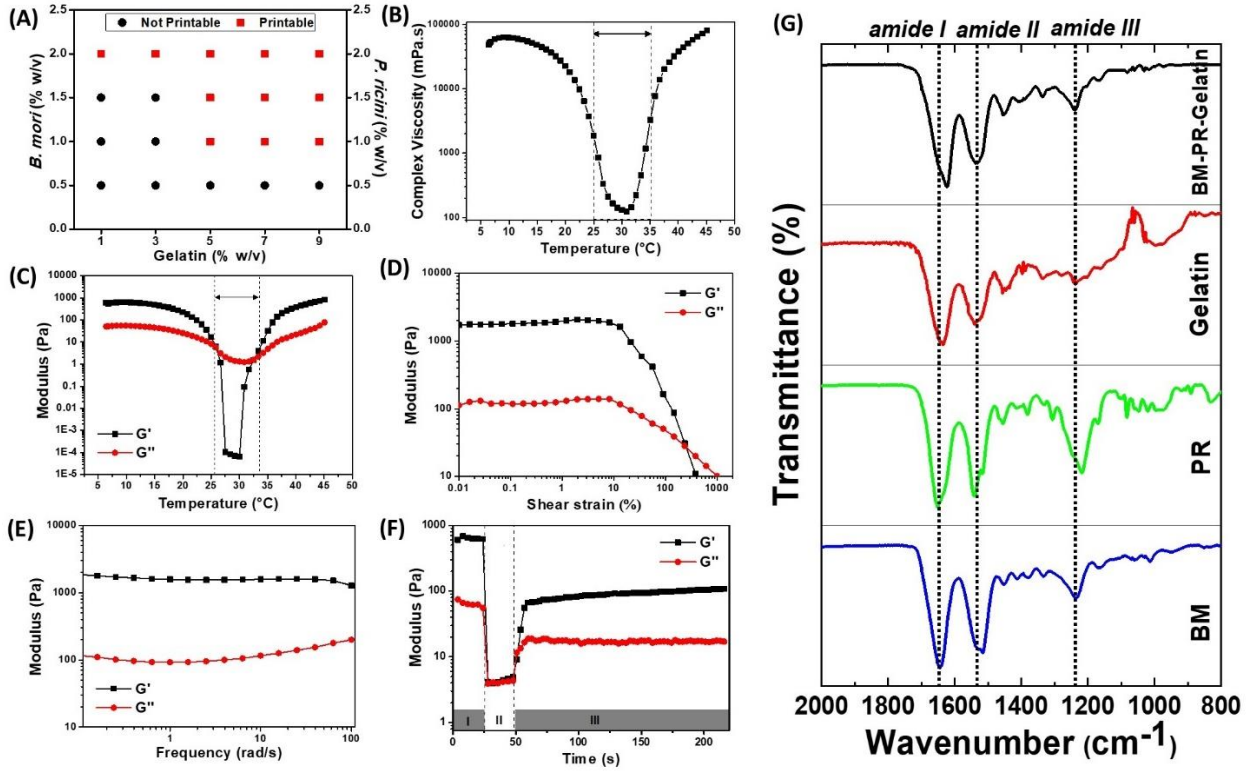

Figure 6.2. *(A) Printability of the ink, (B-F) Rheological assessment- (B) Complex viscosity of the ink from 5°C-45 °C, (C) temperature sweep profile indicating the modulus over the temperature range, (D) amplitude sweep, (E) frequency sweep, (F) 3 interval thixotropy test of the ink (G' represents storage modulus, and G'' represents loss modulus), and (G) Fourier-transform infrared (FTIR) spectra of the ink.*

6.3.2 Print fidelity and geometry of the printed construct

To ascertain the print fidelity of the ink, grid-like structure, and anatomical structure such as human ear was printed according to the specifications mentioned in **Table 6.1**. The constructs were printed with high fidelity, good printability, and dimensional stability. The constructs retained their structural integrity according to gross morphology analysis (**Figure 6.3A-B**). The printed grid construct was 7.25×7.25×3 mm^3 in dimension with inter filament distance of 0.75 mm and inter

layer increment of 0.25 mm. In the case of the anatomical structure resembling human ear, the printed construct was stable without losing its shape or collapsing during the process of printing in spite of the larger dimensions of 33×20×12 mm^3. The high shape fidelity and suitable viscosity of the ink indicated its ability to print larger anatomical structures. The structural geometry studied by FESEM analysis revealed heterogenous distribution of pores (**Figure 6.3C**). Around 94% of the pores were in the range of 0-80 µm, 5% in the 80-160 µm range and 1% in the 160-240 µm range. The porosity followed a similar trend with 79% in the 0-80 µm range, 18% 80-160 µm range and 3% in the 160-240 µm range.

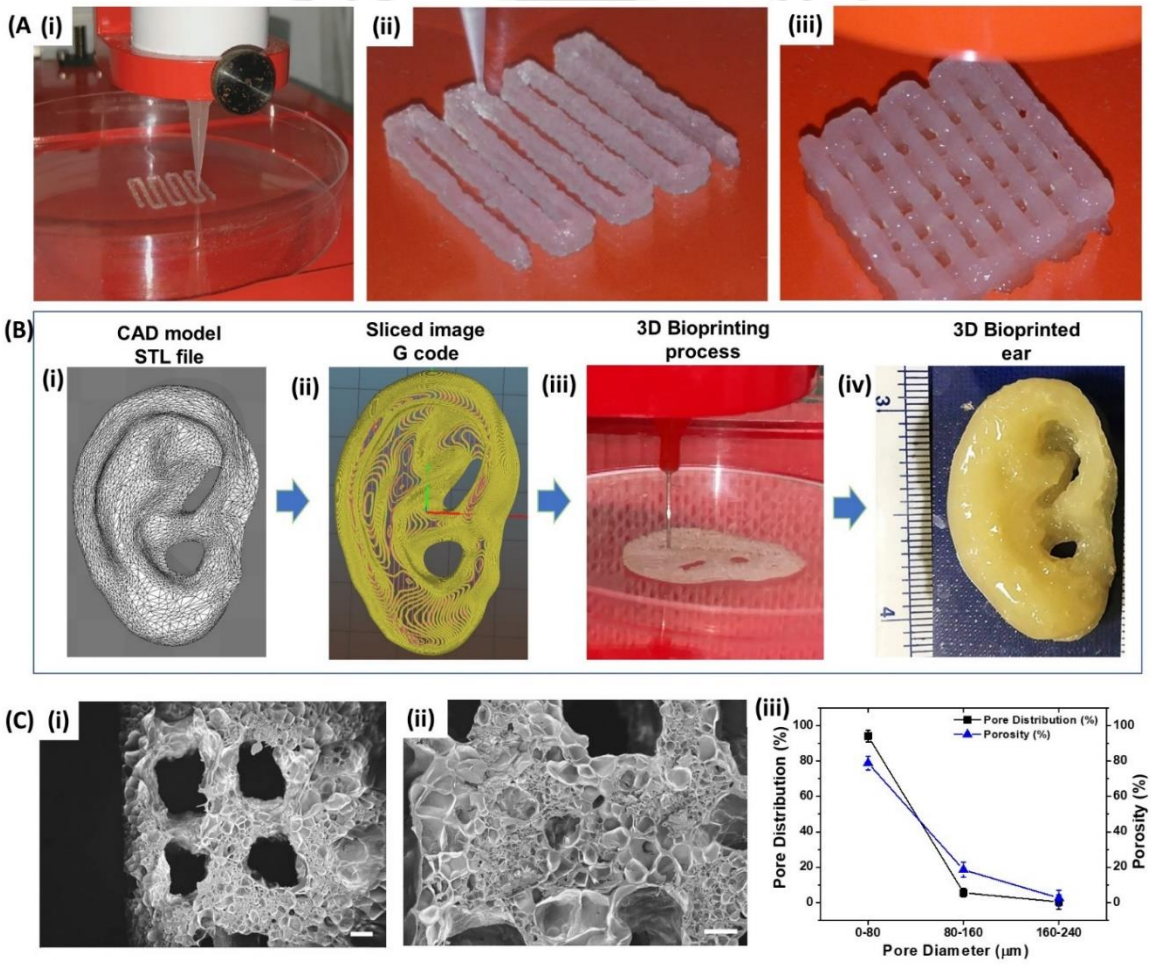

Figure 6.3. *Print fidelity of the ink showing (A) printing of grid-like structure (i) extrusion of the ink through the nozzle, (ii) initial few layers, and (iii) formed grid-like pattern; (B) fabrication of human anatomical ear (i) CAD model and generated STL file, (ii) generated G code using slicer, (iii) printing process, and (iv) printed ear structure. (C) Geometry of the printed construct (i, ii) field emission scanning electron micrographs, (iii) pore geometry and porosity of the printed construct. Scale Bar for (C) is 200 µm*

6.3.3 Physicochemical characterization of the printed construct

6.3.3.1 Swelling study

The swelling behavior of the bioprinted constructs is depicted in **Figure 6.4A**. The constructs showed a rapid swelling within the first 6 h and attained a stable equilibrium in about 12 h. The water uptake capacity increased with time until an equilibrium was reached. The constructs reached a maximum swelling ratio of ~10 due to the higher water retention capacity of silk and gelatin. The ability of the construct to swell vouched for its liquid retention indicating its ability to assist as a nutrient reserve for the cells.

6.3.3.2 Degradation study

The degradation or stability of the construct was assessed by treatment with Protease XIV enzyme. The enzyme treatment caused significant degradation ($p \leq 0.01$) of the construct as compared to the PBS treatment (**Figure 6.4B**). The construct experienced degradation of around 60% in 28 days when treated with enzyme and around 16% in PBS in a period of 28 days. This shows the stability of the construct in PBS and its capability to degrade under physiological conditions.

6.3.3.3 Compression study

Further, a uniaxial compressive test was carried out to assess the compressive strength of the construct. The compressive strain-stress at break was higher in case of 3D printed constructs (9.8 kPa at break) as compared to the non-printed ink (3.8 kPa at break). **Figure 6.4C** shows the compressive stress and compressive strain curve, and the relation between them is non-linear. The compressive stress reached a maximum value before yielding at a compressive strain of 34% and 45% for non-printed ink and the bioprinted construct, respectively. There was no significant difference in the compressive modulus of the bioprinted construct at lower strains of 10%, 20%, and 30%. The compressive modulus at maximum compression was 30 kPa and 114 kPa for non-printed ink and the bioprinted construct, respectively (**Figure 6.4D**). **Figure 6.4E** shows the cyclic loading-unloading curve indicating the energy dissipation capacity of the printed construct. Compressive strain from 0 to 20% was applied with an intention to keep the value close to the actual strain value in normal physiological conditions. The curves indicated typical hysteresis. The hysteresis slope of the first compressive cycle was highest reaching stress of 193 kPa, and it eventually decreased in the successive curves over the time suggesting that it does not regenerate to its original structure; however, it did not collapse. Later it reaches a certain equilibrium and

becomes congruent. The unloading curves follow a different path than the loading curves indicating energy dissipation during the cycles.

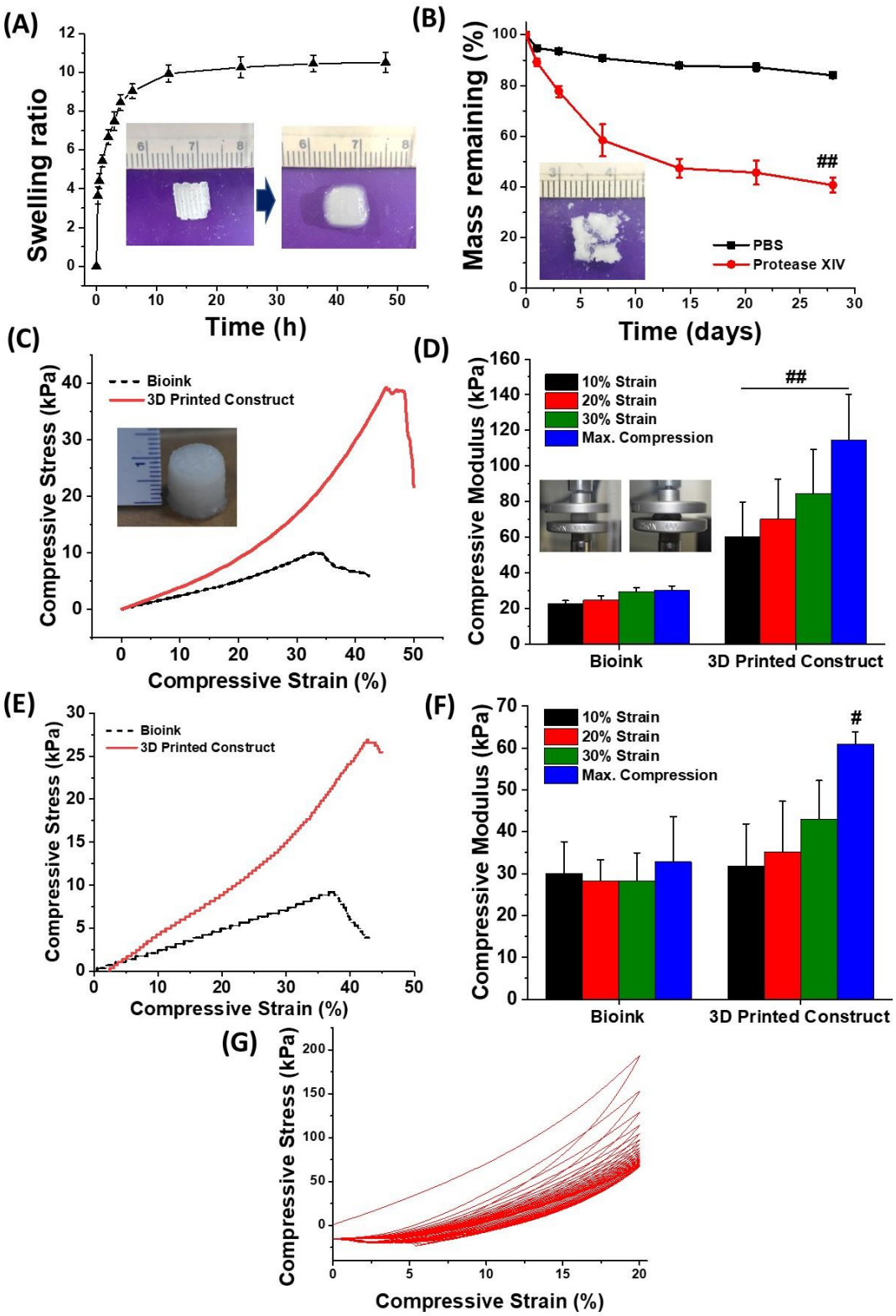

Figure 6.4. *(A) Swelling ratio of the constructs, (B) degradation of the construct in Protease XIV enzyme, (C) compressive stress-strain curve, (D) compressive modulus, and (E) cyclic loading/unloading compressive test of the printed construct. (n=3, $^{\#\#}p \leq 0.01$)*

6.3.4 *In vitro* biological assessment

6.3.4.1 Cell viability and *in vitro* histology

The viability of the encapsulated chondrocytes in the bioprinted construct was evaluated using calcein-AM staining. **Figure 6.5A** shows the live cells indicated by the green fluorescence generated due to the entry of calcein-AM into the cells and its hydrolysis by intracellular esterases producing fluorescence. The construct indicated a uniform distribution of chondrocytes with typical spherical morphology. No significant cell death was noted in the constructs over the 14 days. Further, the *in vitro* cultured cells were fixed and histologically examined using DAPI, which is a blue-fluorescent dye extensively used to detect nuclei in fluorescence microscopy. **Figure 6.5B** shows the presence of cells in the DAPI stained cryosections**.** Complementing the calcein-AM staining, the cells are homogenously distributed and arranged in the grid-like structure. Additionally, H&E staining showed the attachment and homogenous presence of cells all over the construct (**Figure 6.5C**).

6.3.4.2 Biochemical study

The quantification of DNA, secreted sGAG, and collagen content were done using biochemical analysis of the chondrocyte encapsulated bioprinted constructs. The DNA content on day 14 showed significant increment ($p \leq 0.01$) in the constructs as compared to day 1 (**Figure 6.5D i**). The constructs exhibited a DNA content of 900 ng on day 14 in comparison to 430 ng on day 1($p \leq 0.01$). A similar trend was seen on the normalization of DNA with the construct mass, showing ~ 2-fold increase on the 14th day (**Figure 6.5D ii**) ($p \leq 0.01$). Further, the total sGAG content secreted in the culture media and deposited in the construct was quantified using DMMB assay. There was a significant increase in sGAG content after a culture period of 2 weeks ($p \leq 0.01$). The sGAG content quadrupled from 132 μg (day 1) to 512 μg (day 14) (**Figure 6.5E i**). Among the total sGAG, 50% constituted of the secreted amount in media. Further, total sGAG normalized to DNA exhibited an increment (~2 fold) on day 14 in comparison to day 1 (**Figure 6.5E ii**) and its normalization to construct mass showed a similar trend with ~3.5-fold increase (**Figure 6.5E iii**) ($p \leq 0.01$). The content of total collagen in the construct increased from 62 μg (day 1) to 218 μg (~3.5 fold) on day 14 (**Figure 6.5F i**) ($p \leq 0.01$). DNA normalized content of collagen showed a

~1.7-fold increase on day 14 as compared to day 1 (**Figure 6.5F ii**) ($p \leq 0.05$). Similarly, on normalization with construct mass, the construct exhibited higher collagen content (~3.5 fold) on day 14 (**Figure 6.5F iii**) ($p \leq 0.01$).

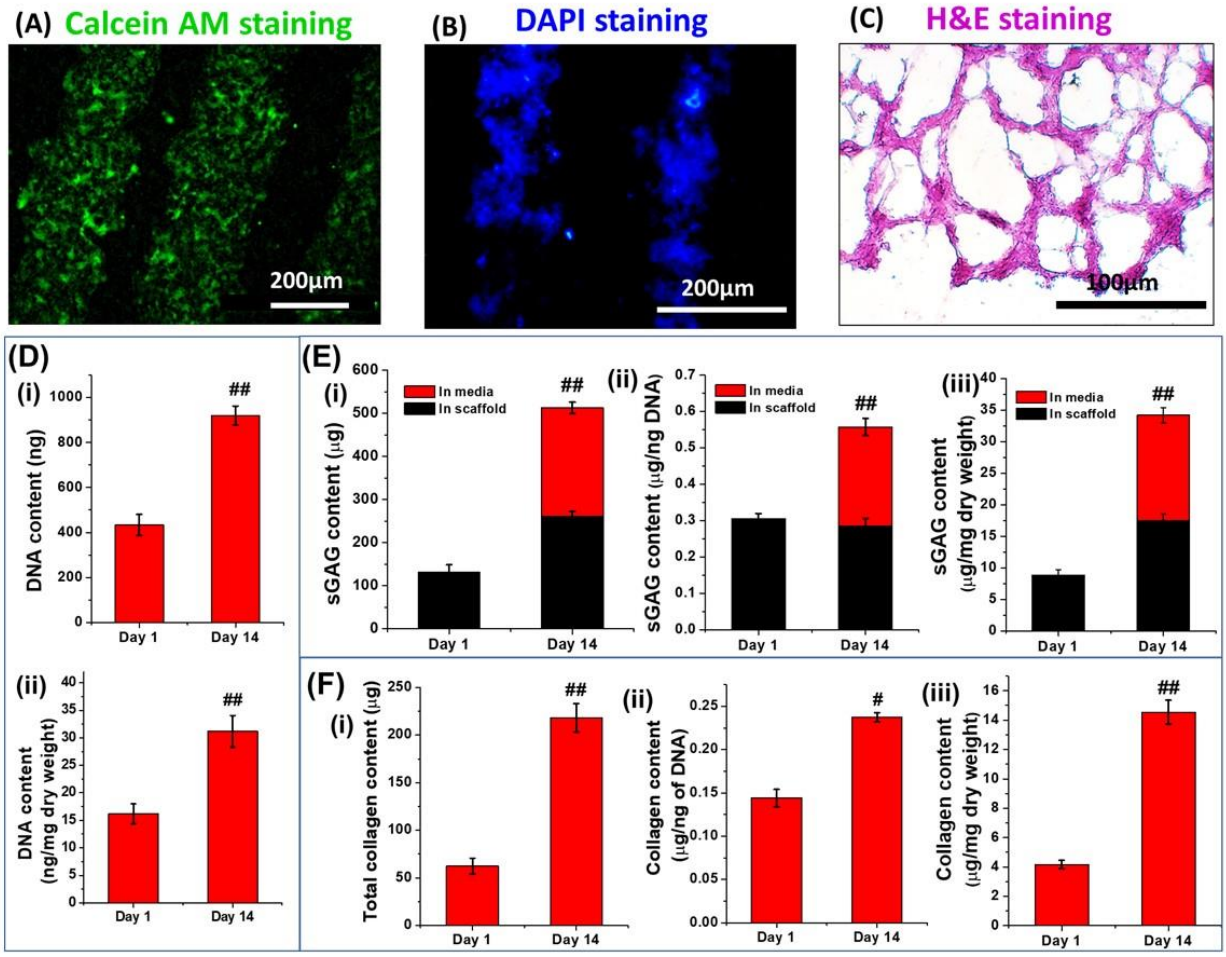

Figure 6.5. *(A) Calcein-AM stained images of the chondrocytes laden bioprinted construct after 14 days of culture. Histological assessment of in vitro cultured bioprinted constructs post 14 days of culture (B) DAPI labeled bright blue cells, and (C) H&E-stained section of the construct. Biochemical quantification showing (D) DNA content- (i) total DNA (ii) dry weight normalized DNA content; (E) GAG content- (i) total GAG, (ii) DNA normalized GAG content, (iii) dry weight normalized GAG content; and (F) collagen content- (i) total collagen, (ii) DNA normalized collagen content, (iii) dry weight normalized collagen content. (n = 3, $^{\#\#}p \leq 0.01$, $^{\#}p \leq 0.05$).*

6.3.4.3 Gene expression and *in vitro* immunocompatibility

Chondrogenic genes were analyzed after a culture period of 14 days using real-time PCR (**Figure 6.6A**). The results indicated an upregulation of the chondrogenic genes (*Col-II*, *ACAN*, *Sox-9*) on day 14 in comparison to day 1. Significantly higher expression levels of *ACAN* (~4 fold), *Col-II*

(~6 fold) and *Sox-9* (~3.7 fold) on day 14 were obtained in comparison to day 1 ($p \leq 0.05$). For hypertrophic marker C*ol-X*, the constructs did not exhibit any significant difference. Proinflammatory cytokines such as IL-6, IL-1β, and TNF-α are formed predominantly by activated macrophages and are chiefly involved in inflammatory reactions. IL-1β is one of the most crucial cytokine mediators of inflammation and host responses to infection. We studied the tendency of the printed constructs to stimulate the secretion of IL-1β from murine macrophage cells (RAW 264.7) (**Figure 6.6B**). After 24 h of incubation, the secretion of IL-1β was comparable with the negative control TCP and significantly lower (~2.5 fold) as compared to positive control LPS ($p \leq 0.01$).

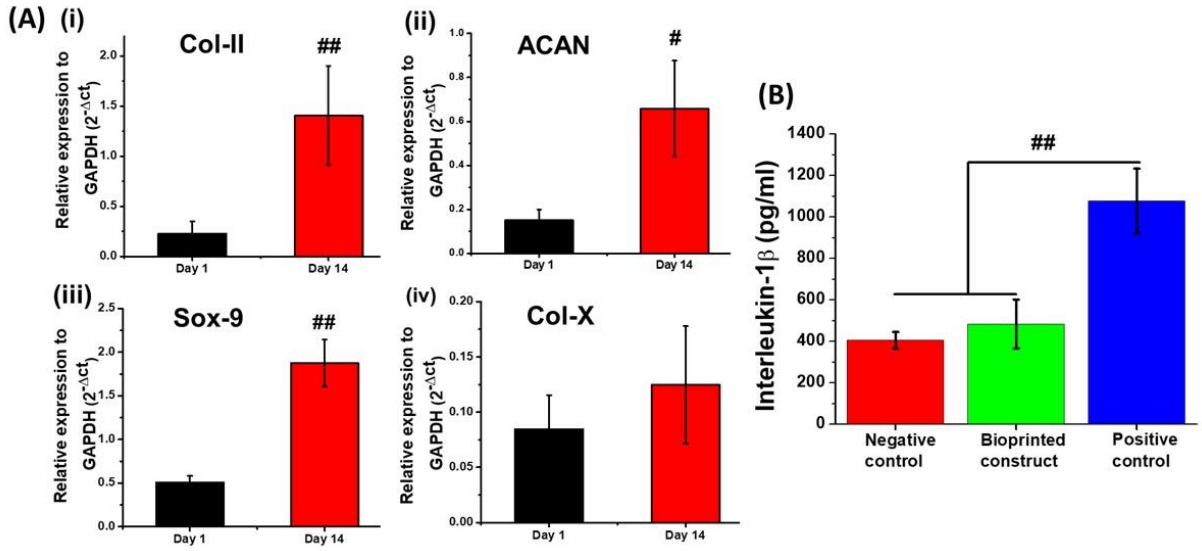

Figure 6.6. *(A) Relative expression of chondrogenic genes (i) collagen II, (ii) aggrecan, (iii) Sox-9, and (iv) collagen X post 2 weeks of culture. (B) ELISA-based assessment of IL-1β secreted from mouse macrophage RAW 264.7 cells induced by printed constructs. TCP (tissue culture plate) and LPS (lipopolysaccharide) were taken as negative and positive controls, respectively. (n = 3, $^{\#\#}p \leq 0.01$, $^{\#}p \leq 0.05$)*

6.3.4.3 *In vivo* cytocompatibility

The *in vivo* biocompatibility of the bioink was assessed by subcutaneous implantation of the acellular bioink blend in mice model. The retrieved implants were histologically assessed using H&E (**Figure 6.7A**) staining; antibody tagged DAB stained (**Figure 6.7B**), and IHC stained (**Figure 6.7C**). H&E staining demonstrated the distribution of cells in the bioprinted construct, suggesting infiltration of surrounding cells. To see the migration and presence of macrophages, the sections were stained with CD68 antibody. CD68 is a marker found in the cytoplasmic granules

of macrophages. 3D surface plot for the CD68 stained cells for infiltrating macrophage population revealed greater infiltration of the macrophages cells at day 7 as compared to day 14 (**Figure 6.7D**). This indicated inflammation in the early phase of post-transplantation healing and an eventual regression of the immune response with suppression of the inflammation in 2-weeks.

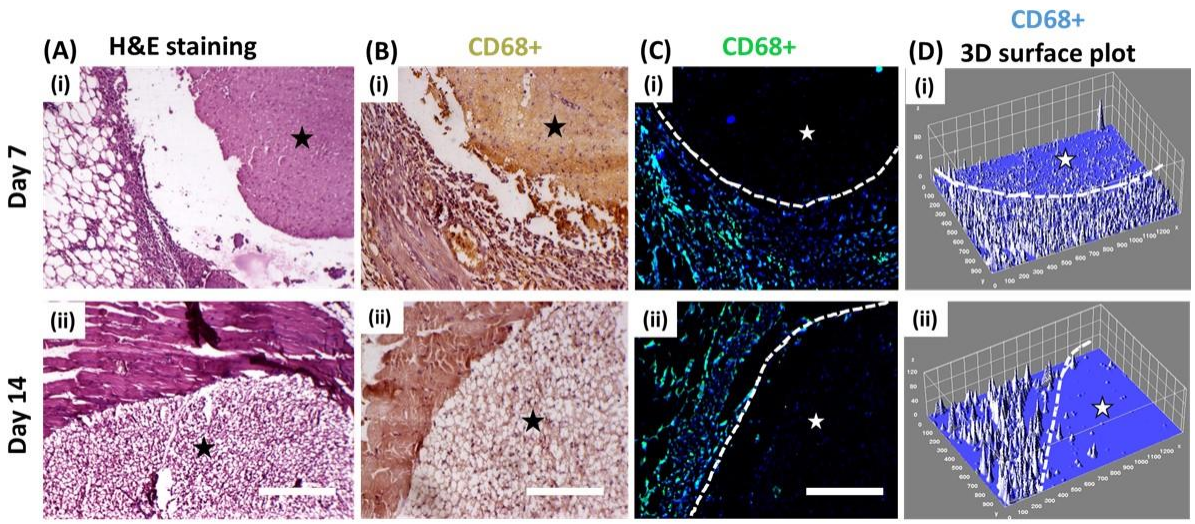

Figure 6.7. *Histological assessment of subcutaneously implanted ink in mice. (A) H&E-stained sections retrieved after (i) 7 days and (ii) 14 days of implantation. Representative images showing CD68 +/- cells using (B) DAB staining, and (C) Immunohistochemistry (IHC) staining for macrophages on (i) day 7 and (ii) day 14. The nuclei are counterstained in blue. (D) 3D surface plot of IHC stained images showing distribution of CD68 positive cells on (i) day 7 and (ii) day 14 using the ImageJ (NIH, USA) software. Star represents the implanted ink (Scale bar: 200µm).*

6.4. Discussion

Currently, most of the research in 3D bioprinting is focused on the development of various bioinks with appropriate performance in terms of their rheological behavior, biocompatibility, and mechanical properties. Hydrogels are the most commonly used supporting matrices in the bioink due to their hydration and swelling capability. The hydrogel encapsulates cells during its gelation, and its hydrated environment favors viable proper cell-cell interaction. Several hydrogels composed of synthetic and natural polymers have been explored, with and without crosslinking to dictate their properties. However, keeping in mind the cytotoxicity, complexity, and high-cost factor associated with most of the crosslinkers, approaches free from crosslinkers have become the most compatible option. Towards this end, we have developed a crosslinker free silk-gelatin bioink for cell-laden 3D bioprinting of cartilage tissue. The silk (blend of *B. mori* and *P. ricini*) component

in the bioink provides structural framework and gelatin provides viscosity and acts as a bulking agent. Additionally, the shear thinning rheological behavior of silk [421] and the thermoreversible action of gelatin at physiological temperatures makes them especially attractive materials for 3D printing. Due to its solubility in aqueous conditions and poor stability, gelatin must be chemically or enzymatically crosslinked or blended with other robust polymers. In general, chemical cross-linking can increase stability, but not without toxic side effects [422]. Even with crosslinking, in some cases the gels of gelatin are not strong enough, and therefore it's physical crosslinking with a polymer such as silk might be required to yields gels with robust mechanical properties and circumvent other less desirable chemical crosslinking options. The blending of gelatin with silk enables its physical entanglement and crosslinking [423]. In the current study, this entanglement and physical crosslinking are enhanced as a result of self-gelling behavior when a mulberry (*B. mori*) and a wild type (*P. ricini*) silk variety are blended.

The development of bioink requires thorough optimization of its composition. Therefore, the printability of the ink with various compositions was tested by extruding it through the printer nozzle. The results indicated that the optimized ink composition of 1.5% (w/v) *B. mori*, 1.5% (w/v) *P. ricini* silk fibroin and 7% (w/v) gelatin was found suitable in terms of its extrusion and possess the necessary gel strength and shear-thinning within the pressure extrusion range of the bioprinter while ensuring high cellular viability [424]. The ink was further validated rheologically for its flow properties using dynamic oscillatory rheometer. First, the temperature-dependent complex viscosity of the ink was studied. The results of the study indicated that the complex viscosity of the ink was lowest in the temperature range of 25 ℃-35 ℃. Similar results were obtained in the temperature-based modulus study where the ink was predominantly solid in nature (indicated by the higher G′) in, the lower and higher temperatures and liquid in nature (indicated by the higher G″) in the mid region. This behavior might be attributed to the two components of the ink blend. In the initial phase, the viscosity decreased as the gelatin starts to undergo gel to sol transition with the increase in temperature, however at temperatures above 37 ℃ we see the viscosity increases again, this might be due to the gelation of the silk component in the ink. Therefore, this provides us with the appropriate window for printability in the temperature range of 25℃-35 ℃. Amplitude sweep indicated the LVER of the ink that was used to carry out the frequency sweep. The frequency sweep indicated stable gel properties with dominating G′ at all frequencies. Further, thixotropy test applying an alteration of high and low shear rates to the ink was performed. The

structure undergoes shear-mediated thinning under high shear followed by regeneration of the structure once the shear is lowered. The results indicated that the ink recovered well to a dominating elastic state. Thus, the rheological assessment exhibited good viscoelastic properties of the ink with a suitable window for printing that potentially helps in the creation of an adequate environment for the cells.

To ascertain the influence of gelatin on silk crystallization due to the physical hindrance presented by the entangled silk and gelatin, we examined their FTIR signatures. The typical amide peaks (II and III) of the constituent polymers (lone silk fibroins and lone gelatin) were maintained in the silk-gelatin blend as well, indicating the consistency in the structural composition of the ink. However, the amide-I showed a red shift to a lower wavenumber, indicating increased β-sheet content leading to the insolubility of the ink. The decreased solubility of the ink showed that silk and gelatin were physically crosslinked with gelatin entangled in the β-sheet structures of the silk. Our results were in agreement with the previous study by Rodriguez *et al.* [419].

To ascertain the print fidelity of the ink, first the grid-like structure was printed. The ink showed commendable printing fidelity, good printability, and dimensional stability of the constructs. After the successful bioprinting of simple grid-like structure, the anatomically complex human ear was 3D printed with high fidelity. The structure remained stable throughout and post-printing without any shrinkage and displayed good texture. However, as a test of feasibility, only acellular ear constructs were printed. Further, cellular anatomical cartilage structures could be fabricated by replacing acellular ink with cell-laden bioink. Taking the geometry of the printed constructs into consideration, the FESEM studies of the printed construct showed a grid-like porous matrix with internal interconnected pore network. Additionally, the constructs possessed suitable porosity. A high porosity in the range of 80-90% is optimal for *in vitro* cellular adhesion and migration along with the exchange of nutrients and oxygen [425].

The printed constructs were then characterized physicochemically and mechanically. The swelling ability and degradability of the constructs are two crucial requirements for the success of a scaffold/matrix in tissue engineering. The swelling or water retention ability helps to lessen nutrients and liquid loss from the matrix. Our results suggested good swelling or water uptake ability of the construct, which was in accordance with other similar reports of silk-gelatin hydrogels [426, 427]. Biodegradability is another essential property that allows the constructs to

degrade within the implantation site at the same rate of tissue formation and to avoid a second surgical intervention for its removal from the body. To ascertain the degradation of the constructs, enzyme protease XIV was used due to its indiscriminate and multiple locale silk protein cleaving nature [420]. The results of our study exhibited the construct to be biodegradable, which can potentially be tuned by variation in the concentration of the ink components. Compressive mechanical properties of the constructs are suggestive of their capability to withstand loads in the native tissue environment.

Our goal was to create a printed construct that functions in a biomechanically similar manner to native cartilage tissue. Hydrogels of polymers such as collagen, and chitosan provide a suitable environment for chondrocyte cell growth and matrix deposition; however, their poor mechanical strength often hinders their physiological loading during clinical implantation. Ideally, compressive modulus of the hyaline articular cartilage ranges approximately from 0.2–2 MPa [428]. The maximum compressive modulus of our bioink (0.1 MPa) was lower than that of native articular cartilage however, this value is well within the range for soft tissue regeneration [308, 429]. Markstedt *et al.* used cellulose nanofibers with alginate for bioink formulation and showed compressive modulus of 75-250 kPa for the printed constructs with cell viability of 86% after 7 days indicating its potential for cartilage tissue engineering application [430]. In case of bioprinted constructs, the mechanical properties mimicking that of native cartilage can be tuned by increasing the polymer concentration and the crosslinking density of the gels, however such bioinks would form a dense network that could compromise with the biological functionality. Cells have shown to function well at lower polymer concentrations with sufficient flexibility for proliferation, differentiation, and new matrix formation [431]. Additionally, studies using mesenchymal stem cells (MSCs) have shown that softer substrates favor chondrogenic differentiation, whereas stiffer substrates induce terminal hypertrophy [432].

For tissue engineering applications, the most important requirement of 3D printed constructs is the long-term survival of cells within the bioink as the pneumatic pressure applied during printing might be stressful to the encapsulated cells [424]. We printed cell-laden grid-like constructs using the bioink and evaluated the cell viability post-bioprinting. The assessment after 2 weeks indicated that the cells were viable and homogenously distributed as shown by the green calcein-AM staining. This was in agreement with previous reports using silk and gelatin polymers [418, 419].

The use of silk-gelatin constructs with exclusive micro spatio-architecture acts to deliver a favorable microenvironment for growth and proliferation of chondrocytes. Additionally, the presence of intrinsic tripeptides–RGD in both gelatin [433] and *P. ricini* silk [411] might have contributed to the enhanced cellular adhesion and viability. Furthermore, increased DNA content of the cell-laden constructs provided the quantitative evidence of enhanced cellular proliferation.

Histological assessment was performed to qualitatively estimate the *in vitro* ECM formation in the constructs. The DAPI and H&E staining of the bioprinted construct showed the presence of homogenously distributed cells. The formation of neo-tissue was evaluated biochemically by quantification of ECM components such as sulfated GAG (sGAG) and collagen type II. Sulfated GAGs are key ECM components of cartilage which play important roles in hydration, cellular communication, and motility [434]. These are produced by chondrocytes and thus echoes the potential of the construct to form new ECM. Similarly, collagen type II is a major component of the cartilage ECM that stabilizes the matrix. It makes up 90%–95% of the collagen (60% of the dry weight of the cartilage) in ECM and forms interwoven fibrils with proteoglycan like aggrecans [435]. The bioprinted constructs in our study showed a higher sGAG and collagen content after 14 days. This provides a good support to develop a hyaline-like cartilage tissue with a high content of collagen. Therefore, in agreement to previous studies [418, 436] , the results of our study showed increased ECM formation, specifically the sGAG and collagen. Interaction between chondrocytes and ECM determine several biological processes vital to cartilage homeostasis, which is further enhanced by the presence of RGD tripeptide in the constructs. These integrin binding sites stimulate intracellular signaling and promote subsequent ECM formation [355].

The capability of the bioprinted constructs for chondroprotection and chondrogenesis was assessed by expression of chondrogenic marker genes namely *Sox-9, ACAN*, *Col-II*, and *Col-X*. The results indicated an increased expression of *Sox-9,* which is an early chondrogenic transcription factor regulating chondrocyte differentiation and cartilage-specific ECM production [437]. Similarly, the increased expression of *ACAN* was seen in the bioprinted constructs. *ACAN* is a chondrogenic redifferentiation marker and a major structural component of cartilage. Thus, it plays a vital role in the maintenance of cartilage structure and function [438]. *ACAN* self-assembles upon its secretion into a supramolecular structure and helps the cartilage to resist compressive loads through osmotic resistance [439]. Similarly, the increased expression *Col-II*, a major cartilage

ECM component indicates a suitable ECM production necessary for cartilage regeneration. Overall, the encapsulated chondrocytes in the bioprinted constructs successfully expressed chondrogenic phenotypes. Moreover, no significant increment in the expression of *Col-X* suggests that chondrocytes did not demonstrate any significant hypertrophy. *Col-X* is a standard marker for chondrocyte hypertrophy [440].

Implantation of biomaterials can elicit an immune response resulting in tissue breakdown, hindrance in healing, and probable graft rejection [441]. Thus, before *in vivo* implantation, the *in vitro* quantification of IL-1β secretion (a pro-inflammatory cytokine) was performed by exposing the printed constructs to murine macrophage cells which are the key regulators to immune responses to foreign materials [408, 441]. The results showed that the construct did not exhibit any adverse immune response, thereby approving the construct for *in vivo* implantation.

Further, *in vivo* biocompatibility of the ink was evaluated by its subcutaneous implantation in a mice model. The results showed an initial cellular infiltration at week 1 and more significantly by week 2 as the ink starts to degrade. Further, CD68, a macrophage marker was stained for analyzing the infiltration of the macrophages within the implanted constructs. The results showed a small population of CD68 positive cells on day 7 that eventually regressed by day 14. This suggests an initial mild inflammatory phase that is later subdued by the proliferative phase of the host non-immunogenic cells. This was in accordance with a previous study [370]. Overall, the study indicated that the construct did not provoke any prolonged immune response, thereby demonstrating its *in vivo* biocompatibility.

Taken together, the present study exhibits a suitable bioink blend for 3D bioprinting of cell-laden constructs for potential cartilage tissue regeneration applications. The bioink blend can be bestowed with tunable degradability and mechanical strength by regulating the concentration of the blend components. Furthermore, the crosslinker free fabrication avoids any possible cytotoxicity or complexity due to chemical crosslinking. Economically, the process is very affordable as it uses cost-effective polymers and avoids the usage of costly chemicals and crosslinkers; and no post process curing is required. Therefore, the high printing resolution due to enhanced physical crosslinking between silk and gelatin and the aqueous, toxic free, facile processing and fabrication makes the developed bioink an affordable alternative to the present cross-linker based bioprinting ink blends.

6.5 Significant findings

1. Herein, a crosslinker free silk-gelatin bioink was developed for 3D bioprinting of cartilage tissue constructs. The shear thinning behavior of silk and the high viscosity of gelatin improved the printability of the bioink.
2. The ink formulation was optimized by modulating the concentrations of silk and gelatin and assessing the extrudability, structural, and rheological parameters to print grid-like structures.
3. The bioprinted 3D constructs possessed suitable microarchitecture, porosity, swelling capability, degradability, and a compressive modulus.
4. Further, the constructs showed good cell viability, higher ECM production, along with an increased sGAG and collagen content. Additionally, gene expression studies revealed upregulation of chondrogenic genes with no significant hypertrophy of the encapsulated chondrocytes.
5. *In vitro* histological assessment indicated the homogenous distribution of the cells in the bioprinted grids. Also, the absence of any significant macrophage stimulated IL-1β levels indicated *in vitro* biocompatibility.
6. Upon their *in vivo* subcutaneous implantation, the acellular constructs supported cell migration into the construct with low infiltration of CD68 positive macrophages demonstrating minimal immune response and *in vivo* biocompatibility.
7. Most importantly, the study showed the feasibility of printing anatomical structures such as human ear enabled by optimized extrudability at adequate resolution.
8. Altogether, the silk-gelatin polymer-blend bioink demonstrated high feasibility for its potential applications in cartilage tissue engineering, which necessitates customizable bioprinting through structural, mechanical, and biological feasibilities.

Chapter 7

Mimicking Early-Stage Osteoarthritis *In Vitro* by 3D Bioprinting Inflamed Osteochondral Unit for High-Throughput Anti-Inflammatory Drug Screening Applications

The study aimed to establish a 3D bioprinted physiologically relevant cytokine induced *in vitro* early-stage OA-model, subsequently to evaluate the effects of widely used anti-inflammatory drugs on the attenuation of the diseased conditions. To induce OA-like pathological conditions, we targeted the inflammatory cascade associated with OA pathogenesis, specifically the combination of IL-1β and TNF-α cytokines. Further, the attenuation of the diseased conditions was validated using CXB and RHN anti-inflammatory drugs and the roles of involved signaling pathways such as the MAPK, and NF-κB were hypothesized.

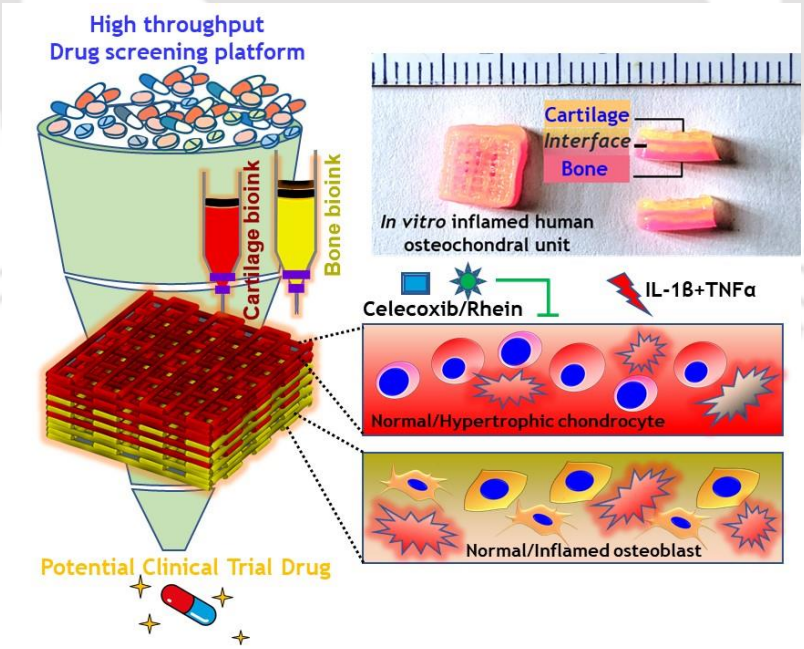

The work embodied in this chapter is submitted for publication as follows:

Yogendra Pratap Singh, Joseph Christakiran Moses, Ashutosh Bandyopadhyay, and Biman B. Mandal. " Mimicking early-stage osteoarthritis *in vitro* by 3D bioprinting inflamed osteochondral unit for high-throughput anti-inflammatory drug screening applications." (*Manuscript under revision in Advanced Functional Materials*)

ABSTRACT

Silk-based 3D bioprinting of osteochondral tissue offers unique opportunities for enabling precise pharmacological interventions in osteoarthritis (OA). The study is a first investigation into the screening potential of anti-inflammatory drugs using bioprinted inflamed human osteochondral units. The biomimetic hierarchical geometry is bioprinted using silk-based bioinks encapsulating pre-differentiated stem cells, creating an *in vitro* model. Inflammation is stimulated in the model, using tumour necrosis factor-alpha (TNF-α) and Interleukin-1 beta (IL-1β) pro-inflammatory cytokines. The resultant degeneration, akin to OA, is flagged by key markers like sulfated glycosaminoglycan (sGAG), collagen, alkaline phosphatase (ALP), and downregulation of osteochondral transcript levels. In the next step, screening of anti-inflammatory drugs is validated using celecoxib (CXB) and rhein (RHN). Consequently, in the inflamed constructs, the initial upregulation of the key inflammatory mediators (nitric oxide (NO), Prostaglandin E2 (PGE2)), is subsequently downregulated, post-drug treatment. In addition, catabolic markers (matrix metalloproteinases (MMPs) and aggrecanase-1), indicative of hypertrophic and apoptosing, chondrocytes, are significantly downregulated in the treatment groups; while the transcript and protein levels required for osteochondral health are attenuated. Therefore, the *in vitro* model mimicked the inflammation in the early stages of OA, and corroborated, a potential high-throughput platform for screening novel anti-inflammatory drugs in OA therapeutics.

7.1 Introduction

Osteoarthritis (OA) is a degenerative and inflammatory joint disease of the osteochondral joint involving a complex cross-talk between the superficial articular cartilage, the underlying subchondral bone, and synovium [30]. It is a multifactorial disease caused by hereditary, aging, obesity, joint injury, or defect; and is characterized mainly by stiffness, pain, crepitus, and loss of flexibility and functioning of the joint. OA is a foremost cause of disability worldwide affecting more than 303 million people [442], with no proven single, generalized intervention for its treatment. The current treatment methods of osteoarthritis include non-pharmacological management such as education, exercise, physiotherapy, etc; pharmacological management such as opioids, acetaminophen, non-steroidal anti-inflammatory drugs (NSAIDs), etc; and ultimately the surgical interventions such as osteotomy, and arthroplasty [443]. Most of the present OA treatment methods help to alleviate pain and symptoms without halting or repairing the damaged tissue mainly due to poorly understood molecular mechanisms of OA initiation and progression. Understanding the interplay between osteochondral tissues, the symptoms and the involved signalling pathways would provide better therapeutic options for OA [444]. In this regard, many models have been described over the years to study the OA disease pathology [155, 445]. Of particular interest is the use of animal models which provides a close reflection of different stages of OA, and remains the hallmark for studying disease prognosis and validating OA therapeutics in the preclinical setting. Dependence of such pre-clinical models for high throughput screening of multi-score drug targets has copious disadvantages and cost ineffective. Moreover, animal models lack the biomimetic human pathophysiological conditions, require a longer timeline, and associated ethical concerns [446]. Thus, a paradigm shift in reducing, refining and replacing (3R philosophy) animal models is desired in pharmacological industry standpoint, making *in vitro* models lucrative.

Designing suitable *in vitro* OA models akin to the preclinical models and human physiological conditions is of paramount importance. Consensus on the use of monolayer culture-derived or 3D cultures derived from *ex vivo* explant cultures from osteoarthritic joints have innate drawbacks. The tendency of dedifferentiation or finite diseased tissue sources plaque such models [447]. Moreover, OA is a multi-faceted disease wherein the heterogenous tissue involving the hyaline cartilage, subchondral bone, synovium all contribute to the disease in varying degrees of severity. Mimicking all these conditions *in vitro* is quite tedious. However, *in vitro* models help us in

delineating this multi-factored pathological circuitry into segregated sovereign pathways not adulterated by a myriad of other non-specific pathways, to precisely understand the downstream signaling of that pathway. Thus, from a pharmacological standpoint decoupling the molecular cross-talk, and targeting a particular pathway for the different drugs available helps in ease of monitoring, assessing its efficacy more effectively.

Towards a physiologically relevant approach, the osteochondral unit consisting of bone and cartilage tissue must be used as a model platform. Use of only the cartilage phase as reported previously [155, 448-450] does not fully recapitulate the osteochondral unit, as there is an intricate cellular cross-talk between the osteoblast, osteocytes in the subchondral bone, and the chondrocytes in the hyaline cartilage [30]. The differential response to biochemical trigger by these cells concomitantly aid in OA development. Though strategies for developing anisotropic gradient osteochondral interfacial units have been reported, for high-throughput screening applications as *in vitro* drug testing platforms, conventional strategies of scaffold fabrication such as freeze-drying [408], electrospinning [451], and hydrogel casting [452] would be laborious and inconsistent. Moreover, seeding cells within such conventionally formed scaffolding structures and maintaining similar cell densities would again be challenging. Thus, 3D bioprinting overcomes these drawbacks and permits the creation of a multi-layered gradient construct allowing the investigation into this interplay between tissues.

Bioprinted osteochondral grafts have the potential for early clinical translations [453]. A suitable biomaterial matrix plays a crucial role in the successful bioprinting of a tissue. Previously, we had developed silk fibroin (SF) based bioinks and showed their efficacy to bioprint stem cell-laden osteochondral unit [147]. SF from mulberry silkworms (*Bombyx mori*) and non-mulberry silkworms (*Antheraea assamensis*) possess varied hydropathicity due to the difference in the amino acid sequence rendering it their characteristic properties [454]. These properties of SF allow the formation of a conducive hydrogel network that is injectable and supports cell survival and maturation [455]. Additionally, the blend of these two silk types exhibits cumulative benefits of the two individual silks and supports the fabrication of tissues such as cartilage [456], meniscus [212], and osteochondral tissue [147]. In the current study, we used a mixture of *B. mori* and *A. assamensis* SF along with polyvinylpyrrolidone (PVP) K90 (molecular weight 360,000) as a bulking agent, which was used as the cartilage ink. As opposed to the cartilage ink, the bone inks

were incorporated with nano-hydroxyapatites to confer osteoinductive traits. The developed bioink was optimized, characterized for print fidelity, rheological property, permeability, and ability to form a biomimetic osteochondral unit in a recent report from our group [147]. In the current study, we have used this established bioink system for bioprinting of cell encapsulated human osteochondral unit towards the establishment of an *in vitro* OA model.

An increasing amount of reports suggests that inflammation plays a pivotal role in the progression of OA [457]. Thus, extensive research now focuses on understanding and targeting the inflammatory pathways and developing suitable anti-inflammatory drugs for the therapeutic management of this early OA stage. TNF-α and IL-1β are two well-known pro-inflammatory cytokines that play crucial roles in the onset and progression of OA pathogenesis, which is secreted by the inflamed synovium. They work by activating the inflammatory response *via* the expression of important pathways, such as the mitogen-activated protein kinase (MAPK) and nuclear factor kappa B (NF-kB). They also increase the synthesis of prostaglandin E2 (PGE2) and initiate the synthesis of ADAMTS in chondrocytes [458, 459]. These cytokines are crucial mediators causing enhanced catabolism and dysregulating remodeling at the interface thus altering the joint haemostasis. They have been used individually [158, 460] or in combination [461, 462] for the induction of OA-like conditions. The synergistic effect of both the cytokines and their role in OA encouraged their use in the present study for induction of OA-like conditions. To the best of our knowledge, this is the first report wherein an inflamed human 3D bioprinted osteochondral unit is developed for modeling the early-stage OA involving inflammatory onset.

NSAIDs are the most commonly used and well-explored anti-inflammatory and analgesic drugs that work *via* the inhibition of the prostaglandin forming enzyme, cyclooxygenase (COX) [463]. Celecoxib (CXB) (commercially available as Celebrex), is an NSAID and a selective inhibitor of COX-2 with comparable cardiovascular safety at moderate doses to non-selective NSAIDs [464]. Celecoxib is effective for the management of pain and inflammation and has received US Food and Drug Administration (USFDA) agreement for some conditions including OA [465]. Rhein (RHN), an active metabolite of diacerein, belongs to the class anthraquinone and is used in OA therapeutics. It works by inhibiting the action and inflammatory effects of IL-1β [466]. Due to their specific mode of action, both these drugs have been explored individually [467, 468] and in combination [469] towards OA management. A combination of diacerein and celecoxib is being

tested for efficacy and safety in patients with knee OA in a Phase-4 clinical trial (ClinicalTrials.gov Identifier: NCT03404479). Thus, we used these two well-studied anti-inflammatory drugs for validation of our *in vitro* model for the attenuation of OA-like condition indicating its potency as a drug-screening platform.

The study consists of 2 main aims: (i) establishment of an inflamed osteochondral unit to mimic early-stage OA-like diseased condition, and (ii) validating the model as a drug testing platform. To induce OA-like pathological conditions, we targeted the inflammatory cascade associated with OA pathogenesis, specifically the combination of IL-1β and TNF-α cytokines. Further, the attenuation of the diseased conditions was validated using CXB and RHN anti-inflammatory drugs. Herein, we also investigated relevant pathways involved such as the MAPK, and NF-κB signaling and their involvement in the inflammatory cascade. Overall, in this study, we aimed to establish a physiologically relevant cytokine induced *in vitro* early-stage OA-model, subsequently to evaluate the effects of widely used anti-inflammatory drugs (CBX and RHN) on the attenuation of the diseased conditions.

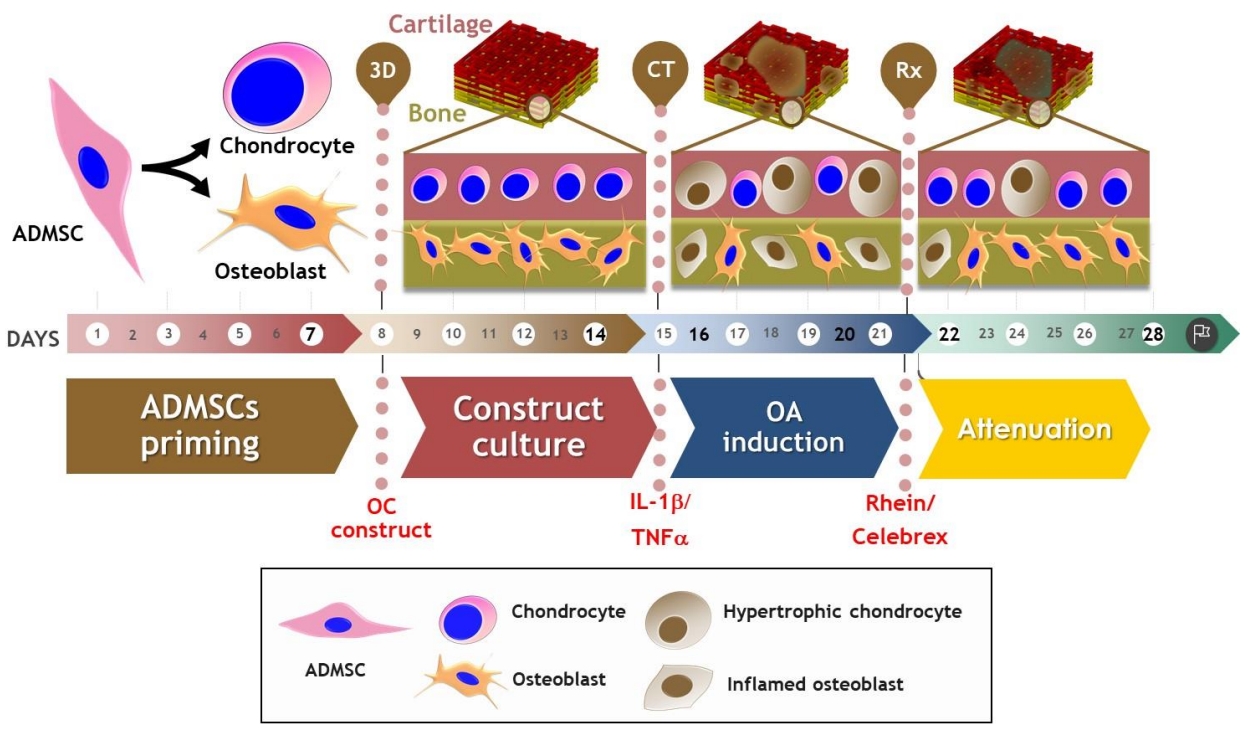

Figure 7.1. *Schematics and timeline of the study. [Abbreviations- ADMSC: adipose-derived mesenchymal stem cells; 3D: 3D bioprinting; CT: cytokine treatment; Rx: drug treatment; OC: osteochondral]*

7.2 Materials and methods

7.2.1 Bioink formulation and bioprinting

The bioink used for bioprinting the osteochondral unit was formulated using silks (*Bombyx mori* silk fibroin, BMSF; and *Antheraea assamensis* silk fibroin, AASF), a hydrophilic bulking agent polyvinylpyrrolidone (PVP) K90 (Sigma-Aldrich, USA), and nano-hydroxyapatite as additives, reported previously in details [147]. Briefly, two bioinks were formed, one for the cartilage phase (a mixture of BMSF and AASF along with PVP) and the other for the bone phase (silk blends, PVP along with nanohydroxyapatite as additives). The bioink was enzymatically crosslinked using horseradish peroxidase (HRP, 10 U) (Sigma-Aldrich, USA) and hydrogen peroxide (H_2O_2, 1.65 μM) (Merck, India). The pre-gelled polymers were mixed with human adipose-derived mesenchymal stem cells (ADMSCs) primed towards chondrocytes and osteoblasts for the cartilage and bone bioink, respectively, and gelled by incubating at 37 °C for 30 min. The ADMSCs were primed in chondrogenic induction media (DMEM supplemented with 5% (v/v) FBS, 100 nM dexamethasone, 50 μg/mL ascorbic acid, 50 μg/mL L-proline and 1X ITS Insulin-Transferrin-Selenium mix) for chondrogenesis and osteogenic induction media (DMEM supplemented with 5% (v/v) FBS, 10 mM β-glycerophosphate, 100 nM dexamethasone and 0.2 mM ascorbic acid) for osteogenesis for a period of 7 days before encapsulation into the bioink at a density of 10^7 cells/mL. The hierarchical geometry (consisting of a cartilage phase, a bone phase, and an interface) was designed using a 3D builder software program (Microsoft Corporation, USA) and sliced to obtain G-Code. The designed osteochondral unit was bioprinted using micro extrusion-based printer BIO X bioprinter (Cellink, USA) at print speeds 8-12 mm/s and extrusion pressures of 40-50 psi using 25 G blunt-ended stainless steel needles. The bioprinted constructs were maintained in osteochondral media (equal parts of chondrogenic and osteogenic media) for 7 days with media change every 48 h.

7.2.2 Cytokine and drug treatment

Cytokines: IL-1β and TNF-α, (Sigma-Aldrich, USA) were used to induce inflammation (early-stage OA-like conditions) in the cell-laden bioprinted constructs. Each construct was exposed to a mixture of IL-1β (10 ng/mL) and TNF-α (10 ng/mL) in basal media (DMEM supplemented with 5% (v/v) FBS, 1% GlutaMAX supplement (Gibco) and 0.5% antibiotics) for a period of 1 day and 5 days. The cytokine containing media was replenished every 48 h. For the validation to attenuate the OA-like pathological conditions, the bioprinted constructs were treated with rhein (RHN,

Sigma-Aldrich, USA) and celecoxib (CXB, Sigma-Aldrich, USA) individually at a concentration of 1 μM in basal media for 1 day and 7 days. Considering the period of cytokine induction (5 days) before the drug treatment, the 1-day drug-treated constructs are represented as day 7 and the 7 days constructs as day 14 in the study towards a continuous timeline. An untreated group (UNT) was used as a control in the study. The drug-containing media was replenished every 48 h.

7.2.3 Cell viability

The viability of cells post-printing was assessed using calcein-AM in combination with ethidium homodimer (Sigma-Aldrich, USA) staining. The cell-laden constructs were rinsed with 1X PBS and incubated with a mixture of calcein-AM (40 nM) and ethidium homodimer (20 nM) and incubated for 20 min at 37 °C. Post-incubation, the dye-treated constructs were washed, and the fluorescent dye (green and red) was visualized using a microscope (EVOS FL, Thermo Fisher Scientific, USA).

7.2.4 Biochemical assays

The cultured constructs were enzymatically digested using papain buffer at 60 °C for 16 h. The sGAG was assessed using DMMB assay as per previously reported protocol [408]. The digested sample was incubated in the presence of DMMB and the absorbance was recorded at 525 nm. The standard curve was prepared using chondroitin sulfate. The total DNA in the constructs was estimated as per instructions of the PicoGreen DNA assay kit (Invitrogen, USA). In brief, the digested samples were diluted with 1X TE buffer followed by the addition of Quant-iT PicoGreen reagent (1:200 dilution). The fluorescence at excitation/emission of 480/528 nm was noted using a microplate reader (Tecan infinite M200 PRO). The standard curve for analysis was generated using lambda phage DNA.

Collagen content was estimated as per the previously reported method [408]. In brief, the constructs were enzymatically digested with a pepsin cocktail for 48 h at 4 °C and dried out at 37 °C for 24 h. To this, Sirius red dye solution was supplemented and incubated for 1 h and washing with 0.01 normality HCl. Further, 0.1 normality NaOH was used to resolve the dye-sample complex and absorbance at 550 nm was recorded. Rat-tail collagen type I (Sigma-Aldrich, USA) was used to generate the standard for analysis.

Alkaline phosphatase (ALP) assay was executed to ascertain the biomineralization state of the human ADMSCs within the bioprinted constructs following our previously published reports [147,

410]. Briefly, the constructs were broken down with cell lysis buffer (20 mM Tris-HCl (Merck, India) (pH 7.5), 5 mM $MgCl_2$ (Himedia, India), 150 mM NaCl (Himedia, India), and 0.5% Triton-X100 (Sigma-Aldrich, USA)). The lysate was used to assess the active ALP content by measuring the hydrolysis of p-nitrophenol phosphate, pNPP (substrate) to yellow colored product p-nitrophenol (λmax = 405 nm) using a microplate reader. The DNA content was also assessed using Quant-iT Picogreen ™ assay kit (Thermo Fisher Scientific, USA) from the cell lysate. The ALP activity is represented as diethanolamine (DEA) units, where 1 DEA unit indicates the enzyme needed to hydrolyze 1 µM of pNPP at pH 9.6 (in 1M diethanolamine buffer) at 25° C. The data is also presented by normalizing with DNA content as DEA units/ µg DNA.

7.2.5 Nitric oxide (NO) quantification

The quantity of nitric oxide was measured using the Griess reagent kit (Thermo Fisher Scientific). The cell culture supernatant from the treated constructs was taken and mixed with Griess reagent (N-(1-naphthyl) ethylenediamine dihydrochloride, sulfanilic acid in 5% phosphoric acid). This blend was then incubated for 30 min and the absorbance was measured using a Multiskan Sky Microplate Spectrophotometer (Thermo Scientific) at 548 nm and the amount of nitrite was quantified using a standard curve of sodium nitrite.

7.2.6 Prostaglandin E2 (PGE2) and ADAMTS4 assay

The cell culture supernatant was collected at definite time points and the level of PGE2 and ADAMTS4 was determined using the PGE2 ELISA kit and ADAMTS4 ELISA kit (Krishgen Biosystems, India) respectively, as per the manufacturers' instruction. Briefly, the samples were incubated in biotin conjugate and HRP conjugate for 60 min at 37 ℃ followed by washing, the addition of substrates, and incubation at 37 °C for 10 min under dark conditions. Finally, the stop solution was supplemented and absorbance at 450 nm was measured using Multiskan Sky Microplate Spectrophotometer (Thermo Scientific).

7.2.7 Matrix metalloproteinases (MMPs) assessment

The conditioned media from the bioprinted constructs was collected at different time points and assessed for the MMPs activity (MMP-1 and MMP-13) through collagen zymography, following a previously published protocol with changes [470]. Briefly, overnight serum-starved conditioned media of constructs were collected and total protein content was estimated using micro-Bradford assay (Sigma-Aldrich, USA). 50µg of the total protein was resolved in 10% polyacrylamide

resolving gel under non-reducing conditions with 0.15 mg/mL purified rat tail collagen type-I (Gibco, USA). The resolved gel was then incubated pre-incubation buffer [50 mM Tris-HCl (pH 7.5), 2.5% (w/v) Triton X-100, 5 mM CaCl2 and 1 mM ZnC4H6O4] for 1 h, followed by renaturation buffer [50 mM Tris-HCl (pH 7.5), 1% (w/v) Triton X-100, 5 mM CaCl2 and 1 mM ZnC4H6O4 (Sigma-Aldrich, USA)] overnight at 37°C [410]. To visualize the clearance zones due to MMP activity, the gels were then stained with 0.5% Coomassie Brilliant Blue R-250, followed by destaining in 40% (v/v) methanol, 10% (v/v) glacial acetic acid. The collagenolytic bands appeared as clear zones against a blue background. Densiometric analyses were carried out using ImageJ (NIH, USA) from the images obtained from a gel documentation system (Bio-rad Gel Doc XR+, USA).

7.2.8 Gene expression analysis

The bioprinted and cultured constructs were taken in TRIzol reagent, disintegrated on ice, and RNA was extracted using acidic chloroform-phenol [410]. RNA (500 ng) was reverse-transcribed *via* a high-capacity reverse transcription kit (Invitrogen, USA) in a thermal cycler (Veriti PCR, Applied Biosystem, USA). Quantitative real-time PCR (qPCR) was executed in a 7500 real-time PCR system (Applied Biosystems, USA) using Power SYBR Green dye (Invitrogen, USA). The relative expression of the genes (collagen-II (*Col-II*), aggrecan (*ACAN*), SRY-(sex-determining region)-box-9 (*Sox-9*), osteocalcin (*OCN*), runt-related transcription factor 2 (*RUNX2*), matrix metalloproteinase 13 (*MMP13*), cyclooxygenase-2 (*COX-2*), and Interleukin 6 (*IL-6*)) were performed at established settings of holding stage (2 min at 50 °C, 10 min at 95 °C) and cycling stage (40 cycles of 95 °C for 15 s, and 60 °C for 45 s). Endogenous housekeeping gene beta-actin (β-actin) was used for normalization. **Table 7.1** list the primers used in the study.

Table 7.1. List of genes and the primer sequences used for qPCR.

Gene	**Primer sequence**	
	Forward (5'-3')	**Reverse (5'-3')**
Col-II	TGAATGGAAGAGCGGAGACT	CCACCATTGATGGTTTCTCC
ACAN	ACCCCTGAGGAACAGGAGTT	GTGCCAGATCATCACCACAC
Sox-9	ACGGCTCCAGCAAGAACAAG	TTGTGCAGATGCGGGTACTG
OCN	GTAGTGAAGAGACCCAGGCG	CGGATTGAGCTCACACACCT
RUNX2	GACTGTGGTTACCGTCATGGC	ACTTGGTTTTTCATAACAGCGGA

MMP13	CTTGATGCCATTACCAGTC	GGTTGGGAAGTTCTGGCCA
COX-2	CCCTTGGGTGTCAAAGGTAA	GCCCTCGCTTATGATCTGTC
IL-6	GCCTTCTTGGGACTGATGCT	TGCCATTGCACAACTCTTTTCT
β-actin	GGCATCCTCACCCTGAAGTA	GGGGTGTTGAAGGTCTCAAA

7.2.9 Protein expression analysis

Immunoblots were performed to assess the protein expression levels of NFκB, ADAMTS4, Collagen-2, and Collagen-X. The bioprinted constructs at different time points were subjected to cell-lysis following our previously published method [147]. Briefly, constructs were disintegrated in ice-cold NP-40 cell lysis buffer added with protease inhibitors 1 mM phenylmethylsulfonyl fluoride, 10 mM sodium fluoride, 1 mM ethylene glycol-bis(β-aminoethyl ether)-N,N,N′,N′-tetraacetic acid (Sigma-Aldrich, USA) *via* sonication (Sonic Vibra-cell, Sonics Inc., USA; 20% amplitude, 10 s with 2 s ON/ OFF cycles). The lysate was estimated for total protein concentration using micro-Bradford assay and 30 μg of protein sample was resolved under reducing condition in 10% polyacrylamide condition. The resolved bands were transferred by wet transfer to PVDF membranes (Merck, USA) and the immunoblots were probed for the presence of target proteins. The primary antibodies used are as follows: rabbit polyclonal to NF-kB p65 (Abcam, UK; 1:200 dilutions), rabbit monoclonal against COX-2 (Abcam, UK; 1:1000 dilutions), mouse monoclonal against COL-X (Abcam, UK; 1:1000 dilutions), rabbit polyclonal to ADAMTS4 (Abcam, UK, 1:10000 dilutions), while rabbit polyclonal to beta Actin (Abcam, UK, 1:1000 dilutions) was used as endogenous house-keeping and loading control. The secondary antibodies used are as follows: HRP conjugated antibodies either secondary goat anti-mouse IgG (Abcam, UK, 1:10000 dilutions) or secondary goat anti-rabbit IgG (Abcam, UK, 1:10000 dilutions). The chemiluminescence signal was developed using an ECL kit (Bio-rad, USA) and detected using a gel documentation system (Bio-rad Gel Doc XR+, USA). Subsequent densiometric profiling of the bands was done using ImageJ (NIH, USA).

7.2.10 Statistical analysis

All experiments were performed in triplicates unless mentioned otherwise. Data are represented as mean ± standard deviation. Statistical analysis was performed by one-way analysis of variance (ANOVA) using Tukey's test (Origin 2018, OriginLabs, USA). *$p \leq 0.05$ was considered as statistically significant and **$p \leq 0.01$ as highly significant.

7.3 Results

7.3.1 Establishing cellular viability in the bioprinted constructs

The cellular viability and shaped fidelity of the constructs were assessed post-printing with calcein-AM that stains the live cells green, and ethidium homodimer which stains the dead cells red. For this, human ADMSCs primed towards osteogenic lineage (in bone ink) or chondrogenic lineage (in cartilage ink) were encapsulated and bioprinted as shown in **Figure 7.2A-B**. The bioprinted constructs retained their grid shapes suggesting their stability and showed good cellular viability as observed from the green-stained live cell in the construct. The healthy constructs showed more viable cells as compared to the disease-induced constructs (**Figure 7.2C-D**). The reduction in viability may be plausible to the chondrocyte and osteoblast apoptosing in response to the inflammatory signals, which is generally noticed under inflamed conditions.

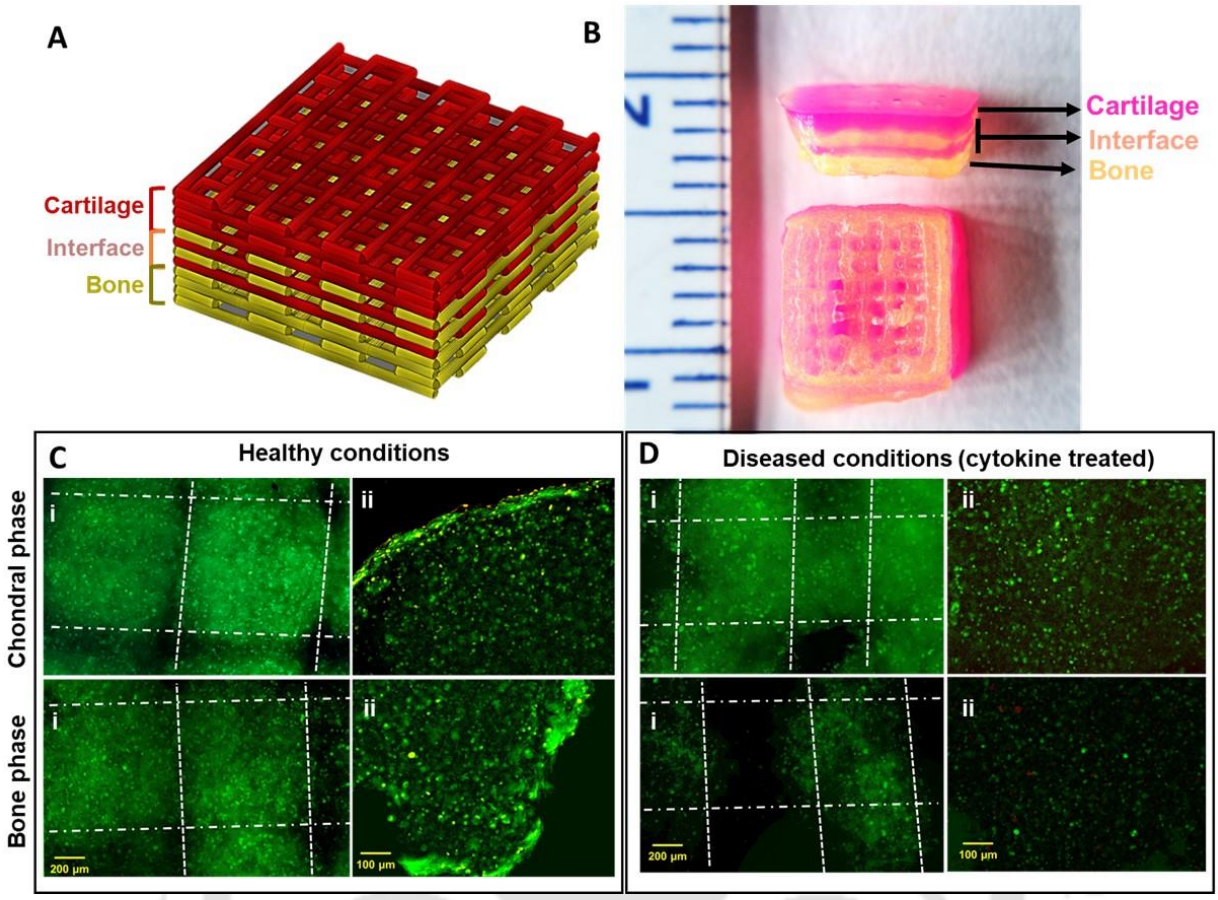

Figure 7.2. *(A) Illustration of the hierarchical construct to be printed, (B) the bioprinted construct with colored dyes representing different phases. Cellular viability assessment post bioprinting using calcein-AM (green clusters indicating live cells)/ethidium homodimer (red spots indicating dead cells) staining (C) healthy conditions; (D) diseased conditions.*

7.3.2 Extracellular matrix (ECM) formation

Once the viability of cells in the bioprinted construct was established, they were exposed to cytokines (a combination of IL-1β and TNF-α) for the induction of OA-like conditions. Following this, the constructs were treated with anti-inflammatory drugs for the attenuation of the diseased conditions. To establish the chondrogenic and osteogenic differentiation of ADMSCs and the formation of ECM, a biochemical analysis was performed. Sulfated GAG and collagen are important ECM components of cartilage formed by chondrocytes and ALP is a hallmark marker expressed by differentiating osteoblasts that regulate mineralization. The results of our study indicated an increase in sGAG and collagen over the 14 days in the healthy constructs indicating chondrogenesis and formation of cartilage matrix (**Figure 7.3A-B**). However, a significant decrease in sGAG (~2 fold on day 5) and collagen (~2.5 fold on day 5) content was observed when

induced with cytokines as compared to the healthy constructs ($p \leq 0.05$). These decreased levels were seen to be attenuated (~1.5 fold) upon treatment with CXB and RHN ($p \leq 0.05$). Similarly, ALP levels were seen to increase over time which decreased at day 14 in the healthy constructs indicating osteogenesis and formation of bone matrix (**Figure 7.3C-D**). The increased ALP levels were significantly decreased (~3 fold on day 5) upon cytokine treatment at both time points ($p \leq 0.05$). The reduced ALP activity was alleviated when treated with the CXB and RHN ($p \leq 0.05$).

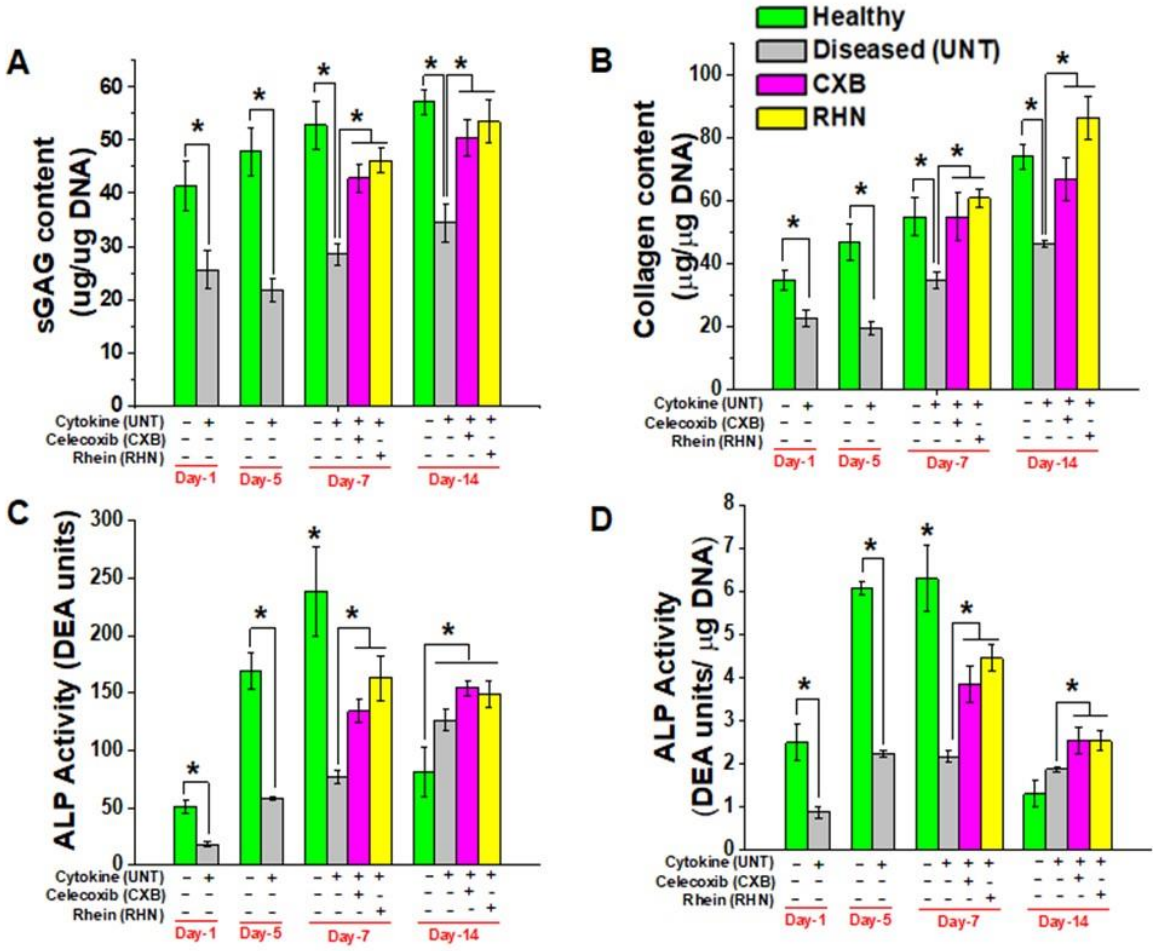

Figure 7.3. Biochemical analysis of treated 3D bioprinted constructs*; (A) sGAG content, and (B) collagen content, and (C-D) ALP activity of the bioprinted constructs. (CXB – celecoxib; RHN – rhein) along with the untreated (UNT) group. A healthy non-cytokine induced group (green) is also used for comparison. Data are presented as Mean ± S.D, *p ≤ 0.05.*

7.3.3 Regulation of inflammatory mediators

Several soluble inflammatory mediators have been involved in the pathogenesis of OA (**Figure 7.4A**). The nitric oxide (NO) pathway including the inducible nitric oxide synthase (iNOS), and NO; and the prostacyclin pathway including the cyclooxygenase-2 (COX-2), prostaglandin E2

(PGE2) are implicated in the OA pathogenesis. The results of the study showed that induction with cytokines significantly upregulated both nitric oxide (NO) (~2-fold) and PGE2 ((~3.5-fold) levels at both time points compared to the healthy constructs ($p \leq 0.05$). These enhanced NO levels were significantly reduced when treated with CXB and RHN ($p \leq 0.05$). Similarly, the increased PGE-2 levels were attenuated when treated with CXB ($p \leq 0.05$) (**Figure 7.4B**). However, the treatment with RHN did not reduce the increased PGE-2 levels (**Figure 7.4C**). The ADAMTS4 level was also increased (~2.5 fold) upon cytokine induction which was attenuated when treated with CXB and RHN (~1.7 fold) ($p \leq 0.05$) (**Figure 7.4D**).

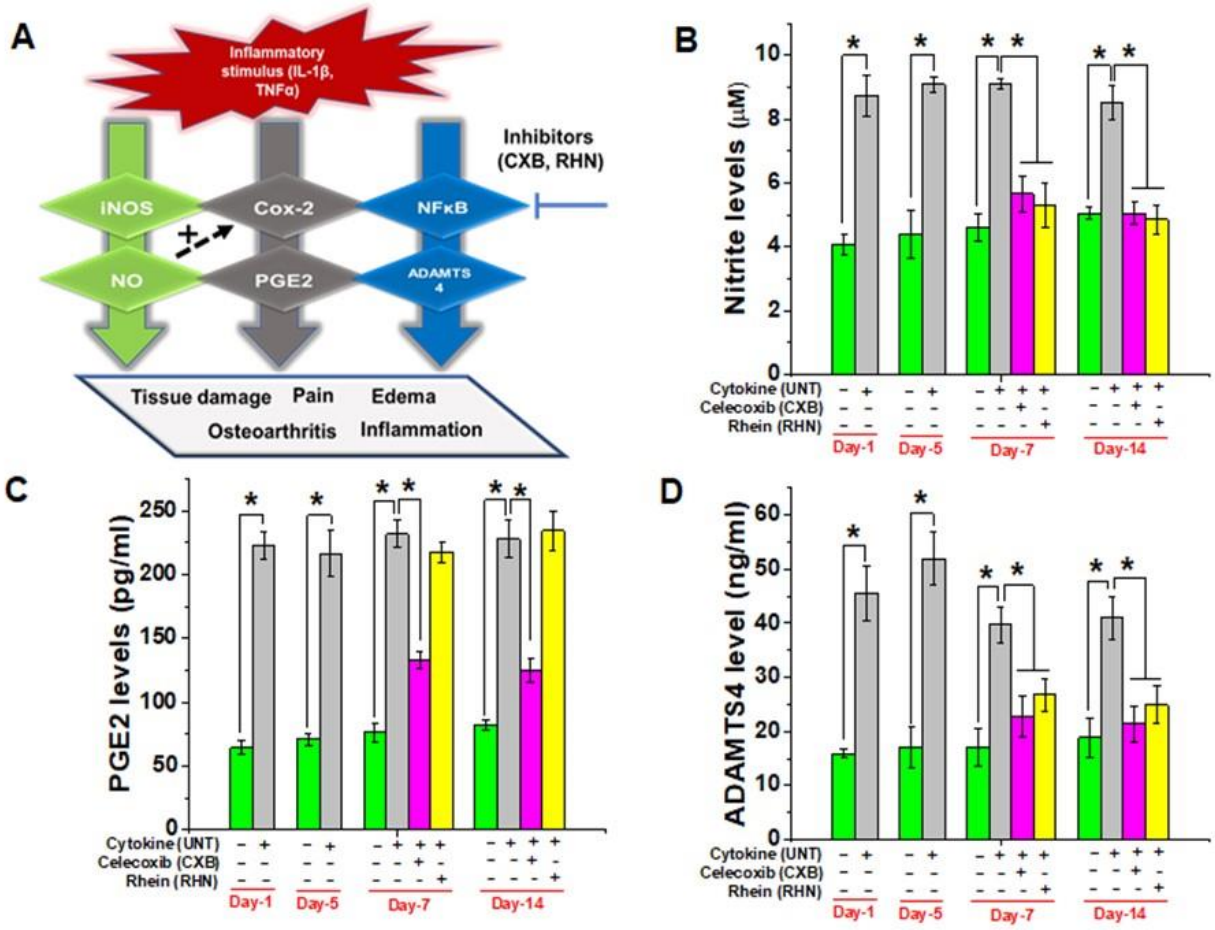

Figure 7.4. Effect of celecoxib and rhein on inflammatory mediators in cytokine-treated osteochondral constructs. *(A) Scheme illustrating the downstream action of inflammatory mediators and the inhibitory roles of the drugs used; (B) Nitric oxide (NO) levels, and (C) PGE2 levels, and (D) ADAMTS4 levels in the cell culture supernatant of the bioprinted constructs. (CXB – celecoxib; RHN – rhein) along with the untreated (UNT) group. Data are presented as Mean ± S.D, *p ≤ 0.05.*

7.3.4 Matrix metalloproteinase (MMP) activity

Another molecule that is frequently implicated in the destruction of the joint tissues is the MMP. MMP-1 (also known as collagenase-1) and MMP-13 (also known as collagenase-3) are crucial downstream targets that are implicated in OA. The results of our study showed that MMP-1 and MMP-13 levels were significantly enhanced on day 5 when induced with cytokines as compared to healthy constructs ($p \leq 0.05$) (**Figure 7.5**). Treatment with the drugs (CXB and RHN) reduced the production of cytokine-induced MMPs towards the attenuation of ECM degradation. The level of MMP-1 (**Figure 7.5Bi**) was attenuated at day 1 and day 7 of the treatment with the drugs, while MMP-13 (**Figure 7.5Bii**) showed attenuation at day 7 of treatment with the drugs ($p \leq 0.05$). The attenuation levels of MMP-13 were comparable to the healthy constructs.

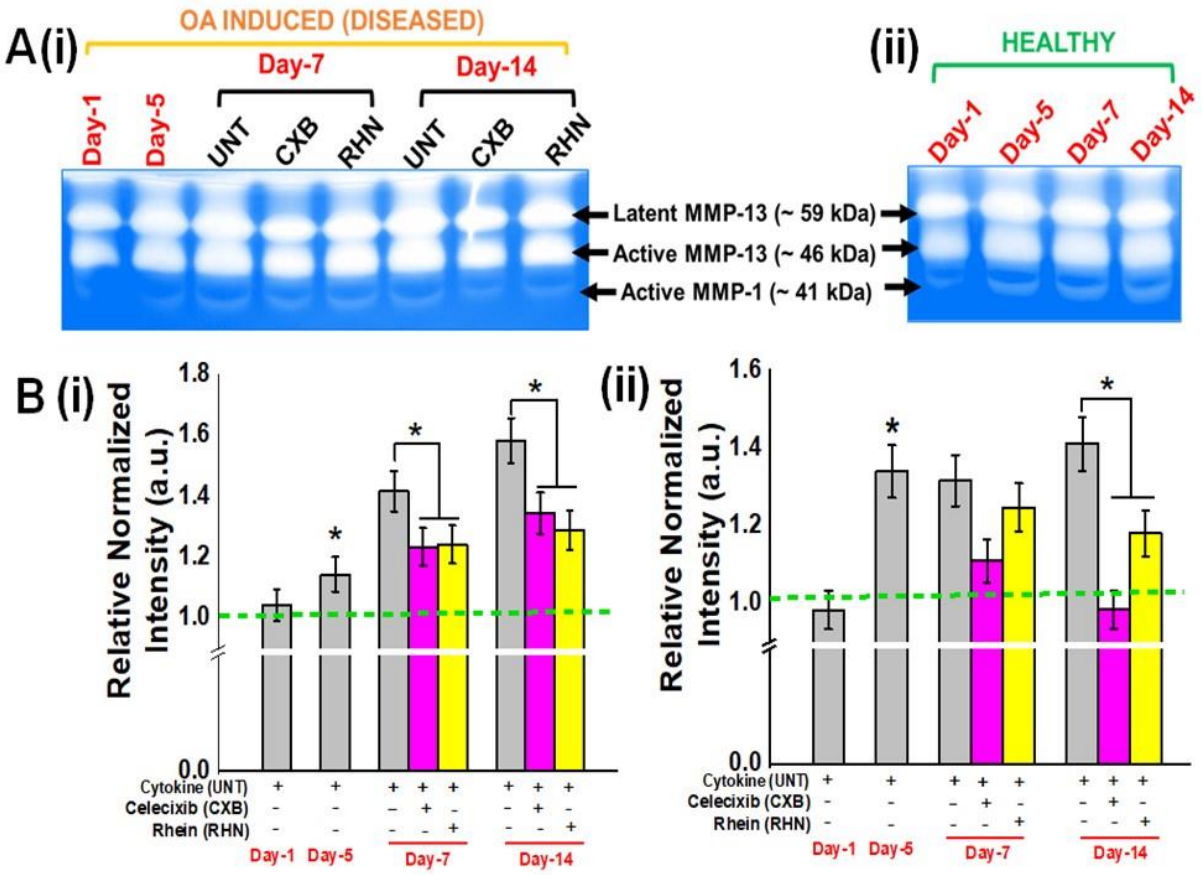

Figure 7.5. Collagen zymography analysis for MMPs. *(A) (i) OA induced group (diseased group) with drug treatment (CXB – celecoxib; RHN – rhein) along with untreated (UNT) group and (ii) Healthy (non-induced) group; corresponding B) densitometric profile for the zymograms for (i) MMP-1, (ii) MMP-13 represented by normalizing with the healthy group considering it as basal levels (denoted with a dotted green line) *p ≤ 0.05.*

7.3.5 Gene expression of anabolic, catabolic, and inflammatory markers

The gene expression analysis of the cardinal anabolic and catabolic markers indicates their status at the gene level. Collagen-II (*Col-II*), aggrecan (*ACAN*), and *Sox-9* are cardinal cartilage markers, while osteocalcin (*OCN*) and *RunX2* are bone markers. The expression of all anabolic markers (*Col-II*, *ACAN*, *OCN*) was increased during the 14-day culture period ($p \leq 0.05$), while the level of *Sox-9* decreased ($p \leq 0.05$) in the healthy constructs (**Figure 7.6A-D**). Induction with cytokine combination significantly decreased the levels of *Col-II* (~2.5 fold), *ACAN* (~1.7 fold), and *Sox-9* (~3 fold) ($p \leq 0.01$) at both the time points (day 1 and day 5) as compared to the healthy constructs i.e., without any cytokine treatment. Treatment with CXB and RHN significantly increased the levels of *Col-II* (~3 fold) and *ACAN* (~2 fold) ($p \leq 0.01$). Similarly, treatment with the drugs increased *Sox-9* expression at day 1 (~2 fold) ($p \leq 0.05$) but no significant difference was seen at day 7 post-treatment. Similarly, the expression of *OCN* was attenuated due to drug treatment at both time points ($p \leq 0.05$). The expression of *RunX2*, a preosteoblast marker decreased upon induction with cytokines which attenuated but showed no significant increase upon drug treatment (**Figure 7.6E**). Further, the expression of inflammatory markers such as COX-2, MMP-13, and IL-6 was assessed. The cytokine induction significantly upregulated the expression of COX-2 (~2.5 fold), MMP-13 (~2.5 fold), and IL-6 (~5 fold) these inflammatory genes ($p \leq 0.01$) (**Figure 7.6F-H**). Treatment with CXB and RHN increased the expression of these genes at the initial time point with no significant difference at 7-days post-treatment. Further, there was no significant difference in the expression of MMP-13 and IL-6 on day 14 of the healthy constructs as compared to day 1.

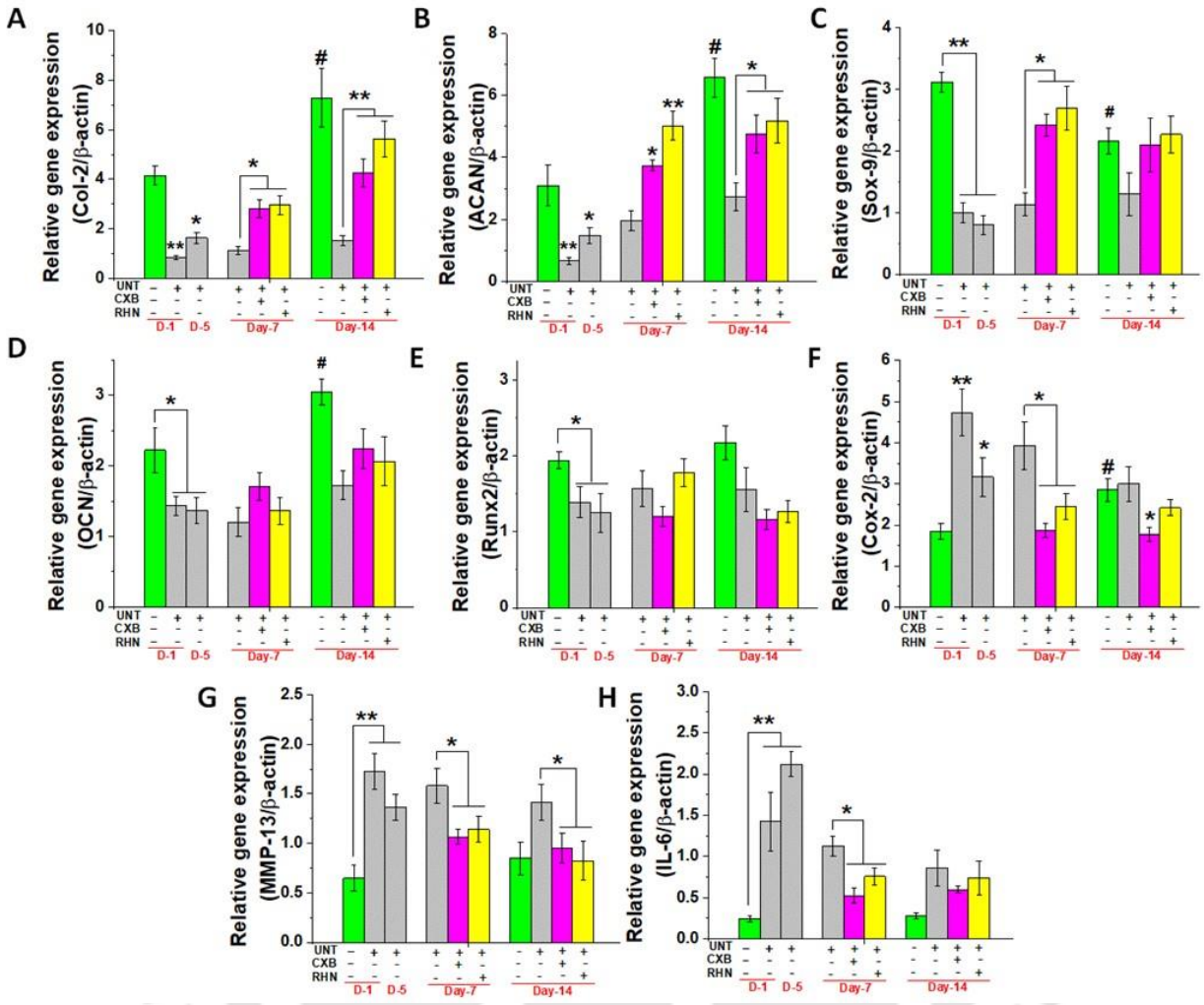

Figure 7.6. Gene expression profile of anabolic, catabolic, and inflammatory markers. *(A) Col-II, (B) aggrecan, (C) Sox-9, and (D) osteocalcin, (E) RunX2, (F) COX-2, (G) MMP-13, and (H) IL-6 in drug-treated cytokine-induced constructs. Data expressed as Mean ± S.D (n = 3), $^{\#}p \leq 0.05$ - statistically significant difference between the healthy constructs; $*p \leq 0.05$, $**p \leq 0.01$ - statistically significant difference between the untreated and drug-treated constructs.*

7.3.6 Protein expression of inflammatory and signaling molecules

To further validate the attenuation effect of the anti-inflammatory drugs on the cytokine-induced constructs, the downstream protein levels of several markers were analyzed by western blot analysis. NF-κB stimulation mediates the effects of crucial pro-inflammatory cytokines, such as IL-1β and TNF-α. The results showed cytokine-induced upregulation of NF-κB protein levels (**Figure 7.7**) as compared to the healthy constructs. These increased protein levels were significantly reduced upon treatment with the drugs RHN and CXB ($p \leq 0.05$), as compared to the diseased samples. Similarly, ADAMTS4, Col-X, and COX-2 showed increased protein levels with

cytokine-induction (**Figure 7.7**). The increased ADAMTS4 levels were significantly decreased upon treatment with CXB and RHN ($p \leq 0.05$). There was no significant reduction observed in Col-X protein levels when treated with the drug molecules. In the case of COX-2, a significant decrease was observed at day-1 ($p \leq 0.05$) of treatment with CXB and RHN but not on day-7, as compared to the cytokine-induced increased level.

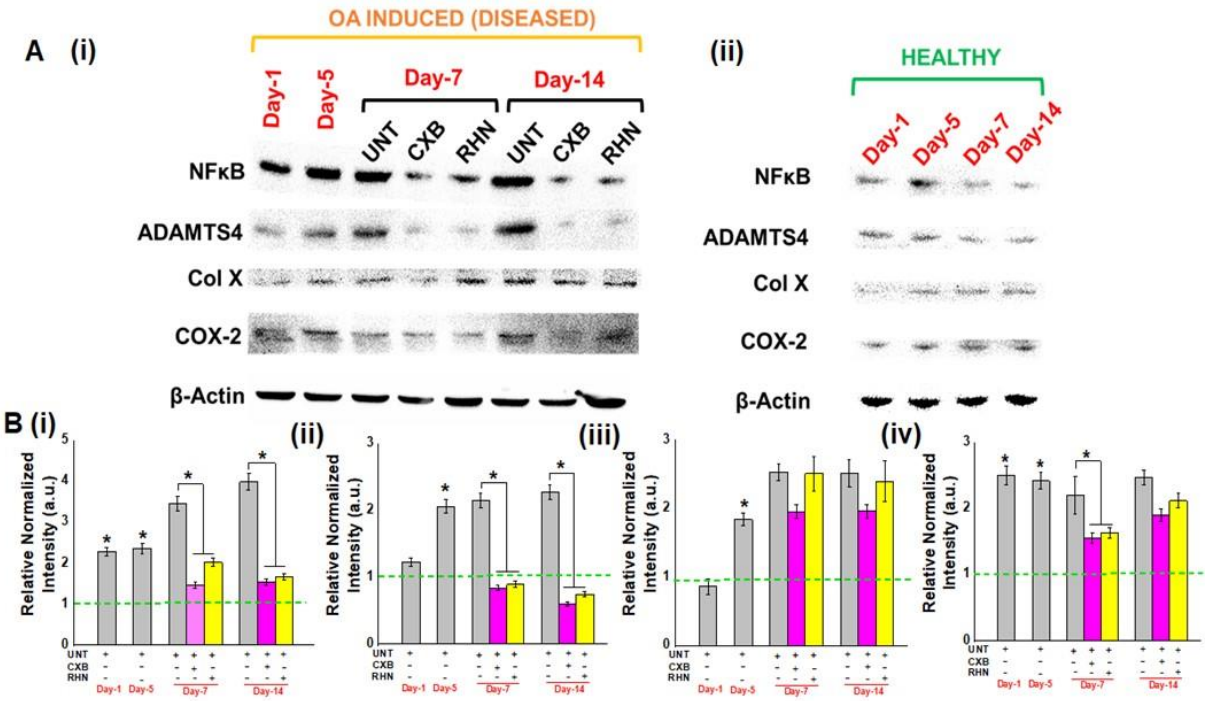

Figure 7.7. *Western blot analysis for A) i. OA induced group (diseased group) and ii. Healthy (non-induced) group, with drug treatment (CXB – celecoxib; RHN – rhein) along with untreated (UNT) group; corresponding B) densiometric profile for the blots for i) NFκ B, ii) ADAMTS4, iii) Col X and iv) COX-2, represented by normalizing with internal housekeeping control β-actin, and normalized with the healthy group considering it as basal levels (denoted with a dotted green line) *$p \leq 0.05$.*

7.4 Discussion

OA is traditionally considered to be a "wear-and-tear" or degenerative musculoskeletal disorder associated with the process of aging, with no cure presently and surgical interventions including joint replacement still a commonly performed treatment strategy. Primarily considered to be cartilage driven, OA is a much more complex condition involving cross-talks between joint tissues such as cartilage, subchondral bone, and synovium. An increasing amount of evidence has shown that inflammation plays a significant role in the pathogenesis of OA along with altered innate and adaptive immune systems, activating the inflammatory cascade [471]. It involves the production of proinflammatory mediators, such as TNF-α, IL-1β, and chemokines by the chondrocytes and synovium which can be measured in the synovial fluid of OA patients. These biomarkers play a crucial role in the early-stage and late-stage progression of OA. This relationship between inflammation and OA is becoming clearer with the recognition of a plethora of ongoing immune processes within the OA joint including the synovium. Earlier, inflammation in OA was perceived to be a result of the broken cartilage fragments, however, the presence of synovitis inflammation in the seemingly healthy joints without the cartilage fragments pointed towards a more complex cross-talk between the joint tissues. Additionally, this indicates that the process of inflammation is initiated in the early stages of OA even before any visible radiographic changes such as bony enlargement or osteophyte formation [472]. Early-stage OA is majorly characterized by inflamed synovium, increased production of pro-inflammatory cytokines and mediators, upregulation of catabolic factors and downregulation of anabolic factors, degradation of ECM, chondrocyte hypertrophy, apoptosis, and cartilage damage. Benito *et al.* compared the inflammation in early and late OA reporting an increased mononuclear cell infiltration and overexpression of inflammatory mediators during the early stage compared to the late stage of OA [473]. Thus, studies mimicking the early OA conditions may provide a suitable platform of opportunity in investigating the inflammation-based disease-modifying interventions for OA therapeutics.

Currently, the literature reports no available human 3D *in vitro* models to study the pathogenesis or therapeutics associated with early-stage OA. Addressing this, in the current study we have developed an inflamed osteochondral unit mimicking the pathophysiology of early-stage OA and further verified its capability to screen anti-inflammatory drugs. Previously, several 2D *in vitro* models have been reported to induce disease-like conditions and evaluate different anti-osteoarthritic drugs [460, 474, 475]. Allas *et al.* developed an *in vitro* model that supported the

induction of hypertrophy in chondrocytes and further established its ability to test drugs towards the reduction of cartilage hypertrophy [476]. Most of these studies provided encouraging results, however, the inability of the 2D system to accurately mimic the native tissue conditions inspired a transition to the 3D models. Towards this, Lin *et al.* developed a multichambered bioreactor for osteochondral differentiation using a biphasic osteochondral plug designed for separate media compartments i.e., the osseous and chondral phases. The results showed that the MSC-based tissues supported IL-1β-induced OA-like pathology with intercompartmental communication [477]. However, the model did not establish its capability to screen any drug. Peck *et al.* reported an *in vitro* model where disease conditions in a hyaline cartilage graft were induced using lipopolysaccharide (LPS)-activated macrophages. The treatment with celecoxib decreased the catabolic markers in the model [455]. However, the study was limited to the use of primary chondrocytes to establish the model. The limitations with most of the current models arise due to the conventional fabrication methods, thus requiring more advanced, affordable, consistent, and comprehensive techniques of biofabrication.

Owing to its ability to fabricate heterogeneous and complex structures *via* a layer-by-layer deposition and capable of high-throughput manufacturing, the advanced technique of 3D bioprinting allows the fabrication of both cartilage and bone-associated zonal compartments of the native human joint. In the current study, we have used 3D bioprinting to produce biomimetic osteochondral tissue using silk-based bioinks. While the cartilage phase was bioprinted using bioink consisting of silk blends along with PVP and encapsulating pre-differentiated chondrocytes; the bone phase was bioprinted using bioink consisting of silk blends with nano-apatite and pre-differentiated osteoblasts; with a tissue interface composed of both the bioinks. The bioprinted constructs were further cultured in an osteochondral medium for 7 days. The bioink hydrogel network used here has a diffusion coefficient (D_e) in the order 3 to 5 X 10^{-11} m^2/s (follows Non-Fickian diffusion kinetics) [147], thus providing a good permeable network for the diffusion of important secretory factors. This is helpful in two ways: (i) the cytokine/ drug treatment provided would easily be available for the encapsulated cells present within the bioink; and (ii) cellular cross-talk between cartilage phase and bone phase, mediated through secretory factors would diffuse between the two layers, mimicking the native-like signaling regime when exposed to any biochemical cue. The crosstalk between the bone and cartilage phases of the osteochondral unit is very critical for understanding the pathogenesis and progression of OA. There is growing evidence

of significant biochemical communication between these tissues [478], which is associated with changes at the osteochondral interface that accelerates cartilage degeneration and accompanying pain and morbidity, requiring a better understanding of the complex network of interactions. Most of the concurrent studies overlook the involvement of the bone phase with an exclusive focus on the cartilage phase while developing an *in vitro* model. Evidence from clinical and *in vivo* studies have showed that subchondral bone lesions may precede cartilage degeneration, implying that OA is an osteochondral disease where the subchondral bone is intricately involved. The subchondral bone lesion in OA is a result of inflamed osteoblast with reduced bone markers, increased inflammatory mediators such as IL-6, and catabolic factors such as MMP-13 [479]. Therefore, the bioprinted triphasic system in our study comprising of cartilage, bone, and an interface, was developed to take into account this cross-talk between the tissues. Lin *et al.* showed this cross-talk in their compartmentalized biphasic system where cytokine induction in the osseous phase resulted in catabolic response in the chondral phase [477].

Next, early-stage OA-like pathological conditions were developed using a combination of pro-inflammatory cytokines namely IL-1β and TNF-α. These cytokines are the major players used individually or in combination for induction of OA-like conditions. The activities of the two cytokines show a synergistic effect when used in combination, activating key pathological markers of OA, where TNF-α drives acute inflammation and IL-1β sustains it [480, 481]. Further, the well-known anti-inflammatory drugs namely RHN and CXB were tested for attenuation of diseased conditions in the model. Rhein, a metabolic product of diacerein has a bone affinity and anti-inflammatory action that inhibits IL-1β synthesis and activity *via* synergistic, comprehensive, and multiple pathways for its therapeutic effect [482]. Celecoxib, an NSAID that selectively inhibits COX-2 activity, has been widely used in the treatment of OA, as it can inhibit the generation of prostaglandin E2 and reduce the inflammation associated with OA. Celecoxib has been regarded as a disease-modifying-drug (DMD) for human OA [483], and its direct effects on OA cartilage have been explored [455]. Additionally, celecoxib combined with diacerein has shown satisfactory treatment effects on OA through inhibitory actions on inflammatory signaling pathways [469]. Thus, we developed and tested our model for its prospective use as an *in vitro* model for OA therapeutics.

Firstly, the viability of the encapsulated cells was assessed in the bioprinted constructs. The bioprinted constructs maintained their shape fidelity and supported the viability of encapsulated pre-differentiated ADMSCs as observed *via* live/dead assay. Next, we assessed the cardinal ECM chondrogenic and osteogenic biochemical markers for their changes at different stages of the study. The results indicated an increase in the total collagen, sGAG, and ALP in the healthy constructs over the culture period indicating successful differentiation of ADMSCs into chondrocytes and osteoblasts and ultimately resulting in the formation of crucial ECM components. Upon cytokine (TNF-α and IL-1β) induction, the results of our study showed a significant decrease in collagen content, sGAG content, and ALP content. Several studies have shown that treatment with these cytokines alone or in combination inhibits the synthesis of collagen-II and proteoglycans [461, 481]. Additionally, these cytokines have been reported to cause bone loss in many inflammatory diseases [484]. The results in our study showed reduced bone markers in the cytokine-induced inflamed model mimicking subchondral bone lesions of OA, which occurred due to the transition of normal osteoblasts to inflamed osteoblasts, which further induced hypertrophy in chondrocytes and amplified cartilage damage. These reduced ECM components were augmented when treated with CXB and RHN. Previous reports have shown that IL-1β/TNF-α-induced reduced collagen and proteoglycan synthesis can be reversed by treatment with CXB and RHN [469, 485].

The major driving force of inflammation in joint degeneration of OA patients is a group of soluble inflammatory mediators including pro-inflammatory cytokines, chemokines, adipokines, and neuropeptides. Thus, we assessed the implication of inflammatory mediators such as NO and PGE2 in our study. NO is implicated in cartilage degeneration *via* inhibition of ECM synthesis and activation of MMPs [486]. Our results showed that the increased NO levels due to cytokine induction were reduced upon treatment with CXB and RHN. Tsutsumi *et al.* reported inhibitory effects of CXB on NO production in chondrocytes [475]. Pelletier *et al.* found that RHN could inhibit the production of NO and block the expression of iNOS [487]. PGE2, a prostanoid produced by COX, is known as a major catabolic mediator and one of the main molecules responsible for pain in arthritis, mainly in OA with inflammation where the level of COX-2 is increased [488]. Our results showed that PGE2 levels were elevated upon cytokine induction. Berenbaum *et al.* reported enhanced PGE2 production and COX-2 activity in articular chondrocytes due to the synergistic effect of IL-1β and TNF-α [489]. The increased PGE2 levels were mitigated upon

CXB treatment, though, RHN treatment did not significantly reduce the PGE2 levels. This was in agreement with a report by Sanchez *et al.* that showed that RHN increased both basal and IL-1β-stimulated PGE2 levels [468]. A previous report indicated that the inhibition of COX-2 by NSAIDs or selective COX-2 inhibitors leads to reduced PGE2 production, inflammation, and mitigates pain in OA patients [490].

The ECM components such as collagen-II and aggrecan provide structural integrity and mechanical properties to the osteochondral tissue, which are degraded in OA *via* proteolytic cleavage by MMPs and ADAMTSs, respectively. Aggrecan degradation precedes collagen-II cleavage and is associated with early stages of OA, thus aggrecan may play a role to manage collagen degradation [491]. In humans, ADAMTS-4 and ADAMTS-5 are the major enzymes that catalyze aggrecan degradation and are characteristic pathology of early-stage OA. Our results showed that cytokine induction stimulated the increase in the ADAMTS4 levels which were mitigated when treated with CXB and RHN. Among MMPs, MMP-1 and MMP-13 are majorly involved in collagen-II degradation *via* collagen cleavage and are crucial downstream targets that are implicated in OA. The treatment with CXB and RHN in our model attenuated the increased cytokine-induced MMPs levels. The increased MMP levels are a result of the hypertrophic chondrocytes and the inflamed osteoblasts in the model. Legendre *et al.* found that IL-1β-induced stimulation of the MMPs and aggrecanase-1 (ADAMTS4) was markedly inhibited by RHN [474].

Further, we assessed the expression of anabolic, catabolic, and inflammatory markers. The anabolic genes showed decreased expression in cytokine-induced samples which were attenuated upon treatment of CXB and RHN in our *in vitro* model. The anabolic genes of cartilage ECM such as collagen-II and aggrecan were significantly upregulated in the healthy constructs. *Sox-9* gene showed hyperactivity on day 7 but not on day 14. Being a key early differentiation marker, this is in agreement with several previous reports where chondrogenic and osteogenic differentiation of MSCs results in a significant decline of *Sox-9* gene and protein expression by day 14 [492, 493]. Furthermore, *RunX2* and *OCN* genes showed an initial increase in expression in healthy constructs which were decreased upon cytokine induction with no significant increase when treated with anti-inflammatory drugs. *RunX2* induces the differentiation of multipotent MSCs into immature osteoblasts, while *OCN* is expressed in mature osteoblasts. The increased *OCN* expression in healthy constructs and no significant increase in *RunX2* levels over the 14-day culture support the

literature [494]. Similar to the bone lesions in OA, the results in our study showed reduced bone markers in the cytokine-induced inflamed model which occurred due to the transition of normal osteoblasts to inflamed osteoblasts, which further induced hypertrophy in chondrocytes and amplified cartilage damage. Furthermore, a considerable increase in the expression of catabolic and inflammatory genes, namely, COX-2, MMP-13, and IL-6, in cytokine-induced constructs was observed which were decreased in the presence of CXB and RHN. IL-6 along with IL-1β and TNF-α are the main proinflammatory cytokines associated with OA pathogenesis [458]. Sanchez *et al.* showed that CXB inhibited PGE2 production, blocked IL-6 synthesis, and augmented aggrecan synthesis in cultured human OA chondrocytes encapsulated in alginate beads [495]. Ge *et al.* showed that RHN attenuates inflammation by inhibiting NF-κB and NALP3 inflammasome shown by the reduced production of a pro-inflammatory cytokine such as IL-6 in macrophages stimulated with lipopolysaccharide [496]. Given that remodeling of subchondral bone is a contributing factor to OA, Pelletier *et al.* demonstrated that RHN reduces the synthetic activity of osteoblasts responsible for abnormal subchondral bone remodeling in OA [497]. Moreover, the expression of key molecules was further validated at the protein level. The western blot results indicated that the protein levels of NFκB, ADAMTS4, Col-X, and COX-2 have increased in the cytokine-induced constructs as compared to the healthy constructs. The results indicated that CXB and RHN could inhibit the NF-κB nucleus translocation induced by cytokines through a probable reduction in IκB phosphorylation status. Additionally, the drugs suppressed PGE2 production *via* inhibition of COX-2 enzyme activity. However, the drugs did not significantly decrease the hypertrophic activity as directed by the increased collagen-X protein level. Col-X is a known marker of late-stage chondrocyte hypertrophy and NSAIDs have been reported to induce its expression in MSCs of healthy and OA donors [498].

The onset and progression of OA pathogenesis *via* regulation of metabolism and inflammation is a result of various cross-linked and interdependent signaling pathways such as the MAPK and NF-κB pathways. MAPK are serine/threonine protein kinases that stimulate signal transmission from outside to inside the cell, resulting in suitable physiological responses such as cellular proliferation, differentiation, inflammation, and apoptosis. The three major subfamilies of the MAPK pathway include ERKs (extracellular signal-regulated kinase), JNK (c-Jun N-terminal kinase), and p38 MAPK which are stimulated during inflammation resulting in their phosphorylation, consequently activating the downstream transduction pathway and the transcription factors, with subsequent

release of pro-inflammatory molecules and activating the cascade. The activated ERK, JNK, and p38 MAPK were observed in OA synovial and cartilage tissue. Several reports indicate that MAPK activation triggered due to cytokines such as TNF-α and IL-1β stimulates MMPs and aggrecanases resulting in degradation of cartilage [499, 500]. In the case of the NF-κB pathway, the inactive NF-κB dimers are located in the cytoplasm due to the inhibitory IκB molecules. Upon stimulation with cytokines, the IκB is phosphorylated and subsequently degraded with NF-κB p65 translocating into the nucleus where it activates the inflammatory mediators such as iNOS, COX-2, ADAMTS, and MMPs, among other factors, ultimately causing ECM degradation [501, 502]. In our model, we hypothesize MAPK and NF-κB pathways to be involved as per the mechanism mentioned above and illustrated in **Figure 7.8**, in the catabolic action of the proinflammatory cytokines and their attenuation by the anti-inflammatory drugs CXB and RHN. Previously, MAPK and NF-κB pathways are involved in the mitigation of OA [469, 475, 500]. Recently, Ding *et al.*, reported that Urolithin A can mitigate the IL-1β-induced deterioration of collagen-II and aggrecan along with reducing the inflammatory mediators through the MAPK and NF-κB pathways in chondrocytes [499]. Additionally, celecoxib combined with diacerein has reported showed well-satisfactory treatment effects on OA *via* inhibiting the p38MAPK, JNK, and NF-κB signaling pathways [469].

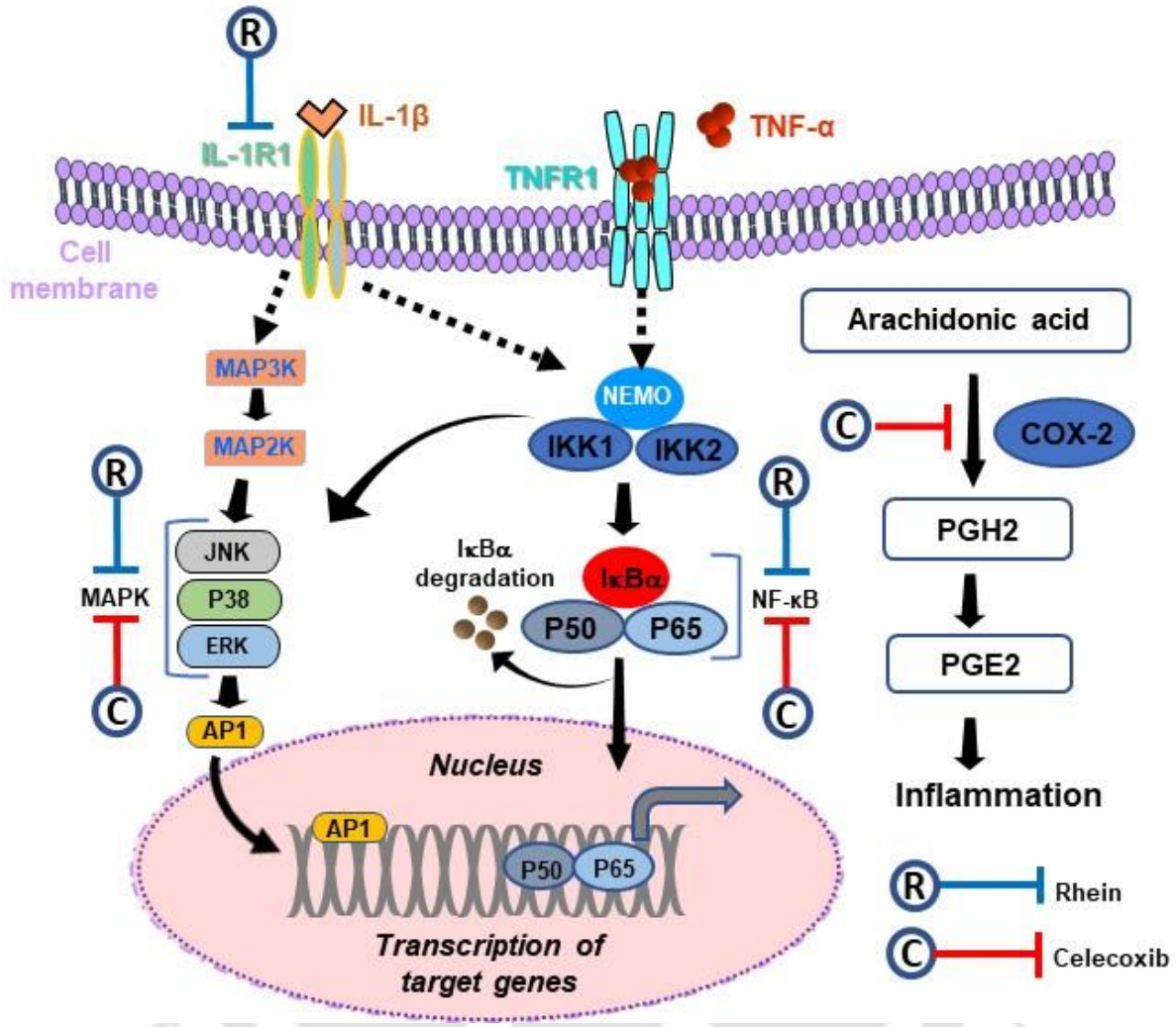

Figure 7.8. *Schematic representation of key signaling pathways in the inflammatory process and its inhibition using anti-inflammatory drugs (Celecoxib and Rhein) in OA model.*

7.5 Significant findings

1. Herein, a potentially more consistent, affordable, and physiologically relevant human early-stage *in vitro* OA model was developed.
2. The results of the study demonstrated that the 3D bioprinted construct supported the viability of encapsulated primed hADMSCs and the formation of ECM resulting in its maturation into a functional osteochondral unit.
3. Further, the establishment of an inflamed osteochondral unit (consisting of hypertrophic chondrocytes and inflamed osteoblasts) *via* cytokine-induction (IL-1β and TNF-α combined), indicated by the key pathological features including the depletion of ECM components such as collagen, proteoglycans, heightened catabolic enzymes, and upregulation of inflammatory mediators akin to early-stage OA.
4. Moreover, both the tested anti-inflammatory drugs (CXB and RHN) inhibited the cytokine-induced inflammatory mediators, MMPs expression, and restored ECM production with inhibition of MAPK/NF-κB signaling pathways.
5. Activated MAPK and NF-κB regulate the expression of molecules directly or indirectly involved in the inflammation (such as MMPs, several catabolic cytokines, NO, PGE2, COX-2, and ADAMTS4), and apoptosis.
6. Overall, a physiologically relevant 3D bioprinted *in vitro* OA model was successfully established and validated for drug-screening, indicating its feasibility for potential pre-clinical high-throughput drug testing and overall OA management.

SUMMARY AND FUTURE PERSPECTIVES

SUMMARY AND FUTURE PERSPECTIVES

The use of external regenerative strategies in OA have claimed a nearly unassailable role in holistic and sustainable repair of osteochondral tissue damage. Consequently, the desired superior characteristics of SF, developed matrices, significant outcomes (**Figure S1**) and prospects of scaffold-based regeneration of cartilage and osteochondral tissue, based on the objectives of this thesis, have yielded very encouraging outcomes which have also been communicated and peer reviewed.

The developed agarose and silk fibroin blended hydrogel to nurture the positive facets of the agarose gold standard and offset the negative aspects, resulted in hydrogels that were biodegradable and immunocompatible, with the ability to support ECM synthesis. The subsequent requirement of mechanical compliance, crucial for load bearing articular joints, was achieved through fiber-reinforced composite scaffolds, fabricated by using silk fibers and SF solution. These fiber-reinforced scaffolds supported improved growth of chondrocytes with an increased compressive modulus and stiffness (nearly 8-fold), in comparison to the fiber-free control groups. The composites also supported the formation of ECM components such as sGAG and collagen type II. Since the entire osteochondral unit (superficial cartilage and underlying bone) is implicated in osteoarthritis, a biphasic silk scaffold was developed that mimicked the native osteochondral joint. It contained a spongy fiber-free phase for cartilage, a fiber-reinforced phase for bone revival and a connecting interface, fabricated using facile reproducible process. The scaffold designed in a continuous and integrated manner using freeze-drying method, negated issues related to individual phase fabrication methodology. The developed hierarchically structured biphasic silk scaffold displayed phase specific porous structures, with suitable mechanical strength, and positive characteristics of in vitro ECM deposition, and *in vivo* regeneration (in rabbit osteochondral models) of osteochondral tissue.

Use of 3D bioprinting neutralized the persistent handicaps of the conventional fabrication methods by fabricating anatomically relevant shapes, patient-specific match to the site of implantation; in a high-throughput, automated, and cost-effective manner. Bioinks crucial to bioprinting were generated from hydrogel blends of blends of mulberry and non-mulberry, *B. mori* with *A. assamensis*, and *B. mori* with *P. ricini*; they were most stable and unaffected by an increase in the

temperature required for bioprinting. Therefore, the self-gelling ability of SF blends (*B. mori* and *P. ricini*) was used along with gelatin as a bulking agent to develop the bioink, to encapsulate chondrocytes for cartilage bioprinting. The bioprinted constructs demonstrated *in vitro* cartilage specific ECM formation and *in vivo* biocompatibility. The developed bioink showed good print fidelity for bioprinting cartilage grids along with state-of-art anatomical structures like the human ear. It is noteworthy that the fabrication is a crosslinker-free approach, thus avoiding the possible toxicity and cost burden associated with it. Disease model development was central to the final objective of understanding the molecular mechanisms of OA initiation and progression. An *in vitro* model was generated by 3D bioprinting an osteochondral unit using silk-based (blend of *B. mori* and *A. assamensis*) bioink. This bioprinted model made up for the lack of biomimetic human pathophysiological conditions, the required longer timeline, and associated ethical concerns of the 2D monolayers and animal models. The model was validated by physiologically relevant results; it successfully mimicked the inflamed OA unit observed in the early stages of OA, and displayed the mitigative effects of the applied anti-inflammatory drugs. Therefore, opportunely, catering to the demand for a robust, high-throughput platform for screening novel anti-inflammatory drugs towards OA therapeutics.

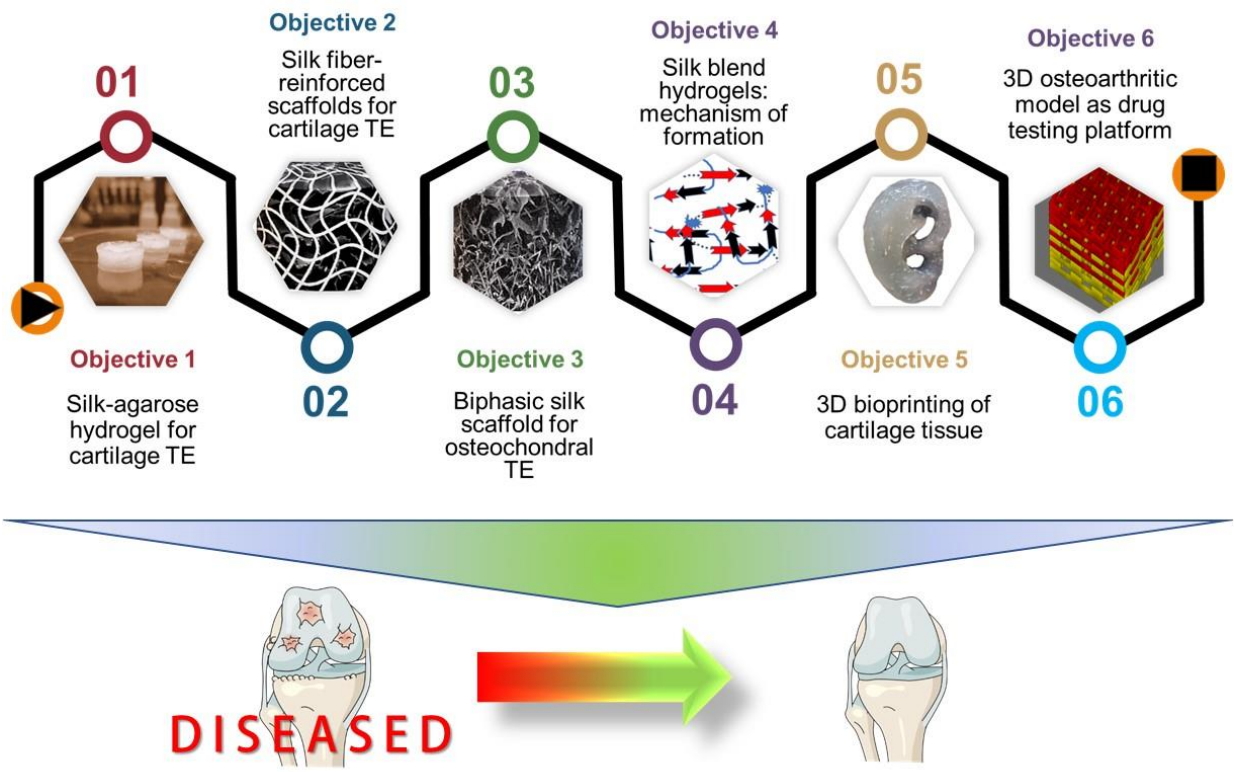

Figure S1. *Schematics illustrating various developed matrices for the cartilage and osteochondral tissue engineering applications.*

The future prospects of the thesis work (**Figure S2**) would include the use of dynamic bioreactors to better mimic the native-like healthy and diseased physiological conditions especially in in terms of nutrients, oxygen, temperature, pH, carbon dioxide, humidity and mechanical stress. The next target would be testing of the developed matrices/constructs in larger animal models which are more relevant to humans; the use of patient-specific induced pluripotent stem cells (iPSCs) to overcome the ethical concerns and reducing the chances of graft rejection. Thus, a whole new arena for testing of new markers and drugs for OA therapeutics would be open to innovation and product development. The making smart bioinks for intraoperative bioprinting strategies would widen the bioresource base for disease alleviation. The objectives undertaken in this thesis will be helpful in the development of a joint-on-a-chip model where other joint tissues could be incorporated. The final frontier to be conquered would be to have an off-the-shelf acellular graft, which when seeded with patients own cells by the clinician, would result in the repair and regeneration of the damaged cartilage and osteochondral tissue, thus, mitigating osteoarthritis.

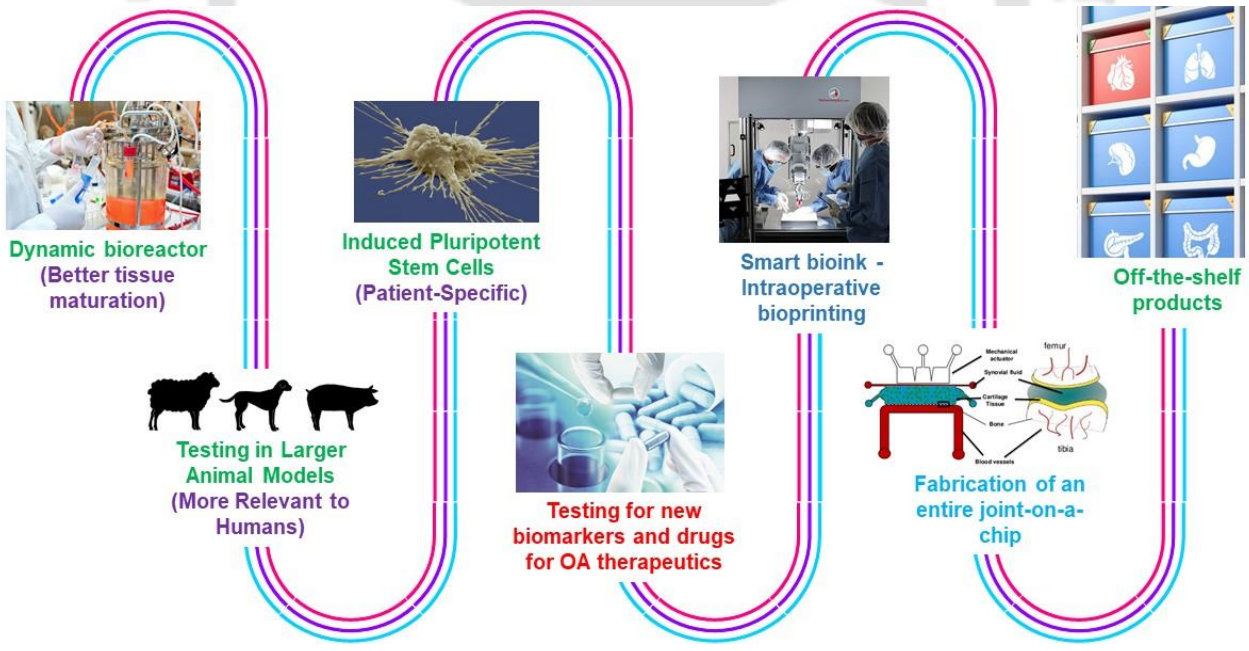

Figure S2. *Illustration of the future prospects of the developed matrices in cartilage and osteochondral tissue engineering.*

In the final analysis, the current thesis, explored various silk biomaterials, including mulberry and non-mulberry type, as matrices for cartilage and osteochondral tissue engineering. The research endeavor focused on advancing the fabrication strategies of silk biomaterial-based matrices. Conventional fabrication methods where scaffolds were fabricated manually using methods such as freeze-drying was the first step. Efforts were subsequently directed at advanced additive manufacturing techniques such as 3D bioprinting where silk-based bioinks were developed to bioprint cartilage and osteochondral tissue. Finally, we developed a 3D bioprinted inflamed *in vitro* model as a drug screening platform for OA therapeutics. By implementing the defined objectives, we have progressively developed novel silk biomaterial-based matrices for cartilage and osteochondral repair and validated their pre-clinical functionality both *in vitro* and *in vivo.*

Bibliography

[1] Sophia Fox AJ, Bedi A, Rodeo SA. The basic science of articular cartilage: structure, composition, and function. Sports health. 2009;1:461-8.
[2] Camarero-Espinosa S, Rothen-Rutishauser B, Foster EJ, Weder C. Articular cartilage: from formation to tissue engineering. Biomaterials science. 2016;4:734-67.
[3] Francis SL, Di Bella C, Wallace GG, Choong PF. Cartilage tissue engineering using stem cells and bioprinting technology—barriers to clinical translation. Frontiers in surgery. 2018;5:70.
[4] Tamaddon M, Wang L, Liu Z, Liu C. Osteochondral tissue repair in osteoarthritic joints: clinical challenges and opportunities in tissue engineering. Bio-design and manufacturing. 2018;1:101-14.
[5] Eyre D. Articular cartilage and changes in arthritis: collagen of articular cartilage. Arthritis Research & Therapy. 2001;4:1-6.
[6] Lodish H, Berk A, Zipursky SL, Matsudaira P, Baltimore D, Darnell J. Section 22.3, Collagen: the fibrous proteins of the matrix. Molecular cell biology. 2000;4.
[7] Poole AR, Kojima T, Yasuda T, Mwale F, Kobayashi M, Laverty S. Composition and structure of articular cartilage: a template for tissue repair. Clinical Orthopaedics and Related Research®. 2001;391:S26-S33.
[8] Aigner T, Reichenberger E, Bertling W, Kirsch T, Stöss H, Von der Mark K. Type X collagen expression in osteoarthritic and rheumatoid articular cartilage. Virchows Archiv B. 1993;63:205.
[9] Varki A, Cummings R, Esko J, Freeze H, Hart G, Marth J. Chapter 11, Proteoglycans and glycosaminoglycans. Essentials of Glycobiology: Cold Spring Harbor Laboratory Press; 1999.
[10] Bergholt MS, St-Pierre J-P, Offeddu GS, Parmar PA, Albro MB, Puetzer JL, et al. Raman spectroscopy reveals new insights into the zonal organization of native and tissue-engineered articular cartilage. ACS central science. 2016;2:885-95.
[11] Cohen NP, Foster RJ, Mow VC. Composition and dynamics of articular cartilage: structure, function, and maintaining healthy state. Journal of Orthopaedic & Sports Physical Therapy. 1998;28:203-15.
[12] Oláh T, Madry H. The osteochondral unit: the importance of the underlying subchondral bone. Cartilage Restoration: Springer; 2018. p. 13-22.
[13] Mosher TJ. Functional anatomy and structure of the “osteochondral unit”. Arthritis in color: advanced imaging of arthritis Philadelphia: Elsevier Saunders. 2009:23-32.
[14] Zhang B, Huang J, Narayan RJ. Gradient scaffolds for osteochondral tissue engineering and regeneration. Journal of Materials Chemistry B. 2020;8:8149-70.
[15] Schinagl RM, Gurskis D, Chen AC, Sah RL. Depth-dependent confined compression modulus of full-thickness bovine articular cartilage. Journal of Orthopaedic Research. 1997;15:499-506.
[16] Mente P, Lewis J. Elastic modulus of calcified cartilage is an order of magnitude less than that of subchondral bone. Journal of Orthopaedic Research. 1994;12:637-47.
[17] Abdulghani S, Morouço PG. Biofabrication for osteochondral tissue regeneration: bioink printability requirements. Journal of Materials Science: Materials in Medicine. 2019;30:20.
[18] Qu H, Fu H, Han Z, Sun Y. Biomaterials for bone tissue engineering scaffolds: a review. RSC advances. 2019;9:26252-62.

[19] Madry H, van Dijk CN, Mueller-Gerbl M. The basic science of the subchondral bone. Knee surgery, sports traumatology, arthroscopy. 2010;18:419-33.
[20] Ateshian GA, Warden W, Kim J, Grelsamer R, Mow VC. Finite deformation biphasic material properties of bovine articular cartilage from confined compression experiments. Journal of biomechanics. 1997;30:1157-64.
[21] Lu X, Mow V. Biomechanics of articular cartilage and determination of material properties. Medicine+ Science in Sports+ Exercise. 2008;40:193.
[22] Armstrong C, Mow VC. Variations in the intrinsic mechanical properties of human articular cartilage with age, degeneration, and water content. The Journal of bone and joint surgery American volume. 1982;64:88-94.
[23] Chen FH, Rousche KT, Tuan RS. Technology Insight: adult stem cells in cartilage regeneration and tissue engineering. Nature clinical practice rheumatology. 2006;2:373-82.
[24] Setton L, Mow VC, Howell D. Mechanical behavior of articular cartilage in shear is altered by transection of the anterior cruciate ligament. Journal of Orthopaedic Research. 1995;13:473-82.
[25] James SL, Abate D, Abate KH, Abay SM, Abbafati C, Abbasi N, et al. Global, regional, and national incidence, prevalence, and years lived with disability for 354 diseases and injuries for 195 countries and territories, 1990–2017: a systematic analysis for the Global Burden of Disease Study 2017. The Lancet. 2018;392:1789-858.
[26] Lefèvre T, Rousseau M-E, Pézolet M. Protein secondary structure and orientation in silk as revealed by Raman spectromicroscopy. Biophysical journal. 2007;92:2885-95.
[27] Loeser RF, Goldring SR, Scanzello CR, Goldring MB. Osteoarthritis: a disease of the joint as an organ. Arthritis & Rheumatism. 2012;64:1697-707.
[28] Man G, Mologhianu G. Osteoarthritis pathogenesis–a complex process that involves the entire joint. Journal of medicine and life. 2014;7:37.
[29] Zhang Y, Jordan JM. Epidemiology of osteoarthritis. Clinics in geriatric medicine. 2010;26:355-69.
[30] Goldring SR, Goldring MB. Changes in the osteochondral unit during osteoarthritis: structure, function and cartilage–bone crosstalk. Nature Reviews Rheumatology. 2016;12:632.
[31] Lories RJ, Luyten FP. The bone–cartilage unit in osteoarthritis. Nature Reviews Rheumatology. 2011;7:43.
[32] Findlay DM, Kuliwaba JS. Bone–cartilage crosstalk: a conversation for understanding osteoarthritis. Bone research. 2016;4:16028.
[33] Santos M, Rodrigues M, Domingues R, Reis R, Gomes M. Regenerative strategies for the treatment of knee joint disabilities. Regenerative Strategies for the Treatment of Knee Joint Disabilities; Oliveira, JM, Ruis, RL, Eds. 2017:349-71.
[34] Bhatia D, Bejarano T, Novo M. Current interventions in the management of knee osteoarthritis. Journal of pharmacy & bioallied sciences. 2013;5:30.

[35] Trigkilidas D, Anand A. The effectiveness of hyaluronic acid intra-articular injections in managing osteoarthritic knee pain. The Annals of The Royal College of Surgeons of England. 2013;95:545-51.
[36] Melton JT, Wilson AJ, Chapman-Sheath P, Cossey AJ. TruFit CB® bone plug: chondral repair, scaffold design, surgical technique and early experiences. Expert review of medical devices. 2010;7:333-41.
[37] Richter DL, Tanksley JA, Miller MD. Osteochondral autograft transplantation: a review of the surgical technique and outcomes. Sports medicine and arthroscopy review. 2016;24:74-8.
[38] Haber DB, Logan CA, Murphy CP, Sanchez A, LaPrade RF, Provencher MT. Osteochondral allograft transplantation for the knee: post-operative rehabilitation. International journal of sports physical therapy. 2019;14:487.
[39] Stone KR, Walgenbach A. Surgical technique for articular cartilage transplantation to full-thickness cartilage defects in the knee joint. Operative Techniques in Orthopaedics. 1997;7:305-11.
[40] Mithoefer K, Peterson L, Saris DB, Mandelbaum BR. Evolution and current role of autologous chondrocyte implantation for treatment of articular cartilage defects in the football (soccer) player. Cartilage. 2012;3:31S-6S.
[41] Pelletier J-P, Martel-Pelletier J, Rannou F, Cooper C. Efficacy and safety of oral NSAIDs and analgesics in the management of osteoarthritis: Evidence from real-life setting trials and surveys. Seminars in arthritis and rheumatism: Elsevier; 2016. p. S22-S7.
[42] Lin AC, Seeto BL, Bartoszko JM, Khoury MA, Whetstone H, Ho L, et al. Modulating hedgehog signaling can attenuate the severity of osteoarthritis. Nature medicine. 2009;15:1421.
[43] Saito T, Fukai A, Mabuchi A, Ikeda T, Yano F, Ohba S, et al. Transcriptional regulation of endochondral ossification by HIF-2α during skeletal growth and osteoarthritis development. Nature medicine. 2010;16:678.
[44] Chen D, Shen J, Zhao W, Wang T, Han L, Hamilton JL, et al. Osteoarthritis: toward a comprehensive understanding of pathological mechanism. Bone research. 2017;5:16044.
[45] Tetsunaga T, Nishida K, Furumatsu T, Naruse K, Hirohata S, Yoshida A, et al. Regulation of mechanical stress-induced MMP-13 and ADAMTS-5 expression by RUNX-2 transcriptional factor in SW1353 chondrocyte-like cells. Osteoarthritis and cartilage. 2011;19:222-32.
[46] Thambyah A, Broom N. On new bone formation in the pre-osteoarthritic joint. Osteoarthritis and cartilage. 2009;17:456-63.
[47] Langer R, Vacanti JP. Tissue engineering. Science. 1993;260:920-6.
[48] Mattei G, Giusti S, Ahluwalia A. Design criteria for generating physiologically relevant in vitro models in bioreactors. Processes. 2014;2:548-69.
[49] Benam KH, Dauth S, Hassell B, Herland A, Jain A, Jang K-J, et al. Engineered in vitro disease models. Annual Review of Pathology: Mechanisms of Disease. 2015;10:195-262.
[50] Takahashi K, Tanabe K, Ohnuki M, Narita M, Ichisaka T, Tomoda K, et al. Induction of pluripotent stem cells from adult human fibroblasts by defined factors. cell. 2007;131:861-72.

[51] Griffith LG, Swartz MA. Capturing complex 3D tissue physiology in vitro. Nature reviews Molecular cell biology. 2006;7:211-24.
[52] Teresa Raimondi M. Engineered tissue as a model to study cell and tissue function from a biophysical perspective. Current drug discovery technologies. 2006;3:245-68.
[53] Seidi A, Ramalingam M. Protocols for biomaterial scaffold fabrication. Integrated Biomaterials in Tissue Engineering. 2012:1-23.
[54] Causa F, Netti PA, Ambrosio L. A multi-functional scaffold for tissue regeneration: the need to engineer a tissue analogue. Biomaterials. 2007;28:5093-9.
[55] Nichol JW, Khademhosseini A. Modular tissue engineering: engineering biological tissues from the bottom up. Soft matter. 2009;5:1312-9.
[56] Martin I, Miot S, Barbero A, Jakob M, Wendt D. Osteochondral tissue engineering. Journal of biomechanics. 2007;40:750-65.
[57] Alexander PG, Gottardi R, Lin H, Lozito TP, Tuan RS. Three-dimensional osteogenic and chondrogenic systems to model osteochondral physiology and degenerative joint diseases. Experimental biology and medicine. 2014;239:1080-95.
[58] Radhakrishnan J, Subramanian A, Krishnan UM, Sethuraman S. Injectable and 3D bioprinted polysaccharide hydrogels: from cartilage to osteochondral tissue engineering. Biomacromolecules. 2016;18:1-26.
[59] Saha S, Kundu B, Kirkham J, Wood D, Kundu SC, Yang XB. Osteochondral tissue engineering in vivo: a comparative study using layered silk fibroin scaffolds from mulberry and nonmulberry silkworms. PloS one. 2013;8:e80004.
[60] Reddy M, Ponnamma D, Choudhary R, Sadasivuni KK. A Comparative Review of Natural and Synthetic Biopolymer Composite Scaffolds. Polymers. 2021;13:1105.
[61] Zhu N, Chen X. Biofabrication of tissue scaffolds. Advances in biomaterials science and biomedical applications. 2013:319.
[62] Glowacki J, Mizuno S. Collagen scaffolds for tissue engineering. Biopolymers: Original Research on Biomolecules. 2008;89:338-44.
[63] Dong C, Lv Y. Application of collagen scaffold in tissue engineering: recent advances and new perspectives. Polymers. 2016;8:42.
[64] Yue K, Trujillo-de Santiago G, Alvarez MM, Tamayol A, Annabi N, Khademhosseini A. Synthesis, properties, and biomedical applications of gelatin methacryloyl (GelMA) hydrogels. Biomaterials. 2015;73:254-71.
[65] Malafaya PB, Silva GA, Reis RL. Natural–origin polymers as carriers and scaffolds for biomolecules and cell delivery in tissue engineering applications. Advanced drug delivery reviews. 2007;59:207-33.
[66] Lien S-M, Ko L-Y, Huang T-J. Effect of crosslinking temperature on compression strength of gelatin scaffold for articular cartilage tissue engineering. Materials Science and Engineering: C. 2010;30:631-5.
[67] Bhardwaj N, Kundu SC. Chondrogenic differentiation of rat MSCs on porous scaffolds of silk fibroin/chitosan blends. Biomaterials. 2012;33:2848-57.

[68] Bhardwaj N, Nguyen QT, Chen AC, Kaplan DL, Sah RL, Kundu SC. Potential of 3-D tissue constructs engineered from bovine chondrocytes/silk fibroin-chitosan for in vitro cartilage tissue engineering. Biomaterials. 2011;32:5773-81.
[69] Hemmati-Sadeghi S, Ringe J, Dehne T, Haag R, Sittinger M. Hyaluronic Acid Influence on Normal and Osteoarthritic Tissue-Engineered Cartilage. International journal of molecular sciences. 2018;19:1519.
[70] Ramamurthi A, Vesely I. Ultraviolet light-induced modification of crosslinked hyaluronan gels. Journal of Biomedical Materials Research Part A: An Official Journal of The Society for Biomaterials, The Japanese Society for Biomaterials, and The Australian Society for Biomaterials and the Korean Society for Biomaterials. 2003;66:317-29.
[71] van Bilsen PH, Krenning G, Billy D, Duval J-L, Huurdeman-Vincent J, van Luyn MJ. Heparin coating of poly (ethylene terephthalate) decreases hydrophobicity, monocyte/leukocyte interaction and tissue interaction. Colloids and Surfaces B: Biointerfaces. 2008;67:46-53.
[72] Van Vlierberghe S, Dubruel P, Schacht E. Biopolymer-based hydrogels as scaffolds for tissue engineering applications: a review. Biomacromolecules. 2011;12:1387-408.
[73] Sun J, Tan H. Alginate-based biomaterials for regenerative medicine applications. Materials. 2013;6:1285-309.
[74] Konwarh R, Bhunia BK, Mandal BB. Opportunities and Challenges in Exploring Indian Non-mulberry Silk for Biomedical Applications. Proc Indian Natn Sci Acad. 2017. p. 85-101.
[75] Vepari C, Kaplan DL. Silk as a biomaterial. Progress in polymer science. 2007;32:991-1007.
[76] Rockwood DN, Preda RC, Yücel T, Wang X, Lovett ML, Kaplan DL. Materials fabrication from Bombyx mori silk fibroin. Nature protocols. 2011;6:1612.
[77] Steinmetz NJ, Bryant SJ. Chondroitin sulfate and dynamic loading alter chondrogenesis of human MSCs in PEG hydrogels. Biotechnology and bioengineering. 2012;109:2671-82.
[78] Wang D-A, Varghese S, Sharma B, Strehin I, Fermanian S, Gorham J, et al. Multifunctional chondroitin sulphate for cartilage tissue–biomaterial integration. Nature materials. 2007;6:385.
[79] Kwon HJ, Han Y. Chondroitin sulfate-based biomaterials for tissue engineering. Turkish Journal of Biology. 2016;40:290-9.
[80] Yan S, Wang T, Feng L, Zhu J, Zhang K, Chen X, et al. Injectable in situ self-cross-linking hydrogels based on poly (L-glutamic acid) and alginate for cartilage tissue engineering. Biomacromolecules. 2014;15:4495-508.
[81] Yan S, Zhang X, Zhang K, Di H, Feng L, Li G, et al. Injectable in situ forming poly (L-glutamic acid) hydrogels for cartilage tissue engineering. Journal of Materials Chemistry B. 2016;4:947-61.
[82] Zhu J. Bioactive modification of poly (ethylene glycol) hydrogels for tissue engineering. Biomaterials. 2010;31:4639-56.
[83] Martina M, Hutmacher DW. Biodegradable polymers applied in tissue engineering research: a review. Polymer International. 2007;56:145-57.

[84] Baker MI, Walsh SP, Schwartz Z, Boyan BD. A review of polyvinyl alcohol and its uses in cartilage and orthopedic applications. Journal of Biomedical Materials Research Part B: Applied Biomaterials. 2012;100:1451-7.
[85] Sabir MI, Xu X, Li L. A review on biodegradable polymeric materials for bone tissue engineering applications. Journal of materials science. 2009;44:5713-24.
[86] Drury JL, Mooney DJ. Hydrogels for tissue engineering: scaffold design variables and applications. Biomaterials. 2003;24:4337-51.
[87] Johnstone B, Alini M, Cucchiarini M, Dodge GR, Eglin D, Guilak F, et al. Tissue engineering for articular cartilage repair—the state of the art. Eur Cell Mater. 2013;25:e67.
[88] Nash ME, Healy D, Carroll WM, Elvira C, Rochev YA. Cell and cell sheet recovery from pNIPAm coatings; motivation and history to present day approaches. Journal of Materials Chemistry. 2012;22:19376-89.
[89] Roach BL, Nover AB, Ateshian GA, Hung CT. Agarose hydrogel characterization for regenerative medicine applications: Focus on engineering cartilage. Biomaterials from Nature for Advanced Devices and Therapies; John Wiley & Sons: Hoboken, NJ, USA. 2016:258.
[90] Selmi TAS, Verdonk P, Chambat P, Dubrana F, Potel J-F, Barnouin L, et al. Autologous chondrocyte implantation in a novel alginate-agarose hydrogel: outcome at two years. The Journal of bone and joint surgery British volume. 2008;90:597-604.
[91] Benya PD, Shaffer JD. Dedifferentiated chondrocytes reexpress the differentiated collagen phenotype when cultured in agarose gels. Cell. 1982;30:215-24.
[92] Buschmann MD, Gluzband YA, Grodzinsky AJ, Kimura JH, Hunziker EB. Chondrocytes in agarose culture synthesize a mechanically functional extracellular matrix. Journal of orthopaedic research. 1992;10:745-58.
[93] Mauck RL, Soltz MA, Wang CC, Wong DD, Chao P-HG, Valhmu WB, et al. Functional tissue engineering of articular cartilage through dynamic loading of chondrocyte-seeded agarose gels. Journal of biomechanical engineering. 2000;122:252-60.
[94] Rennerfeldt DA, Renth AN, Talata Z, Gehrke SH, Detamore MS. Tuning mechanical performance of poly (ethylene glycol) and agarose interpenetrating network hydrogels for cartilage tissue engineering. Biomaterials. 2013;34:8241-57.
[95] Cigan AD, Roach BL, Nims RJ, Tan AR, Albro MB, Stoker AM, et al. High seeding density of human chondrocytes in agarose produces tissue-engineered cartilage approaching native mechanical and biochemical properties. Journal of biomechanics. 2016;49:1909-17.
[96] Mouw J, Case N, Guldberg R, Plaas A, Levenston M. Variations in matrix composition and GAG fine structure among scaffolds for cartilage tissue engineering. Osteoarthritis and Cartilage. 2005;13:828-36.
[97] Pei B, Wang W, Fan Y, Wang X, Watari F, Li X. Fiber-reinforced scaffolds in soft tissue engineering. Regenerative biomaterials. 2017;4:257-68.
[98] Agrawal A, Rahbar N, Calvert PD. Strong fiber-reinforced hydrogel. Acta biomaterialia. 2013;9:5313-8.

[99] Yodmuang S, McNamara SL, Nover AB, Mandal BB, Agarwal M, Kelly T-AN, et al. Silk microfiber-reinforced silk hydrogel composites for functional cartilage tissue repair. Acta biomaterialia. 2015;11:27-36.
[100] Visser J, Melchels FP, Jeon JE, Van Bussel EM, Kimpton LS, Byrne HM, et al. Reinforcement of hydrogels using three-dimensionally printed microfibres. Nature communications. 2015;6:1-10.
[101] Khorshidi S, Karkhaneh A. A Review on Gradient hydrogel/fiber scaffolds for osteochondral regeneration. Journal of tissue engineering and regenerative medicine. 2018;12:e1974-e1990.
[102] Yin D, Wu H, Liu C, Zhang J, Zhou T, Wu J, et al. Fabrication of composition-graded collagen/chitosan–polylactide scaffolds with gradient architecture and properties. Reactive and Functional Polymers. 2014;83:98-106.
[103] Orr T, Villars P, Mitchell S, Hsu H-P, Spector M. Compressive properties of cancellous bone defects in a rabbit model treated with particles of natural bone mineral and synthetic hydroxyapatite. Biomaterials. 2001;22:1953-9.
[104] Ho STB, Hutmacher DW, Ekaputra AK, Hitendra D, Hui JH. The evaluation of a biphasic osteochondral implant coupled with an electrospun membrane in a large animal model. Tissue Engineering Part A. 2009;16:1123-41.
[105] Waldman SD, Grynpas MD, Pilliar RM, Kandel RA. Characterization of cartilagenous tissue formed on calcium polyphosphate substrates in vitro. Journal of Biomedical Materials Research: An Official Journal of The Society for Biomaterials, The Japanese Society for Biomaterials, and The Australian Society for Biomaterials and the Korean Society for Biomaterials. 2002;62:323-30.
[106] Kandel R, Grynpas M, Pilliar R, Lee J, Wang J, Waldman S, et al. Repair of osteochondral defects with biphasic cartilage-calcium polyphosphate constructs in a sheep model. Biomaterials. 2006;27:4120-31.
[107] Gao J, Dennis JE, Solchaga LA, Awadallah AS, Goldberg VM, Caplan AI. Tissue-engineered fabrication of an osteochondral composite graft using rat bone marrow-derived mesenchymal stem cells. Tissue engineering. 2001;7:363-71.
[108] Galperin A, Oldinski RA, Florczyk SJ, Bryers JD, Zhang M, Ratner BD. Integrated bi-layered scaffold for osteochondral tissue engineering. Advanced healthcare materials. 2013;2:872-83.
[109] Oliveira JM, Rodrigues MT, Silva SS, Malafaya PB, Gomes ME, Viegas CA, et al. Novel hydroxyapatite/chitosan bilayered scaffold for osteochondral tissue-engineering applications: Scaffold design and its performance when seeded with goat bone marrow stromal cells. Biomaterials. 2006;27:6123-37.
[110] Li JJ, Kim K, Roohani-Esfahani S-I, Guo J, Kaplan DL, Zreiqat H. A biphasic scaffold based on silk and bioactive ceramic with stratified properties for osteochondral tissue regeneration. Journal of Materials Chemistry B. 2015;3:5361-76.
[111] Murphy SV, Atala A. 3D bioprinting of tissues and organs. Nature biotechnology. 2014;32:773-85.

[112] Mota C, Camarero-Espinosa S, Baker MB, Wieringa P, Moroni L. Bioprinting: From Tissue and Organ Development to in Vitro Models. Chemical Reviews. 2020;120:10547-607.
[113] Das S, Basu B. An Overview of Hydrogel-Based Bioinks for 3D Bioprinting of Soft Tissues. Journal of the Indian Institute of Science. 2019;99:405–28.
[114] Gopinathan J, Noh I. Recent trends in bioinks for 3D printing. Biomaterials research. 2018;22:11.
[115] Sherwood JK, Riley SL, Palazzolo R, Brown SC, Monkhouse DC, Coates M, et al. A three-dimensional osteochondral composite scaffold for articular cartilage repair. Biomaterials. 2002;23:4739-51.
[116] Cui X, Breitenkamp K, Finn M, Lotz M, D'Lima DD. Direct human cartilage repair using three-dimensional bioprinting technology. Tissue Engineering Part A. 2012;18:1304-12.
[117] Xu T, Binder KW, Albanna MZ, Dice D, Zhao W, Yoo JJ, et al. Hybrid printing of mechanically and biologically improved constructs for cartilage tissue engineering applications. Biofabrication. 2012;5:015001.
[118] Kundu J, Shim JH, Jang J, Kim SW, Cho DW. An additive manufacturing-based PCL–alginate–chondrocyte bioprinted scaffold for cartilage tissue engineering. Journal of tissue engineering and regenerative medicine. 2015;9:1286-97.
[119] Pati F, Jang J, Ha D-H, Kim SW, Rhie J-W, Shim J-H, et al. Printing three-dimensional tissue analogues with decellularized extracellular matrix bioink. Nature communications. 2014;5:1-11.
[120] Datta P, Dhawan A, Yu Y, Hayes D, Gudapati H, Ozbolat IT. Bioprinting of osteochondral tissues: A perspective on current gaps and future trends. International Journal of Bioprinting. 2017;3.
[121] Schek RM, Taboas JM, Segvich SJ, Hollister SJ, Krebsbach PH. Engineered osteochondral grafts using biphasic composite solid free-form fabricated scaffolds. Tissue engineering. 2004;10:1376-85.
[122] Zhang W, Lian Q, Li D, Wang K, Hao D, Bian W, et al. Cartilage repair and subchondral bone migration using 3D printing osteochondral composites: a one-year-period study in rabbit trochlea. BioMed research international. 2014;2014:746138.
[123] Cao T, Ho K-H, Teoh S-H. Scaffold design and in vitro study of osteochondral coculture in a three-dimensional porous polycaprolactone scaffold fabricated by fused deposition modeling. Tissue engineering. 2003;9:103-12.
[124] Yang SS, Choi WH, Song BR, Jin H, Lee SJ, Lee SH, et al. Fabrication of an osteochondral graft with using a solid freeform fabrication system. Tissue Engineering and Regenerative Medicine. 2015;12:239-48.
[125] Fedorovich NE, Schuurman W, Wijnberg HM, Prins HJ, Van Weeren PR, Malda J, et al. Biofabrication of osteochondral tissue equivalents by printing topologically defined, cell-laden hydrogel scaffolds. Tissue Engineering - Part C: Methods. 2012;18:33-44.

[126] Shim J-H, Lee J-S, Kim JY, Cho D-W. Bioprinting of a mechanically enhanced three-dimensional dual cell-laden construct for osteochondral tissue engineering using a multi-head tissue/organ building system. Journal of Micromechanics and Microengineering. 2012;22:085014.
[127] Kundu J, Shim J-H, Jang J, Kim S-W, Cho D-W. An additive manufacturing-based PCL-alginate-chondrocyte bioprinted scaffold for cartilage tissue engineering. Journal of Tissue Engineering and Regenerative Medicine. 2015;9:1286-97.
[128] Pati F, Jang J, Ha DH, Won Kim S, Rhie JW, Shim JH, et al. Printing three-dimensional tissue analogues with decellularized extracellular matrix bioink. Nature Communications. 2014;5.
[129] Levato R, Visser J, Planell JA, Engel E, Malda J, Mateos-Timoneda MA. Biofabrication of tissue constructs by 3D bioprinting of cell-laden microcarriers. Biofabrication. 2014;6:035020.
[130] Kesti M, Müller M, Becher J, Schnabelrauch M, D'Este M, Eglin D, et al. A versatile bioink for three-dimensional printing of cellular scaffolds based on thermally and photo-triggered tandem gelation. Acta Biomaterialia. 2015;11:162-72.
[131] Costantini M, Idaszek J, Szöke K, Jaroszewicz J, Dentini M, Barbetta A, et al. 3D bioprinting of BM-MSCs-loaded ECM biomimetic hydrogels for in vitro neocartilage formation. Biofabrication. 2016;8:035002.
[132] Duchi S, Onofrillo C, O'Connell CD, Blanchard R, Augustine C, Quigley AF, et al. Handheld Co-Axial Bioprinting: Application to in situ surgical cartilage repair. Scientific Reports. 2017;7:5837.
[133] Di Bella C, Duchi S, O'Connell CD, Blanchard R, Augustine C, Yue Z, et al. In situ handheld three-dimensional bioprinting for cartilage regeneration. Journal of Tissue Engineering and Regenerative Medicine. 2018;12:611-21.
[134] Apelgren P, Amoroso M, Lindahl A, Brantsing C, Rotter N, Gatenholm P, et al. Chondrocytes and stem cells in 3D-bioprinted structures create human cartilage in vivo. PLOS ONE. 2017;12:e0189428.
[135] Mouser VHM, Levato R, Mensinga A, Dhert WJA, Gawlitta D, Malda J. Bio-ink development for three-dimensional bioprinting of hetero-cellular cartilage constructs. Connective Tissue Research. 2020;61:137-51.
[136] Kaye R, Goldstein T, Grande DA, Zeltsman D, Smith LP. A 3-dimensional bioprinted tracheal segment implant pilot study: Rabbit tracheal resection with graft implantation. International Journal of Pediatric Otorhinolaryngology. 2019;117:175-8.
[137] Apelgren P, Karabulut E, Amoroso M, Mantas A, Martínez Ávila H, Kölby L, et al. In Vivo Human Cartilage Formation in Three-Dimensional Bioprinted Constructs with a Novel Bacterial Nanocellulose Bioink. ACS Biomaterials Science and Engineering. 2019;5:2482-90.
[138] Armstrong JPK, Burke M, Carter BM, Davis SA, Perriman AW. 3D Bioprinting Using a Templated Porous Bioink. Advanced Healthcare Materials. 2016;5:1724-30.
[139] Singh YP, Bandyopadhyay A, Mandal BB. 3D Bioprinting Using Cross-Linker-Free Silk–Gelatin Bioink for Cartilage Tissue Engineering. ACS applied materials & interfaces. 2019;11:33684-96.

[140] Sun Y, You Y, Jiang W, Zhai Z, Dai K. 3D-bioprinting a genetically inspired cartilage scaffold with GDF5-conjugated BMSC-laden hydrogel and polymer for cartilage repair. Theranostics. 2019;9:6949-61.
[141] Möller T, Amoroso M, Hägg D, Brantsing C, Rotter N, Apelgren P, et al. In Vivo Chondrogenesis in 3D Bioprinted Human Cell-laden Hydrogel Constructs. Plastic and Reconstructive Surgery - Global Open. 2017;5:e1227.
[142] Melo BAG, Jodat YA, Mehrotra S, Calabrese MA, Kamperman T, Mandal BB, et al. 3D Printed Cartilage-Like Tissue Constructs with Spatially Controlled Mechanical Properties. Advanced Functional Materials. 2019;29:1906330.
[143] Nguyen D, Hgg DA, Forsman A, Ekholm J, Nimkingratana P, Brantsing C, et al. Cartilage Tissue Engineering by the 3D Bioprinting of iPS Cells in a Nanocellulose/Alginate Bioink. Scientific Reports. 2017;7:1-10.
[144] Yi HG, Choi YJ, Jung JW, Jang J, Song TH, Chae S, et al. Three-dimensional printing of a patient-specific engineered nasal cartilage for augmentative rhinoplasty. Journal of Tissue Engineering. 2019;10:1-14.
[145] Galarraga JH, Kwon MY, Burdick JA. 3D bioprinting via an in situ crosslinking technique towards engineering cartilage tissue. Scientific Reports. 2019;9:19987.
[146] Henrionnet C, Pourchet L, Neybecker P, Messaoudi O, Gillet P, Loeuille D, et al. Combining Innovative Bioink and Low Cell Density for the Production of 3D-Bioprinted Cartilage Substitutes: A Pilot Study. Stem Cells International. 2020;2020:2487072.
[147] Moses JC, Saha T, Mandal BB. Chondroprotective and osteogenic effects of silk-based bioinks in developing 3D bioprinted osteochondral interface. Bioprinting. 2020;17:e00067.
[148] Li Z, Zhang X, Yuan T, Zhang Y, Luo C, Zhang J, et al. Addition of Platelet-Rich Plasma to Silk Fibroin Hydrogel Bioprinting for Cartilage Regeneration. Tissue Engineering Part A. 2020;26:886-95.
[149] Ruiz-Cantu L, Gleadall A, Faris C, Segal J, Shakesheff K, Yang J. Multi-material 3D bioprinting of porous constructs for cartilage regeneration. Materials Science and Engineering C. 2020;109:110578.
[150] Ma K, Zhao T, Yang L, Wang P, Jin J, Teng H, et al. Application of robotic-assisted in situ 3D printing in cartilage regeneration with HAMA hydrogel: An in vivo study. Journal of Advanced Research. 2020;23:123-32.
[151] De Vries-van Melle ML, Mandl EW, Kops N, Koevoet WJ, Verhaar JA, van Osch GJ. An osteochondral culture model to study mechanisms involved in articular cartilage repair. Tissue Engineering Part C: Methods. 2012;18:45-53.
[152] Grenier S, Bhargava MM, Torzilli PA. An in vitro model for the pathological degradation of articular cartilage in osteoarthritis. Journal of biomechanics. 2014;47:645-52.
[153] Dechant JE, Baxter G, Frisbie D, Trotter G, McIlwraith C. Effects of glucosamine hydrochloride and chondroitin sulphate, alone and in combination, on normal and interleukin-1 conditioned equine articular cartilage explant metabolism. Equine veterinary journal. 2005;37:227-31.

[154] Sawitzke AD, Shi H, Finco MF, Dunlop DD, Harris CL, Singer NG, et al. Clinical efficacy and safety of glucosamine, chondroitin sulphate, their combination, celecoxib or placebo taken to treat osteoarthritis of the knee: 2-year results from GAIT. Annals of the rheumatic diseases. 2010;69:1459-64.
[155] Johnson CI, Argyle DJ, Clements DN. In vitro models for the study of osteoarthritis. The Veterinary Journal. 2016;209:40-9.
[156] Martel-Pelletier J, Alaaeddine N, Pelletier J-P. Cytokines and their role in the pathophysiology of osteoarthritis. Front Biosci. 1999;4:d694-703.
[157] Maccoux LJ, Salway F, Day PJ, Clements DN. Expression profiling of select cytokines in canine osteoarthritis tissues. Veterinary immunology and immunopathology. 2007;118:59-67.
[158] Liacini A, Sylvester J, Li WQ, Huang W, Dehnade F, Ahmad M, et al. Induction of matrix metalloproteinase-13 gene expression by TNF-α is mediated by MAP kinases, AP-1, and NF-κB transcription factors in articular chondrocytes. Experimental cell research. 2003;288:208-17.
[159] Klatt AR, Paul-Klausch B, Klinger G, Kühn G, Renno JH, Banerjee M, et al. A critical role for collagen II in cartilage matrix degradation: collagen II induces pro-inflammatory cytokines and MMPs in primary human chondrocytes. Journal of orthopaedic research. 2009;27:65-70.
[160] Cortial D, Gouttenoire J, Rousseau C, Ronziere M-C, Piccardi N, Msika P, et al. Activation by IL-1 of bovine articular chondrocytes in culture within a 3D collagen-based scaffold. An in vitro model to address the effect of compounds with therapeutic potential in osteoarthritis. Osteoarthritis and cartilage. 2006;14:631-40.
[161] Sun L, Wang X, Kaplan DL. A 3D cartilage–inflammatory cell culture system for the modeling of human osteoarthritis. Biomaterials. 2011;32:5581-9.
[162] Aydin O, Korkusuz F, Korkusuz P, Tezcaner A, Bilgic E, Yaprakci V, et al. I n vitro and in vivo evaluation of doxycycline-chondroitin sulfate/PCL microspheres for intraarticular treatment of osteoarthritis. Journal of Biomedical Materials Research Part B: Applied Biomaterials. 2015;103:1238-48.
[163] Zhang Z, Wei X, Gao J, Zhao Y, Zhao Y, Guo L, et al. Intra-articular injection of cross-linked hyaluronic acid-dexamethasone hydrogel attenuates osteoarthritis: an experimental study in a rat model of osteoarthritis. International journal of molecular sciences. 2016;17:411.
[164] Tamaddon M, Wang L, Liu Z, Liu CJB-d, manufacturing. Osteochondral tissue repair in osteoarthritic joints: clinical challenges and opportunities in tissue engineering. 2018;1:101-14.
[165] Mollon B, Kandel R, Chahal J, Theodoropoulos JJO, cartilage. The clinical status of cartilage tissue regeneration in humans. 2013;21:1824-33.
[166] Marcacci M, Kon E, Moukhachev V, Lavroukov A, Kutepov S, Quarto R, et al. Stem cells associated with macroporous bioceramics for long bone repair: 6-to 7-year outcome of a pilot clinical study. 2007;13:947-55.
[167] Cengiz IF, Pereira H, de Girolamo L, Cucchiarini M, Espregueira-Mendes J, Reis RL, et al. Orthopaedic regenerative tissue engineering en route to the holy grail: disequilibrium between the demand and the supply in the operating room. 2018;5:14.

[168] Oryan A, Alidadi S, Moshiri A, Maffulli N. Bone regenerative medicine: classic options, novel strategies, and future directions. Journal of orthopaedic surgery and research. 2014;9:1-27.
[169] Bicho D, Pina S, Reis RL, Oliveira JM. Commercial products for osteochondral tissue repair and regeneration. Osteochondral Tissue Engineering. 2018:415-28.
[170] Ling S, Qin Z, Li C, Huang W, Kaplan DL, Buehler MJ. Polymorphic regenerated silk fibers assembled through bioinspired spinning. Nature communications. 2017;8:1-12.
[171] Holland C, Numata K, Rnjak-Kovacina J, Seib FP. The biomedical use of silk: past, present, future. Advanced healthcare materials. 2019;8:1800465.
[172] Malay AD, Sato R, Yazawa K, Watanabe H, Ifuku N, Masunaga H, et al. Relationships between physical properties and sequence in silkworm silks. Scientific reports. 2016;6:1-11.
[173] Salehi S, Koeck K, Scheibel T. Spider silk for tissue engineering applications. Molecules. 2020;25:737.
[174] Panilaitis B, Altman GH, Chen J, Jin H-J, Karageorgiou V, Kaplan DL. Macrophage responses to silk. Biomaterials. 2003;24:3079-85.
[175] Kapoor S, Kundu SC. Silk protein-based hydrogels: Promising advanced materials for biomedical applications. Acta biomaterialia. 2016;31:17-32.
[176] Kim U-J, Park J, Li C, Jin H-J, Valluzzi R, Kaplan DL. Structure and properties of silk hydrogels. Biomacromolecules. 2004;5:786-92.
[177] Zhang Q, Yan S, Li M. Silk fibroin based porous materials. Materials. 2009;2:2276-95.
[178] Hu Y, Zhang Q, You R, Wang L, Li M. The relationship between secondary structure and biodegradation behavior of silk fibroin scaffolds. Advances in Materials Science and Engineering. 2012;2012.
[179] Asakura T, Ohgo K, Ishida T, Taddei P, Monti P, Kishore R. Possible Implications of Serine and Tyrosine Residues and Intermolecular Interactions on the Appearance of Silk I Structure of Bombyx m ori Silk Fibroin-Derived Synthetic Peptides: High-Resolution 13C Cross-Polarization/Magic-Angle Spinning NMR Study. Biomacromolecules. 2005;6:468-74.
[180] Bandyopadhyay A, Chowdhury SK, Dey S, Moses JC, Mandal BB. Silk: A promising biomaterial opening new vistas towards affordable healthcare solutions. Journal of the Indian Institute of Science. 2019;99:445-87.
[181] Konwarh R, Bhunia BK, Mandal BB. Opportunities and challenges in exploring Indian nonmulberry silk for biomedical applications. Proceedings of the Indian National Science Academy. 2017;83:85-101.
[182] Mandal BB, Das S, Choudhury K, Kundu SC. Implication of silk film RGD availability and surface roughness on cytoskeletal organization and proliferation of primary rat bone marrow cells. Tissue Engineering Part A. 2010;16:2391-403.
[183] Zhang W, Ling C, Zhang A, Liu H, Jiang Y, Li X, et al. An all-silk-derived functional nanosphere matrix for sequential biomolecule delivery and in situ osteochondral regeneration. Bioactive Materials. 2020;5:832-43.
[184] Ding Z, Han H, Fan Z, Lu H, Sang Y, Yao Y, et al. Nanoscale silk–hydroxyapatite hydrogels for injectable bone biomaterials. ACS applied materials & interfaces. 2017;9:16913-21.

[185] Han C, Zhou J, Liu B, Liang C, Pan X, Zhang Y, et al. Delivery of miR-675 by stem cell-derived exosomes encapsulated in silk fibroin hydrogel prevents aging-induced vascular dysfunction in mouse hindlimb. Materials Science and Engineering: C. 2019;99:322-32.
[186] Yuan T, Li Z, Zhang Y, Shen K, Zhang X, Xie R, et al. Injectable ultrasonication-induced silk fibroin hydrogel for cartilage repair and regeneration. Tissue Engineering Part A. 2021.
[187] Wu J, Zheng K, Huang X, Liu J, Liu H, Boccaccini AR, et al. Thermally triggered injectable chitosan/silk fibroin/bioactive glass nanoparticle hydrogels for in-situ bone formation in rat calvarial bone defects. Acta biomaterialia. 2019;91:60-71.
[188] Cipriani F, Krüger M, De Torre IG, Sierra LQ, Rodrigo MA, Kock L, et al. Cartilage regeneration in preannealed silk elastin-like co-recombinamers injectable hydrogel embedded with mature chondrocytes in an ex vivo culture platform. Biomacromolecules. 2018;19:4333-47.
[189] Oliveira IM, Gonçalves C, Shin ME, Lee S, Reis RL, Khang G, et al. Anti-Inflammatory Properties of Injectable Betamethasone-Loaded Tyramine-Modified Gellan Gum/Silk Fibroin Hydrogels. Biomolecules. 2020;10:1456.
[190] Singh YP, Bandyopadhyay A, Mandal BB. 3D Bioprinting Using Cross-Linker-Free Silk–Gelatin Bioink for Cartilage Tissue Engineering. ACS Applied Materials & Interfaces. 2019;11:33684-96.
[191] Bhunia BK, Mandal BB. Exploring gelation and physicochemical behavior of in situ bioresponsive silk hydrogels for disc degeneration therapy. ACS Biomaterials Science & Engineering. 2018;5:870-86.
[192] Qi C, Liu J, Jin Y, Xu L, Wang G, Wang Z, et al. Photo-crosslinkable, injectable sericin hydrogel as 3D biomimetic extracellular matrix for minimally invasive repairing cartilage. Biomaterials. 2018;163:89-104.
[193] Li Y, Liu Y, Guo Q. Silk fibroin hydrogel scaffolds incorporated with chitosan nanoparticles repair articular cartilage defects by regulating TGF-β1 and BMP-2. Arthritis Research & Therapy. 2021;23:1-11.
[194] Dong Y, Sun X, Zhang Z, Liu Y, Zhang L, Zhang X, et al. Regional and sustained dual-release of growth factors from biomimetic tri-layered scaffolds for the repair of large-scale osteochondral defects. Applied Materials Today. 2020;19:100548.
[195] Ribeiro VP, Pina SCA, Canadas RF, Morais A, Vilela C, Vieira SCA, et al. In vivo performance of hierarchical HRP-crosslinked silk fibroin/β-TCP scaffolds for osteochondral tissue regeneration. Regen Med Front. 2019;1:e190007.
[196] Ribeiro VP, Pina S, Gheduzzi S, Araújo AC, Reis RL, Oliveira JM. Hierarchical HRP-crosslinked silk fibroin/ZnSr-TCP scaffolds for osteochondral tissue regeneration: Assessment of the mechanical and antibacterial properties. Frontiers in Materials. 2020;7:49.
[197] Reardon P, Konwarh R, Knowles JC, Mandal BB. Mimicking hierarchical complexity of the osteochondral interface using electrospun silk-bioactive glass composites. ACS applied materials & interfaces. 2017;9:8000-13.

[198] Shang L, Ma B, Wang F, Li J, Shen S, Li X, et al. Nanotextured silk fibroin/hydroxyapatite biomimetic bilayer tough structure regulated osteogenic/chondrogenic differentiation of mesenchymal stem cells for osteochondral repair. Cell proliferation. 2020;53:e12917.
[199] Midha S, Kumar S, Sharma A, Kaur K, Shi X, Naruphontjirakul P, et al. Silk fibroin-bioactive glass based advanced biomaterials: towards patient-specific bone grafts. Biomedical Materials. 2018;13:055012.
[200] Zheng L, Li D, Wang W, Zhang Q, Zhou X, Liu D, et al. Bilayered scaffold prepared from a kartogenin-loaded hydrogel and bmp-2-derived peptide-loaded porous nanofibrous scaffold for osteochondral defect repair. ACS Biomaterials Science & Engineering. 2019;5:4564-73.
[201] Zhou F, Zhang X, Cai D, Li J, Mu Q, Zhang W, et al. Silk fibroin-chondroitin sulfate scaffold with immuno-inhibition property for articular cartilage repair. Acta biomaterialia. 2017;63:64-75.
[202] Eivazzadeh-Keihan R, Radinekiyan F, Aliabadi HAM, Sukhtezari S, Tahmasebi B, Maleki A, et al. Chitosan hydrogel/silk fibroin/Mg (OH) 2 nanobiocomposite as a novel scaffold with antimicrobial activity and improved mechanical properties. Scientific Reports. 2021;11:1-13.
[203] Li Z, Zhang X, Yuan T, Zhang Y, Luo C, Zhang J, et al. Addition of Platelet-Rich Plasma to Silk Fibroin Hydrogel Bioprinting for Cartilage Regeneration. Tissue Engineering Part A. 2020:ten.tea.2019.0304.
[204] Barlian A, Judawisastra H, Ridwan A, Wahyuni AR, Lingga ME. Chondrogenic differentiation of Wharton's Jelly mesenchymal stem cells on silk spidroin-fibroin mix scaffold supplemented with L-ascorbic acid and platelet rich plasma. Scientific Reports. 2020;10:1-18.
[205] Wei L, Wu S, Kuss M, Jiang X, Sun R, Reid P, et al. 3D printing of silk fibroin-based hybrid scaffold treated with platelet rich plasma for bone tissue engineering. Bioactive materials. 2019;4:256-60.
[206] Hong H, Seo YB, Lee JS, Lee YJ, Lee H, Ajiteru O, et al. Digital light processing 3D printed silk fibroin hydrogel for cartilage tissue engineering. Biomaterials. 2020;232:119679.
[207] Sun K, Li R, Li H, Li D, Jiang W. Comparison of three-dimensional printing for fabricating silk fibroin-blended scaffolds. International Journal of Polymeric Materials and Polymeric Biomaterials. 2018;67:480-6.
[208] Jung CS, Kim BK, Lee J, Min B-H, Park S-H. Development of printable natural cartilage matrix bioink for 3D printing of irregular tissue shape. Tissue Engineering and Regenerative Medicine. 2018;15:155-62.
[209] Shi W, Sun M, Hu X, Ren B, Cheng J, Li C, et al. Structurally and functionally optimized silk-fibroin–gelatin scaffold using 3D printing to repair cartilage injury in vitro and in vivo. Advanced materials. 2017;29:1701089.
[210] Lee JM, Sultan M, Kim SH, Kumar V, Yeon YK, Lee OJ, et al. Artificial auricular cartilage using silk fibroin and polyvinyl alcohol hydrogel. International journal of molecular sciences. 2017;18:1707.
[211] Chen C-H, Liu JM-J, Chua C-K, Chou S-M, Shyu VB-H, Chen J-P. Cartilage tissue engineering with silk fibroin scaffolds fabricated by indirect additive manufacturing technology. Materials. 2014;7:2104-19.

[212] Bandyopadhyay A, Mandal BB. A three-dimensional printed silk-based biomimetic tri-layered meniscus for potential patient-specific implantation. Biofabrication. 2019;12:015003.
[213] Costa JB, Silva-Correia J, Oliveira JM, Reis RL. Fast setting silk fibroin bioink for bioprinting of patient-specific memory-shape implants. Advanced Healthcare Materials. 2017;6:1701021.
[214] Costa JB, Silva-Correia J, Ribeiro VP, da Silva Morais A, Oliveira JM, Reis RL. Engineering patient-specific bioprinted constructs for treatment of degenerated intervertebral disc. Materials Today Communications. 2019;19:506-12.
[215] Huang L, Du X, Fan S, Yang G, Shao H, Li D, et al. Bacterial cellulose nanofibers promote stress and fidelity of 3D-printed silk based hydrogel scaffold with hierarchical pores. Carbohydrate polymers. 2019;221:146-56.
[216] Hinman RS, Hunt MA, Creaby MW, Wrigley TV, McManus FJ, Bennell KL. Hip muscle weakness in individuals with medial knee osteoarthritis. Arthritis care & research. 2010;62:1190-3.
[217] Piscitelli P, Iolascon G, Di Tanna G, Bizzi E, Chitano G, Argentiero A, et al. Socioeconomic burden of total joint arthroplasty for symptomatic hip and knee osteoarthritis in the Italian population: A 5-year analysis based on hospitalization records. Arthritis care & research. 2012;64:1320-7.
[218] Wang Y, Kim U-J, Blasioli DJ, Kim H-J, Kaplan DL. In vitro cartilage tissue engineering with 3D porous aqueous-derived silk scaffolds and mesenchymal stem cells. Biomaterials. 2005;26:7082-94.
[219] Redman S, Oldfield S, Archer C. Current strategies for articular cartilage repair. Eur Cell Mater. 2005;9:23-32.
[220] Abdel-Sayed P, Pioletti DP. Strategies for improving the repair of focal cartilage defects. Nanomedicine. 2015;10:2893-905.
[221] Langer R, Vacanti J. Tissue engineering. Science. 1993;260:920-6.
[222] O'brien FJ. Biomaterials & scaffolds for tissue engineering. Materials Today. 2011;14:88-95.
[223] Lee KY, Mooney DJ. Hydrogels for tissue engineering. Chemical reviews. 2001;101:1869-80.
[224] Wang HY, Zhang YQ. Processing silk hydrogel and its applications in biomedical materials. Biotechnology progress. 2015;31:630-40.
[225] Bellamkonda R, Ranieri JP, Bouche N, Aebischer P. Hydrogel-based three-dimensional matrix for neural cells. Journal of biomedical materials research. 1995;29:663-71.
[226] Selmi T, Verdonk P, Chambat P, Dubrana F, Potel J-F, Barnouin L, et al. Autologous chondrocyte implantation in a novel alginate-agarose hydrogel OUTCOME AT TWO YEARS. Journal of Bone & Joint Surgery, British Volume. 2008;90:597-604.
[227] Buschmann MD, Gluzband YA, Grodzinsky AJ, Hunziker EB. Mechanical compression modulates matrix biosynthesis in chondrocyte/agarose culture. Journal of cell science. 1995;108:1497-508.

[228] Francioli SE, Candrian C, Martin K, Heberer M, Martin I, Barbero A. Effect of three-dimensional expansion and cell seeding density on the cartilage-forming capacity of human articular chondrocytes in type II collagen sponges. Journal of Biomedical Materials Research Part A. 2010;95:924-31.
[229] Lima EG, Bian L, Ng KW, Mauck RL, Byers BA, Tuan RS, et al. The beneficial effect of delayed compressive loading on tissue-engineered cartilage constructs cultured with TGF-β3. Osteoarthritis and Cartilage. 2007;15:1025-33.
[230] Chao PHG, Yodmuang S, Wang X, Sun L, Kaplan DL, Vunjak-Novakovic G. Silk hydrogel for cartilage tissue engineering. Journal of Biomedical Materials Research Part B: Applied Biomaterials. 2010;95:84-90.
[231] Gruber HE, Fisher Jr EC, Desai B, Stasky AA, Hoelscher G, Hanley Jr EN. Human intervertebral disc cells from the annulus: three-dimensional culture in agarose or alginate and responsiveness to TGF-β1. Experimental Cell Research. 1997;235:13-21.
[232] Hunter CJ, Levenston ME. Maturation and integration of tissue-engineered cartilages within an in vitro defect repair model. Tissue engineering. 2004;10:736-46.
[233] Doulabi AH, Mequanint K, Mohammadi H. Blends and nanocomposite biomaterials for articular cartilage tissue engineering. Materials. 2014;7:5327-55.
[234] Bhat S, Tripathi A, Kumar A. Supermacroprous chitosan–agarose–gelatin cryogels: in vitro characterization and in vivo assessment for cartilage tissue engineering. Journal of the Royal Society Interface. 2011;8:540-54.
[235] Vepari C, Kaplan DL. Silk as a biomaterial. Progress in polymer science. 2007;32:991-1007.
[236] Rockwood DN, Preda RC, Yücel T, Wang X, Lovett ML, Kaplan DL. Materials fabrication from Bombyx mori silk fibroin. Nature protocols. 2011;6:1612-31.
[237] Meinel L, Hofmann S, Karageorgiou V, Kirker-Head C, McCool J, Gronowicz G, et al. The inflammatory responses to silk films in vitro and in vivo. Biomaterials. 2005;26:147-55.
[238] Mandal BB, Grinberg A, Gil ES, Panilaitis B, Kaplan DL. High-strength silk protein scaffolds for bone repair. Proceedings of the National Academy of Sciences. 2012;109:7699-704.
[239] Altman GH, Horan RL, Lu HH, Moreau J, Martin I, Richmond JC, et al. Silk matrix for tissue engineered anterior cruciate ligaments. Biomaterials. 2002;23:4131-41.
[240] Kang JH, Gimble JM, Kaplan DL. In vitro 3D model for human vascularized adipose tissue. Tissue Engineering Part A. 2009;15:2227-36.
[241] Wang Y, Blasioli DJ, Kim H-J, Kim HS, Kaplan DL. Cartilage tissue engineering with silk scaffolds and human articular chondrocytes. Biomaterials. 2006;27:4434-42.
[242] Park SY, Ki CS, Park YH, Jung HM, Woo KM, Kim HJ. Electrospun silk fibroin scaffolds with macropores for bone regeneration: an in vitro and in vivo study. Tissue Engineering Part A. 2010;16:1271-9.
[243] Lovett M, Eng G, Kluge J, Cannizzaro C, Vunjak-Novakovic G, Kaplan DL. Tubular silk scaffolds for small diameter vascular grafts. Organogenesis. 2010;6:217-24.

[244] Mauney JR, Nguyen T, Gillen K, Kirker-Head C, Gimble JM, Kaplan DL. Engineering adipose-like tissue in vitro and in vivo utilizing human bone marrow and adipose-derived mesenchymal stem cells with silk fibroin 3D scaffolds. Biomaterials. 2007;28:5280-90.
[245] Kar S, Talukdar S, Pal S, Nayak S, Paranjape P, Kundu S. Silk gland fibroin from Indian muga silkworm Antheraea assama as potential biomaterial. Tissue Engineering and Regenerative Medicine. 2013;10:200-10.
[246] Bhardwaj N, Rajkhowa R, Wang X, Devi D. Milled non-mulberry silk fibroin microparticles as biomaterial for biomedical applications. International journal of biological macromolecules. 2015;81:31-40.
[247] Gupta A, Mita K, Arunkumar KP, Nagaraju J. Molecular architecture of silk fibroin of Indian golden silkmoth, Antheraea assama. Scientific reports. 2015;5.
[248] Loeser RF. Integrins and chondrocyte–matrix interactions in articular cartilage. Matrix Biology. 2014;39:11-6.
[249] Talukdar B, Saikia M, Handique PJ, Devi D. Effect of organic solvents on tensile strength of muga silk produced by Antheraea assamensis. Int J Pure Appl Sci Technol. 2011;7:81-6.
[250] Bhardwaj N, Singh YP, Devi D, Kandimalla R, Kotoky J, Mandal BB. Potential of silk fibroin/chondrocyte constructs of muga silkworm Antheraea assamensis for cartilage tissue engineering. Journal of Materials Chemistry B. 2016;4:3670-3684.
[251] Gupta P, Kumar M, Bhardwaj N, Kumar JP, Krishnamurthy C, Nandi SK, et al. Mimicking form and function of native small diameter vascular conduits using mulberry and non-mulberry patterned silk films. ACS applied materials & interfaces. 2016;8:15874-88.
[252] Maličev E, Kregar-Velikonja N, Barlič A, Alibegović A, Drobnič M. Comparison of articular and auricular cartilage as a cell source for the autologous chondrocyte implantation. Journal of Orthopaedic Research. 2009;27:943-8.
[253] Mandal BB, Park S-H, Gil ES, Kaplan DL. Multilayered silk scaffolds for meniscus tissue engineering. Biomaterials. 2011;32:639-51.
[254] Mandal BB, Kundu S. A novel method for dissolution and stabilization of non-mulberry silk gland protein fibroin using anionic surfactant sodium dodecyl sulfate. Biotechnology and bioengineering. 2008;99:1482-9.
[255] Whitley C, Ridnour M, Draper K, Dutton C, Neglia J. Diagnostic test for mucopolysaccharidosis. I. Direct method for quantifying excessive urinary glycosaminoglycan excretion. Clinical chemistry. 1989;35:374-9.
[256] Tullberg-Reinert H, Jundt G. In situ measurement of collagen synthesis by human bone cells with a Sirius Red-based colorimetric microassay: effects of transforming growth factor β2 and ascorbic acid 2-phosphate. Histochemistry and cell biology. 1999;112:271-6.
[257] Wang L, Stegemann JP. Extraction of high quality RNA from polysaccharide matrices using cetlytrimethylammonium bromide. Biomaterials. 2010;31:1612-8.
[258] Lien S-M, Ko L-Y, Huang T-J. Effect of pore size on ECM secretion and cell growth in gelatin scaffold for articular cartilage tissue engineering. Acta biomaterialia. 2009;5:670-9.

[259] Liao J, Qu Y, Chu B, Zhang X, Qian Z. Biodegradable CSMA/PECA/graphene porous hybrid scaffold for cartilage tissue engineering. Scientific reports. 2015;5.
[260] Cao Z, Gilbert RJ, He W. Simple Agarose− Chitosan gel composite system for enhanced neuronal growth in three dimensions. Biomacromolecules. 2009;10:2954-9.
[261] Wang X, Kluge JA, Leisk GG, Kaplan DL. Sonication-induced gelation of silk fibroin for cell encapsulation. Biomaterials. 2008;29:1054-64.
[262] Li M, Ogiso M, Minoura N. Enzymatic degradation behavior of porous silk fibroin sheets. Biomaterials. 2003;24:357-65.
[263] Horan RL, Antle K, Collette AL, Wang Y, Huang J, Moreau JE, et al. In vitro degradation of silk fibroin. Biomaterials. 2005;26:3385-93.
[264] You R, Xu Y, Liu Y, Li X, Li M. Comparison of the in vitro and in vivo degradations of silk fibroin scaffolds from mulberry and nonmulberry silkworms. Biomedical Materials. 2014;10:015003.
[265] Brown J, Lu C-L, Coburn J, Kaplan DL. Impact of silk biomaterial structure on proteolysis. Acta biomaterialia. 2015;11:212-21.
[266] Baimark Y, Srisa-ard M, Srihanam P. Morphology and thermal stability of silk fibroin/starch blended microparticles. Express Polymer Letters. 2010;4:781-9.
[267] Mahmoud AA, Osman O, Eid K, Ashkar E, Okasha A, Atta D, et al. FTIR spectroscopy of natural bio-polymers blends. Middle East Journal of Applied Sciences. 2014;4:816-24.
[268] Forget A, Christensen J, Lüdeke S, Kohler E, Tobias S, Matloubi M, et al. Polysaccharide hydrogels with tunable stiffness and provasculogenic properties via α-helix to β-sheet switch in secondary structure. Proceedings of the National Academy of Sciences. 2013;110:12887-92.
[269] Le Goff KJ, Gaillard C, Helbert W, Garnier C, Aubry T. Rheological study of reinforcement of agarose hydrogels by cellulose nanowhiskers. Carbohydrate polymers. 2015;116:117-23.
[270] Priya MV, Kumar RA, Sivashanmugam A, Nair SV, Jayakumar R. Injectable Amorphous Chitin-Agarose Composite Hydrogels for Biomedical Applications. Journal of functional biomaterials. 2015;6:849-62.
[271] Matsiko A, Gleeson JP, O'Brien FJ. Scaffold mean pore size influences mesenchymal stem cell chondrogenic differentiation and matrix deposition. Tissue Engineering Part A. 2014;21:486-97.
[272] Han K-S, Song JE, Tripathy N, Kim H, Moon BM, Park CH, et al. Effect of pore sizes of silk scaffolds for cartilage tissue engineering. Macromolecular Research. 2015;23:1091-7.
[273] Sakai S, Hashimoto I, Kawakami K. Synthesis of an agarose-gelatin conjugate for use as a tissue engineering scaffold. Journal of bioscience and bioengineering. 2007;103:22-6.
[274] Kwon H, Sun L, Cairns DM, Rainbow RS, Preda RC, Kaplan DL, et al. The influence of scaffold material on chondrocytes under inflammatory conditions. Acta biomaterialia. 2013;9:6563-75.
[275] Zhang Q, Lu H, Kawazoe N, Chen G. Pore size effect of collagen scaffolds on cartilage regeneration. Acta biomaterialia. 2014;10:2005-13.

[276] Fernández-Cossío S, León-Mateos A, Sampedro FG, Oreja MTC. Biocompatibility of agarose gel as a dermal filler: histologic evaluation of subcutaneous implants. Plastic and reconstructive surgery. 2007;120:1161-9.
[277] Xing D, Xu Y, Liu Q, Ke Y, Wang B, Li Z, et al. Osteoarthritis and all-cause mortality in worldwide populations: grading the evidence from a meta-analysis. Scientific reports. 2016;6.
[278] Rönn K, Reischl N, Gautier E, Jacobi M. Current surgical treatment of knee osteoarthritis. Arthritis. 2011;2011:454873.
[279] Steinert AF, Ghivizzani SC, Rethwilm A, Tuan RS, Evans CH, Nöth U. Major biological obstacles for persistent cell-based regeneration of articular cartilage. Arthritis research & therapy. 2007;9:213.
[280] Jao D, Mou X, Hu X. Tissue Regeneration: A Silk Road. Journal of Functional Biomaterials. 2016;7:22.
[281] Liao CJ, Chen CF, Chen JH, Chiang SF, Lin YJ, Chang KY. Fabrication of porous biodegradable polymer scaffolds using a solvent merging/particulate leaching method. Journal of biomedical materials research. 2002;59:676-81.
[282] Yoon JJ, Park TG. Degradation behaviors of biodegradable macroporous scaffolds prepared by gas foaming of effervescent salts. Journal of biomedical materials research. 2001;55:401-8.
[283] Nam YS, Yoon JJ, Park TG. A novel fabrication method of macroporous biodegradable polymer scaffolds using gas foaming salt as a porogen additive. Journal of biomedical materials research. 2000;53:1-7.
[284] Whang K, Thomas C, Healy K, Nuber G. A novel method to fabricate bioabsorbable scaffolds. Polymer. 1995;36:837-42.
[285] Nooeaid P, Salih V, Beier JP, Boccaccini AR. Osteochondral tissue engineering: scaffolds, stem cells and applications. Journal of cellular and molecular medicine. 2012;16:2247-70.
[286] Subramanian A, Lin HY. Crosslinked chitosan: its physical properties and the effects of matrix stiffness on chondrocyte cell morphology and proliferation. Journal of Biomedical Materials Research Part A. 2005;75:742-53.
[287] Rowland CR, Lennon DP, Caplan AI, Guilak F. The effects of crosslinking of scaffolds engineered from cartilage ECM on the chondrogenic differentiation of MSCs. Biomaterials. 2013;34:5802-12.
[288] Moutos FT, Guilak F. Functional properties of cell-seeded three-dimensionally woven poly (ε-caprolactone) scaffolds for cartilage tissue engineering. Tissue Engineering Part A. 2009;16:1291-301.
[289] Liu W, Li Z, Zheng L, Zhang X, Liu P, Yang T, et al. Electrospun fibrous silk fibroin/poly (L-lactic acid) scaffold for cartilage tissue engineering. Tissue Engineering and Regenerative Medicine. 2016;13:516-26.
[290] Altman GH, Diaz F, Jakuba C, Calabro T, Horan RL, Chen J, et al. Silk-based biomaterials. Biomaterials. 2003;24:401-16.

[291] Singh YP, Bhardwaj N, Mandal BB. Potential of Agarose/Silk Fibroin Blended Hydrogel for In Vitro Cartilage Tissue Engineering. ACS Applied Materials & Interfaces. 2016;8:21236–21249.
[292] Bhardwaj N, Singh YP, Devi D, Kandimalla R, Kotoky J, Mandal BB. Potential of silk fibroin/chondrocyte constructs of muga silkworm Antheraea assamensis for cartilage tissue engineering. Journal of Materials Chemistry B. 2016;4:3670-84.
[293] Gloria A, Ronca D, Russo T, D'Amora U, Chierchia M, De Santis R, et al. Technical features and criteria in designing fiber-reinforced composite materials: From the aerospace and aeronautical field to biomedical applications. J Appl Biomater Biomech. 2011;9:151-63.
[294] Saturveithan C, Premganesh G, Fakhrizzaki S, Mahathir M, Karuna K, Rauf K, et al. Intra-articular hyaluronic acid (HA) and platelet rich plasma (PRP) injection versus hyaluronic acid (HA) injection alone in patients with grade III and IV knee osteoarthritis (OA): a retrospective study on functional outcome. Malaysian orthopaedic journal. 2016;10:35.
[295] Li G, Li F, Zheng Z, Luo T, Liu J, Wu J, et al. Silk microfiber-reinforced silk composite scaffolds: fabrication, mechanical properties, and cytocompatibility. Journal of Materials Science. 2016;51:3025-35.
[296] Gupta P, Adhikary M, Kumar M, Bhardwaj N, Mandal BB. Biomimetic, Osteoconductive Non-mulberry Silk Fiber Reinforced Tricomposite Scaffolds for Bone Tissue Engineering. ACS applied materials & interfaces. 2016;8:30797-30810.
[297] Nazarov R, Jin H-J, Kaplan DL. Porous 3-D scaffolds from regenerated silk fibroin. Biomacromolecules. 2004;5:718-26.
[298] Mandal BB, Ghosh B, Kundu S. Non-mulberry silk sericin/poly (vinyl alcohol) hydrogel matrices for potential biotechnological applications. International journal of biological macromolecules. 2011;49:125-33.
[299] Bhardwaj N, Sow WT, Devi D, Ng KW, Mandal BB, Cho N-J. Silk fibroin–keratin based 3D scaffolds as a dermal substitute for skin tissue engineering. Integrative Biology. 2015;7:53-63.
[300] Rio DC, Ares M, Hannon GJ, Nilsen TW. Purification of RNA using TRIzol (TRI reagent). Cold Spring Harbor Protocols. 2010;2010:pdb. prot5439.
[301] Seda Tığlı R, Ghosh S, Laha MM, Shevde NK, Daheron L, Gimble J, et al. Comparative chondrogenesis of human cell sources in 3D scaffolds. Journal of tissue engineering and regenerative medicine. 2009;3:348-60.
[302] Moutos FT, Freed LE, Guilak F. A biomimetic three-dimensional woven composite scaffold for functional tissue engineering of cartilage. Nature materials. 2007;6:162-7.
[303] Loh QL, Choong C. Three-dimensional scaffolds for tissue engineering applications: role of porosity and pore size. Tissue Engineering Part B: Reviews. 2013;19:485-502.
[304] Griffon DJ, Sedighi MR, Schaeffer DV, Eurell JA, Johnson AL. Chitosan scaffolds: interconnective pore size and cartilage engineering. Acta biomaterialia. 2006;2:313-20.
[305] Bhardwaj T, Pilliar RM, Grynpas MD, Kandel RA. Effect of material geometry on cartilagenous tissue formation in vitro. Journal of biomedical materials research. 2001;57:190-9.

[306] Nehrer S, Breinan HA, Ramappa A, Young G, Shortkroff S, Louie LK, et al. Matrix collagen type and pore size influence behaviour of seeded canine chondrocytes. Biomaterials. 1997;18:769-76.
[307] Zeltinger J, Sherwood JK, Graham DA, Müeller R, Griffith LG. Effect of pore size and void fraction on cellular adhesion, proliferation, and matrix deposition. Tissue engineering. 2001;7:557-72.
[308] Mohabatpour F, Karkhaneh A, Sharifi AM. A hydrogel/fiber composite scaffold for chondrocyte encapsulation in cartilage tissue regeneration. RSC Advances. 2016;6:83135-45.
[309] Athanasiou KA, Shah AR, Hernandez RJ, LeBaron RG. Basic science of articular cartilage repair. Clinics in sports medicine. 2001;20:223-47.
[310] McCullen SD, Haslauer CM, Loboa EG. Fiber-reinforced scaffolds for tissue engineering and regenerative medicine: use of traditional textile substrates to nanofibrous arrays. Journal of Materials Chemistry. 2010;20:8776-88.
[311] Place ES, Evans ND, Stevens MM. Complexity in biomaterials for tissue engineering. Nature materials. 2009;8:457-70.
[312] Bhardwaj N, Devi D, Mandal BB. Tissue-engineered cartilage: The crossroads of biomaterials, cells and stimulating factors. Macromolecular bioscience. 2015;15:153-82.
[313] Coburn J, Gibson M, Bandalini PA, Laird C, Mao H-Q, Moroni L, et al. Biomimetics of the extracellular matrix: an integrated three-dimensional fiber-hydrogel composite for cartilage tissue engineering. Smart structures and systems. 2011;7:213.
[314] Coburn JM, Gibson M, Monagle S, Patterson Z, Elisseeff JH. Bioinspired nanofibers support chondrogenesis for articular cartilage repair. Proceedings of the National Academy of Sciences. 2012;109:10012-7.
[315] Nukavarapu SP, Dorcemus DL. Osteochondral tissue engineering: current strategies and challenges. Biotechnology advances. 2013;31:706-21.
[316] Di Luca A, Van Blitterswijk C, Moroni L. The osteochondral interface as a gradient tissue: From development to the fabrication of gradient scaffolds for regenerative medicine. Birth Defects Research Part C: Embryo Today: Reviews. 2015;105:34-52.
[317] Radin EL, Paul IL, Lowy M. A comparison of the dynamic force transmitting properties of subchondral bone and articular cartilage. J Bone Joint Surg Am. 1970;52:444-56.
[318] Niederauer GG, Slivka MA, Leatherbury NC, Korvick DL, Harroff Jr HH, Ehler WC, et al. Evaluation of multiphase implants for repair of focal osteochondral defects in goats. Biomaterials. 2000;21:2561-74.
[319] Lima EG, Chao P-hG, Ateshian GA, Bal BS, Cook JL, Vunjak-Novakovic G, et al. The effect of devitalized trabecular bone on the formation of osteochondral tissue-engineered constructs. Biomaterials. 2008;29:4292-9.
[320] Scotti C, Wirz D, Wolf F, Schaefer DJ, Bürgin V, Daniels AU, et al. Engineering human cell-based, functionally integrated osteochondral grafts by biological bonding of engineered cartilage tissues to bony scaffolds. Biomaterials. 2010;31:2252-9.

[321] Seo S-J, Mahapatra C, Singh RK, Knowles JC, Kim H-W. Strategies for osteochondral repair: Focus on scaffolds. Journal of tissue engineering. 2014;5:2041731414541850.
[322] Sharma AR, Jagga S, Lee S-S, Nam J-S. Interplay between cartilage and subchondral bone contributing to pathogenesis of osteoarthritis. International Journal of Molecular Sciences. 2013;14:19805-30.
[323] Yang PJ, Temenoff JS. Engineering orthopedic tissue interfaces. Tissue Engineering Part B: Reviews. 2009;15:127-41.
[324] Keeney M, Pandit A. The osteochondral junction and its repair via bi-phasic tissue engineering scaffolds. Tissue Engineering Part B: Reviews. 2009;15:55-73.
[325] Song K, Li L, Yan X, Zhang Y, Li R, Wang Y, et al. Fabrication and development of artificial osteochondral constructs based on cancellous bone/hydrogel hybrid scaffold. Journal of Materials Science: Materials in Medicine. 2016;27:1-12.
[326] Camarero-Espinosa S, Cooper-White J. Tailoring biomaterial scaffolds for osteochondral repair. International Journal of Pharmaceutics. 2016;523:476-489.
[327] Puppi D, Chiellini F, Piras A, Chiellini E. Polymeric materials for bone and cartilage repair. Progress in polymer science. 2010;35:403-40.
[328] Unger RE, Wolf M, Peters K, Motta A, Migliaresi C, Kirkpatrick CJ. Growth of human cells on a non-woven silk fibroin net: a potential for use in tissue engineering. Biomaterials. 2004;25:1069-75.
[329] Lovett M, Cannizzaro C, Daheron L, Messmer B, Vunjak-Novakovic G, Kaplan DL. Silk fibroin microtubes for blood vessel engineering. Biomaterials. 2007;28:5271-9.
[330] Soffer L, Wang X, Zhang X, Kluge J, Dorfmann L, Kaplan DL, et al. Silk-based electrospun tubular scaffolds for tissue-engineered vascular grafts. Journal of Biomaterials Science, Polymer Edition. 2008;19:653-64.
[331] Liu X, Bai S, Zhao H. Silk fibroin-based scaffold for neural tissue engineering. Journal of Biomaterials and Tissue Engineering. 2014;4:1012-8.
[332] Ding X, Zhu M, Xu B, Zhang J, Zhao Y, Ji S, et al. Integrated trilayered silk fibroin scaffold for osteochondral differentiation of adipose-derived stem cells. ACS applied materials & interfaces. 2014;6:16696-705.
[333] M JC, Reardon PJ, Konwarh R, Knowles JC, Mandal BB. Mimicking Hierarchical Complexity of the Osteochondral Interface Using Electrospun Silk-Bioactive Glass Composites. ACS Appl Mater Interfaces. 2017;9:8000-13.
[334] Gupta P, Adhikary M, Kumar M, Bhardwaj N, Mandal BB. Biomimetic, osteoconductive non-mulberry silk fiber reinforced tricomposite scaffolds for bone tissue engineering. ACS applied materials & interfaces. 2016;8:30797-810.
[335] Mandal BB, Kundu SC. Cell proliferation and migration in silk fibroin 3D scaffolds. Biomaterials. 2009;30:2956-65.
[336] Singh YP, Bhardwaj N, Mandal BB. Potential of agarose/silk fibroin blended hydrogel for in vitro cartilage tissue engineering. ACS applied materials & interfaces. 2016;8:21236-49.

[337] Cao Y, Wang B. Biodegradation of silk biomaterials. International Journal of Molecular Sciences. 2009;10:1514-24.
[338] Song K, Li L, Yan X, Zhang Y, Li R, Wang Y, et al. Fabrication and development of artificial osteochondral constructs based on cancellous bone/hydrogel hybrid scaffold. Journal of Materials Science: Materials in Medicine. 2016;27:114.
[339] Kon E, Filardo G, Robinson D, Eisman J, Levy A, Zaslav K, et al. Osteochondral regeneration using a novel aragonite-hyaluronate bi-phasic scaffold in a goat model. Knee Surgery, Sports Traumatology, Arthroscopy. 2014;22:1452-64.
[340] Wang X, Grogan SP, Rieser F, Winkelmann V, Maquet V, La Berge M, et al. Tissue engineering of biphasic cartilage constructs using various biodegradable scaffolds: an in vitro study. Biomaterials. 2004;25:3681-8.
[341] Singh YP, Adhikary M, Bhardwaj N, Bhunia BK, Mandal BB. Silkfiber reinforcement modulatesin vitrochondrogenesis in 3D composite scaffolds. Biomed Mater. 2017;12:045012.
[342] Murphy CM, Haugh MG, O'Brien FJ. The effect of mean pore size on cell attachment, proliferation and migration in collagen–glycosaminoglycan scaffolds for bone tissue engineering. Biomaterials. 2010;31:461-6.
[343] Baksh D, Davies J, Kim S. Three-dimensional matrices of calcium polyphosphates support bone growth in vitro and in vivo. Journal of Materials Science: Materials in Medicine. 1998;9:743-8.
[344] Lee SJ, Lee IW, Lee YM, Lee HB, Khang G. Macroporous biodegradable natural/synthetic hybrid scaffolds as small intestine submucosa impregnated poly (D, L-lactide-co-glycolide) for tissue-engineered bone. Journal of Biomaterials Science, Polymer Edition. 2004;15:1003-17.
[345] Underwood RA, Usui ML, Zhao G, Hauch KD, Takeno MM, Ratner BD, et al. Quantifying the effect of pore size and surface treatment on epidermal incorporation into percutaneously implanted sphere-templated porous biomaterials in mice. Journal of Biomedical Materials Research Part A. 2011;98:499-508.
[346] Madden LR, Mortisen DJ, Sussman EM, Dupras SK, Fugate JA, Cuy JL, et al. Proangiogenic scaffolds as functional templates for cardiac tissue engineering. Proceedings of the National Academy of Sciences. 2010;107:15211-6.
[347] Fukano Y, Usui M, Underwood R, Isenhath S, Marshall A, Hauch K, et al. Epidermal and dermal integration into sphere-templated porous poly (2-hydroxyethyl methacrylate) implants in mice. Journal of Biomedical Materials Research Part A. 2010;94:1172-86.
[348] Marshall AJ, Irvin CA, Barker T, Sage EH, Hauch KD, Ratner BD. Biomaterials with tightly controlled pore size that promote vascular in-growth. Papers presented at the meeting-American Chemical Society Division of Polymer Chemistry: American Chemical Society; 2004. p. 100-1.
[349] Pan Z, Duan P, Liu X, Wang H, Cao L, He Y, et al. Effect of porosities of bilayered porous scaffolds on spontaneous osteochondral repair in cartilage tissue engineering. Regenerative biomaterials. 2015;2:9-19.

[350] Harley BA, Lynn AK, Wissner-Gross Z, Bonfield W, Yannas IV, Gibson LJ. Design of a multiphase osteochondral scaffold III: Fabrication of layered scaffolds with continuous interfaces. Journal of Biomedical Materials Research Part A. 2010;92:1078-93.
[351] Malay AD, Sato R, Yazawa K, Watanabe H, Ifuku N, Masunaga H, et al. Relationships between physical properties and sequence in silkworm silks. Scientific reports. 2016;6:27573.
[352] Da H, Jia S-J, Meng G-L, Cheng J-H, Zhou W, Xiong Z, et al. The impact of compact layer in biphasic scaffold on osteochondral tissue engineering. PloS one. 2013;8:e54838.
[353] Rucci N. Molecular biology of bone remodelling. Clinical cases in mineral and bone metabolism. 2008;5:49.
[354] Penido MGM, Alon US. Phosphate homeostasis and its role in bone health. Pediatric nephrology. 2012;27:2039-48.
[355] Loeser RF. Chondrocyte integrin expression and function. Biorheology. 2000;37:109-16.
[356] Schroeppel J, Crist J, Anderson H, Wang J. Molecular regulation of articular chondrocyte function and its significance in osteoarthritis. Histol Histopathol. 2011;26:377-94.
[357] Yuan X, Meng H, Wang Y, Peng J, Guo Q, Wang A, et al. Bone–cartilage interface crosstalk in osteoarthritis: potential pathways and future therapeutic strategies. Osteoarthritis and cartilage. 2014;22:1077-89.
[358] Sanchez C, Deberg M, Piccardi N, Msika P, Reginster J-Y, Henrotin Y. Subchondral bone osteoblasts induce phenotypic changes in human osteoarthritic chondrocytes. Osteoarthritis and cartilage. 2005;13:988-97.
[359] Nguyen BV, Wang QG, Kuiper NJ, El Haj AJ, Thomas CR, Zhang Z. Biomechanical properties of single chondrocytes and chondrons determined by micromanipulation and finite-element modelling. Journal of the Royal Society Interface. 2010;7:1723-33.
[360] Sugawara Y, Ando R, Kamioka H, Ishihara Y, Murshid SA, Hashimoto K, et al. The alteration of a mechanical property of bone cells during the process of changing from osteoblasts to osteocytes. Bone. 2008;43:19-24.
[361] Moses JC, Nandi SK, Mandal BB. Multifunctional Cell Instructive Silk-Bioactive Glass Composite Reinforced Scaffolds Toward Osteoinductive, Proangiogenic, and Resorbable Bone Grafts. Advanced healthcare materials. 2018;7:e1701418.
[362] Jiang J, Nicoll SB, Lu HH. Co-culture of osteoblasts and chondrocytes modulates cellular differentiation in vitro. Biochemical and biophysical research communications. 2005;338:762-70.
[363] Velnar T, Bunc G, Klobucar R, Gradisnik L. Biomaterials and host versus graft response: a short review. Bosnian journal of basic medical sciences. 2016;16:82.
[364] Yan L-P, Silva-Correia J, Oliveira MB, Vilela C, Pereira H, Sousa RA, et al. Bilayered silk/silk-nanoCaP scaffolds for osteochondral tissue engineering: in vitro and in vivo assessment of biological performance. Acta biomaterialia. 2015;12:227-41.
[365] Wang Z, Zhang Y, Zhang J, Huang L, Liu J, Li Y, et al. Exploring natural silk protein sericin for regenerative medicine: an injectable, photoluminescent, cell-adhesive 3D hydrogel. Scientific reports. 2014;4:1-11.

[366] Laity P, Gilks S, Holland C. Rheological behaviour of native silk feedstocks. Polymer. 2015;67:28-39.
[367] Matsumoto A, Chen J, Collette AL, Kim U-J, Altman GH, Cebe P, et al. Mechanisms of silk fibroin sol− gel transitions. The Journal of Physical Chemistry B. 2006;110:21630-8.
[368] Bini E, Knight DP, Kaplan DL. Mapping domain structures in silks from insects and spiders related to protein assembly. Journal of molecular biology. 2004;335:27-40.
[369] Floren M, Migliaresi C, Motta A. Processing techniques and applications of silk hydrogels in bioengineering. Journal of functional biomaterials. 2016;7:26.
[370] Chouhan D, Lohe Tu, Samudrala PK, Mandal BB. In Situ Forming Injectable Silk Fibroin Hydrogel Promotes Skin Regeneration in Full Thickness Burn Wounds. Advanced healthcare materials. 2018;7:1801092.
[371] Kumar M, Gupta P, Bhattacharjee S, Nandi SK, Mandal BB. Immunomodulatory injectable silk hydrogels maintaining functional islets and promoting anti-inflammatory M2 macrophage polarization. Biomaterials. 2018;187:1-17.
[372] Vollrath F, Knight DP. Liquid crystalline spinning of spider silk. Nature. 2001;410:541-8.
[373] Sehnal F, Sutherland T. Silks produced by insect labial glands. Prion. 2008;2:145-53.
[374] Koeppel A, Laity PR, Holland C. The influence of metal ions on native silk rheology. Acta Biomaterialia. 2020;117:204-12.
[375] Singh YP, Moses JC, Bhardwaj N, Mandal BB. Injectable hydrogels: a new paradigm for osteochondral tissue engineering. Journal of Materials Chemistry B. 2018;6:5499-529.
[376] Kwak HW, Ju JE, Shin M, Holland C, Lee KH. Sericin promotes fibroin silk I stabilization across a phase-separation. Biomacromolecules. 2017;18:2343-9.
[377] Hu X, Kaplan D, Cebe P. Determining beta-sheet crystallinity in fibrous proteins by thermal analysis and infrared spectroscopy. Macromolecules. 2006;39:6161-70.
[378] Penkman K, Kaufman DS, Maddy D, Collins M. Closed-system behaviour of the intra-crystalline fraction of amino acids in mollusc shells. Quaternary Geochronology. 2008;3:2-25.
[379] Kaufman DS, Manley WF. A new procedure for determining DL amino acid ratios in fossils using reverse phase liquid chromatography. Quaternary Science Reviews. 1998;17:987-1000.
[380] Lu Q, Hu X, Wang X, Kluge JA, Lu S, Cebe P, et al. Water-insoluble silk films with silk I structure. Acta biomaterialia. 2010;6:1380-7.
[381] Um IC, Kweon H, Park YH, Hudson S. Structural characteristics and properties of the regenerated silk fibroin prepared from formic acid. International journal of biological macromolecules. 2001;29:91-7.
[382] Jin HJ, Park J, Karageorgiou V, Kim UJ, Valluzzi R, Cebe P, et al. Water-stable silk films with reduced β-sheet content. Advanced Functional Materials. 2005;15:1241-7.
[383] DeMuth PC, Min Y, Irvine DJ, Hammond PT. Implantable silk composite microneedles for programmable vaccine release kinetics and enhanced immunogenicity in transcutaneous immunization. Advanced healthcare materials. 2014;3:47-58.
[384] Foo CWP, Bini E, Hensman J, Knight D, Lewis R, Kaplan D. Role of pH and charge on silk protein assembly in insects and spiders. Applied Physics A. 2006;82:223-33.

[385] Gupta P, Kumar M, Bhardwaj N, Kumar JP, Krishnamurthy C, Nandi SK, et al. Mimicking form and function of native small diameter vascular conduits using mulberry and non-mulberry patterned silk films. ACS applied materials & interfaces. 2016;8:15874-88.
[386] Lee J, Ju M, Cho OH, Kim Y, Nam KT. Tyrosine-rich peptides as a platform for assembly and material synthesis. Advanced Science. 2019;6:1801255.
[387] Partlow BP, Applegate MB, Omenetto FG, Kaplan DL. Dityrosine cross-linking in designing biomaterials. ACS Biomaterials Science & Engineering. 2016;2:2108-21.
[388] Gupta P, Moses JC, Mandal BB. Surface patterning and innate physicochemical attributes of silk films concomitantly govern vascular cell dynamics. ACS Biomaterials Science & Engineering. 2018;5:933-49.
[389] Laity PR, Baldwin E, Holland C. Changes in silk feedstock rheology during cocoon construction: the role of calcium and potassium ions. Macromolecular bioscience. 2019;19:1800188.
[390] Schaefer C, Laity PR, Holland C, McLeish TC. Silk protein solution: A natural example of sticky reptation. Macromolecules. 2020;53:2669-76.
[391] Tulachan B, Meena SK, Rai RK, Mallick C, Kusurkar TS, Teotia AK, et al. Electricity from the silk cocoon membrane. Scientific reports. 2014;4:1-15.
[392] Andiappan M, Kumari T, Sundaramoorthy S, Meiyazhagan G, Manoharan P, Venkataraman G. Comparison of eri and tasar silk fibroin scaffolds for biomedical applications. Progress in biomaterials. 2016;5:81-91.
[393] Chouhan D, Chakraborty B, Nandi SK, Mandal BB. Role of non-mulberry silk fibroin in deposition and regulation of extracellular matrix towards accelerated wound healing. Acta biomaterialia. 2017;48:157-74.
[394] Mazzi S, Zulker E, Buchicchio J, Anderson B, Hu X. Comparative thermal analysis of Eri, Mori, Muga, and Tussar silk cocoons and fibroin fibers. Journal of Thermal Analysis and Calorimetry. 2014;116:1337-43.
[395] Hu X, Shmelev K, Sun L, Gil E-S, Park S-H, Cebe P, et al. Regulation of silk material structure by temperature-controlled water vapor annealing. Biomacromolecules. 2011;12:1686-96.
[396] Wang Z, Wang J, Ayarza J, Steeves T, Hu Z, Manna S, et al. Bio-inspired mechanically adaptive materials through vibration-induced crosslinking. Nature Materials. 2021:1-6.
[397] Hazra S, Nandi S, Naskar D, Guha R, Chowdhury S, Pradhan N, et al. Non-mulberry silk fibroin biomaterial for corneal regeneration. Scientific reports. 2016;6:1-13.
[398] Jin H-J, Kaplan DL. Mechanism of silk processing in insects and spiders. Nature. 2003;424:1057-61.
[399] Sparkes J, Holland C. Analysis of the pressure requirements for silk spinning reveals a pultrusion dominated process. Nature communications. 2017;8:1-10.
[400] Richter DL, Schenck Jr RC, Wascher DC, Treme G. Knee articular cartilage repair and restoration techniques: a review of the literature. Sports health. 2016;8:153-60.

[401] Makris EA, Gomoll AH, Malizos KN, Hu JC, Athanasiou KA. Repair and tissue engineering techniques for articular cartilage. Nature Reviews Rheumatology. 2015;11:21.
[402] O'Connell G, Garcia J, Amir J. 3D bioprinting: new directions in articular cartilage tissue engineering. ACS Biomaterials Science & Engineering. 2017;3:2657-68.
[403] Mehrotra S, Moses JC, Bandyopadhyay A, Mandal BB. 3D printing/bioprinting based tailoring of in vitro tissue models: Recent advances and challenges. ACS Applied Bio Materials. 2019;2:1385-405.
[404] Nguyen D, Hägg DA, Forsman A, Ekholm J, Nimkingratana P, Brantsing C, et al. Cartilage tissue engineering by the 3D bioprinting of iPS cells in a nanocellulose/alginate bioink. Scientific reports. 2017;7:658.
[405] Zhang YS, Yue K, Aleman J, Mollazadeh-Moghaddam K, Bakht SM, Yang J, et al. 3D bioprinting for tissue and organ fabrication. Annals of biomedical engineering. 2017;45:148-63.
[406] Malda J, Visser J, Melchels FP, Jüngst T, Hennink WE, Dhert WJ, et al. 25th anniversary article: engineering hydrogels for biofabrication. Advanced materials. 2013;25:5011-28.
[407] Kim JE, Kim SH, Jung Y. Current status of three-dimensional printing inks for soft tissue regeneration. Tissue engineering and regenerative medicine. 2016;13:636-46.
[408] Singh YP, Moses JC, Bhunia BK, Nandi SK, Mandal BB. Hierarchically structured seamless silk scaffolds for osteochondral interface tissue engineering. Journal of Materials Chemistry B. 2018;6:5671-88.
[409] Kundu B, Kurland NE, Bano S, Patra C, Engel FB, Yadavalli VK, et al. Silk proteins for biomedical applications: Bioengineering perspectives. Progress in Polymer Science. 2014;39:251-67.
[410] Moses JC, Nandi SK, Mandal BB. Multifunctional cell instructive silk-bioactive glass composite reinforced scaffolds toward osteoinductive, proangiogenic, and resorbable bone grafts. Advanced healthcare materials. 2018;7:1701418.
[411] Sezutsu H, Yukuhiro K. The complete nucleotide sequence of the Eri-silkworm (Samia cynthia ricini) fibroin gene. Journal of Insect Biotechnology and Sericology. 2014;83:3_059-3_70.
[412] Konwarh R, Bhunia BK, Mandal BB. Opportunities and challenges in exploring Indian nonmulberry silk for biomedical applications. Proceedings of the Indian National Science Academy. 2017;83.
[413] Chawla S, Midha S, Sharma A, Ghosh S. Silk-based bioinks for 3D bioprinting. Advanced healthcare materials. 2018;7:1701204.
[414] Kim SH, Yeon YK, Lee JM, Chao JR, Lee YJ, Seo YB, et al. Precisely printable and biocompatible silk fibroin bioink for digital light processing 3D printing. Nature communications. 2018;9:1620.
[415] Zheng Z, Wu J, Liu M, Wang H, Li C, Rodriguez MJ, et al. 3D Bioprinting of Self-Standing Silk-Based Bioink. Advanced healthcare materials. 2018;7:1701026.
[416] Das S, Pati F, Chameettachal S, Pahwa S, Ray AR, Dhara S, et al. Enhanced redifferentiation of chondrocytes on microperiodic silk/gelatin scaffolds: toward tailor-made tissue engineering. Biomacromolecules. 2013;14:311-21.

[417] Chawla S, Kumar A, Admane P, Bandyopadhyay A, Ghosh S. Elucidating role of silk-gelatin bioink to recapitulate articular cartilage differentiation in 3D bioprinted constructs. Bioprinting. 2017;7:1-13.
[418] Das S, Pati F, Choi YJ, Rijal G, Shim JH, Kim SW, et al. Bioprintable, cell-laden silk fibroin-gelatin hydrogel supporting multilineage differentiation of stem cells for fabrication of three-dimensional tissue constructs. Acta biomaterialia. 2015;11:233-46.
[419] Rodriguez MJ, Brown J, Giordano J, Lin SJ, Omenetto FG, Kaplan DL. Silk based bioinks for soft tissue reconstruction using 3-dimensional (3D) printing with in vitro and in vivo assessments. Biomaterials. 2017;117:105-15.
[420] Singh YP, Bhardwaj N, Mandal BB. Potential of agarose/silk fibroin blended hydrogel for in vitro cartilage tissue engineering. ACS applied materials and interfaces. 2016;8:21236-49.
[421] Partlow BP, Tabatabai AP, Leisk GG, Cebe P, Blair DL, Kaplan DL. Silk fibroin degradation related to rheological and mechanical properties. Macromolecular bioscience. 2016;16:666-75.
[422] Roseti L, Cavallo C, Desando G, Parisi V, Petretta M, Bartolotti I, et al. Three-dimensional bioprinting of cartilage by the use of stem cells: a strategy to improve regeneration. Materials. 2018;11:1749.
[423] He J, Liu Y, Hao X, Mao M, Zhu L, Li D. Bottom-up generation of 3D silk fibroin–gelatin microfluidic scaffolds with improved structural and biological properties. Materials Letters. 2012;78:102-5.
[424] Nair K, Gandhi M, Khalil S, Yan KC, Marcolongo M, Barbee K, et al. Characterization of cell viability during bioprinting processes. Biotechnology Journal: Healthcare Nutrition Technology. 2009;4:1168-77.
[425] Utomo DN, Mahyudin F, Wardhana TH, Purwati P, Brahmana F, Gusti AWR. Physicobiochemical Characteristics and Chondrogenic Differentiation of Bone Marrow Mesenchymal Stem Cells (hBM-MSCs) in Biodegradable Porous Sponge Bovine Cartilage Scaffold. International journal of biomaterials. 2019;2019.
[426] Xiao W, He J, Nichol JW, Wang L, Hutson CB, Wang B, et al. Synthesis and characterization of photocrosslinkable gelatin and silk fibroin interpenetrating polymer network hydrogels. Acta biomaterialia. 2011;7:2384-93.
[427] Gil ES, Frankowski DJ, Spontak RJ, Hudson SM. Swelling behavior and morphological evolution of mixed gelatin/silk fibroin hydrogels. Biomacromolecules. 2005;6:3079-87.
[428] Daly AC, Critchley SE, Rencsok EM, Kelly DJ. A comparison of different bioinks for 3D bioprinting of fibrocartilage and hyaline cartilage. Biofabrication. 2016;8:045002.
[429] Mirahmadi F, Tafazzoli-Shadpour M, Shokrgozar MA, Bonakdar S. Enhanced mechanical properties of thermosensitive chitosan hydrogel by silk fibers for cartilage tissue engineering. Materials science and engineering: c. 2013;33:4786-94.
[430] Markstedt K, Mantas A, Tournier I, Martínez Ávila Hc, Hägg D, Gatenholm P. 3D bioprinting human chondrocytes with nanocellulose–alginate bioink for cartilage tissue engineering applications. Biomacromolecules. 2015;16:1489-96.

[431] Erickson IE, Huang AH, Sengupta S, Kestle S, Burdick JA, Mauck RL. Macromer density influences mesenchymal stem cell chondrogenesis and maturation in photocrosslinked hyaluronic acid hydrogels. Osteoarthritis and Cartilage. 2009;17:1639-48.
[432] Bian L, Hou C, Tous E, Rai R, Mauck RL, Burdick JA. The influence of hyaluronic acid hydrogel crosslinking density and macromolecular diffusivity on human MSC chondrogenesis and hypertrophy. Biomaterials. 2013;34:413-21.
[433] Hersel U, Dahmen C, Kessler H. RGD modified polymers: biomaterials for stimulated cell adhesion and beyond. Biomaterials. 2003;24:4385-415.
[434] Chen Y-L, Lee H-P, Chan H-Y, Sung L-Y, Chen H-C, Hu Y-C. Composite chondroitin-6-sulfate/dermatan sulfate/chitosan scaffolds for cartilage tissue engineering. Biomaterials. 2007;28:2294-305.
[435] Akkiraju H, Nohe A. Role of chondrocytes in cartilage formation, progression of osteoarthritis and cartilage regeneration. Journal of developmental biology. 2015;3:177-92.
[436] Chameettachal S, Midha S, Ghosh S. Regulation of chondrogenesis and hypertrophy in silk fibroin-gelatin-based 3D bioprinted constructs. ACS Biomaterials Science & Engineering. 2016;2:1450-63.
[437] Stokes DG, Gang L, Dharmavaram R, Hawkins D, Piera-Velazquez S, Jimenez SA. Regulation of type-II collagen gene expression during human chondrocyte de-differentiation and recovery of chondrocyte-specific phenotype in culture involves Sry-type high-mobility-group box (SOX) transcription factors. Biochemical Journal. 2001;360:461-70.
[438] Watanabe H, Yamada Y, Kimata K. Roles of aggrecan, a large chondroitin sulfate proteoglycan, in cartilage structure and function. The journal of biochemistry. 1998;124:687-93.
[439] Knudson CB, Knudson W. Cartilage proteoglycans. Seminars in cell & developmental biology: Elsevier; 2001. p. 69-78.
[440] Kielty C, Kwan A, Holmes D, Schor SL, Grant M. Type X collagen, a product of hypertrophic chondrocytes. Biochemical Journal. 1985;227:545-54.
[441] Boehler RM, Graham JG, Shea LD. Tissue engineering tools for modulation of the immune response. Biotechniques. 2011;51:239-54.
[442] Kloppenburg M, Berenbaum F. Osteoarthritis year in review 2019: epidemiology and therapy. Osteoarthritis and Cartilage. 2020;28:242-8.
[443] Latourte A, Kloppenburg M, Richette P. Emerging pharmaceutical therapies for osteoarthritis. Nature Reviews Rheumatology. 2020;16:673-88.
[444] Chen D, Shen J, Zhao W, Wang T, Han L, Hamilton JL, et al. Osteoarthritis: toward a comprehensive understanding of pathological mechanism. Bone research. 2017;5:1-13.
[445] Singh YP, Moses JC, Bandyopadhyay A, Bhar B, Birru B, Bhardwaj N, et al. Chapter 11 - State-of-the-art strategies and future interventions in bone and cartilage repair for personalized regenerative therapy. In: Sharma CP, editor. Regenerated Organs: Academic Press; 2021. p. 203-48.

[446] Moran CJ, Ramesh A, Brama PA, O'Byrne JM, O'Brien FJ, Levingstone TJ. The benefits and limitations of animal models for translational research in cartilage repair. Journal of experimental orthopaedics. 2016;3:1.
[447] Kuyinu EL, Narayanan G, Nair LS, Laurencin CT. Animal models of osteoarthritis: classification, update, and measurement of outcomes. Journal of orthopaedic surgery and research. 2016;11:1-27.
[448] Yeung P, Cheng K, Yan C, Chan B. Collagen microsphere based 3D culture system for human osteoarthritis chondrocytes (hOACs). Scientific reports. 2019;9:1-14.
[449] Sun L, Wang X, Kaplan DL. A 3D cartilage – Inflammatory cell culture system for the modeling of human osteoarthritis. Biomaterials. 2011;32:5581-9.
[450] Galuzzi M, Perteghella S, Antonioli B, Tosca MC, Bari E, Tripodo G, et al. Human Engineered Cartilage and Decellularized Matrix as an Alternative to Animal Osteoarthritis Model. Polymers. 2018;10:738.
[451] JC M, Reardon P, Konwarh R, Knowles J, Mandal B. Mimicking Hierarchical Complexity of the Osteochondral Interface Using Electrospun Silk-Bioactive Glass Composites. ACS Applied Materials & Interfaces. 2017;9:8000-13.
[452] Canadas RF, Ren T, Marques AP, Oliveira JM, Reis RL, Demirci U. Biochemical Gradients to Generate 3D Heterotypic-Like Tissues with Isotropic and Anisotropic Architectures. Advanced Functional Materials. 2018;28:1804148.
[453] Kang H-W, Lee SJ, Ko IK, Kengla C, Yoo JJ, Atala A. A 3D bioprinting system to produce human-scale tissue constructs with structural integrity. Nature biotechnology. 2016;34:312-9.
[454] Bandyopadhyay A, Chowdhury SK, Dey S, Moses JC, Mandal BB. Silk: a promising biomaterial opening new vistas towards affordable healthcare solutions. Journal of the Indian Institute of Science. 2019:1-43.
[455] Peck Y, Ng LY, Goh JYL, Gao C, Wang D-A. A three-dimensionally engineered biomimetic cartilaginous tissue model for osteoarthritic drug evaluation. Molecular pharmaceutics. 2014;11:1997-2008.
[456] Singh YP, Bandyopadhyay A, Mandal BB. 3D Bioprinting Using Cross-Linker-Free Silk–Gelatin Bioink for Cartilage Tissue Engineering. ACS applied materials and interfaces. 2019;11:33684-96.
[457] Berenbaum F. Osteoarthritis as an inflammatory disease (osteoarthritis is not osteoarthrosis!). Osteoarthritis and cartilage. 2013;21:16-21.
[458] Kapoor M, Martel-Pelletier J, Lajeunesse D, Pelletier J-P, Fahmi H. Role of proinflammatory cytokines in the pathophysiology of osteoarthritis. Nature Reviews Rheumatology. 2011;7:33.
[459] Primorac D, Molnar V, Rod E, Jeleč Ž, Čukelj F, Matišić V, et al. Knee Osteoarthritis: A Review of Pathogenesis and State-Of-The-Art Non-Operative Therapeutic Considerations. Genes. 2020;11:854.
[460] Cheleschi S, Pascarelli NA, Valacchi G, Di Capua A, Biava M, Belmonte G, et al. Chondroprotective effect of three different classes of anti-inflammatory agents on human

osteoarthritic chondrocytes exposed to IL-1β. International immunopharmacology. 2015;28:794-801.
[461] Henderson B, Pettipher E. Arthritogenic actions of recombinant IL-1 and tumour necrosis factor alpha in the rabbit: evidence for synergistic interactions between cytokines in vivo. Clinical & experimental immunology. 1989;75:306.
[462] Zwerina J, Redlich K, Polzer K, Joosten L, Krönke G, Distler J, et al. TNF-induced structural joint damage is mediated by IL-1. Proceedings of the National Academy of Sciences. 2007;104:11742-7.
[463] Zhang W, Ouyang H, Dass CR, Xu J. Current research on pharmacologic and regenerative therapies for osteoarthritis. Bone research. 2016;4:1-14.
[464] Nissen SE, Yeomans ND, Solomon DH, Lüscher TF, Libby P, Husni ME, et al. Cardiovascular safety of celecoxib, naproxen, or ibuprofen for arthritis. New England Journal of Medicine. 2016;375:2519-29.
[465] Kuehn BM. FDA approves first celecoxib generics. JAMA. 2014;311:2470-.
[466] Martel-Pelletier J, Pelletier J-P. Effects of diacerein at the molecular level in the osteoarthritis disease process. Therapeutic advances in musculoskeletal disease. 2010;2:95-104.
[467] Yorifuji M, Sawaji Y, Endo K, Kosaka T, Yamamoto K. Limited efficacy of COX-2 inhibitors on nerve growth factor and metalloproteinases expressions in human synovial fibroblasts. Journal of Orthopaedic Science. 2016;21:381-8.
[468] Sanchez C, Mathy-Hartert M, Deberg MA, Ficheux H, Reginster J-YL, Henrotin YE. Effects of rhein on human articular chondrocytes in alginate beads. Biochemical pharmacology. 2003;65:377-88.
[469] Li Z, Meng D, Li G, Xu J, Tian K, Li Y. Celecoxib combined with diacerein effectively alleviates osteoarthritis in rats via regulating JNK and p38MAPK signaling pathways. Inflammation. 2015;38:1563-72.
[470] Inanc S, Keles D, Oktay G. An improved collagen zymography approach for evaluating the collagenases MMP-1, MMP-8, and MMP-13. BioTechniques. 2017;63:174-80.
[471] Malemud CJ. The biological basis of osteoarthritis: State of the evidence. Current opinion in rheumatology. 2015;27:289.
[472] Sokolove J, Lepus CM. Role of inflammation in the pathogenesis of osteoarthritis: latest findings and interpretations. Therapeutic advances in musculoskeletal disease. 2013;5:77-94.
[473] Benito MJ, Veale DJ, FitzGerald O, van den Berg WB, Bresnihan B. Synovial tissue inflammation in early and late osteoarthritis. Annals of the rheumatic diseases. 2005;64:1263-7.
[474] Legendre F, Bogdanowicz P, Martin G, Domagala F, Leclercq S, Pujol J, et al. Rhein, a diacerhein-derived metabolite, modulates the expression of matrix degrading enzymes and the cell proliferation of articular chondrocytes by inhibiting ERK and JNK-AP-1 dependent pathways. Clinical and experimental rheumatology. 2007;25:546.
[475] Tsutsumi R, Ito H, Hiramitsu T, Nishitani K, Akiyoshi M, Kitaori T, et al. Celecoxib inhibits production of MMP and NO via down-regulation of NF-κB and JNK in a PGE2 independent manner in human articular chondrocytes. Rheumatology international. 2008;28:727-36.

[476] Allas L, Rochoux Q, Leclercq S, Boumediene K, Baugé C. Development of a simple osteoarthritis model useful to predict in vitro the anti-hypertrophic action of drugs. Laboratory Investigation. 2020;100:64-71.
[477] Lin H, Lozito TP, Alexander PG, Gottardi R, Tuan RS. Stem cell-based microphysiological osteochondral system to model tissue response to interleukin-1β. Molecular pharmaceutics. 2014;11:2203-12.
[478] Pan J, Zhou X, Li W, Novotny JE, Doty SB, Wang L. In situ measurement of transport between subchondral bone and articular cartilage. Journal of Orthopaedic Research. 2009;27:1347-52.
[479] Henrotin Y, Pesesse L, Sanchez C. Subchondral bone and osteoarthritis: biological and cellular aspects. Osteoporosis International. 2012;23:847-51.
[480] van den Berg WB. Uncoupling of inflammatory and destructive mechanisms in arthritis. Seminars in arthritis and rheumatism: Elsevier; 2001. p. 7-16.
[481] Goldring SR, Goldring MB. The role of cytokines in cartilage matrix degeneration in osteoarthritis. Clinical Orthopaedics and Related Research®. 2004;427:S27-S36.
[482] Sun H, Luo G, Chen D, Xiang Z. A comprehensive and system review for the pharmacological mechanism of action of rhein, an active anthraquinone ingredient. Frontiers in pharmacology. 2016;7:247.
[483] Zweers MC, de Boer TN, van Roon J, Bijlsma JW, Lafeber FP, Mastbergen SC. Celecoxib: considerations regarding its potential disease-modifying properties in osteoarthritis. Arthritis research & therapy. 2011;13:1-11.
[484] Ding J, Ghali O, Lencel P, Broux O, Chauveau C, Devedjian J, et al. TNF-α and IL-1β inhibit RUNX2 and collagen expression but increase alkaline phosphatase activity and mineralization in human mesenchymal stem cells. Life sciences. 2009;84:499-504.
[485] Mastbergen S, Lafeber F, Bijlsma J. Selective COX-2 inhibition prevents proinflammatory cytokine-induced cartilage damage. Rheumatology. 2002;41:801-8.
[486] Blanco FJ, Ochs RL, Schwarz H, Lotz M. Chondrocyte apoptosis induced by nitric oxide. The American journal of pathology. 1995;146:75.
[487] Martel-Pelletier J, Mineau F, Jolicoeur F, Cloutier J, Pelletier J. In vitro effects of diacerhein and rhein on interleukin 1 and tumor necrosis factor-alpha systems in human osteoarthritic synovium and chondrocytes. The Journal of rheumatology. 1998;25:753-62.
[488] Hardy MM, Seibert K, Manning PT, Currie MG, Woerner BM, Edwards D, et al. Cyclooxygenase 2-dependent prostaglandin E2 modulates cartilage proteoglycan degradation in human osteoarthritis explants. Arthritis & Rheumatism: Official Journal of the American College of Rheumatology. 2002;46:1789-803.
[489] Berenbaum F, Jacques C, Thomas G, Corvol MT, Béréziat G, Masliah J. Synergistic effect of interleukin-1β and tumor necrosis factor α on PGE2Production by articular chondrocytes does not involve PLA2Stimulation. Experimental cell research. 1996;222:379-84.

[490] Bensen WG, Fiechtner JJ, McMillen JI, Zhao WW, Shawn SY, Woods EM, et al. Treatment of osteoarthritis with celecoxib, a cyclooxygenase-2 inhibitor: a randomized controlled trial. Mayo Clinic Proceedings: Elsevier; 1999. p. 1095-105.
[491] Pratta MA, Yao W, Decicco C, Tortorella MD, Liu R-Q, Copeland RA, et al. Aggrecan protects cartilage collagen from proteolytic cleavage. Journal of Biological Chemistry. 2003;278:45539-45.
[492] Weissenberger M, Weissenberger M, Gilbert F, Groll J, Evans C, Steinert A. Reduced hypertrophy in vitro after chondrogenic differentiation of adult human mesenchymal stem cells following adenoviral SOX9 gene delivery. BMC musculoskeletal disorders. 2020;21:1-14.
[493] Loebel C, Czekanska EM, Bruderer M, Salzmann G, Alini M, Stoddart MJ. In vitro osteogenic potential of human mesenchymal stem cells is predicted by Runx2/Sox9 ratio. Tissue Engineering Part A. 2015;21:115-23.
[494] Komori T. Regulation of osteoblast differentiation by Runx2. Osteoimmunology: Springer; 2009. p. 43-9.
[495] Sanchez C, Mateus MM, Defresne M-P, Crielaard J-MR, Reginster J-YL, Henrotin YE. Metabolism of human articular chondrocytes cultured in alginate beads. Longterm effects of interleukin 1beta and nonsteroidal antiinflammatory drugs. The Journal of rheumatology. 2002;29:772-82.
[496] Ge H, Tang H, Liang Y, Wu J, Yang Q, Zeng L, et al. Rhein attenuates inflammation through inhibition of NF-κB and NALP3 inflammasome in vivo and in vitro. Drug design, development and therapy. 2017;11:1663.
[497] Pelletier J-P, Lajeunesse D, Reboul P, Mineau F, Fernandes JC, Sabouret P, et al. Diacerein reduces the excess synthesis of bone remodeling factors by human osteoblast cells from osteoarthritic subchondral bone. The Journal of rheumatology. 2001;28:814-24.
[498] Almaawi A, Wang HT, Ciobanu O, Rowas SA, Rampersad S, Antoniou J, et al. Effect of acetaminophen and nonsteroidal anti-inflammatory drugs on gene expression of mesenchymal stem cells. Tissue engineering Part A. 2013;19:1039-46.
[499] Ding S-l, Pang Z-y, Chen X-m, Li Z, Liu X-x, Zhai Q-l, et al. Urolithin a attenuates IL-1β-induced inflammatory responses and cartilage degradation via inhibiting the MAPK/NF-κB signaling pathways in rat articular chondrocytes. Journal of Inflammation. 2020;17:1-13.
[500] Domagala F, Martin G, Bogdanowicz P, Ficheux H, Pujol J-P. Inhibition of interleukin-1β-induced activation of MEK/ERK pathway and DNA binding of NF-κB and AP-1: Potential mechanism for Diacerein effects in osteoarthritis. Biorheology. 2006;43:577-87.
[501] B Marcu K, Otero M, Olivotto E, Maria Borzi R, B Goldring M. NF-κB signaling: multiple angles to target OA. Current drug targets. 2010;11:599-613.
[502] Rigoglou S, Papavassiliou AG. The NF-κB signalling pathway in osteoarthritis. The international journal of biochemistry & cell biology. 2013;45:2580-4.

Publications from Ph.D. Thesis:

(A) Journal Publications:

1. **Yogendra Pratap Singh**, Ashutosh Bandyopadhyay, and Biman B. Mandal. "3D bioprinting using cross-linker-free silk–gelatin bioink for cartilage tissue engineering." *ACS Applied Materials & Interfaces* 11(37), 2019: 33684-33696.
2. **Yogendra Pratap Singh**, Joseph Christakiran Moses, Bibhas K. Bhunia, Samit K. Nandi, Biman B Mandal. "Hierarchically structured seamless silk scaffolds for osteochondral interface tissue engineering." *Journal of Materials Chemistry B* 6(36), 2018: 5671-5688. (Journal Coverpage) (Included in the themed collection: Editor's Choice: Scaffold Engineering)
3. **Yogendra Pratap Singh**, Mimi Adhikary, Nandana Bhardwaj, Bibhas Kumar Bhunia, Biman B. Mandal. "Silk fiber reinforcement modulates *in vitro* chondrogenesis in 3D composite scaffolds." *Biomedical Materials* 12(4), 2017: 045012.
4. **Yogendra Pratap Singh**, Nandana Bhardwaj, and Biman B. Mandal. "Potential of agarose/silk fibroin blended hydrogel for *in vitro* cartilage tissue engineering." *ACS Applied Materials & Interfaces* 8(33), 2016: 21236-21249.
5. **Yogendra Pratap Singh**, Joseph Christakiran Moses, Biman B. Mandal. 3D bioprinted osteoarthritic *in vitro* biomimetic model as high-throughput anti-inflammatory drug screening platform. (*Manuscript under consideration*)
6. **Yogendra Pratap Singh**, Chris Holland, Biman B. Mandal. "Wild Silk Gelators in Fibroin-Based Biomaterials." (*Manuscript under preparation*)
7. **Yogendra Pratap Singh**, Joseph Christakiran Moses, Nandana Bhardwaj, Biman B Mandal. "Injectable hydrogels: A new paradigm for osteochondral tissue engineering." *Journal of Materials Chemistry B* 6(35), 2018: 5499-5529.
8. **Yogendra Pratap Singh**, Joseph Christakiran Moses, Nandana Bhardwaj, Biman B Mandal. "Overcoming the Dependence on Animal Models for Osteoarthritis Therapeutics–The Promises and Prospects of In Vitro Models." *Advanced Healthcare Materials* 10(20), 2021: 2100961.
9. **Yogendra Pratap Singh**, Ashutosh Bandyopadhyay, Souradeep Dey, Nandana Bhardwaj, Biman B. Mandal. "Trends and advances in silk based bioprinting towards cartilage regeneration." (*Manuscript under revision in Biofabrication*)

(B) Patents:

1. Biman B. Mandal, **Yogendra Pratap Singh**, Ashutosh Bandyopadhyay, Shreya Mehrotra, Joseph Christakiran Moses, Bibhas K. Bhunia, G. Janani, Dimple Chauhan. "Development of silk based bioinks for 3D printing and uses thereof". Patent submitted on 12th October 2018 with application number 201831038727.
2. Biman B. Mandal, **Yogendra Pratap Singh**, Joseph Christakiran Moses, Ashutosh Bandyopadhyay. "3D bioprinted osteochondral *in vitro* osteoarthritis model construct and applications thereof". Patent submitted on 18th June 2021 with application number 202131027358.

(C) Book Chapters:

1. **Yogendra Pratap Singh,** Joseph Christakiran Moses, Ashutosh Bandyopadhyay, Bibrita Bhar, Bhaskar Birru, Nandana Bhardwaj, Biman B. Mandal, Chapter 11 – "State-of-the-art strategies and future interventions in bone and cartilage repair for personalized regenerative therapy", Editor(s): Chandra P. Sharma, Regenerated Organs, Academic Press, 2021, Pages 203-248, ISBN 9780128210857.
2. **Yogendra Pratap Singh**, Ashutosh Bandyopadhyay, Nandana Bhardwaj, Biman B. Mandal. "Silk hydrogel-based delivery of cell and bioactive molecules for osteochondral tissue engineering applications". *Hydrogels for Tissue Engineering and Regenerative Medicine: From Fundamentals to Applications, Elsevier*. (*Chapter submitted*)

(D) Conference Publications:

1. **Yogendra Pratap Singh**, Joseph Christakiran M, Bibhas Kumar Bhunia, Biman B Mandal. "Bi-phasic silk scaffolds for osteochondral tissue engineering." (TERMIS-EU Meeting, 28 June - 1 July 2016) June 2016, *European cells & materials* 06/2016; 31(1):326.
2. **Yogendra Pratap Singh**, Mimi Adhikary, Nandana Bhardwaj, Bibhas Kumar Bhunia, Shreya Mehrotra and Biman B. Mandal. "Bioinspired three-dimensional construct with silk fiber reinforcement for regeneration of load bearing soft tissues." (TERMIS-AM 2017, Charlotte, NC, 3-6 Dec 2017), *Tissue Engineering Part A*. December 2017, 23(S1): S-1-S-159.

(E) <u>Conference, Seminar, Workshop Participation/Presentations:</u>

1. **Yogendra Pratap Singh**, Joseph Christakiran Moses, Biman B. Mandal. 3D bioprinted osteoarthritic *in vitro* biomimetic model as high-throughput anti-inflammatory drug screening platform. *International Conference on Biomedical Materials Innovation (ICBMI-2020)*, Dec 06 to 09, 2020 -Virtual Conference. **(Oral).**
2. **Yogendra Pratap Singh**, Ashutosh Bandyopadhyay, Biman B. Mandal. 3D bioprinting using cross-linker free silk-gelatin bioink for cartilage tissue engineering. *International Conference on Functional Nanomaterials (ICFNM-2019)*, IIT BHU. 22-25 February 2019. **(Poster).**
3. **Yogendra Pratap Singh**, Ashutosh Bandyopadhyay, Biman B. Mandal. Self-gelling silk gelatin bioink for 3D bioprinting of cartilage tissue. *20th White Rose Biomaterials and Tissue Engineering Group (BiTEG 2018)*, University of Sheffield, UK. 17th December 2018. **(Oral).**
4. **Yogendra Pratap Singh**, Joseph C. Moses, Bibhas K. Bhunia, Samit K. Nandi, Biman B Mandal. Seamless biphasic silk construct for the repair of osteochondral defect. *Advanced Functional Polymers for Medicine (AFPM) 2018*, Montpellier, France, 16-18 May 2018. (**Poster**).
5. **Yogendra Pratap Singh**, Mimi Adhikary, Nandana Bhardwaj, Bibhas Kumar Bhunia, Shreya Mehrotra, and Biman B. Mandal. Bioinspired three-dimensional construct with silk fiber reinforcement for regeneration of load bearing soft tissues. *Tissue Engineering and Regenerative Medicine International Society Americas 2017 (TERMIS-AM 2017)*, Charlotte, North Carolina, 3-6 December 2017. (**Poster**).
6. **Yogendra Pratap Singh**, Mimi Adhikary, Nandana Bhardwaj, Bibhas Kumar Bhunia, and Biman B. Mandal. A robust silk fiber-reinforced composite for cartilage tissue engineering. *Research Conclave 2017*, Indian Institute of Technology Guwahati, March 16-19, 2017. **(Poster**).
7. **Yogendra Pratap Singh**, Nandana Bhardwaj, and Biman B. Mandal. Potential of agarose/silk fibroin blended hydrogel for *in vitro* cartilage tissue engineering. *International Conference of Young Researchers on Advanced Materials (IUMRS-ICYRAM 2016)*, Indian Institute of Science, Bangalore, 11-15 Dec 2016. **(Oral).**
8. **Yogendra P. Singh**, Mimi Adhikary, Salma Jasmine, Biman B. Mandal. Silk fibre reinforced silk scaffolds for cartilage tissue engineering. *International Conference on Biomaterials, Biodiagnostics, Tissue Engineering, Drug Delivery and Regenerative medicine (BiTERM*

2016), Indian Institute of Technology (IIT) Delhi, New Delhi, India. **(Poster)- BEST POSTER AWARD.**

9. **Yogendra Pratap Singh**, Joseph Christakiran M, Bibhas Kumar Bhunia, Biman B Mandal. Bi-phasic silk scaffolds for osteochondral tissue engineering. *European Chapter Meeting of the Tissue Engineering and Regenerative Medicine International Society 2016 (TERMIS-EU 2016)*, Uppsala, Sweden, 28 June - 1 July 2016. (**Poster**).
10. **Yogendra P. Singh** and Biman B. Mandal. Silk/agarose hydrogel for cartilage tissue engineering. *Research Conclave-2016*, IIT Guwahati, Guwahati, Assam, India. **(Poster).**

Publications from Other Collaborative Research Projects:

(A) Journal Publications:

1. Piyali Das*, **Yogendra Pratap Singh***, Siddhartha Narayan Joardar, Bikash Kanti Biswas, Rup Narayan Bhattacharya, Samit Kumar Nandi, Biman B. Mandal. "Decellularized caprine conchal cartilage toward repair and regeneration of damaged cartilage." *ACS Applied Bio Materials* 2(5), 2019: 2037-2049. *(*Equal contribution)*
2. Nandana Bhardwaj, **Yogendra Pratap Singh**, and Biman B. Mandal. "Silk fibroin scaffold-based 3D co-culture model for modulation of chondrogenesis without hypertrophy via reciprocal cross-talk and paracrine signaling." *ACS Biomaterials Science & Engineering* 5(10), 2019: 5240-5254.
3. Nandana Bhardwaj, **Yogendra Pratap Singh**, Dipali Devi, Raghuram Kandimalla, Jibon Kotoky and Biman B. Mandal. "Potential of silk fibroin/chondrocyte constructs of muga silkworm *Antheraea assamensis* for cartilage tissue engineering." *Journal of Materials Chemistry B* 4(21), 2016: 3670-3684.
4. Rituparna Duarah, **Yogendra Pratap Singh**, Biman B. Mandal and Niranjan Karak. "Sustainable starch modified polyol based tough, biocompatible, hyperbranched polyurethane with a shape memory attribute." *New Journal of Chemistry* 40(6), 2016: 5152-5163.
5. Rituparna Duarah, **Yogendra Pratap Singh**, Prerak Gupta, Biman B. Mandal, and Niranjan Karak. "High performance bio-based hyperbranched polyurethane/carbon dot-silver nanocomposite: a rapid self-expandable stent." *Biofabrication* 8(4), 2016: 045013.

6. Rituparna Duarah, **Yogendra Pratap Singh**, Prerak Gupta, Biman B. Mandal, and Niranjan Karak. "Smart self-tightening surgical suture from a tough bio-based hyperbranched polyurethane/reduced carbon dot nanocomposite." *Biomedical Materials* 13(4), 2018: 045004. (Special highlight in "MedicalPhysicsWeb")

(B) <u>Book Chapters:</u>

1. **Yogendra Pratap Singh**, Shreya Mehrotra, Jadi Praveen Kumar, Bibhas Kumar Bhunia, Nandana Bhardwaj, Biman B. Mandal. "Tissue engineering therapies for ocular regeneration." Edited By Swaminathan Sethuraman, Uma Maheswari Krishnan, Anuradha Subramanian; *Biomaterials and Nanotechnology for Tissue Engineering*, CRC Press: 2016, pp 173-197 (DOI: 10.1201/9781315368955-9).
2. Piyali Das*, **Yogendra Pratap Singh***, Biman B. Mandal and Samit Kumar Nandi. Chapter 12: "Tissue-derived decellularized extracellular matrices towards cartilage repair and regeneration." Edited by David Caballero, Subhas C. Kundu, Rui L. Reis; *Methods in Cell Biology: Cell-derived Matrices Part B*, Volume 157, Pages 2-247 (2020), Elsevier (https://doi.org/10.1016/bs.mcb.2019.11.005) *(*Equal contribution)*

<u>Selected Awards & Achievements:</u>

1. Awarded **Newton Bhabha Ph.D. Placement Programme 2017-18** by Department of Biotechnology, Government of India and British Council, UK, to carry out research work with *Dr. Chris Holland* at The University of Sheffield, UK for a period of 4 months (Oct 2018 to Jan 2019).
2. Awarded **Raman-Charpak fellowship 2017-18** by Indo-French Centre for the Promotion of Advanced Research (IFCPAR/CEFIPRA) to carry out research with *Prof. Daniele Noel* at the Institute for Regenerative Medicine and Biotherapy (IRMB, INSERM U1183), Montpellier, France, for a period of 6-months (Feb to Aug 2018).
3. **Best poster award** at International Conference on Biomaterials, Biodiagnostics, Tissue Engineering, Drug Delivery and Regenerative Medicine (**BiTERM 2016**), Indian Institute of Technology (IIT) Delhi, New Delhi, India.

4. Team (Silk-Bots), presented our work on "3D Bioprinting" and was awarded the "**Best project from IIT Guwahati**" in **TechExpo 2018** organized by Techniche 2018 at IIT Guwahati from 30th August to 2nd September 2018.
5. Team (Silk-Bioengineers), presented our work on "Tissue Engineering of Organs" and was awarded **2nd position** (Cash prize of Rs. 40,000) in the senior category in **Techexpo 2017** organized by Techniche 2017 at IIT Guwahati from 31st August to 3rd September 2017.
6. Team awarded the **2nd position** (Cash prize Rs. 20,000) in the Technology Incubation Competition held at Indian Institute of Technology Guwahati-Technology Incubation Centre (**IITG-TIC 2016**), Indian Institute of Technology, Guwahati (Silk based affordable tissue grafts and healthcare products).
7. Invited speaker to the "**3D PRINTING WORLD 2019**" -5th International Conference, Show & Awards held on 29th November 2019 @ The Orchid Hotel, Mumbai, on the topic *"Silk based 3D Bioprinting of human load-bearing tissues".*
8. The biphasic silk scaffold work, highlighted as **Journal coverpage** by *Journal of Materials Chemistry B*; and included in the *themed collection*: *Editor's Choice: Scaffold Engineering*.